Distribution Agreement

In presenting this thesis or dissertation as a partial fulfillment of the requirements for an advanced degree from Emory University, I hereby grant to Emory University and its agents the non-exclusive license to archive, make accessible, and display my thesis or dissertation in whole or in part in all forms of media, now or hereafter known, including display on the world wide web. I understand that I may select some access restrictions as part of the online submission of this thesis or dissertation. I retain all ownership rights to the copyright of the thesis or dissertation. I also retain the right to use in future works (such as articles or books) all or part of this thesis or dissertation.

Signature:

_____

Tolulope O. Omosun Date

CROSS-β FOLDS OF AMYLOID AS A VERSATILE SELF-PROPAGATING CATALYST

By

Tolulope O. Omosun
Doctor of Philosophy

Chemistry

_____

Dr. David G. Lynn
Advisor

_____

Dr. R. Brian Dyer
Committee Member

_____

Dr. Vincent Conticello
Committee Member

Accepted:

_____

Lisa A. Tedesco, Ph.D.
Dean of the James T. Laney School of Graduate Studies

_____ Date

CROSS-β FOLDS OF AMYLOID AS A VERSATILE SELF-PROPAGATING CATALYST

By

Tolulope O. Omosun

B.Sc., University of Ibadan, Nigeria 2000

M.Sc., University of Ibadan, Nigeria 2002

Advisor: David G. Lynn, PhD.

An abstract of

A dissertation submitted to the Faculty of the

James T. Laney School of Graduate Studies of Emory University

in partial fulfillment of the requirements for the degree of

Doctor of Philosophy

in Chemistry

2016

Abstract

Cross-β Folds of Amyloid as a Versatile Self-propagating Catalyst

By Tolulope O. Omosun

While the proportion of functional folded structures that exist within protein sequence space may be small, most peptides appear to access the cross-β fold. These stacks of β-sheets, initially identified in protein misfolding diseases, form highly ordered soluble assemblies that can access polymorphically diverse phases whose template-directed propagation as ordered supramolecular paracrystalline phases is highly responsive to environmental fluctuations. The minimal nucleating core (LVFF) of the Aβ peptide of Alzheimer's disease constituted within the peptide Ac-KLVFFAL-NH_2 assembles at neutral pH into homogeneous nanotubes. Each peptide strand is arranged antiparallel in out-of-register sheets, positioning the N-terminal lysine residue outside the H-bonded β-sheet array creating well-defined surfaces on the faces of the hollow nanotubes composed of rows of binding sites, akin to those in naturally occurring enzymes. The amyloid specific dye Congo red (CR) binds to the peptide nanotubes. The proximity of the binding sites was evaluated through polymerization of 6-amino-2-naphthaldeyde, designed to couple end-to-end through imine condensation along the nanotube surface. This substrate in aqueous solutions of peptide nanotubes (Ac-KLVFFAL-NH_2, Ac-HLVFFAL-NH_2 and Ac-RLVFFAL-NH_2) react to form dimers while the analogous 6-*N*,*N*-dimethylamino-2-naphthaldehyde substrate binds the nanotubes without condensation.

The catalytic range of the peptide assemblies was further explored with methodol for retro-aldol catalysis. These β-rich assemblies show detectable retro-aldolase activity.

Subtle changes in peptide sequence and/or assembly conditions significantly impact final morphology, catalyst efficiency and enantioselectivity. These lysine-rich amyloid assemblies also enantioselectively catalyze aldol condensation of 2-acetonaphthone and 6-methoxy-2-naphthaldehyde. Metal ions such as Cu^{2+}, Zn^{2+}, Ni^{2+} and Co^{2+} modulates the assemblies of Ac-Aβ(13-21)H14A and NH_2-Aβ(13-21)K16A peptides into fibers and ribbons. The Cu^{2+}-Aβ assemblies are capable of redox activity similar to cupro-enzymes while the Zn^{2+}-Aβ fibers catalyzed retro-aldol cleavage reminiscent of class II aldolase, further extending the catalytic range of these self-propagating Aβ assemblies.

These results suggest that simple self-propagating peptide assemblies can produce new enzymes, while also providing a new perspective on the metabolic functions that underlie the fifty odd amyloid diseases. And maybe more importantly, they implicate amyloid as a primitive infective life form, struggling to survive in the nutrient rich eukaryotic cell, acquiring new chemical functions as cellular complexity grows.

CROSS-β FOLDS OF AMYLOID AS A VERSATILE SELF-PROPAGATING CATALYST

By

Tolulope O. Omosun

B.Sc., University of Ibadan, Nigeria 2000

M.Sc., University of Ibadan, Nigeria 2002

Advisor: David G. Lynn, PhD

A dissertation submitted to the Faculty of the

James T. Laney School of Graduate Studies of Emory University

in partial fulfillment of the requirements for the degree of

Doctor of Philosophy

in Chemistry

2016

For Yusuf, John and Ayrton.

Acknowledgements

My scientific endeavors during these past six years would not have arrived at this pinnacle without the support of my research group, collaborators, friends and family. First and foremost, I would like to express my deepest appreciation to my advisor, Dr. David Lynn (Dave), for giving me the opportunity to do research in his lab. His brilliant and somewhat crazy ideas, his patience, humility, good humor, enthusiasm and immense knowledge has been a constant source of motivation for me. He has contributed a great deal to my development as a scientist by continually challenging my ideas and work, encouraging and teaching me how to critically think about the problems I find most interesting, thereby giving me the freedom to explore subject matters on my own and providing the guidance necessary to recover when my steps faltered. I could not have imagined a better mentor and advisor for my PhD research work.

I would also like to thank my committee members, Dr. Vince Conticello and Dr. Brian Dyer for their insightful comments and encouragement. Their constructive criticisms at different stages of my research have benefited me immensely greatly and helped focus my ideas.

I am grateful to Dr. Anil Mehta for helping me develop my background in peptide self-assembly; and also for the long discussions that helped me sort out the “technical” details involved in my study, and also for reading and commenting on countless revisions of my thesis. I would also like to thank Dr. Seth Childers for the initial idea of the project and for always willing to help and give his best suggestions whenever necessary. I would also like to thank Dr. Dibyendu Das for his encouragements and practical ideas, for being

my counselor who calmed me down whenever I got frustrated. I also would like to appreciate Dr. Jay Goodwin for his interest in my project and for all the positive feedback. Special thanks to Dr. Neil Anthony for training me to use fluorescence microscopy efficiently for my study.

I appreciate the all the friendships and support of the Lynn lab members both past and present. I have enjoyed all the time I spent together with Dr. Yue Liu, Phoebe Young, Dr. Daniel Pierce and Allisandra Rha, I could not have asked for better office mates. I have enjoyed working with Li Zhang, my brother from another mother; Ting “Fish” Pan for all the help she rendered on synthesizing some of the compounds needed for my work; my fellow Team Peptide members including Rolando Rengifo, Chen Liang, Noel Li, Sha Li, Allisandra Rha and the newest member, Anthony Sementilli. I also extend my thanks to other past Lynn lab members with whom I have had the chance to interact with including Dr. Yi-Han Lin, Anthony, Masha Massey, Dr. Jillian Smith, Dr. Erin Schuler, Dr. James Simmons and Dr. Junjun Tan to mention a few.

I have enjoyed the friendship with Dr. Savannah Johnson, Dr. Chenrui Chen and Dr. Sha (Lisa) Li. We have shared many adventures together, and I will always remember all the useful discussions and fun I had riding with Savannah to and from many lab functions. I also cannot forget the time spent with Chenrui and Lisa in Hawaii, the snorkeling experience with you guys was the craziest adventure ever for a non-swimmer like me. You guys made the time I spent in the lab go by effortlessly and I would like to think that I have gained friends for life.

Special thanks to our collaborators, Dr. Martha Grover and Ming-Chien Hsieh, for developing the models for kinetic evaluation of my observed catalysis. I would also like to extend my gratitude to Hong Yi and Jeanette Taylor for helping with my microscopy and diffraction experiments; Fred Strobel for mass spectrometric analysis; John Bacsa for x-ray diffraction; and Steve Krebs for making it easy to stock up on materials necessary for my research work. Without you guys, my materials and methods section would have been cut in half. Special thanks also go to Mike (echelp) for assisting me when my computer got hijacked by the ransom virus. Even though we never could recover the files, I am still very grateful for the effort and time you spent in the endeavor. I also have enjoyed the interaction with Dr. Shaoxiong Wu during my time as the NMR service instructor.

I cannot continue this acknowledgement without mentioning my close friends outside of Emory. I appreciate the members of Jesus Family Chapel (JFC) for their prayers and support. I am very grateful to Vivid Oguntoyinbo, Chizube Iriemenam, Adeola Adekoya, Mojisola Bakare, Nike Fashakin and Franca Chigbu for all their support in taking care of my kids while I was away in the lab.

Finally, I would like to extend a very special thanks to my family. Words cannot express how grateful I am to my mother (Mrs. Phebean Olusoga) and mother-in-law (Mrs. Rose Omosun) for all the sacrifices they have made on my behalf, always ready to board a plane and travel from Nigeria to come and render assistance whenever I get overwhelmed with juggling my research work and caring for my family. I would also like to thank my loving dad (Mr. Zacheus Olusoga) for his constant prayers and words of encouragement. Gratitude also goes to my sister (Mrs. Titilayo Johnny) and brothers (Seye, Segun and Seun Olusoga) for always supporting and encouraging me with their best wishes.

My utmost appreciation goes to my amazing husband; Dr. Yusuf Omosun; and sons; John and Ayrton Omosun; for their endless support, love and encouragement each and every day. They have been amazing in so many ways, they have given up a lot for me to achieve my dreams, always cheering me up and standing by me through the whole experience. This dissertation would not have been possible without your support and loyalty and I would like to say that I love you all dearly, and would always be there for you munchkins, now that I “hopefully” might have more time (lol).

Table of Contents

List of Figures

Chapter 1

Chapter 2

Chapter 3

Chapter 4

Chapter 5

Chapter 6

List of Tables

Abbreviations

Å	Angstrom
aa	amino acids
Aβ	amyloid-β
AD	Alzheimer's disease
AFM	atomic force microscopy
AI	Antiparallel In-registry
AO	Antiparallel Out-of registry
APP	amyloid precursor protein
Arg	Arginine
CD	circular dichroism
CHCA	Cyano-4-hydroxycinnamic acid
CR	Congo red
Cryo-SEM	Cryo-scanning electron microscope
Dab	2, 4-diaminobutyric acid
Dap	2, 3-diaminopropionic acid
DCM	Dichloromethane
DIPEA	N,N-diisopropylethylamine
DMF	Dimethylformamide
DMSO	Dimethyl sulfoxide
EDT	1,2-ethanedithiol
FSPS	Fmoc solid phase synthesis

FMOC	9-fluorenylmethoxycarbonyl
FT-IR	Fourier Transform Infrared Raman Spectroscopy
GdnHCl	guanidine hydrochloride
HBTU	2-(1H-Benzotriazol-1-yl)-1,1,3,3-TetramethylUronium hexafluorophosphate
HFIP	hexafluoroisopropanol
HPLC	high-performance liquid chromatograph
Hr	hour
IAPP	islet amyloid polypeptide
IE-IR	isotope-editing IR
LRD	lamination repeating distance
Lys	lysine
MALDI-TOF	matrix assisted laser desorption ionization - time of flight mass spectrometry
MD	molecular dynamics
MeCN	Acetonitrile
MES	2-(N-morpholino)ethanesulfonic acid
Min	minute
mM	milli molar
mL	milliliter

NADH	nicotinamide adenine dinucleotide
NMR	Nuclear Magnetic Resonance
Orn	Ornithine
PI	Parallel In-registry.
PrP	Prion Protein
RP-HPLC	reversed-phase high-performance liquid chromatograph
SAXS	small angle X-ray scattering
SEM	scanning electron microscopy
STEM	scanning and transmission electron microscopy
ss-NMR	solid state Nuclear Magnetic Resonance
TEM	transmission electron microscopy
TFA	trifluoroacetic acid
TLC	thin layer chromatograph
UV	ultra-violet
μL	microliter
μM	micromolar

Chapter 1

Introduction

Enzyme Catalysis

Enzymes are the most highly specialized biological macromolecules that have been developed by nature over billions of years [1, 2]. These proteins catalyze chemical reactions within the biological systems with extraordinary regio and stereo-selectivity and thus over the past several decades, have inspired chemists to mimic and extend these remarkable processes.

Enzymes differ from ordinary synthetic chemical catalysts in several ways. First, the rates of chemical reactions are accelerated by factors of up to 10^{20} compared to a corresponding uncatalyzed reaction [3]. Second, the reactions occur under very mild conditions in aqueous solutions, at low temperatures generally below 100 °C under atmospheric pressure, and at nearly neutral pH. Third, enzymes are structurally specific, for example discriminating between sulfate and phosphate [4], and the reactions catalyzed are generally more stereospecific and stereoselective than synthetic catalysts [5].

The catalytic activities of enzymes depend on their primary, secondary, tertiary and quaternary structure. Proteins fold into precise forms to create a substrate binding site, an active site that can include ten to twelve amino acids. Four or more residues are generally catalytic [6], and their role may be in transition state stabilization through general acid/base events, nucleophilic covalent catalysis [7, 8], or other events for

transition states stabilization. Some residues may polarize the substrate or change the orientation of other residues in order to maximize catalysis [6].

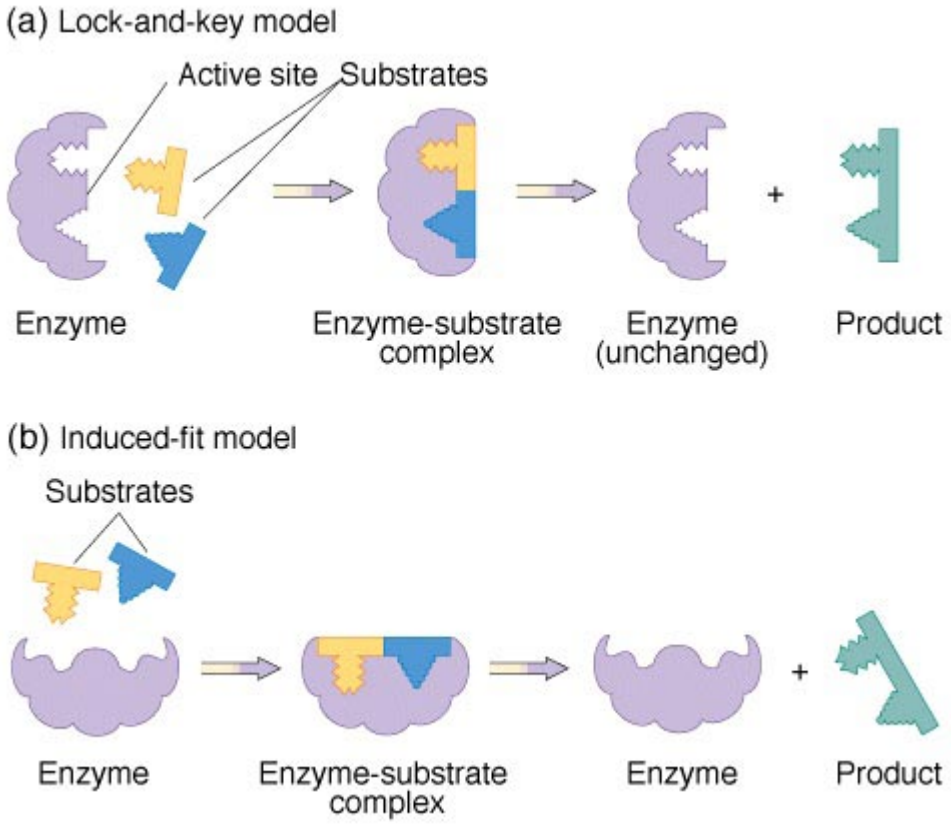

Figure 1-1: *Enzyme catalyzing the reaction of two substrates forming one product. http://leavingbio.net/enzymes.htm*

Substrate recognition can be covalent or non-covalent, and mediated by intermolecular forces including electrostatic interactions, van der Waals forces [9], hydrogen bonding, hydrophobic interactions [10], and π-stacking [11] to lower the activation energy. For example, in the serine protease family, the binding pocket of chymotrypsin contains hydrophobic amino acids that interact with the hydrophobic side chains of its preferred substrates. In contrast, the binding pocket of trypsin contains a

negatively charged acidic amino acid (aspartate), which is able to form an ionic bond with the lysine or arginine residues of its substrates (Figure 1-2).

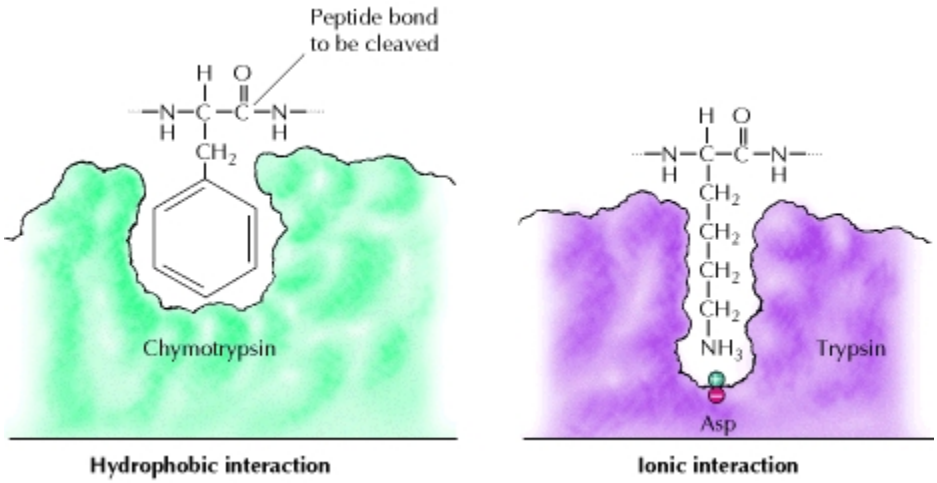

Figure 1-2: *Substrate binding by serine proteases.*

Many enzymes exploit cofactors, organic molecules or metal ion such as Zn^{2+}, Fe^{2+}, Cu^{2+} and Mn^{2+} that binds to the active site and are essential for catalysis. The use of cofactors allows enzymes to expand the catalytic abilities beyond the 20 naturally occurring amino acids [12].

Significant effort has focused to generating artificial enzymes [13-20], but few have the catalytic factors of enzymes. The major problem is how to achieve the long polymers that fold properly. The question is can unique strategies emerge with supramolecular assemblies to address this problem? It is not clear however that self-assembly will compete directly with long polymer folded enzymes.

Supramolecular catalysis

Supramolecular chemistry was initially defined by Jean-Marie Lehn as "the chemistry of intermolecular bond, covering structures and functions of the entities formed by association of two or more chemical species" in his Nobel lecture in 1987 [21]. Supramolecular catalysis generally refers to an application of supramolecular chemistry, especially molecular recognition and guest binding, toward catalysis [22]. It involves the assembly of catalyst species by harnessing multiple weak intramolecular interactions [23-37] and has recently been dominated by enzyme-inspired approaches which often attempt to design and create catalysts with an enzyme-like ‘active site’ and have concentrated on reactions similar to those catalyzed by enzymes themselves. To make supramolecular systems capable of mimicking the catalytic ability of natural enzymes, macromolecular receptors are developed in which the substrates binding site is placed close to a reactive site such that the substrate’s functional group is positioned in close proximity to the reactive group of the host to increase the possibility that the reaction could occur and thus the reaction rate is enhanced. In most cases, the catalyst is preorganized such that no major conformational changes are required for the reaction to occur [38, 39]. Such self-assembled reaction vessels developed to simulate the performance of enzymes include cyclodextrins [40, 41], metal-organic frameworks [42-44], inorganic nanoparticles [45-47], synthetic nanostructures [48, 49], dendrimers [50], micelles [51, 52], nanofibers [53, 54], and nanotubes [55-58]; however, the overall performance of these artificial catalytic systems does not generally reach the catalytic efficiency of natural enzymes [59, 60]. The question is can we have a simple, low-cost, dynamic system that efficiently generates highly ordered structures as tunable enzymes?

Amyloids

Amyloid fibrils are highly ordered self-assembled filamentous aggregates formed by peptides and proteins with diverse amino acid sequences [61]. Amyloid formation is implicated in a variety of diseases including Alzheimer's disease (AD), type 2 diabetes, prion diseases, Parkinson syndrome, Creutzfeldt–Jakob disease and other protein misfolding disorders [62]. AD is probably the best known as a fatal and progressive neurodegenerative disorder that imparts approximately 26 million people worldwide [63]. The deposition of extracellular protein plaques of the amyloid-β (Aβ) peptide is necessary but may not be sufficient to cause the disease [64]. The amyloid fibers can be visualized with the sulfonated azo dye Congo Red (CR), which imparts a distinct apple-green birefringence to amyloid deposits under cross-polarized filters [65, 66], or the fluorescent dye Thioflavin T (ThT) [67] which fluoresces on binding.

Aside from being implicated in diseases, amyloids are beneficial to many organisms. For example, curli fibers features for biofilm formation and cell adhesion in *E.coli* [68-72], hydrophobin produced to form amphipathic surface layer protecting its cell surface in fungi [73-78]. HpaG, a harpin from *Xanthomonas spp* is a cytotoxin that elicits the hypersensitive response in plant [79, 80], HETs from *P. anserina* function in hyphal fusion [81-85], and MSP2 from *Plasmodium falciparum* is critical for erythrocyte invasion [86]. Overall, amyloids are defined by cross β-sheet X-ray fiber-diffraction pattern and generally lack sequence homology. Even with this broad general propensity for folding, there are specific codes that control the assembly of amyloid.

Supramolecular Assembly of Simple Aβ Peptides

Aβ(16-22) or KLVFFAE, a peptide sequence derived from the nucleating core of the 39-42 residue Aβ peptide implicated in Alzheimer's disease, can assemble into highly organized supramolecular assemblies and have been well studied [87-92]. By acetylating the N-terminus and capping the C-terminus as an amide, the only changes are on the lysine and glutamic acid side chains. Figure 1-3A shows the TEM image of Ac-KLVFFAE-NH_2 peptide assembled at neutral pH, the peptide assemble into twisted 5 nm-diameter fibers that are morphologically similar to those formed by the full length Aβ peptide. Figure 1-3D is the TEM image of Ac-KLVFFAE-NH_2 peptide assembled at acidic pH, the peptide assemble into soluble hollow 52 nm-diameter nanotubes. Solid-state NMR analyses assign the fiber and nanotube β-sheets as anti-parallel [93]. The fibers assembled at pH 2 contain in-register β-sheets stabilized by K-E cross-strand salt bridges shown in Figure 1-3B. However, the nanotube strands are shifted out-of-register as shown in Figure 1-3E.

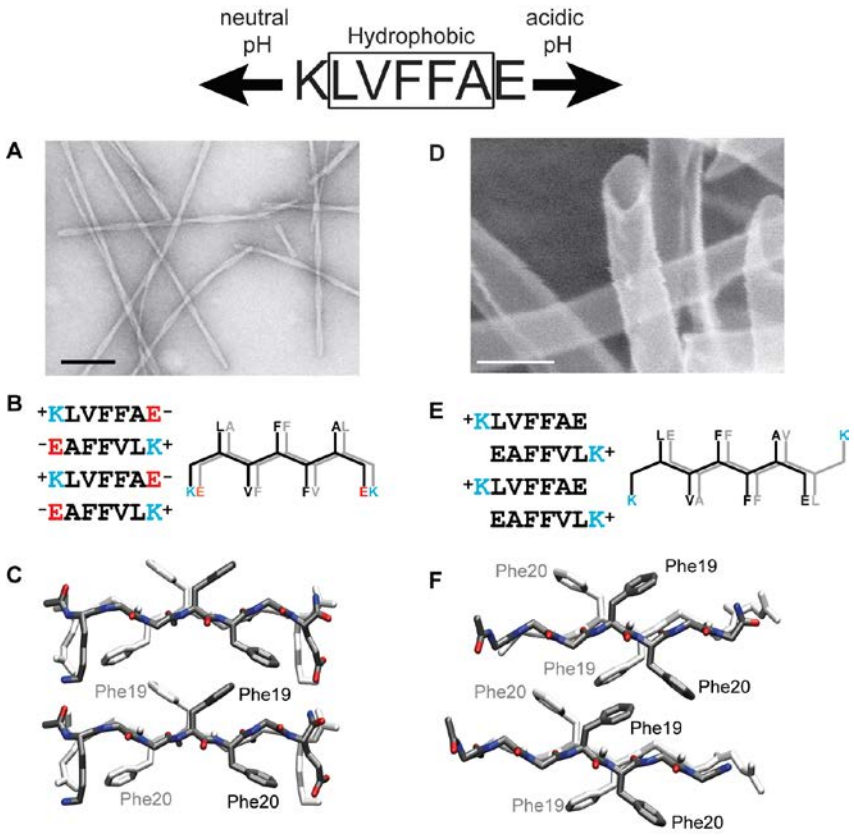

Figure 1-3: *Transmission Electron Microscopy images highlighting the pH-dependent morphology of KLVFFAE, Aβ(16-22), fibers (**A**), and nanotubes (**D**). The arrangement of the peptide within the fiber assembly depicting how the salt bridges between the Lysine (K) and Glutamic acid (E) directs antiparallel in-register β-sheets (**B**) whereas the packing of the β-branched valine against the less bulky alanine directs an out-of register orientation (**E**). Structures from molecular dynamics simulations that match the laminate diffraction distance of ~10 Å for (**C**) fibers and (**F**) tubes, highlighting the phenylalanine orientations. Scale bars in (**A**) and (**D**) are 100 nm. Reprinted from Mehta et al., (2008) Facial Symmetry in Protein Self-Assembly. JACS 130(30): 9829-9835 with permission from American Chemical Society.*

Scattering analyses show a bilayer architecture for the nanotubes [87] exposing the terminal lysine on the tube surface with half of the charged lysine side chains buried within a bilayer interface (Figure 1-4).

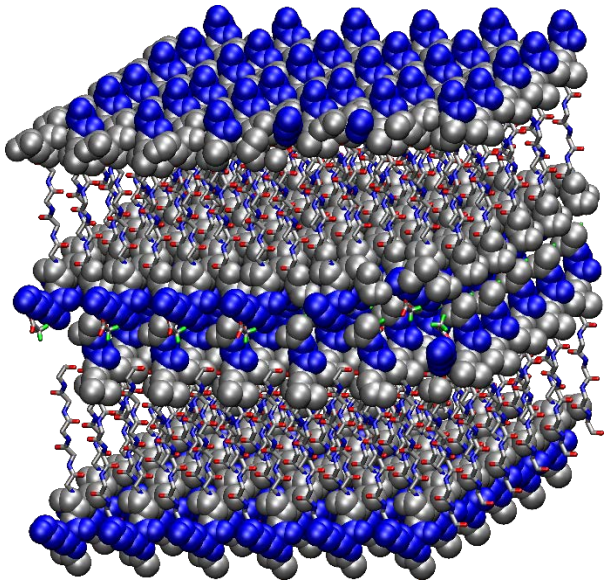

Figure 1-4: *Structural model of the Ac-KLVFFAE-NH_2 showing the bilayer with half of the lysine buried (represented by the blue)*

The registry switch in Ac-KLVFFAE-NH_2 peptide assembly from fiber to nanotube is correlated with the protonation of the glutamic acid. This suggests that cross-strand pairing directs the β-sheet configuration.

Cross-strand Pairing in Peptide Assembly

Cross-strand pairing contributes considerably to β-strand registry [93, 94] and this was first established by replacing glutamic acid in the K-E salt-bridge in Aβ(16-22) with leucine or valine, the E22L and E22V, which gave exclusively homogenous nanotube assemblies independent of pH [93]. The shift to out-of-register has been assigned to cross-strand interactions between the β-branched V18 residue and its preferential packing against alanine in the adjacent strand [94] (Figure 1-3E, 1-5B). Substituting V18 with a bulkier *t*-butyl side chain, assembles as the out-of-register strands even overcoming the

K-E cross-strand pairing at low pH. Consequently, the strand registry is dictated by the steric advantage of packing side-chain residues at position 18 against the less bulky alanine-at position 21. Replacing E22 with Q, a residue common in larger prions, the E22Q peptide assemble into parallel in-register strands [95]. In this instance, the strand orientation was dictated by the self-complementary cross-strand pairing of Q–Q (Figure 1-5C). Cross-Strand pairing therefore significantly contributes to the amount of cross-β polymorphs that can be accessible.

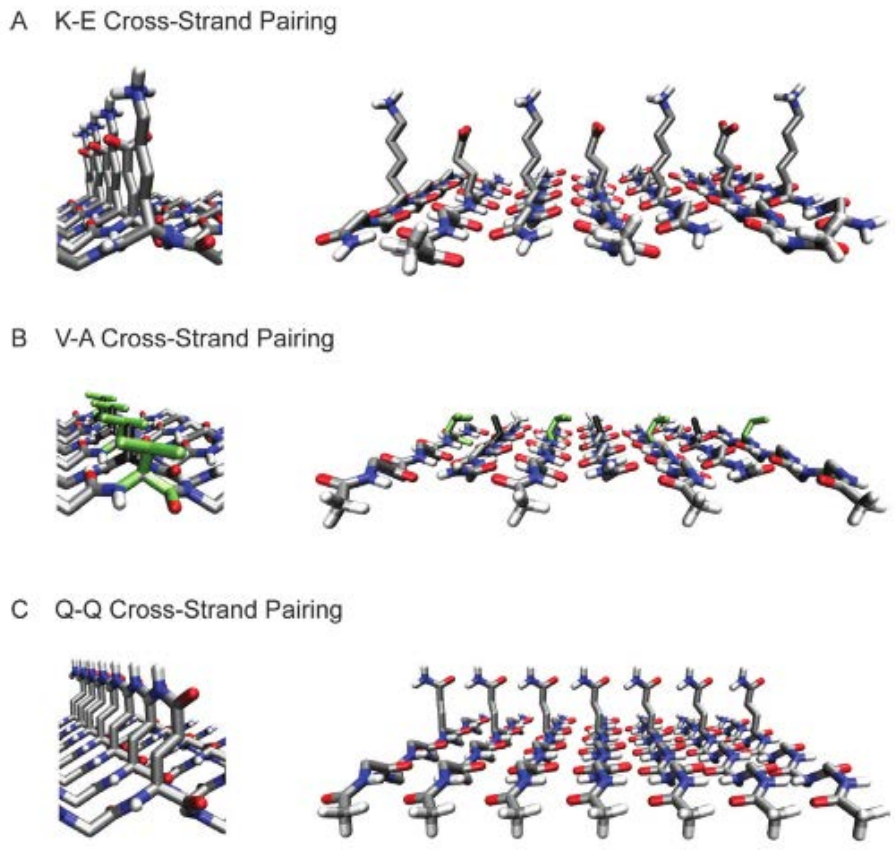

Figure 1-5: *The concept of programming peptide ß-sheet organization within molecular assemblies through incorporation of cross-strand pairing interactions. (**A**) Salt bridge interactions between K-E and (**B**) packing of bulky ß-branched amino acids preferably against less bulk amino acids, and (**C**) Side-chain hydrogen bonding via glutamine. Adapted and modified with permission from Childers et al. (2012). Towards Intelligent Materials, in Molecular Self-Assembly. Pan Stanford Publishing. Pages 1-36*

Based on cross-strand pairing, different phases can be accessible to amyloids. These well-ordered phases can present distinct solvent-accessible faces.

Solvent Accessible Faces in Cross-β Assemblies

Amyloid assemblies contain two pairs of solvent exposed surfaces, the pleat surface lined with side chains emerging from the β-sheet pleats and the termini surface that exposes the N- and C- terminal residues of the β-sheet laminates [96]. As shown in Figure 1-6A, the anti-parallel β-sheet fibers display the pleat surface and the termini surface. The pleat surfaces contain alternate amino acid side chains of the peptide backbone projecting from each pleat of the backbone (Figure 1-6B), and the termini surfaces are made up of the accumulated ends of the peptide strands (Figure 1-6C). Figure 1-7A–C show the surfaces present by the antiparallel β-sheet fibers seen in Aβ(16-22), the two termini surfaces are identical and are composed of residues K-16 and E-22, but the two pleat surfaces display the side chains of either KVFE or LFA residues giving rise to at least three distinct surfaces [93]. However, for the parallel β-sheet assemblies, seen in Aβ(16-22)E22Q [95], there are four different faces with one of the termini surfaces composed of K while the other displays Q. As shown in Figure 1-7D and E, the symmetry of the nanotube is very different from those of the fibers because the solvent-exposed surfaces are reduced. Due to increase in the number of β-sheets laminates, the resulting helical ribbons fuse into nanotubes. The pleat surfaces are sequestered away from solvent and sealed upon tube formation leaving only the termini surfaces exposed. These different surfaces presented by peptide assemblies create opportunities for ligand binding or recruitment of exogenous molecules and other molecular recognition events such as chemo or biosensing and catalysis.

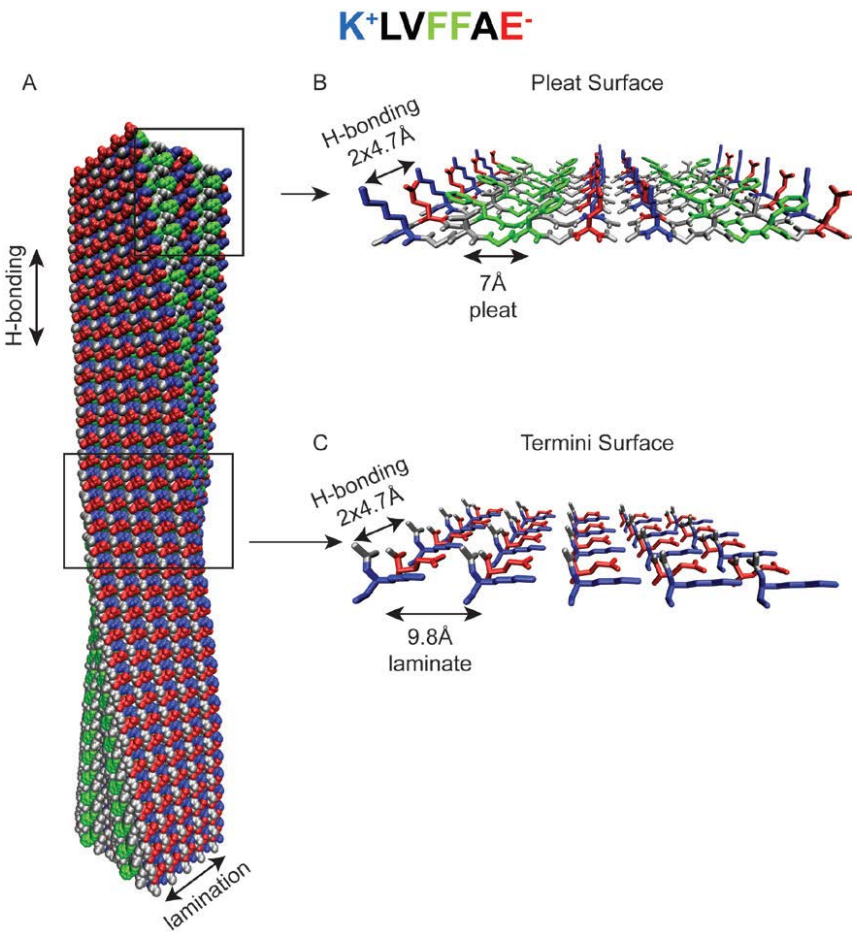

Figure 1-6: *(**A**) Structural model of the KLVFFAE 5 nm x 5 nm cross-β fiber consistent with dimensions from electron microscopy (Figure 1-3A) [23]. H-bonding between β-strands runs along the fiber long axis and β-sheet stacking (lamination) is perpendicular to the H-bond axis. H-bonding places the peptide repeat at 4.7 Å (**B**) Polar pleat surface, as highlighted in Figure 1-3B, is composed of lysine (blue), valine (gray), phenylalanine (green), and glutamic acid (red) residues. The remaining residues are displayed on the opposite β-sheet face. The pleat channels are defined by the exposed amino acid side chains, which are spaced every 7 Å. As illustrated in Figure 1-8, the pleat surfaces are hidden when the number of laminates increases and helically coil into tubes. (**C**) The termini surface is composed of peptide termini, lysine (blue) and glutamic acid (red) residues, and capping groups (gray). The β-sheets are stacked on top of each other and separated by 9.8 Å. Reprinted with permission from Childers et al. (2012). Towards Intelligent Materials, in Molecular Self-Assembly. Pan Stanford Publishing. Pages 1-36*

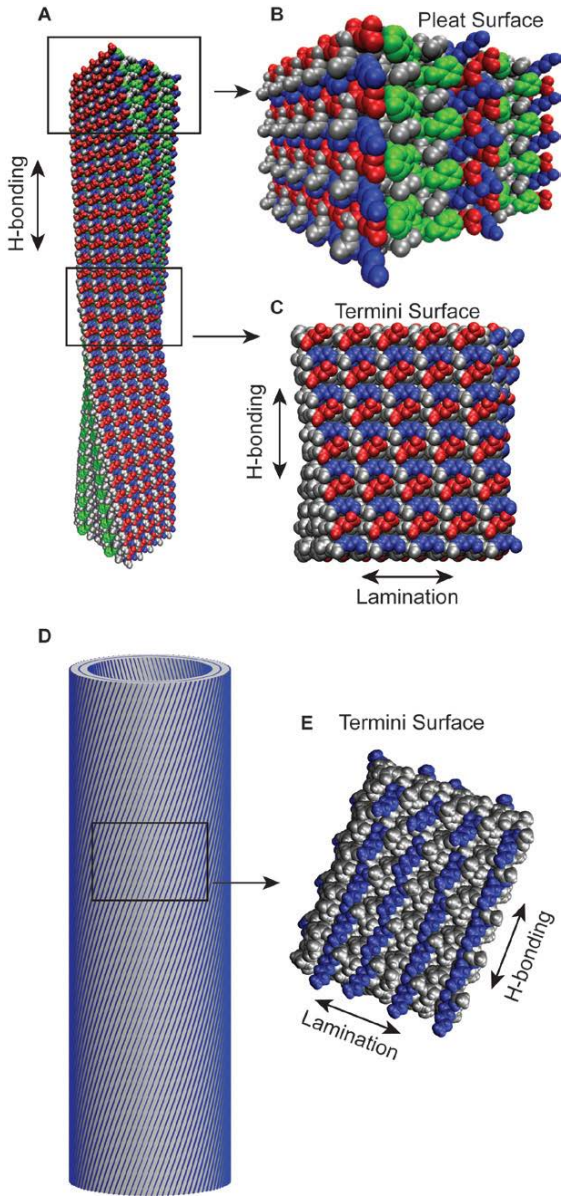

Figure 1-7: *(**A**) Fiber-pleat (**B**) and -termini (**C**) surfaces vs. tube termini (**D, E**) surface of KLVFFAE. Extended β-sheet lamination in the tube hides the pleat surface, exposing only the termini surface which is composed of only the side chains at the peptide termini and displays the laminate grooves. The antiparallel β-sheets results in both N and C terminal residues being displayed at the termini surfaces, resulting in the blue (lysine) and red (glutamic acid) alternating pattern (**A–C**) for the fibers. The tubes which are also anti-parallel, but out-of-register β-sheets, result in prominently displayed lysines (**D, E**). Parallel β-sheets (not shown) would have unique termini surfaces composed of the N and C terminal side chains, respectively. The protonation of the charged glutamic acid in KLVFFAE nanotubes or mutation to non-charged leucine (KLVFFAL), results in distinct surface charge modulation. This charge enables binding of negatively charge Au nanoparticles. Reprinted with permission from Childers et al. (2012). Towards Intelligent Materials, in Molecular Self-Assembly. Pan Stanford Publishing. Pages 1-36*

Ligand Binding in Cross-β Assemblies

In Aβ(16-22)E22L, the floor of the surface is composed of Leucine-17 (gray) and Leucine 22 (gray) side chains, creating a hydrophobic groove. The N-terminal lysines are located outside of the H-bonded array so arranging each peptide strand as antiparallel out-of-register within the β-sheets places the lysines on the tube hydrophobic surface like the knobs of a herringbone stitch (Figure 1-8, inset) creating an extended binding crevice such that there are repeating array of binding sites on the tube surface. Optical signatures and linear dichroism analyses showed that the bound CR are aligned along the laminate grooves parallel to the amyloid long axis. (Figure 1-8). The structural model places the CR spanning across six peptides (5 × 4.7 Å), compatible with each sulfate charge specifically associating with the positively charged lysines that line the laminate grooves. It was determined that CR association completely passivates the grooves of the surface in such a way as to hold the CR molecules proximally both end to end and side to side.

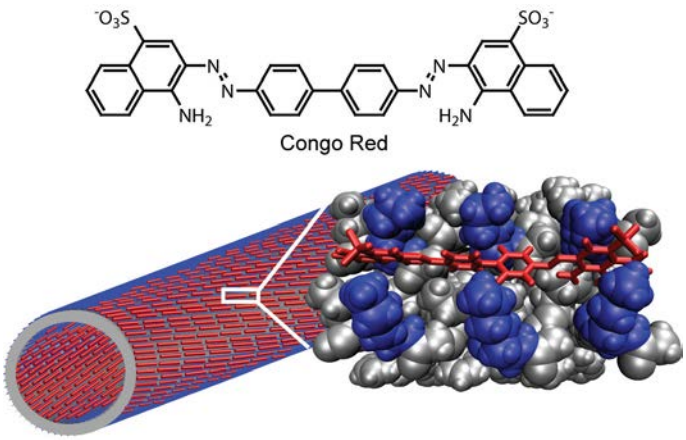

Figure 1-8: *Model of the Congo red, KLVFFAL laminate-groove binding site. The residues in close proximity to CR are shown in space-filling format as follows: hydrophobic residues (gray), lysines (blue), Congo red (red, displayed in stick format). Reprinted from Childers et al. (2009). Templating Molecular Arrays in Amyloid's Cross-β Grooves. JACS 131(29):10165-10172 with permission from American Chemical Society.*

To demonstrate specificity in binding, Thioflavin-T, another histochemical dye used extensively for amyloid, does not bind to the nanotubes whereas the fluorescent Alexa dyes, which bear more structural resemblance to CR, bind strongly and extensively along the grooves [97].

In summary, amyloid assemblies share many common structural features of well folded enzymes including the capacity to bind and interact with small molecules and metal binding sites [98-100]. However, in contrast to enzymes which contain highly specific and effective single active sites, the amyloid assemblies contain multiple binding sites all organized side-by-side in a grid arrangement and in close proximity allowing them to bind small molecules in high density. Also, amyloid assemblies creates a two-dimensional organized array of metals at well-defined intervals along the entire solvent-accessible interface. These arrays of binding sites in amyloids increases the possibility of a chemical reaction occurring. In addition, these amyloidogenic peptides are easily synthesized can be engineered and chemically or biologically modified to fine-tune its functionality. Therefore, my research focus is to exploit these arrays of binding sites on amyloid surface in the construction of supramolecular peptide catalyst model capable of manipulating C-C and C-N bonds reactions in an ecologically friendly media.

References

1. Scheper, T., *New Enzymes for Organic Synthesis: Screening, Supply and Engineering*. 1999: Springer.

2. Copley, S.D., *Toward a Systems Biology Perspective on Enzyme Evolution.* Journal of Biological Chemistry, 2012. **287**(1): p. 3-10.

3. Lad, C., N.H. Williams, and R. Wolfenden, *The rate of hydrolysis of phosphomonoester dianions and the exceptional catalytic proficiencies of protein and inositol phosphatases.* Proceedings of the National Academy of Sciences, 2003. **100**(10): p. 5607-5610.

4. Ringe, D. and G.A. Petsko, *How Enzymes Work.* Science, 2008. **320**(5882): p. 1428-1429.

5. Voet, D. and J.G. Voet, *Biochemistry*. 2010: Wiley.

6. Gutteridge, A. and J.M. Thornton, *Understanding nature's catalytic toolkit.* Trends Biochem Sci, 2005. **30**(11): p. 622-9.

7. Bartlett, G.J., et al., *Analysis of catalytic residues in enzyme active sites.* J Mol Biol, 2002. **324**(1): p. 105-21.

8. Holliday, G.L., J.B. Mitchell, and J.M. Thornton, *Understanding the functional roles of amino acid residues in enzyme catalysis.* J Mol Biol, 2009. **390**(3): p. 560-77.

9. Mader, M.M. and P.A. Bartlett, *Binding Energy and Catalysis: The Implications for Transition-State Analogs and Catalytic Antibodies.* Chem Rev, 1997. **97**(5): p. 1281-1302.

10. Davis, A.M. and S.J. Teague, *Hydrogen Bonding, Hydrophobic Interactions, and Failure of the Rigid Receptor Hypothesis.* Angewandte Chemie International Edition, 1999. **38**(6): p. 736-749.

11. Heginbotham, L. and R. MacKinnon, *The aromatic binding site for tetraethylammonium ion on potassium channels.* Neuron, 1992. **8**(3): p. 483-91.

12. Holliday, G.L., et al., *Evolution of enzymes and pathways for the biosynthesis of cofactors.* Nat Prod Rep, 2007. **24**(5): p. 972-87.

13. Breslow, R. and S.D. Dong, *Biomimetic Reactions Catalyzed by Cyclodextrins and Their Derivatives.* Chem Rev, 1998. **98**(5): p. 1997-2012.

14. Gerlt, J.A. and P.C. Babbitt, *Enzyme (re)design: lessons from natural evolution and computation.* Curr Opin Chem Biol, 2009. **13**(1): p. 10-8.

15. Wu, Z.P. and D. Hilvert, *Conversion of a protease into an acyl transferase: selenolsubtilisin.* Journal of the American Chemical Society, 1989. **111**(12): p. 4513-4514.

16. Kirby, A.J., *Enzyme Mechanisms, Models, and Mimics.* Angewandte Chemie International Edition in English, 1996. **35**(7): p. 706-724.

17. Qi, D., et al., *Generation of new enzymes via covalent modification of existing proteins.* Chem Rev, 2001. **101**(10): p. 3081-111.

18. Murakami, Y., et al., *Artificial Enzymes.* Chem Rev, 1996. **96**(2): p. 721-758.

19. Wulff, G., *Enzyme-like catalysis by molecularly imprinted polymers.* Chem Rev, 2002. **102**(1): p. 1-27.

20. Liu, X., et al., *Incorporation of Tellurocysteine into Glutathione Transferase Generates High Glutathione Peroxidase Efficiency.* Angewandte Chemie International Edition, 2009. **48**(11): p. 2020-2023.

21. Lehn, J.-M., *Supramolecular Chemistry—Scope and Perspectives Molecules, Supermolecules, and Molecular Devices (Nobel Lecture).* Angewandte Chemie International Edition in English, 1988. **27**(1): p. 89-112.

22. Hastings, C.J., et al., *Enzymelike catalysis of the Nazarov cyclization by supramolecular encapsulation.* J Am Chem Soc, 2010. **132**(20): p. 6938-40.

23. Dhotel, A., et al., *Molecular Motions in Functional Self-Assembled Nanostructures.* International Journal of Molecular Sciences, 2013. **14**(2): p. 2303-2333.

24. Jiang, J., et al., *Dipole-induced, thermally stable lamellar structure by polar aromatic silane.* J Am Chem Soc, 2009. **131**(3): p. 900-1.

25. Vericat, C., et al., *Self-assembled monolayers of thiols and dithiols on gold: new challenges for a well-known system.* Chem Soc Rev, 2010. **39**(5): p. 1805-34.

26. Van Oss, C.J., R.J. Good, and M.K. Chaudhury, *The role of van der Waals forces and hydrogen bonds in "hydrophobic interactions" between biopolymers and low energy surfaces.* Journal of Colloid and Interface Science, 1986. **111**(2): p. 378-390.

27. Silverstein, T.P., *The Real Reason Why Oil and Water Don't Mix.* Journal of Chemical Education, 1998. **75**(1): p. 116.

28. Beaujuge, P.M. and J.M.J. Fréchet, *Molecular Design and Ordering Effects in π-Functional Materials for Transistor and Solar Cell Applications.* Journal of the American Chemical Society, 2011. **133**(50): p. 20009-20029.

29. Jiang, J., et al., *Self-assembled nanolayers of conjugated silane with pi-pi interlocking.* ACS Nano, 2010. **4**(7): p. 3773-80.

30. Pluth, M.D. and K.N. Raymond, *Reversible guest exchange mechanisms in supramolecular host-guest assemblies.* Chem Soc Rev, 2007. **36**(2): p. 161-71.

31. Ferri, T., et al., *Spatially oriented and reversible surface assembly of single-walled carbon nanotubes: a strategy based on pi-pi interactions.* Angew Chem Int Ed Engl, 2011. **50**(31): p. 7074-8.

32. Rose, G.D., et al., *A backbone-based theory of protein folding.* Proc Natl Acad Sci U S A, 2006. **103**(45): p. 16623-33.

33. Deng, R., et al., *Mesoporous block copolymer nanoparticles with tailored structures by hydrogen-bonding-assisted self-assembly.* Adv Mater, 2012. **24**(14): p. 1889-93.

34. Deechongkit, S., et al., *Context-dependent contributions of backbone hydrogen bonding to beta-sheet folding energetics.* Nature, 2004. **430**(6995): p. 101-5.

35. Mignon, P., et al., *Influence of the pi-pi interaction on the hydrogen bonding capacity of stacked DNA/RNA bases.* Nucleic Acids Res, 2005. **33**(6): p. 1779-89.

36. Yakovchuk, P., E. Protozanova, and M.D. Frank-Kamenetskii, *Base-stacking and base-pairing contributions into thermal stability of the DNA double helix.* Nucleic Acids Res, 2006. **34**(2): p. 564-74.

37. Kool, E.T., *Hydrogen bonding, base stacking, and steric effects in dna replication.* Annu Rev Biophys Biomol Struct, 2001. **30**: p. 1-22.

38. Lehn, J.-M. and C. Sirlin, *Molecular catalysis: enhanced rates of thiolysis with high structural and chiral recognition in complexes of a reactive macrocyclic receptor molecule.* Journal of the Chemical Society, Chemical Communications, 1978(21): p. 949-951.

39. Beer, P.D., P.A. Gale, and D.K. Smith, *Supramolecular Chemistry*. 1999: Oxford University Press.

40. Houk, K.N., et al., *Binding Affinities of Host–Guest, Protein–Ligand, and Protein–Transition-State Complexes.* Angewandte Chemie International Edition, 2003. **42**(40): p. 4872-4897.

41. Rekharsky, M.V. and Y. Inoue, *Complexation Thermodynamics of Cyclodextrins.* Chem Rev, 1998. **98**(5): p. 1875-1918.

42. Hasegawa, S., et al., *Three-dimensional porous coordination polymer functionalized with amide groups based on tridentate ligand: selective sorption and catalysis.* J Am Chem Soc, 2007. **129**(9): p. 2607-14.

43. Fujita, M., et al., *Preparation, Clathration Ability, and Catalysis of a Two-Dimensional Square Network Material Composed of Cadmium(II) and 4,4'-Bipyridine.* Journal of the American Chemical Society, 1994. **116**(3): p. 1151-1152.

44. Valvekens, P., F. Vermoortele, and D. De Vos, *Metal-organic frameworks as catalysts: the role of metal active sites.* Catalysis Science & Technology, 2013. **3**(6): p. 1435-1445.

45. Astruc, D., F. Lu, and J.R. Aranzaes, *Nanoparticles as Recyclable Catalysts: The Frontier between Homogeneous and Heterogeneous Catalysis.* Angewandte Chemie International Edition, 2005. **44**(48): p. 7852-7872.

46. Zaramella, D., P. Scrimin, and L.J. Prins, *Self-assembly of a catalytic multivalent peptide-nanoparticle complex.* J Am Chem Soc, 2012. **134**(20): p. 8396-9.

47. Lin, Y., J. Ren, and X. Qu, *Nano-gold as artificial enzymes: hidden talents.* Adv Mater, 2014. **26**(25): p. 4200-17.

48. Kisailus, D., et al., *Self-assembled bifunctional surface mimics an enzymatic and templating protein for the synthesis of a metal oxide semiconductor.* Proc Natl Acad Sci U S A, 2006. **103**(15): p. 5652-7.

49. Dong, Z., Q. Luo, and J. Liu, *Artificial enzymes based on supramolecular scaffolds.* Chemical Society Reviews, 2012. **41**(23): p. 7890-7908.

50. Kofoed, J. and J.L. Reymond, *Dendrimers as artificial enzymes.* Curr Opin Chem Biol, 2005. **9**(6): p. 656-64.

51. Huang, X., et al., *Selenium-mediated micellar catalyst: an efficient enzyme model for glutathione peroxidase-like catalysis.* Langmuir, 2007. **23**(3): p. 1518-22.

52. Mancin, F., et al., *Amphiphilic metalloaggregates: Catalysis, transport, and sensing.* Coordination Chemistry Reviews, 2009. **253**(17–18): p. 2150-2165.

53. Guler, M.O. and S.I. Stupp, *A Self-Assembled Nanofiber Catalyst for Ester Hydrolysis.* Journal of the American Chemical Society, 2007. **129**(40): p. 12082-12083.

54. Rufo, C.M., et al., *Short peptides self-assemble to produce catalytic amyloids.* Nat Chem, 2014. **6**(4): p. 303-309.

55. Tang, Y., et al., *Giant Nanotubes Loaded with Artificial Peroxidase Centers: Self-Assembly of Supramolecular Amphiphiles as a Tool To Functionalize Nanotubes.* Angewandte Chemie International Edition, 2010. **49**(23): p. 3920-3924.

56. Huang, X., et al., *Artificial selenoenzymes: Designed and redesigned.* Chemical Society Reviews, 2011. **40**(3): p. 1171-1184.

57. Huang, Z., et al., *Self-assembly of amphiphilic peptides into bio-functionalized nanotubes: a novel hydrolase model.* Journal of Materials Chemistry B, 2013. **1**(17): p. 2297-2304.

58. Hou, C., et al., *Construction of GPx active centers on natural protein nanodisk/nanotube: a new way to develop artificial nanoenzyme.* ACS Nano, 2012. **6**(10): p. 8692-701.

59. Korendovych, I.V. and W.F. DeGrado, *Catalytic efficiency of designed catalytic proteins.* Current Opinion in Structural Biology, 2014. **27**(0): p. 113-121.

60. Corey, M.J. and E. Corey, *On the failure of de novo-designed peptides as biocatalysts.* Proceedings of the National Academy of Sciences of the United States of America, 1996. **93**(21): p. 11428-11434.

61. Sunde, M. and C.C.F. Blake, *From the globular to the fibrous state: protein structure and structural conversion in amyloid formation.* Quarterly Reviews of Biophysics, 1998. **31**(1): p. 1-+.

62. Caughey, B. and P.T. Lansbury, *Protofibrils, pores, fibrils, and neurodegeneration: Separating the responsible protein aggregates from the innocent bystanders.* Annual Review of Neuroscience, 2003. **26**: p. 267-298.

63. Cleusa, P.F., et al., *Global prevalence of dementia: a Delphi consensus study.* LANCET, 2005. **366**(9503): p. 2112-2117.

64. Cohen, F.E. and J.W. Kelly, *Therapeutic approaches to protein-misfolding diseases.* Nature, 2003. **426**(6968): p. 905-909.

65. Westermark, G.T., K.H. Johnson, and P. Westermark, *Staining methods for identification of amyloid in tissue.* Methods Enzymol, 1999. **309**: p. 3-25.

66. Linke, R.P., *Highly sensitive diagnosis of amyloid and various amyloid syndromes using Congo red fluorescence.* Virchows Arch, 2000. **436**(5): p. 439-48.

67. Krebs, M.R., et al., *The mechanism of amyloid spherulite formation by bovine insulin.* Biophys J, 2005. **88**(3): p. 2013-21.

68. Barnhart, M.M. and M.R. Chapman, *Curli biogenesis and function.* Annu Rev Microbiol, 2006. **60**: p. 131-47.

69. Chapman, M.R., et al., *Role of Escherichia coli curli operons in directing amyloid fiber formation.* Science, 2002. **295**(5556): p. 851-5.

70. Hammer, N.D., J.C. Schmidt, and M.R. Chapman, *The curli nucleator protein, CsgB, contains an amyloidogenic domain that directs CsgA polymerization.* Proc Natl Acad Sci U S A, 2007. **104**(30): p. 12494-9.

71. Robinson, L.S., et al., *Secretion of curli fibre subunits is mediated by the outer membrane-localized CsgG protein.* Mol Microbiol, 2006. **59**(3): p. 870-81.

72. Cherny, I., et al., *The Formation of Escherichia coli Curli Amyloid Fibrils is Mediated by Prion-like Peptide Repeats.* Journal of Molecular Biology, 2005. **352**(2): p. 245-252.

73. Butko, P., et al., *Spectroscopic Evidence for Amyloid-like Interfacial Self-Assembly of Hydrophobin Sc3.* Biochemical and Biophysical Research Communications, 2001. **280**(1): p. 212-215.

74. Kwan, A.H.Y., et al., *Structural basis for rodlet assembly in fungal hydrophobins.* Proceedings of the National Academy of Sciences of the United States of America, 2006. **103**(10): p. 3621-3626.

75. Mackay, J.P., et al., *The hydrophobin EAS is largely unstructured in solution and functions by forming amyloid-like structures.* Structure, 2001. **9**(2): p. 83-91.

76. Sunde, M., et al., *Structural analysis of hydrophobins.* Micron, 2008. **39**(7): p. 773-84.

77. Wosten, H.A. and M.L. de Vocht, *Hydrophobins, the fungal coat unravelled.* Biochim Biophys Acta, 2000. **1469**(2): p. 79-86.

78. Gebbink, M.F., et al., *Amyloids--a functional coat for microorganisms.* Nat Rev Microbiol, 2005. **3**(4): p. 333-41.

79. Oh, J., et al., *Amyloidogenesis of type III-dependent harpins from plant pathogenic bacteria.* J Biol Chem, 2007. **282**(18): p. 13601-9.

80. Otzen, D. and P.H. Nielsen, *We find them here, we find them there: functional bacterial amyloid.* Cell Mol Life Sci, 2008. **65**(6): p. 910-27.

81. Balguerie, A., et al., *Domain organization and structure–function relationship of the HET-s prion protein of Podospora anserina.* The EMBO Journal, 2003. **22**(9): p. 2071-2081.

82. Coustou, V., et al., *The protein product of the het-s heterokaryon incompatibility gene of the fungus Podospora anserina behaves as a prion analog.* Proc Natl Acad Sci U S A, 1997. **94**(18): p. 9773-8.

83. Dos Reis, S., et al., *The HET-s prion protein of the filamentous fungus Podospora anserina aggregates in vitro into amyloid-like fibrils.* J Biol Chem, 2002. **277**(8): p. 5703-6.

84. Maddelein, M.L., et al., *Amyloid aggregates of the HET-s prion protein are infectious.* Proc Natl Acad Sci U S A, 2002. **99**(11): p. 7402-7.

85. Ritter, C., et al., *Correlation of structural elements and infectivity of the HET-s prion.* Nature, 2005. **435**(7043): p. 844-848.

86. Adda, C.G., et al., *Plasmodium falciparum merozoite surface protein 2 is unstructured and forms amyloid-like fibrils.* Mol Biochem Parasitol, 2009. **166**(2): p. 159-71.

87. Lu, K., et al., *Exploiting Amyloid Fibril Lamination for Nanotube Self-Assembly.* Journal of the American Chemical Society, 2003. **125**(21): p. 6391-6393.

88. Balbach, J.J., et al., *Amyloid Fibril Formation by Aβ16-22, a Seven-Residue Fragment of the Alzheimer's β-Amyloid Peptide, and Structural Characterization by Solid State NMR†.* Biochemistry, 2000. **39**(45): p. 13748-13759.

89. Klimov, D.K. and D. Thirumalai, *Dissecting the Assembly of Aβ16–22 Amyloid Peptides into Antiparallel β Sheets.* Structure, 2003. **11**(3): p. 295-307.

90. Childers, W.S., et al., *Phase Networks of Cross-β Peptide Assemblies.* Langmuir, 2012. **28**(15): p. 6386-6395.

91. Favrin, G., A. Irbäck, and S. Mohanty, *Oligomerization of Amyloid Aβ(16–22) Peptides Using Hydrogen Bonds and Hydrophobicity Forces.* Biophysical Journal, 2004. **87**(6): p. 3657-3664.

92. Cheon, M., I. Chang, and Carol K. Hall, *Spontaneous Formation of Twisted Aβ(16-22) Fibrils in Large-Scale Molecular-Dynamics Simulations.* Biophysical Journal, 2011. **101**(10): p. 2493-2501.

93. Mehta, A.K., et al., *Facial Symmetry in Protein Self-Assembly.* Journal of the American Chemical Society, 2008. **130**(30): p. 9829-9835.

94. Liang, Y., et al., *Cross-Strand Pairing and Amyloid Assembly.* Biochemistry, 2008. **47**(38): p. 10018-10026.

95. Liang, C., et al., *Kinetic Intermediates in Amyloid Assembly.* Journal of the American Chemical Society, 2014. **136**(43): p. 15146-15149.

96. Childers, W.S., et al., *Templating Molecular Arrays in Amyloid's Cross-β Grooves.* Journal of the American Chemical Society, 2009. **131**(29): p. 10165-10172.

97. Liang, Y., et al., *Light harvesting antenna on an amyloid scaffold.* Chemical Communications, 2008(48): p. 6522-6524.

98. Dong, J., et al., *Engineering Metal Ion Coordination to Regulate Amyloid Fibril Assembly and Toxicity.* Proceedings of the National Academy of Sciences of the United States of America, 2007. **104**(33): p. 13313-13318.

99. Dong, J., et al., *Modulating Amyloid Self-Assembly and Fibril Morphology with Zn(II).* Journal of the American Chemical Society, 2006. **128**(11): p. 3540-3542.

100. Morgan, D.M., et al., *Metal Switch for Amyloid Formation: Insight into the Structure of the Nucleus.* Journal of the American Chemical Society, 2002. **124**(43): p. 12644-12645.

Chapter 2: Peptide Nanotubes as Selective Condensation Catalyst

Introduction

The cross-β grooves of 7-residue peptide assemblies are composed of rows of substrate binding grooves positioned proximally along the nanotube surface. These supramolecular assemblies bind arrays of transition metals [1, 2], organize chromogenic substrates [3], and serve as scaffolds for nucleobase-pairing [4], suggesting the possibility that the binding sites might template polymerization reactions. The condensation of primary amines with carbonyl compounds (aldehydes and less commonly ketones) to produce the corresponding imines (Schiff bases or azomethines) was first discovered in 1864 by Hugo Schiff [5]. Imine formation is one of the most important reactions in organic and medicinal chemistry and serves as a versatile and useful intermediates of a variety of organic reactions [6-8]. Indeed, imines are found in anti-inflammatory, anti-cancer [9-11], antibacterial, and antifungal agents [12]. Several procedures and techniques have been described for the preparation of imines [9, 13-18] and all require water-removal or reagents that remove water under environmentally benign conditions [19]. Here I will highlight the remarkable potential of self-assembled Aβ peptides to template the condensation of aromatic imines in water.

Results and Discussion

Secondary Structure Analysis of Ac-KLVFFAL-NH_2

The ability of peptides to access polymorphically diverse microphases with remarkably ordered surfaces has been investigated [20], and the seven residue

peptide Ac-KLVFFAL-NH_2 assembles into homogenous nanotubes (Figure 2-1B) under acidic conditions. At neutral pH, the peptides still assemble into nanotubes, but with less homogeneity as observed by Transmission Electron Microscopy (TEM). The widths of the nanotubes formed at pH 2 maintain average tube widths of 43.1 ± 4.1 nm (Figure 2-1C).

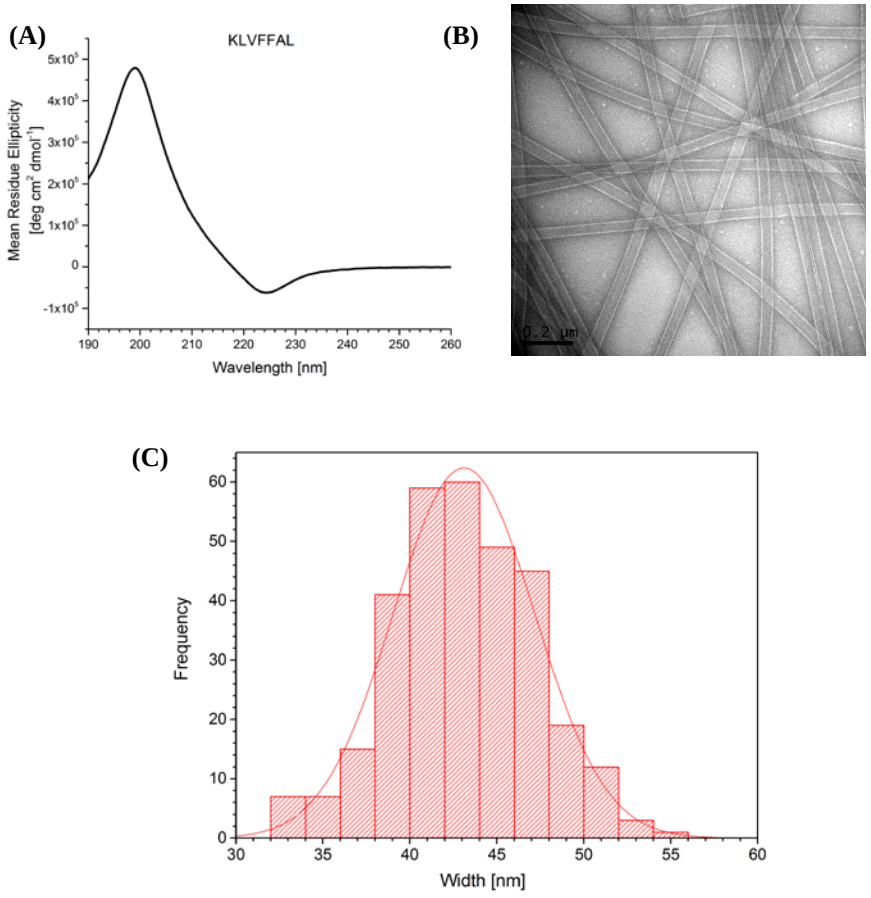

Figure 2-1*: (A) Circular Dichroism of 0.5 mM Ac-KLVFFAL-NH_2 assembled at pH 2 in 40% MeCN/H_2O at 4ºC. (B) TEM Micrographs of Ac-KLVFFAL-NH_2 assembled at pH 2 in 40% MeCN/H_2O, Scale bar is 200 nm (C) Width measurement from TEM image, ~300 measurements were taken and the frequency was plotted against widths and fit to Gaussian distributions with the center width of* 43.1 ± 4.1 nm.

Circular dichroism (CD) is widely used for interrogating the secondary structures of proteins and polypeptides in solution [21-23]. CD spectra of 0.5 mM Ac-KLVFFAL-NH_2 assembled at pH 2 display a minimum at 225 nm and a strong positive Cotton effect at 200 nm most consistent with β-sheet secondary structure (Figure 2-1A). Fourier transform infrared absorption spectroscopy (FT-IR) [24-28] support the assignment with amide I stretch modes at 1623 cm^{-1} (Figure 2-2). A weak absorption at 1694 cm^{-1} is correlated with anti-parallel β-strands arrangements [29].

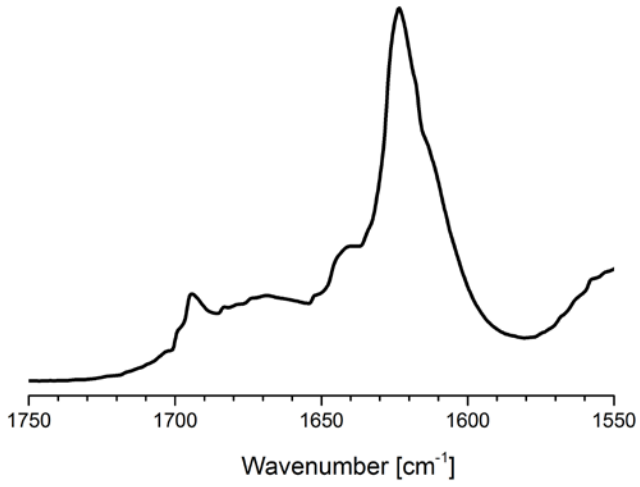

***Figure 2-2**: FT-IR of Ac-KLVFFAL-NH_2 assembled at pH 2 in 40% MeCN/H_2O showing a strong IR stretch at 1623* cm^{-1} *and a weaker band at 1694* cm^{-1}.

Support further came from distinctive X-ray diffraction pattern "cross-β" peptide architecture [30-33]. X-ray diffraction gives reflections at 4.7Å for the periodic spacing of H-bonded peptides of the β-sheets while the orthogonal 10.2Å reflection is the repeat distance between laminated sheets [30, 33-38]. The lamination distance can vary by ±0.5

Å depending on sample preparation. When the Ac-KLVFFAL-NH_2 nanotubes are bundled with SO_4^{2-} before lyophilization, the lamination distance is 10.2Å, but when the samples are lyophilized without bundling, the lamination distance is 10.6Å. Because the nanotubes walls are flexible, this variation in lamination distance could be as a result of the tight packing that result from SO_4^{2-} bundling. Henceforth, samples are prepared by bundling the nanotubes or fibers with Na_2SO_4 before freezing and lyophilization unless otherwise stated.

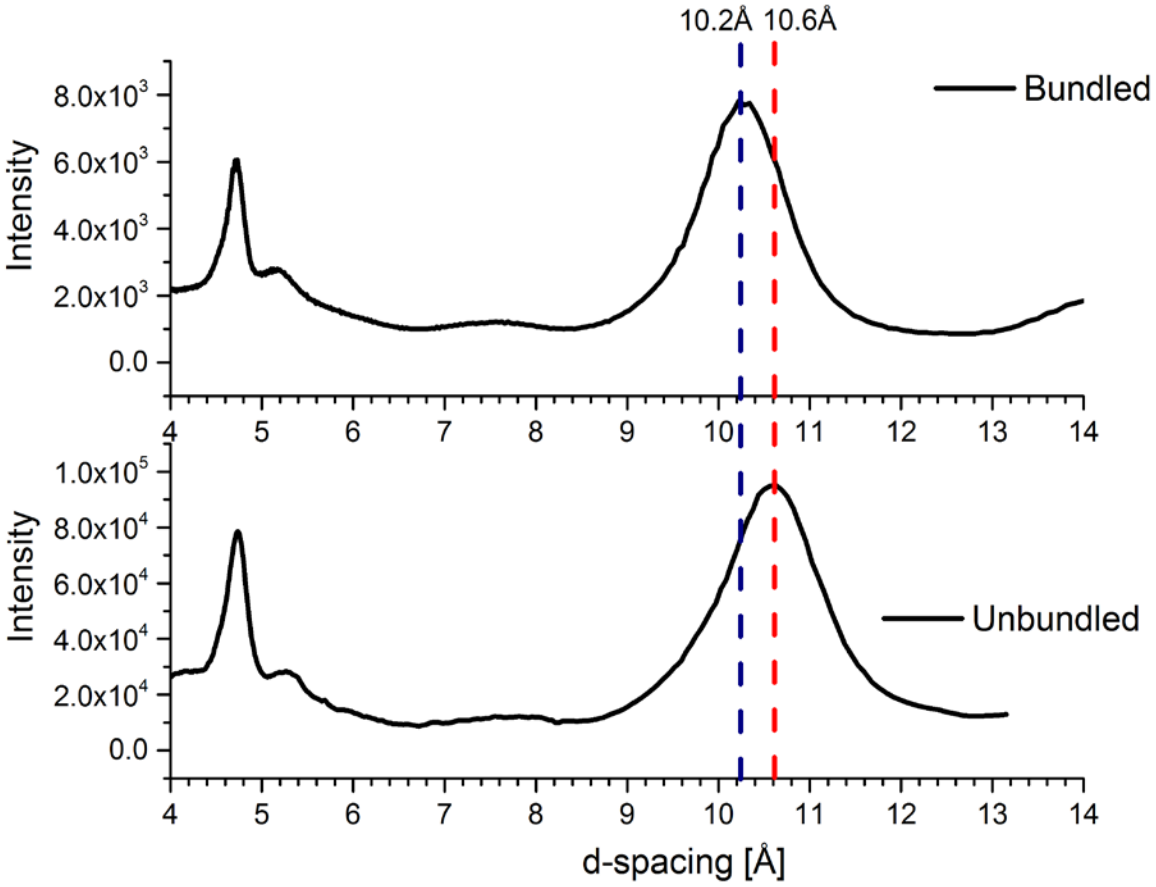

Figure 2-3: *X-ray powder diffraction of Ac-KLVFFAL-NH_2 assembled in 40% MeCN/H_2O, with 0.1% TFA, showing reflections at 4.7 Å for both salt bundled and unbundled samples. The laminate distance is 10.2 Å for bundled sample and 10.6 Å for unbundled samples.*

Ac-KLVFFAE-NH_2 nanotubes melt cooperatively and exist as spherical particles above 37ºC [20] but melting of Ac-KLVFFAL-NH_2 nanotubes is less cooperative (Figure 2-4) and by CD remains 50% folded at 56.7 ºC as monitored by the ellipticity at 225 nm.

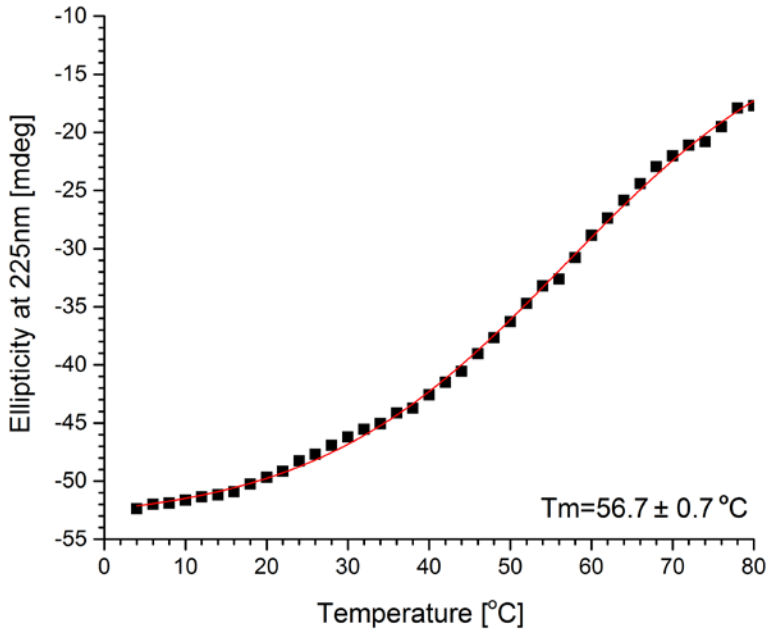

Figure 2-4: *CD melting profile of Ac-KLVFFAL-NH_2 nanotubes assembled in 40% MeCN/H_2O with 0.1% TFA at 4*ºC*. Ellipticity at 225 nm was plotted against temperature (2* ºC*/min) over a range of 4*ºC *to 80*ºC*. The melting curve was fit to a Boltzmann Nonlinear Curve to give a melting point of* 56.7± 0.7 ºC.

Finally, atomic level resolution of the Ac-KLVFFAL-NH_2 nanotubes obtained with solid-state NMR revealed that each peptide strand in Ac-KLVFFAL-NH_2 nanotubes is arranged antiparallel in out-of-register sheets, and this architecture places the N-terminal lysine (K) outside the H-bonded β-sheet array (Figure 2-5A). These assemblies then create well-defined surfaces on the inner and outer faces of the hollow nanotubes [39] (Figure 2-5B) with the lysine residues appearing as “knots” stitching together

parallel cross-β grooves that spiral 13° off axis around the nanotube [40]. Congo red (CR) gives signatures of both J- and H-aggregates on binding to the Ac-KLVFFAL-NH_2 nanotubes [40], establishing that these well defined surfaces on the nanotubes can bind small molecules. The structural constraints led to the hypothesis that these cross-β laminate grooves are proximal enough to serve as templates for small molecule polymerization and led to the design of carbon-heteroatom (imine) formation reactions to test these predictions.

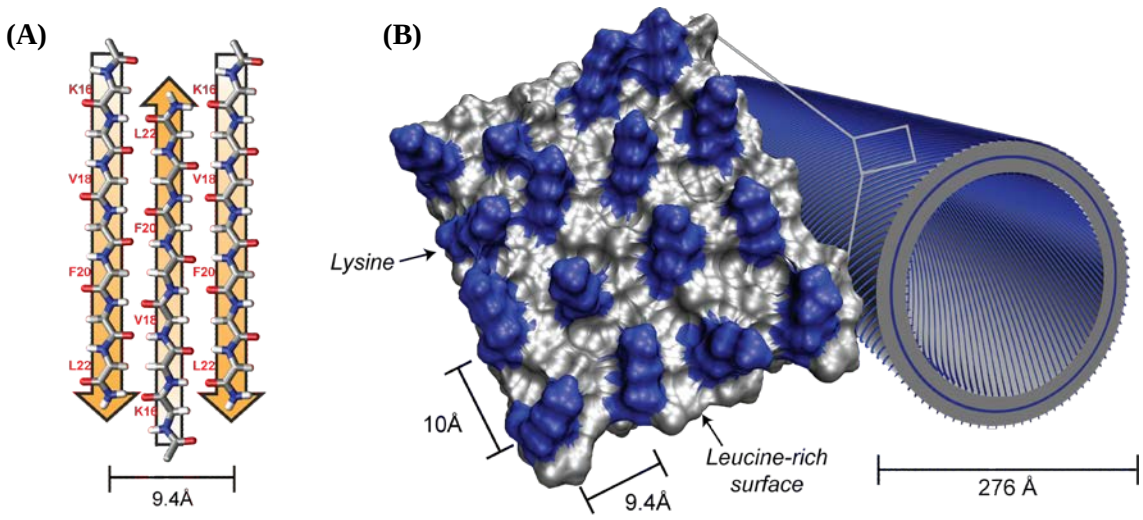

Figure 2-5: *(**A**) Three anti-parallel out-of-register β-strands and (**B**) Structural model for the K16 nanotube with a van der Waal surface expansion displaying the lysine (blue) and leucine (grey) residues. Peptide sequences are indicated with the standard single letter code amino acid code.*

Ac-KLVFFAL-NH_2 Nanotubes as Templates for Imine Condensation

From the combination of the structural models of the Ac-KLVFFAL-NH_2 nanotubes and their proven ability to bind and organize CR, functionalized aromatic monomers were designed to specifically condense as conjugated imines along the

nanotube surface. As an initial test of this proposal (Figure 2-6), the substrates 1,4-diamino benzene sulfonic acid (**1**) and naphthalene-2,7-dicarbaldehyde (**2),** were chosen as substrates for conversion to product **(3).**

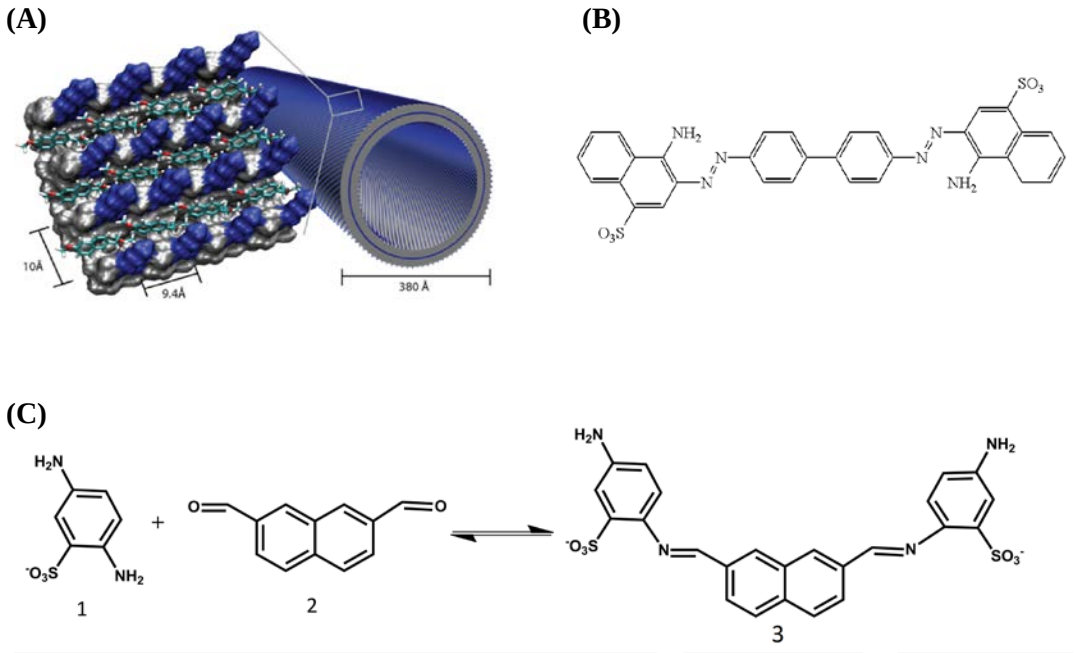

Figure 2-6: ***(A)*** *Cartoon of Ac-KLVFFAL-NH_2 with bound substrates* ***(B)*** *Structure of congo red* ***(C)*** *Proposed condensation of 1,4-diamino benzene sulfonic acid (**1**) and naphthalene-2,7-dicarbaldehyde (**2**) to give (**3**)*

As shown in Figure 2-7, incubation of **1** and **2** in presence of Ac-KLVFFAL-NH_2 assemblies in water is followed by UV-Vis spectroscopy and a new peak ~380 nm is assigned to product **3** (Figure 2-7A). The formation of **3** is confirmed from ESI-MS (Figure 2-8). While the yield appear low, the peak is not formed in the absence of tubes and the low yield is probably the result of the required binding of the substrates in the proper alignment for the further condensation. Interestingly, CD analysis showed an

induced cotton effect near ~380 nm (Figure 2-7B) consistent with the condensation of product **3** bound to the surface of the peptide assemblies. The end-to-end substrate stacks within the ordered microenvironment of the groove (Figure 2-6A) is proposed.

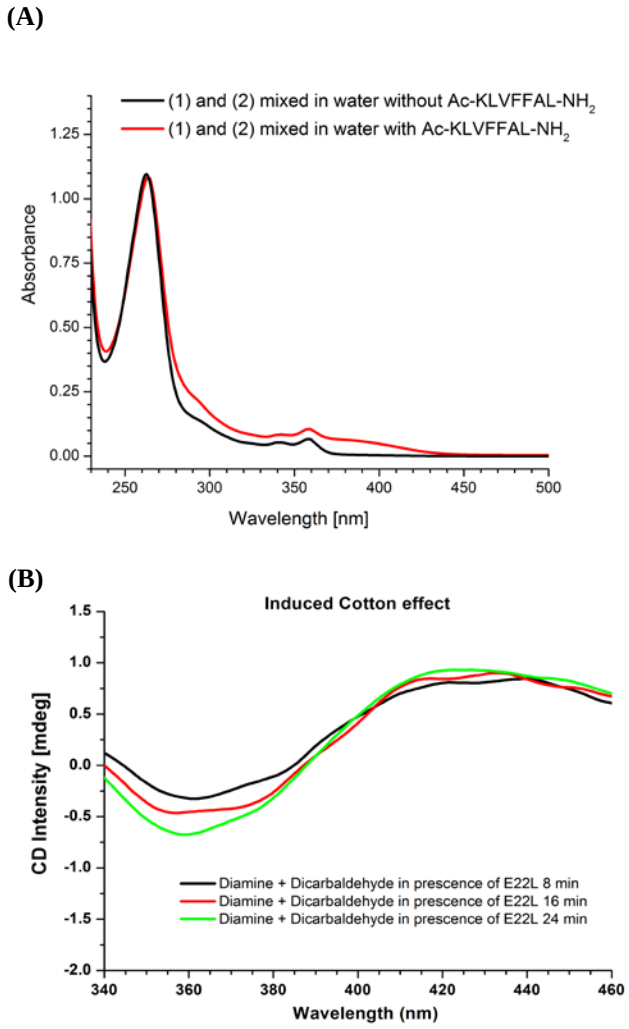

Figure 2-7: (A) *UV-vis of **1** and **2** in the absence (black) and presence of Ac-KLVFFAL-NH_2 nanotubes (red).* ***(B)*** *Induced cotton effect from **3** bound on the nanotube surface.*

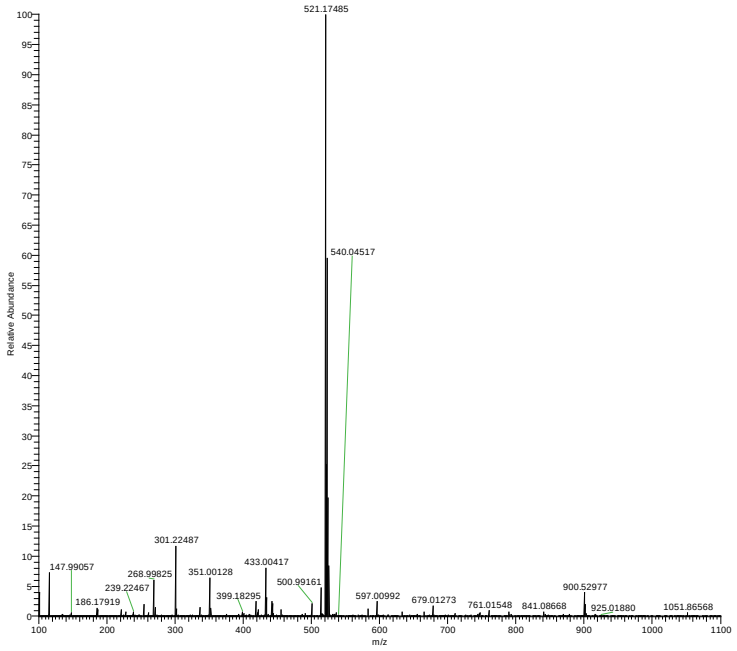

Figure 2-8: *ESI mass spectrum of the product (**3**) from condensation of 1,4-diamino benzene sulfonic acid (**1**) and naphthalene-2,7-dicarbaldehyde (**2**) gives $[M-H]^+$: 521.17*

To further explore the proposed alignment of substrates on the nanotube surface for polymerization, I worked in collaboration with Dr. Dibyendu Das (a postdoctoral fellow in our lab at that time) to design a new substrate 6-amino-2-naphthaldehyde (**4**) (Figure 2-9) featuring a nucleophilic amine and electrophilic aldehyde on the same substrate. This amine and aldehyde functionality on the substrate creates the possibility of imine condensation and oligomerization (Figure 2-10A), also detected by the resulting extended conjugation.

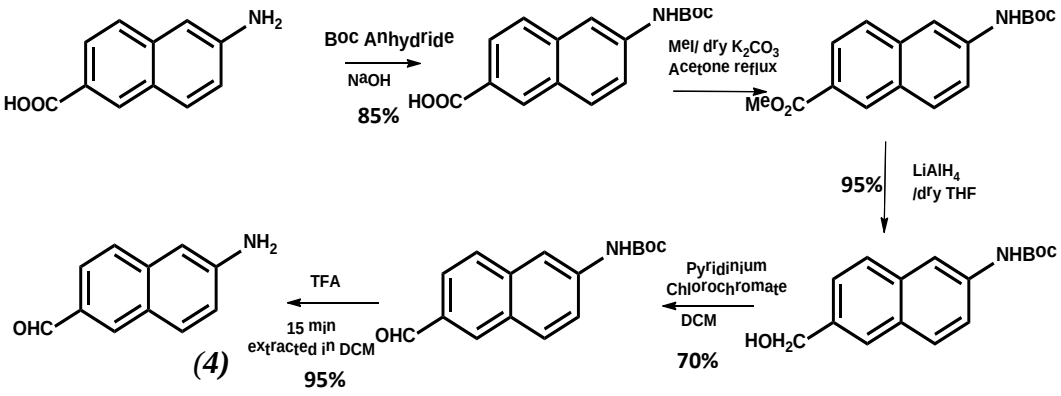

Figure 2-9: *Scheme for the synthesis of 6-amino-2-naphthaldehyde* ***(4)***

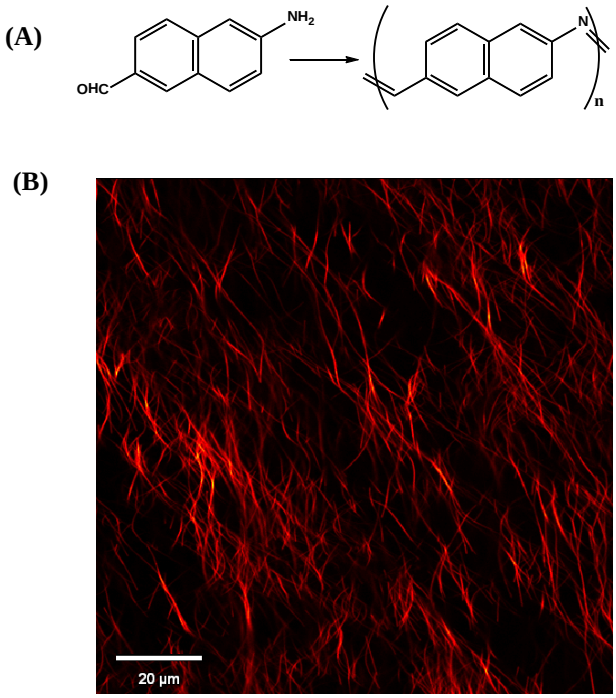

Figure 2-10: ***(A)*** *Condensation of 6-amino-2-naphthaldehyde.* ***(B)*** *Fluorescence intensity imaging of 6-amino-2-naphthaldehyde in presence of Ac-KLVFFAL-NH_2 nanotubes.*

Dehydrative oligomerization of 6-amino-2-naphthaldehyde occurs quite readily in organic solvents (CH_2Cl_2) to give a distinctly red-shifted chromogenic product. When the substrate is incubated with 500 µM of Ac-KLVFFAL-NH_2 nanotubes in water, the

electronic transition (λ_{max} = 350 nm) red-shifts within minutes to 450 nm (Figure 2-11A) and the reaction mixture turning visibly pale yellow. No such change is observed in water in the absence of nanotubes even after incubation for 12 hours (Figure 2-11A, dash line).

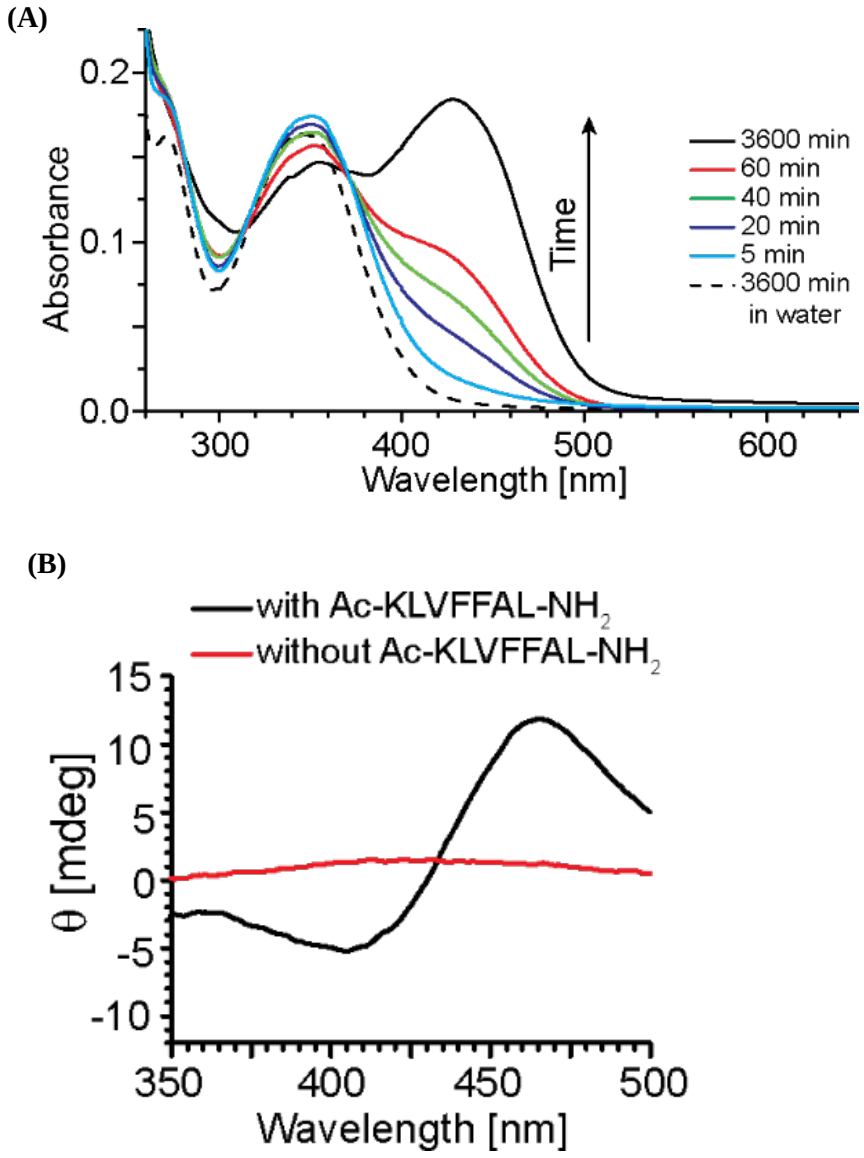

Figure 2-11: *(**A**) Time-dependent UV–Vis spectra of 0.1 mM 6-amino-2-naphthaldehyde in the absence and presence of 0.5 mM Ac-KLVFFAL-NH_2 nanotubes. (**B**) CD spectra of 0.1 mM 6-amino-2-naphthaldehyde in absence (red) and presence (black) of 0.5 mM Ac-KLVFFAL-NH_2 nanotubes.*

Fluorescence microscopy confirms that the amino napthaldehyde binds to the nanotubes (Figure 2-10B) and circular dichroism gives a characteristic Cotton effect centered at 450 nm (Figure 2-11B), further supporting the achiral product being bound to the chiral peptide nanotube surface.

6-*N,N*-dimethylamino-2-naphthaldehyde ***(5)*** analog was prepared (Figure 2-12) to determine whether this large 100 nm shift in λ_{max} is the result of oligomerization. 6-*N,N*-dimethylamino-2-naphthaldehyde binds to give fluorescent Ac-KLVFFAL-NH_2 nanotubes (Figure 2-13B), but no red shift in electronic transition is observed in the presence of the nanotubes (Figure 2-13A). This result suggest that the red shift of 6-amino-2-naphthaldehyde in the presence of Ac-KLVFFAL-NH_2 nanotubes is due to oligomerization.

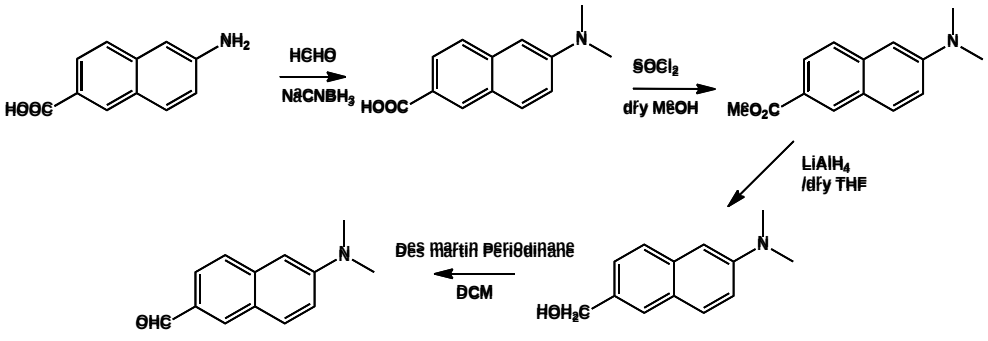

(5)

Figure 2-12: *Scheme for the synthesis of 6-N,N-dimethylamino-2-naphthaldehyde* ***(5)***

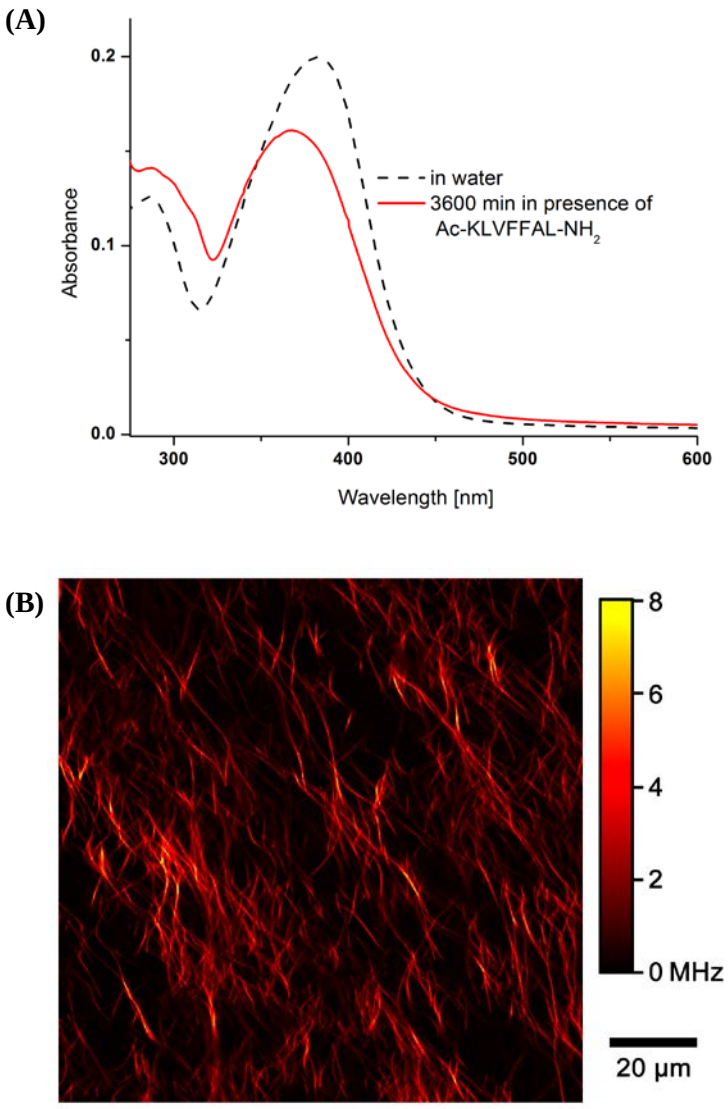

Figure 2-13: Binding 6-(N,N-dimehtylamino)-2-naphthaldeyde to Ac-KLVFFAL-NH₂ nanotubes. *(A) UV-Vis spectra of 2-7 mM 6-(N,N-dimehtylamino)-2-naphthaldeyde in the absence and presence of 0.5 mM Ac-KLVFFAL-NH₂ nanotubes. (B) Fluorescence lifetime microscopy of 6-(N,N-dimehtylamino)-2-naphthaldeyde in presence of 0.5 mM Ac-KLVFFAL-NH₂ nanotubes.*

Fluorescence lifetime measurements of the 6-amino-2-napthaldeyde lifetime bound to the nanotubes (Figure 2-14B) is significantly shorter, in contrast, the life time of the 6-N,N-dimethyl amino-2-napthaldehyde changes little on binding to the nanotubes (Figure 2-15B). The explanation for the significant lifetime change with the 6-amino

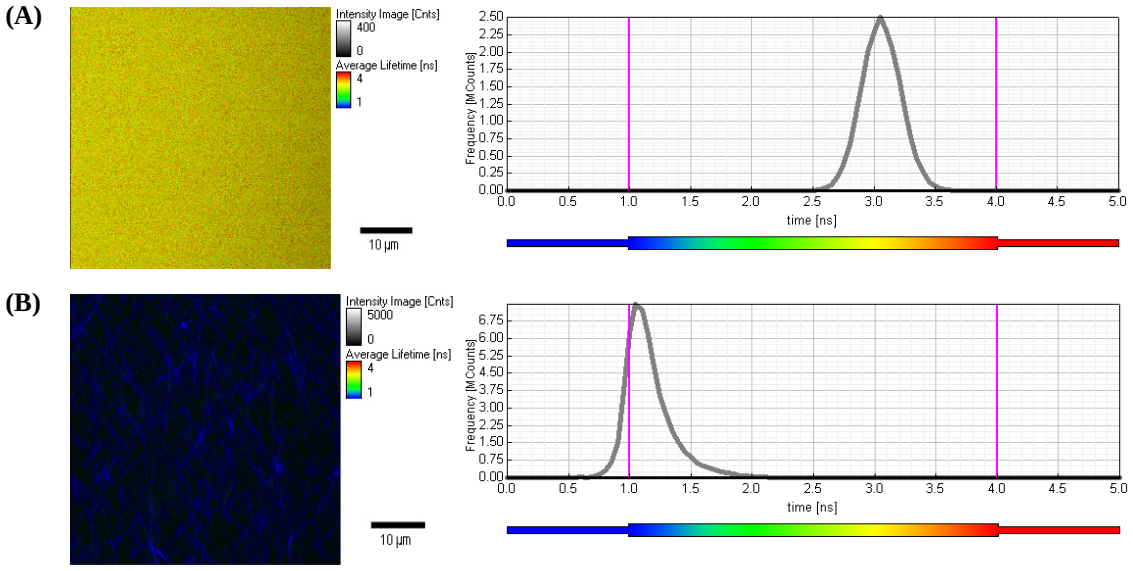

Figure 2-14: *FLIM fluorescence lifetime of 6-amino-2-napthaldeyde (A) without nanotubes (B) with nanotubes.*

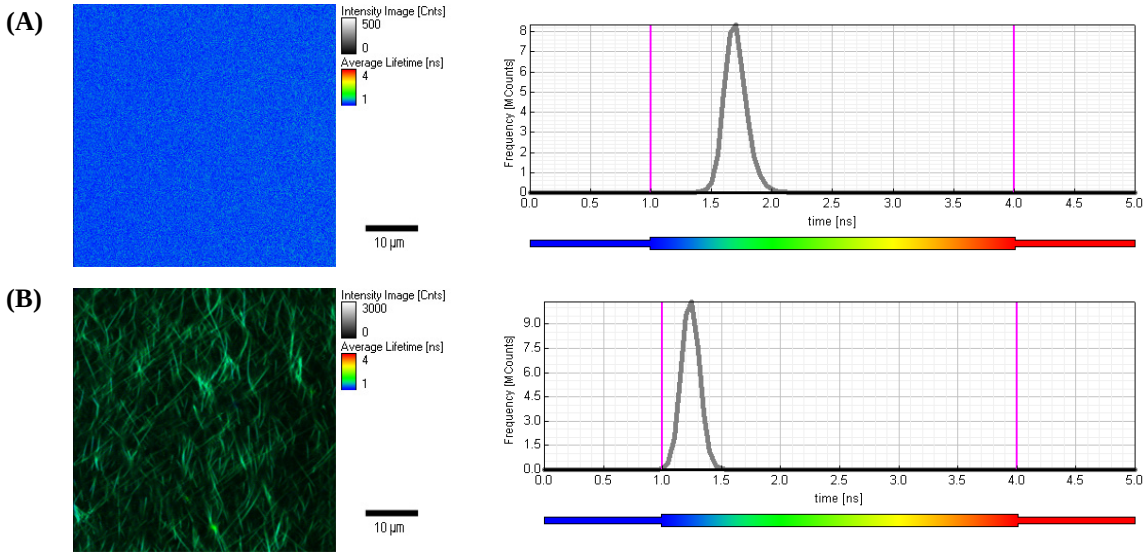

Figure 2-15: *FLIM fluorescence lifetime of 6-N,N-dimethyl amino-2-napthaldehyde (A) without nanotubes (B) with nanotubes.*

derivative is the oligomerization. Mass analysis by ESI (Figure 2-16) confirmed formation of dimers from the Ac-KLVFFAL-NH_2 templated condensation of 6-amino-2-naphthaldehyde.

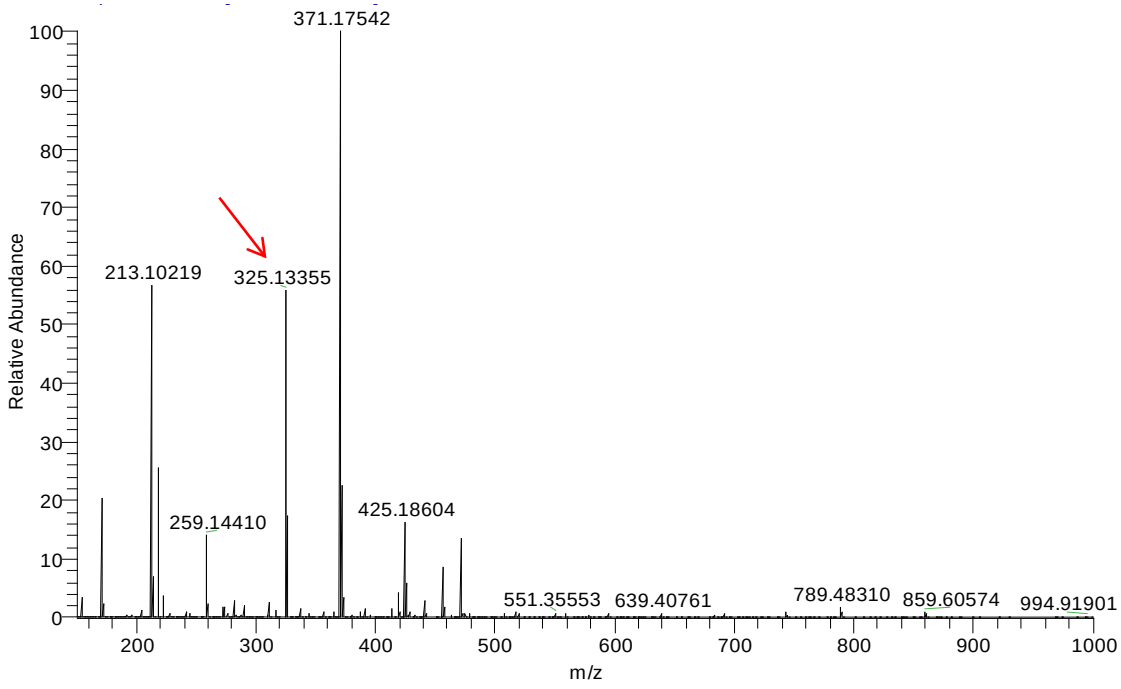

Figure 2-16: *ESI mass spectrum of the dimer product from condensation of 6-amino-2-naphthaldehyde gives* $[M+H]^+$*: 325.13.*

To test for the ability of oligomers to bind to the nanotubes, the model dimer (**6**) was synthesized (Figure 2-17). The UV spectrum of this amide dimer shows a broad absorbance centered at about 375 nm like the dimethylamine in the presence of Ac-KLVFFAL-NH_2 nanotubes. No red-shift is detected but there is a significant increase in the intensity (Figure 2-18).

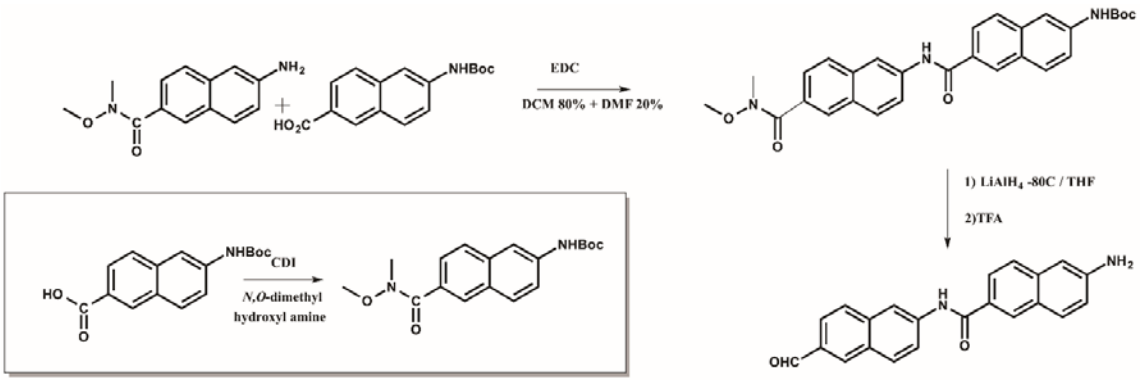

(6)

Figure 2-17: *Scheme for the synthesis of model dimer* ***(6)***

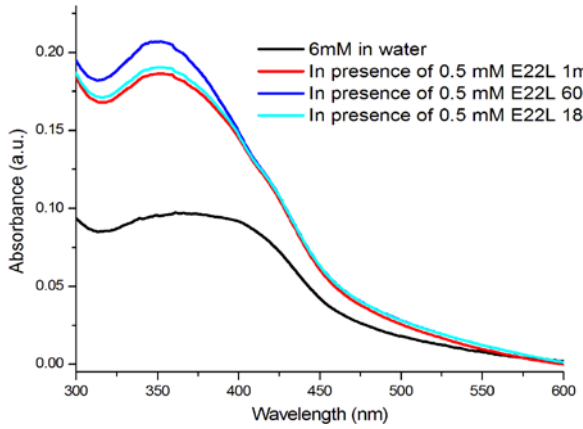

Figure 2-18: Binding of the amide dimer to Ac-KLVFFAL-NH₂ nanotubes. *UV-Vis spectra of the dimer in the absence and presence of 0.5 mM Ac-KLVFFAL-NH₂ nanotubes.*

The changes in the electronic transitions followed for determination of the binding constants for both the monomer **(5)** and the dimer **(6).** As shown in Figure 2-19B, the dissociation constant of dimer **(6)** is two orders of magnitude greater than the monomer **(5)** (Figure 2-19A). This striking result suggests the unique binding pocket on the nanotubes may be able to catalyze dimerization and avoid product inhibition, but may have limited utility polymerizing these substrates.

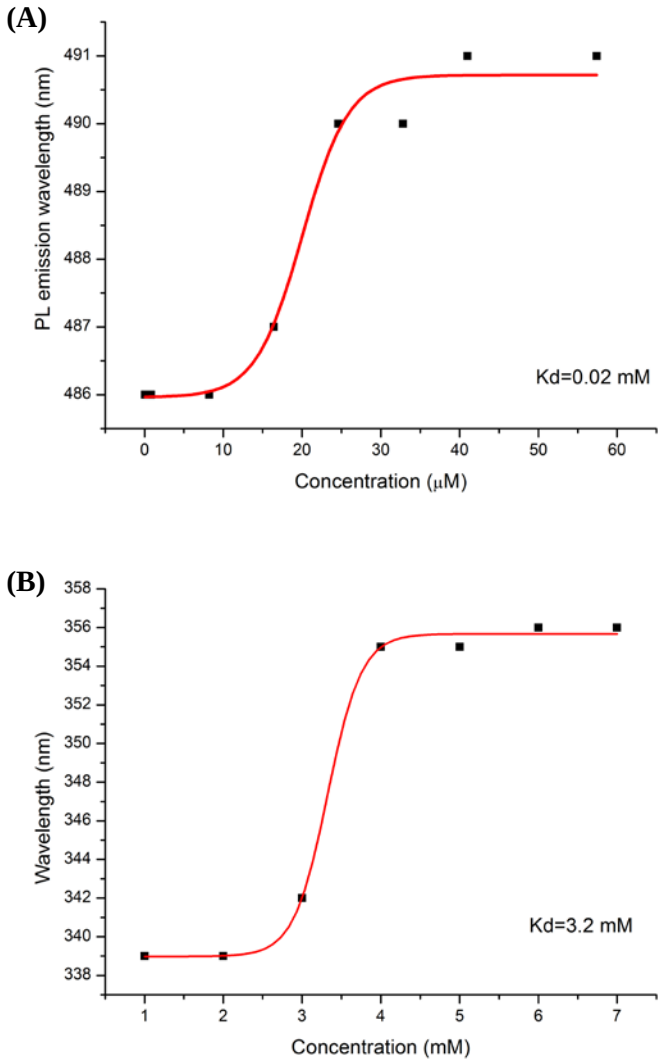

Figure 2-19: *Dissociation constants of* ***(A)*** *6-N,N-dimethylamino-2-naphthaldehyde with 0.5 mM of Ac-KLVFFAL-NH_2, and* ***(B)*** *model dimer with 0.5 mM of Ac-KLVFFAL-NH_2. The curve was fit to a Boltzmann Nonlinear Curve to give the corresponding K_d.*

Optimizing Aß(16-22)E22L for Catalysis

Structural model and experimental data position the lysine in Ac-KLVFFAL-NH_2 residue outside the H-bonded β-sheet array leaving the N-terminus flexible enough for substitution with very little impact on morphology. Three substitutions, proline (K16P),

arginine (K16R) and histidine (K16H) give NH_2-PLVFFAL-NH_2, Ac-RLVFFAL-NH_2 and Ac-HLVFFAL-NH_2 respectively and all were assembled in 40% acetonitrile at pH 2.

The CD of both K16H and K16R display β-sheet minima at 225 nm with a strong positive ellipticity at ~ 200 nm (Figure 2-20A,C), comparable to the CD spectrum of the K16 assemblies. K16P on the other hand displays a different β-sheet signature with a minimum at ~ 198 nm and a maximum at 206 nm (Figure 2-20E), most likely random coil or some assemblies. TEM micrographs show that both K16R and K16H peptides assemble into homogeneous nanotubes at pH 2 (Figure 2-20B,D), maintaining average tube widths of 46.0 ± 5.3 nm and 43.7 ± 4.2 nm respectively (Figure 2-21), morphologically similar to the the K16 nanotubes. By TEM, K16P appears as short sheets of varying widths (Figure 2-20F).

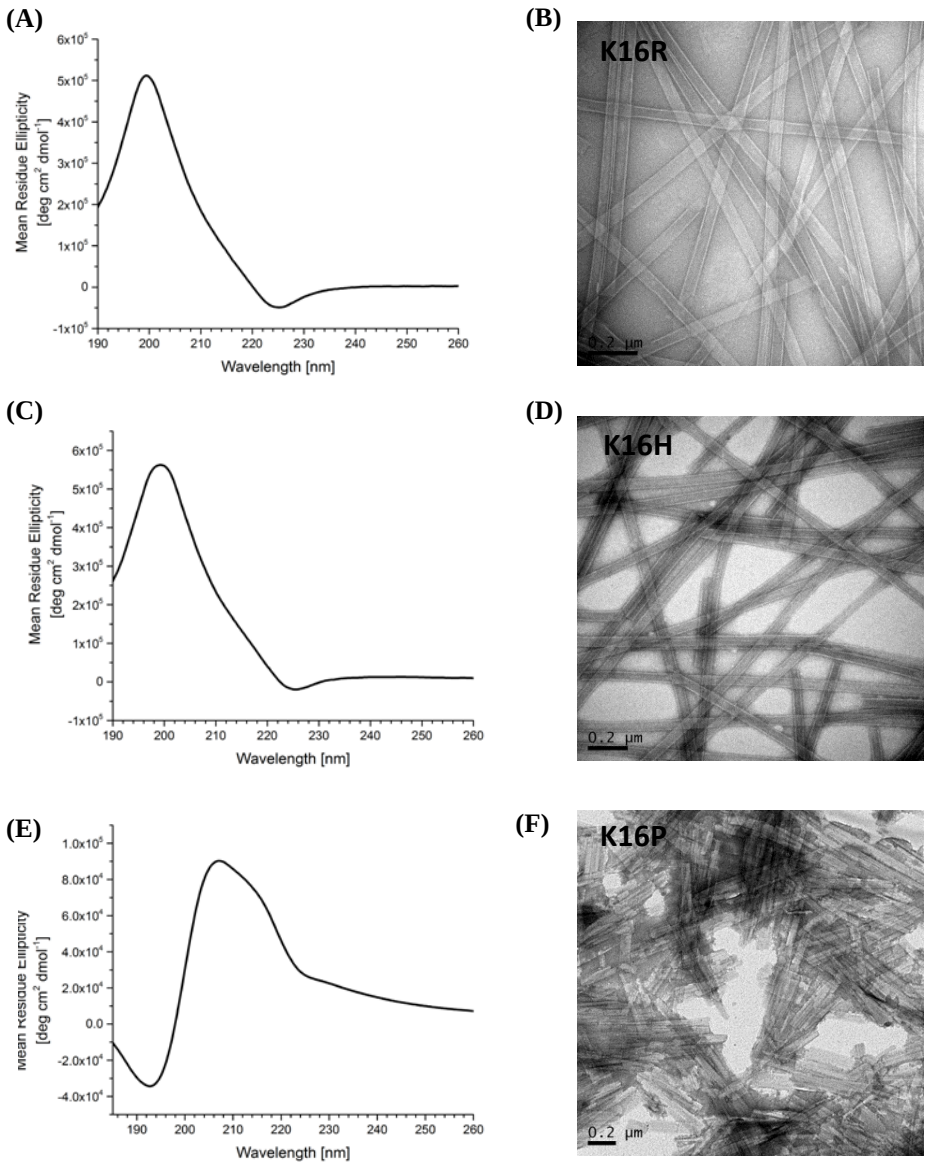

Figure 2-20: *CD Wavelength scans of (A) 0.5 mM Ac-RLVFFAL-NH_2 (C) 0.5 mM Ac-HLVFFAL-NH_2 and (E) 2.5 mM NH_2-PLVFFA-NH_2. TEM micrographs of 2.5 mM (B) Ac-RLVFFAL-NH_2 (D) Ac-HLVFFAL-NH_2 and (F) NH_2-PLVFFAL-NH_2. Scale bar is 200 nm. All samples were assembled at 4* ºC.

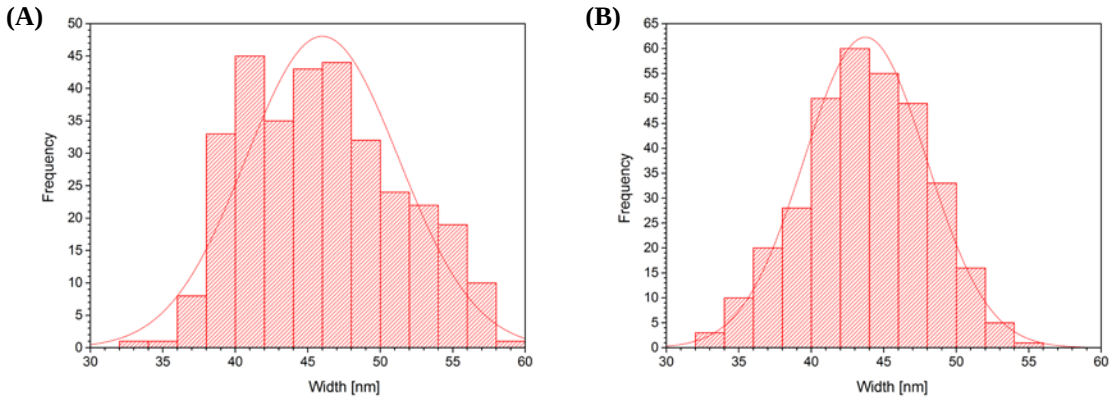

Figure 2-21: *Width measurement from TEM image of (A) K16R and (B) K16H. ~300 measurements were taken and the frequency was plotted against widths and fit to Gaussian distributions with the center width of 46.0 ± 5.3 nm for K16R and 43.7 ± 4.2 nm for K16H*

As shown in Figure 2-22, the FT-IR spectra of the K16R and K16H nanotubes provide evidence for antiparallel β-sheet structure, as in the K16 nanotubes, with an intense amide I absorption at ~1623 cm^{-1} and a weaker absorption at 1694 cm^{-1} [29, 41, 42]. The peptide nanotubes also have a very weak shoulder at 1648 cm^{-1}, consistent with more disordered assemblies. Although the K16P assemblies have the intense amide I absorption at ~1623 cm^{-1}, the absorption characteristic of antiparallel β-sheet structure is very weak and shifted to ~1697 cm^{-1}. While the CD for K16P is distinct from the other two congeners, the IR data confirm the sheets shown in the TEM are composed of β-sheet assemblies. Overall, IR analysis confirmed that all the assemblies formed by the N-terminal congeners maintain the similar antiparallel β-sheet structure as seen in K16 assemblies.

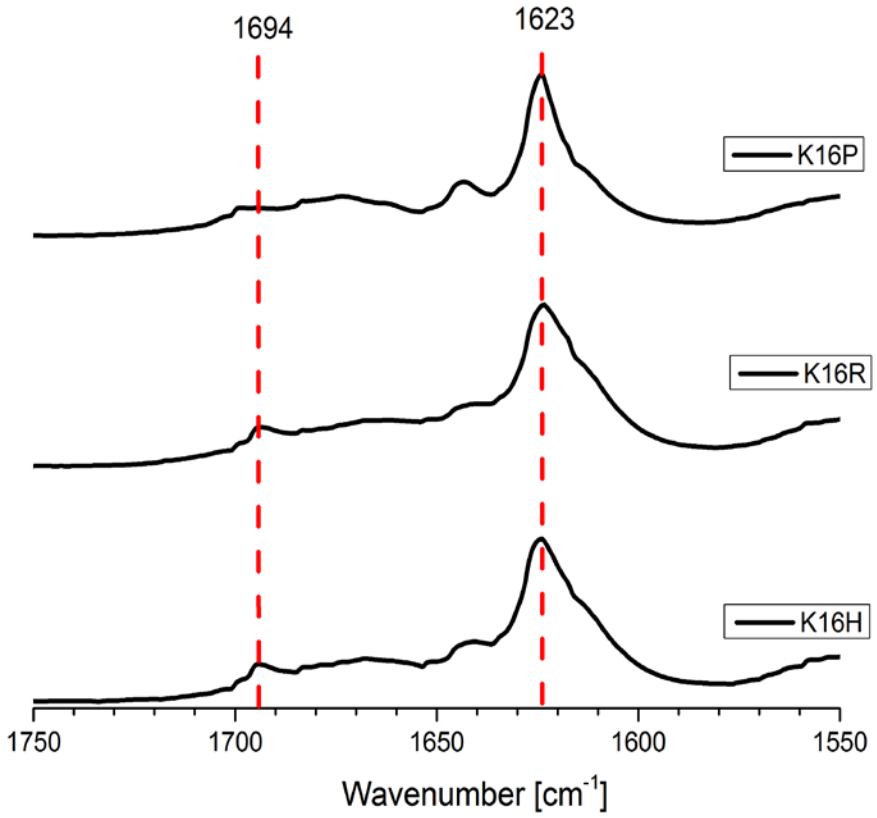

Figure 2-22: *FTIR of the Amide I region of the N-terminus congeners assembled at 2.5 mM in 40% MeCN/H_2O with 0.1% TFA. The spectra show characteristic absorbance increase at the ß-sheet stretching frequency near 1623 cm^{-1} and a weaker band at 1694* cm^{-1}, however, the *1648 cm^{-1} peak representing the random coil peptide conformation is more pronounced in the K16P spectra.*

To further evaluate these β-sheets, X-ray powder diffraction is consistent with all the K16 congeners (K16R, K16H and K16P) maintaining the classic cross-β assembly of amyloid with d-spacing of 4.7Å, the distances between hydrogen-bonded peptides with laminated β-sheets d-spacing of 10.4Å for K16R, 10.2Å for K16H and 9.9Å for K16P (Figure 2-23).

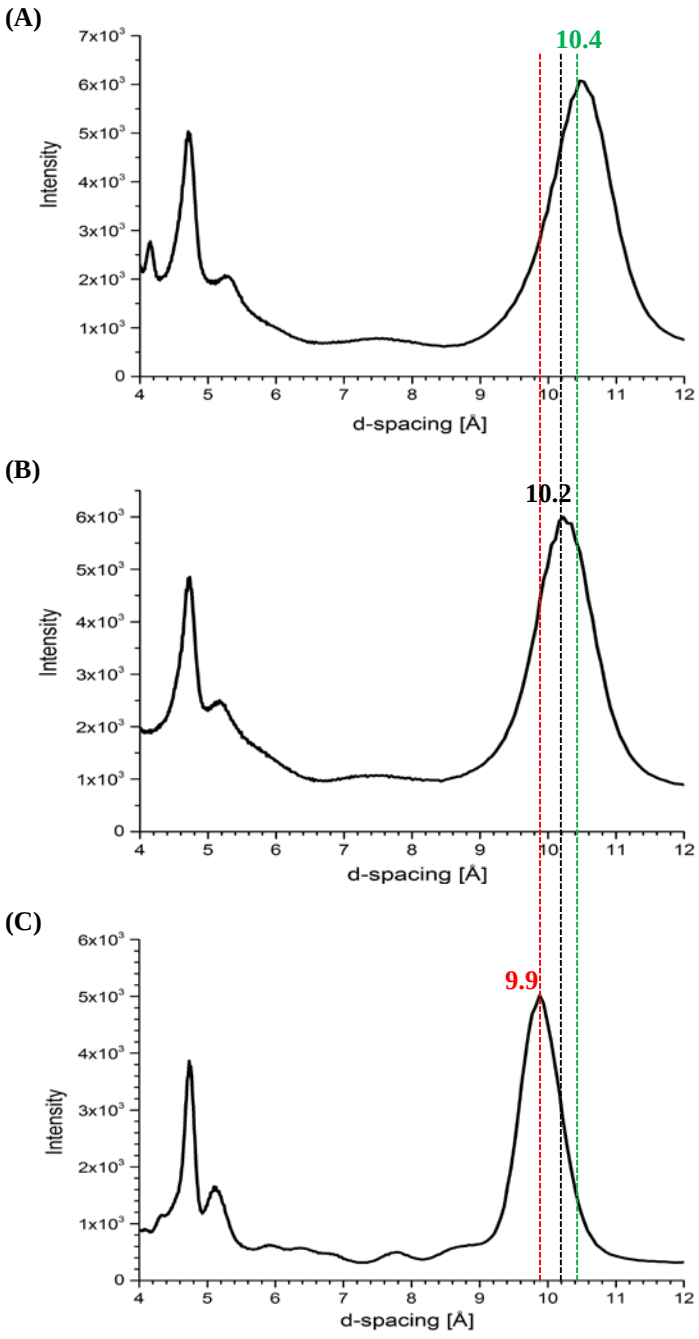

Figure 2-23: *X-ray powder diffraction of (A) Ac-RLVFFAL-NH_2 (B) Ac-HLVFFAL-NH_2 and (C) NH_2-PLVFFAL, assembled in 40% MeCN/H_2O, with 0.1% TFA, showing reflections at the d-spacings of 4.7* Å for H-bonding *and 10.4* Å*, 10.2* Å *and 9.9 Å respectively for the lamination distance.*

The thermal stability of these assemblies were evaluated by CD. K16R melted cooperatively at 46.7±0.2ºC very similar to K16 assemblies (Figure 2-24A). However, K16H did not melt completely up to 76.4±2.6ºC (Figure 2-24B). K16P was not evaluated because of the non-homogeneity of the assemblies.

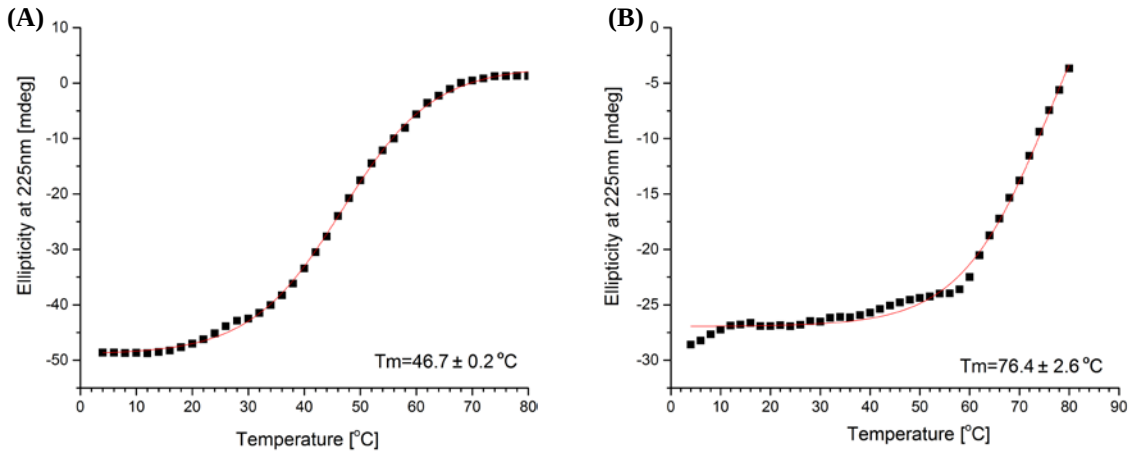

Figure 2-24: *CD melting profile of (A) Ac-RLVFFAL-NH_2 and (B) Ac-HLVFFAL-NH_2 nanotubes assembled in 40% MeCN/H_2O with 0.1% TFA at 4*ºC*. Ellipticity at 225 nm was plotted against temperature (2*ºC */min) over a range of 4*ºC *to 80*ºC*. The melting curve was fit to a Boltzmann Nonlinear Curve corresponding to a melting point of* 46.7± *0.2 ºC for Ac-RLVFFAL-NH_2 and 76.4±2.6 ºC for Ac-HLVFFAL-NH_2.*

Imine Condensation with K16 Congeners

As shown in Figure 2-25, changing the amino acid exposed on the nanotubes surface significantly improved the rate of amino naphthaldehyde condensation. K16H proceeded significantly faster (Figure 2-25A), and K16R was considerably

slower (Figure 2-25B). The estimated relative rates for K16R:K16:K16H was 1:10:30 respectively (Figure 2-26), and again, only dimers are produced.

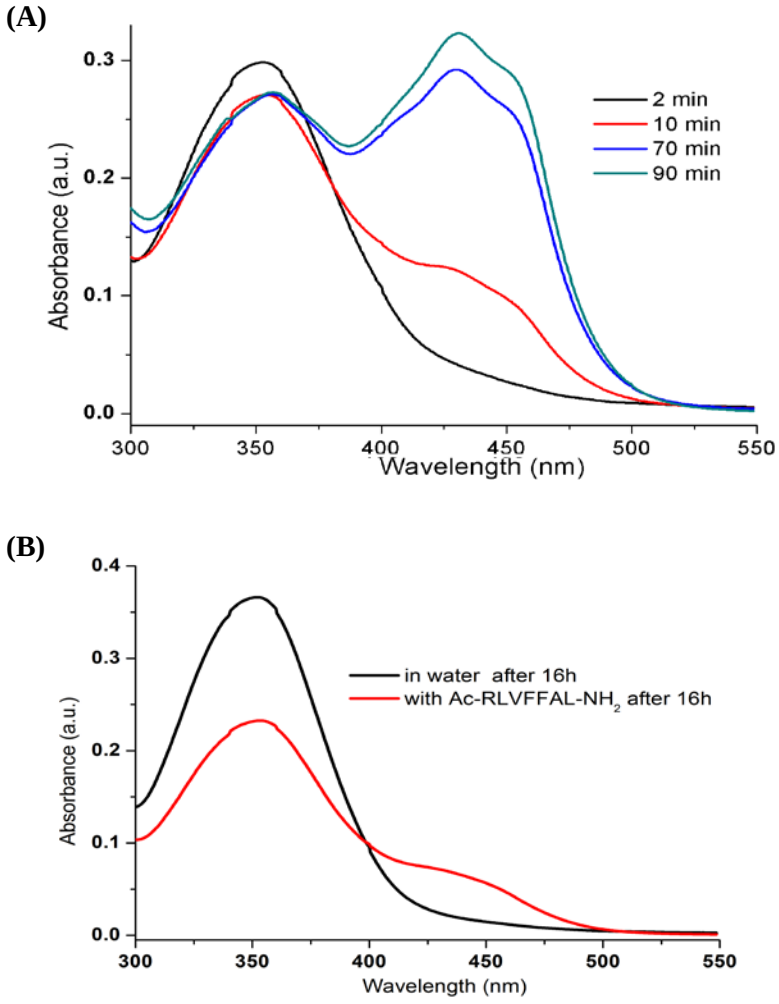

Figure 2-25: *(**A**) Time-dependent UV –Vis spectra of 0.1 mM 6-amino-2-naphthaldehyde in the presence of 0.5 mM Ac-HLVFFAL-NH_2 nanotubes. (**B**) UV –Vis spectra of 0.1 mM 6-amino-2-naphthaldehyde in the presence of 0.5 mM Ac-RLVFFAL-NH_2 nanotubes.*

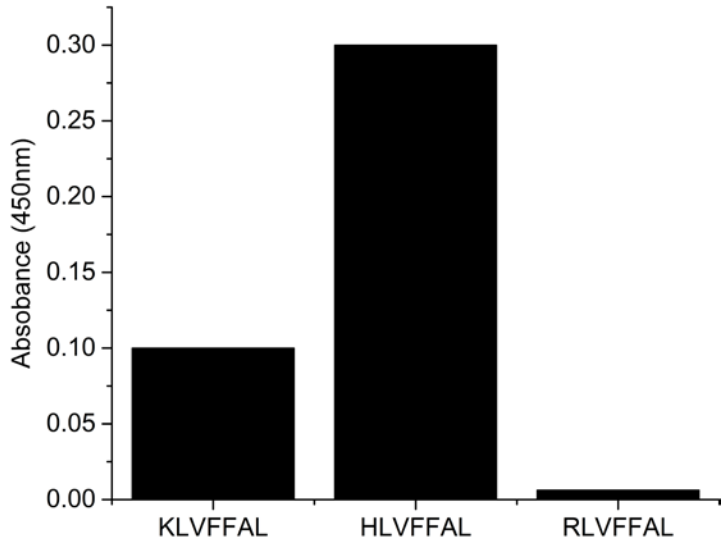

Figure 2-26: *Initial rate of conversion of 6-amino-2-naphthaldehyde to imine dimer with K16, K1H and K1R peptide nanotubes. Absorbance at 450 nm after 1 hour of incubation of 500 μM peptide with 100μM 6-amino-2-naphthaldehyde.*

Conclusion

Our current model of repetitive cross-β structure of amyloid assemblies places several binding sites positioned along the laminate grooves. The possibility of these sites templating imine condensation was investigated with aminonaphthaldehyde monomers designed to couple end-to-end through imine condensation to give a conjugated product along the nanotube surface. Initial studies with Ac-KLVFFAL-NH_2 nanotubes and naphthalene-2,7-dicarbaldehyde (**1**) and 1,4-diamino benzene sulfonic acid (**2)** supported the proximity of the binding sites. The polymerizable 6-amino-2-naphthaldehyde gave a red-shifted transition over a few minutes with K16 nanotubes. The K16R and K16H peptide nanotubes modulate the initial condensation rates, but do not impact the degree of polymerization. It is possible that the histidine nanotubes strengthens the binding of the stable transition state, resulting in an improved rate of

reaction. Another possibility is that the histidine on the nanotubes might act as a general base catalyst promoting nucleophilic addition to the carbonyl group. The different reactivity with different peptide assemblies reiterates the argument that the nanotubes are not just serving as templates for the reaction but that the nanotubes are indeed oligomerization catalysts.

Of particular significance is the finding that the dynamic supramolecular templates selectively facilitate the formation of dimers. The critical chemical question we must address relates to why these nanotubes are so effective at inducing dimerization, but destabilize dimer binding?. It is possible that the imine bond formed after dimerization is too rigid to allow proper binding of the dimer to the nanotubes. Changing the substrates to another functional group that will result in more flexible bonds might lead to higher oligomers. To address these questions, I first selected a reaction that could be directly analyzed to evaluate the catalytic mechanism of the active sites as will be discussed in the next chapter.

Materials and Methods

Microwave Assisted Solid-Phase Peptide Synthesis

Peptides were synthesized on a Liberty CEM Microwave Automated Peptide Synthesizer (NC, USA) utilizing a FMOC-Rink Amide MBHA Resin (AnaSpec, CA, USA). All FMOC protected amino acids were purchased from Anaspec, and remaining chemicals from Sigma-Aldrich. Each peptide synthesis was performed at 0.1 mmol using a 30 mL reaction vessel at a scale of 0.1 mmol. FMOC-Rink Amide MBHA Resin was initially swollen using ~7 mL dimethylformamide for 15 minutes. FMOC deprotection

was achieved by addition of 20% piperidine and 0.1 M N-Hydroxybenzotriazole (HOBt) in dimethylformamide with microwave power set to maintain temperature between 45-55°C for 180 seconds, followed by 3X flushing with dimethylformamide. Each coupling step was performed using 0.1M FMOC protected amino acid, and activated with 0.1 M 2-(1H-Benzotriazole-1-yl)-1,1,3,3-tetramethyluronium hexafluorophosphate (HBTU), and 0.2 M N,N –Diisopropylethylamine (DIEA) in DMF. Coupling temperatures were maintained between 75-82°C by optimizing microwave power for 300 seconds. After coupling, the resin was rinsed with three aliquots of dimethylformamide. At the end of coupling steps, 20% acetic anhydride in dimethylformamide was added to acetylate the N-terminus of the peptides. The capping reaction was allowed to proceed for 3 hours at room temperature. Resin was filtered and washed with dichloromethane and allowed to air dry. Peptides were cleaved from the resin using trifluoroacetic acid/thioanisole/1,2-ethanedithiol/anisole (90:5:3:2, v/v/v/v) at room temperature for 3 hours. The cleaved peptide-TFA solution was filtered, and precipitated by dropwise addition of cold (-20°C) diethyl ether. Precipitated product was centrifuged at 3500 rpm for 10 minutes, and the pellet was subjected to 3 additional rounds of washing with cold diethyl ether. Precipitated product was desiccated overnight.

Dried peptides were dissolved in minimal volume of 40% acetonitrile + 0.1% trifluoroacetic acid and purified by RP-HPLC using a C18-reverse phase column with an acetonitrile-water gradient. Samples eluted from HPLC (10 μL) were mixed with 2,5-dihydroxybenzoic acid (10 μL), and 3x2 μL drops were placed as spots on a MALDI plate and allow to dry in a desiccator prior to analysis.

Peptide assembly

Peptides (2.5 mM) were dissolved in 40% CH_3CN/H_2O with 0.1% TFA. Dissolution was assisted by ~2 minutes of continuous vortex, followed by ~15 minutes of sonication until solution became clear. Peptides were allowed to assemble for approximately 2 weeks at 4 °C until mature as monitored by CD β-sheet signature and homogenous population either tubes or fibers as visualized by TEM. Prior to kinetic analysis, peptide assemblies were centrifuged at 13,800 g for 60 minutes and resuspended in distilled water prior to being buffered for reaction.

Circular Dichroism

Samples (18 μl) were placed into a quartz cuvette with a 0.1 mm path length (Starna Cells). Each spectra was obtained by scanning wavelength from 300 nm to 185 nm at a scanning rate of 100 nm/min with a resolution of 0.2 nm using Jasco J-810 spectropolarimeter. For each CD run temperature was controlled at 22°C, unless otherwise stated. Prior to recording the presented final wavelength scan CD at 225 nm was recorded for approximately 15 minute period to ensure sample had stabilized at the CD measurement conditions. Three successive wavelength scans were averaged for each sample. Buffer control spectra were averaged and subtracted from the sample spectra. The ellipticity ($[\theta]_{obs}$ mdeg) was converted to mean residue ellipticity ([θ], $deg \cdot cm^2 \cdot dmol^{-1}$) with the equation $[\theta]=[\theta]_{obs}/(10\times n\times C\times l)$, in which, n is the number of peptide bonds, C is the concentration (mol/L) and l is the path length of the cell (cm).

Fourier-Transform Infrared Spectroscopy

Sample aliquots (15 μL) were dried as thin films on an ATR diamond cell. The IR spectra were acquired using a Jasco FT-IR 4100 ATR with a diamond crystal at room temperature and averaging 400 scans with 2 cm^{-1} resolution. Background spectra were acquired immediately before each sample and were subtracted from each sample spectrum. Data was imported into OriginPro for graphing and analysis.

Transmission Electron Microscopy

10 μL of 2.5 mM peptide assemblies diluted 1:9 was added to TEM grids (200 mesh copper grids with a thin carbon film support – Electron Microscopy Sciences, Hatfield, PA). Peptide assemblies were allowed to adsorb on the grid for 1 minute before excess peptide solution was wicked away with filter paper. 10 μL of freshly prepared 2-wt % uranyl acetate solutions were added to TEM grids and incubated for 1-2 minutes for fibers and 4-5 minutes for nanotubes, before wicking away excess stain and then the grids were placed in a vacuum desiccator overnight or until imaging to remove any residual solvents. All staining solutions were prepared fresh and filtered prior to staining to minimize artifacts. TEM micrographs were recorded with a Hitachi 7500 TEM at magnifications ranging from 2000x to 200,000x with a Tungsten filament at an accelerating voltage of 75 kV. Widths measured from TEM were converted into diameters by setting 2 x width = the tube circumference and solving for the diameter. The standard deviations of the width measurements were converted into error bars.

UV-Vis Absorption Measurements

UV-vis absorption spectra were recorded with a Jasco V-530 UV spectrophotometer using a 2-10 mm cuvette path length. UV spectra were background subtracted using peptide nanotubes in the absence of substrates to minimize scattering effects.

Synthesis of 6-(tert-butoxymethyl)naphthalen-2-amine

Tert-butyl 6-amino-2-naphthoic acid was prepared following previously published protocols [43]. Briefly, 6-amino-2-naphthoic acid (3g, 16 mmol) was dissolved in 40 mL of water and t-BuOH (1:1 by volume). To this solution, NaOH (0.7 g, 17.6 mmol) and Boc_2O (4.2 g, 19.2 mmol) were added, stirred for 12 hours at room temperature, and the reaction mixture diluted with water and washed with dichloromethane. HCl (1N) was added to acidify the aqueous layer (pH~2) and the product was extracted with ethyl acetate and subsequently purified by column chromatography on SiO_2 with ethyl acetate and hexane as eluents to give the white solid in 85% yield. The resulting tert-butyl 6-amino-2-naphthoic acid (3 g, 10.4 mmol) was converted to its methyl ester via refluxing with iodomethane (excess) and K_2CO_3 (2.88 g, 2 equivalent) in dry acetone for 3 hours. The solvent was removed in vacuo, the residue triturated with ethyl acetate, and the product purified by column chromatography on SiO_2 with ethyl acetate and hexane as eluents to give the ester in 75% yield. The tert-butyl 6-amino-2-naphthoic acid methyl ester (2 g, 6.6 mmol) was dissolved in anhydrous THF and stirred at 4°C for 15 minutes before $LiAlH_4$ (0.302 mg, 7.9 mmol) suspended in THF was slowly added under N_2 and

the mixture was stirred for 2 hours at room temperature. The solution was filtered and the resulting alcohol (in the filtrate) was purified by column chromatography on SiO_2 with ethyl acetate and hexane as eluents to yield a white solid in 74% yield. This resultant alcohol (1.2 g, 4.3 mmol) was dissolved in dichloromethane (50 mL) containing Des-Martin periodinane (2.23 g, 5.2 mmol) and after stirring for 1 hour, saturated aqueous sodium bicarbonate (2 mL) and sodium thiosulfate (2 mL) were added. The organic layer was evaporated and purified by column chromatography on SiO_2 with ethyl acetate and hexane as eluents to give the solid in 90% yield. Overall, the yield of tert-butyl 6-amino-2-naphthaldehyde was 42.4 %. ^{1}H NMR (600 MHz, CD_2Cl_2) δ (ppm) = 10.08 (s, 1H), 8.25 (s, 1H), 8.09 (s, 1H), 7.95 (d, 1H), 7.91 (d, 1H), 7.85 (d,1H), 7.46 (d, 1H), 6.94 (s, 1H), 1.54 (s, 9H)

Preparation of 6-amino-2-naphthaldehyde (4) stock solutions

Tert-butyl (6-formylnaphthalen-2-yl) carbamate (10 mg, 36 μmole) was weighed in a glass vial and dissolved in dichloromethane (1 mL) before trifluoroacetic acid (200 μL) was added. NMR showed the deprotection of the Boc group was generally complete within 30 minutes, and a saturated solution of Na_2CO_3 was added slowly until the effervescence stopped and the pH of the aqueous layer was ~10. The organic layer was washed with brine to neutrality, the organic layer dried in vacuo, and the resulting yellow solid was dissolved in DMSO to the desired concentration.

Synthesis of 6-(N,N-dimethylamino)-2-naphthaldehyde (5)

6-Amino-2-naphthoic acid (2 g, 10.6 mmol) was dissolved in methanol (30 mL), charged with sodium cyanoborohydride (2.35 g, 37.4 mmol) and formaldehyde (37%, 16

mL), and the suspension stirred at room temperature for 2 hours. The solvents were removed in vacuo, the residue suspended in water and ethyl acetate, and the aqueous layer acidified with HCl (5 M) until the pH was ~1. The ethyl acetate layer was washed with brine to neutrality and dried in vacuo to yield 6 *N*,*N*-dimethyl amino-2-naphthoic acid in 90% yield. The acid was converted to the corresponding aldehyde following similar reaction protocols developed above for tert-butyl 6-amino-2-naphthaldehyde to give an overall yield of 6 *N*,*N*-amino-2-naphthaldehyde in 45%. ^{1}H NMR (600 MHz, CD_2Cl_2) δ (ppm) = 9.96 (s, 1H), 8.12 (s, 1H), 7.82 (d, 1H), 7.75 (d, 1H), 7.65 (d, 1H), 7.20 (d,1H), 6.8 (s, 1H), 3.09 (s, 1H).

Synthesis of model dimer (6)

6-(tert-Butoxycarbonyl) 6-amino-2-naphthoic acid (1) was prepared following previously published protocols. Briefly, 6-amino-2-naphthoic acid (6 g, 32 mmol) was dissolved in 40 mL of water and t-BuOH (1:1 by volume). To this solution, NaOH (1.4 g, 35 mmol) and Boc_2O (8.4 g, 40 mmol) were added, stirred for 12 hours at room temperature, and the reaction mixture diluted with water and washed with dichloromethane. HCl (1N) was added to acidify the aqueous layer (pH~2) and the product was extracted with ethyl acetate and subsequently purified by column chromatography on SiO_2 with ethyl acetate and hexane as eluents to give the white solid in 85% yield.

Half of the synthesized tert-butyl 6-amino-2-naphthoic acid (~3 g, 10.4 mmol, 1) was coupled with N,O Dimethylhydroxylamine hydrochloride (11.5 mmol, 1.06 g) in presence of 1.2 equivalent CDI as coupling agent to yield the Weinreb amide (2). After

removal of DCM, the product (2) was extracted with ethyl acetate and subsequently purified by column chromatography on SiO_2 with ethyl acetate and hexane as eluents to give the white solid in 95% yield. Boc group (2) was removed by addition of 20 ml TFA in dry DCM. Removal of solvents and extractions after basification yielded the amine. This amine was coupled with the 6-(tert-Butoxycarbonyl) 6-amino-2-naphthoic acid (1) in presence of EDC, DMAP in dry DCM. The mixture was stirred overnight in dry DCM under anhydrous conditions. After removal of DCM, the product (3) was extracted with ethyl acetate and subsequently purified by column chromatography on SiO_2 with ethyl acetate and hexane as eluents to give the white solid in 95% yield. The obtained product (3) was dissolved in anhydrous THF and stirred at -80°C for 15 minutes before LiAlH4 (0.302 mg, 7.9 mmol) suspended in THF was slowly added under N_2 and the mixture was stirred for 30 minutes at room temperature. The solution was filtered and the resulting aldehyde (in the filtrate) was purified by column chromatography on SiO_2 with ethyl acetate and hexane as eluents to yield a white solid. Finally, Boc protection was removed by addition of 20 ml TFA in dry DCM. Removal of solvents and extractions after basification yielded the amine dimer. Overall, the yield of dimer product was ~30 %.

Oligomerization of 6-amino-2-naphthaldehye on Ac-KLVFFAL-NH_2 nanotube surface

6-Amino-2-naphthaldehye (3 μL) from a 184 mM stock in DMSO was added to an aqueous solution (197 μL) containing Ac-KLVFFAL-NH_2 peptide nanotubes in water (0.5 mM). The final concentration of 6 -amino-2-naphthaldehye was 2.7 mM. The electronic signature was followed spectroscopically (JASCO V-530) in a 1 mm quartz cell over a period of 12 hours and compared to control solutions with no peptide. The

same experiment was performed with 6 *N,N* dimethyl amino-2-naphthaldehyde.

Binding of 6-amino-2-naphthaldehye to Ac-KLVFFAL-NH_2 nanotubes

6-Amino-2-naphthaldehye (3 µL) from a 460 mM stock in DMSO was added to an aqueous solution (197 µL) containing Ac-KLVFFAL-NH_2 peptide nanotubes in water (0.5 mM). The final concentration of 6-amino-2-naphthaldehye was 7 mM. After 12 hours, the sample was monitored by Jasco V-810 CD polarimeter using a 1 mm path length cell. The peptide solution (0.5 mM) and the aqueous solution of 6-amino-2-naphthaldehye (7 mM) were also monitored separately.

Two-photon fluorescence imaging

Fluorescence imaging was performed on a home-built two photon laser-scanning microscope previously described elsewhere [44]. Briefly, the microscope was constructed around an Olympus inverted microscope (IX71, Olympus, Melville, NY), using a Ti:Sapphire pulsed laser (Spectra Physics, CA) tuned above 780 nm with an average laser power at the sample of 3 mW. Using a water immersion 60X NA 1.2 Olympus objective lens (UPLSAPO60XW Olympus, Melville, NY) collected signals were sent to a photomultiplier module (H7421-40, Hamamatsu, Bridgewater, NJ) controlled by a custom laser scanning acquisition platform (Visµm). Samples were mounted on glass slides with 22×30 mm cover slips (Corning, Lowell, MA) sealed with nail varnish.

References:

1. Dong, J., et al., *Modulating amyloid self-assembly and fibril morphology with Zn(II).* Journal of the American Chemical Society, 2006. **128**(11): p. 3540-3542.

2. Dong, J., et al., *Engineering metal ion coordination to regulate amyloid fibril assembly and toxicity.* Proc Natl Acad Sci, 2007. **104**(33): p. 13313-13318.

3. Liang, Y., et al., *Light harvesting antenna on an amyloid scaffold.* Chemical Communications, 2008(48): p. 6522-6524.

4. Liu, P., et al., *Nucleobase-directed amyloid nanotube assembly.* Journal of the American Chemical Society, 2008. **130**(50): p. 16867-16869.

5. Layer, R.W., *The Chemistry of Imines.* Chemical Reviews, 1963. **63**(5): p. 489-510.

6. Jiao, Z., et al., *Enantioselective Strecker Reactions between Aldimines and Trimethylsilyl Cyanide Promoted by Chiral N,N'-Dioxides.* European Journal of Organic Chemistry, 2003. **2003**(19): p. 3818-3826.

7. Cao, Y.-Q., et al., *Sodium borohydride reduction of ketones, aldehydes and imines using PEG400 as catalyst without solvent.* Journal of Chemical Technology & Biotechnology, 2005. **80**(7): p. 834-836.

8. Moustafa, M.M.A.R. and B.L. Pagenkopf, *Ytterbium Triflate Catalyzed Synthesis of Alkoxy-Substituted Donor−Acceptor Cyclobutanes and Their Formal [4 + 2] Cycloaddition with Imines: Stereoselective Synthesis of Piperidines.* Organic Letters, 2010. **12**(21): p. 4732-4735.

9. Gopalakrishnan, M., et al., *New environmentally-friendly solvent-free synthesis of imines using calcium oxide under microwave irradiation.* Research on Chemical Intermediates, 2007. **33**(6): p. 541-548.

10. Hadjipavlou-Litina, D.J. and A.A. Geronikaki, *Thiazolyl and benzothiazolyl Schiff bases as novel possible lipoxygenase inhibitors and anti inflammatory agents. Synthesis and biological evaluation.* Drug Des Discov, 1998. **15**(3): p. 199-206.

11. Cushman, M., et al., *Synthesis and evaluation of a series of benzylaniline hydrochlorides as potential cytotoxic and antimitotic agents acting by inhibition of tubulin polymerization.* J Med Chem, 1993. **36**(19): p. 2817-21.

12. Hania, M.M., *Synthesis of Some Imines and Investigation of their Biological Activity.* E-Journal of Chemistry, 2009. **6**(3): p. 629-632.

13. Simion, A., et al., *Synthesis of imines, diimines and macrocyclic diimines as possible ligands, in aqueous solution.* Journal of the Chemical Society, Perkin Transactions 1, 2001(17): p. 2071-2078.

14. Barluenga, J., F. Aznar, and C. Valdes, *N-trialkylsilylimines as coupling partners for pd-catalyzed C[bond]N-forming reactions: one-step synthesis of imines and azadienes from aryl and alkenyl bromides.* Angew Chem Int Ed Engl, 2004. **43**(3): p. 343-5.

15. Annunziata, R., et al., *Poly(ethylene glycol)-Supported 4-Alkylthio-Substituted Aniline − a Useful Starting Material for the Soluble Polymer-Supported Synthesis of Imines and 1,2,3,4-Tetrahydroquinolines.* European Journal of Organic Chemistry, 2002. **2002**(7): p. 1184-1190.

16. Law, M.C., et al., *Synthetic and Mechanistic Studies of Indium-Mediated Allylation of Imines in Ionic Liquids.* The Journal of Organic Chemistry, 2007. **72**(3): p. 923-929.

17. Vázquez, M.Á., et al., *Infrared Irradiation: Effective Promoter in the Formation of N-Benzylideneanilines in the Absence of Solvent.* Synthetic Communications, 2004. **34**(15): p. 2705-2718.

18. Guzen, K.P., et al., *Eco-friendly synthesis of imines by ultrasound irradiation.* Tetrahedron Letters, 2007. **48**(10): p. 1845-1848.

19. Anastas, P.T., *Introduction: Green Chemistry.* Chemical Reviews, 2007. **107**(6): p. 2167-2168.

20. Childers, W.S., et al., *Phase Networks of Cross-β Peptide Assemblies.* Langmuir, 2012. **28**(15): p. 6386-6395.

21. Greenfield, N.J., *Methods to estimate the conformation of proteins and polypeptides from circular dichroism data.* Anal Biochem, 1996. **235**(1): p. 1-10.

22. Johnson, W.C., Jr., *Secondary structure of proteins through circular dichroism spectroscopy.* Annu Rev Biophys Biophys Chem, 1988. **17**: p. 145-66.

23. Johnson, W.C., *Analyzing protein circular dichroism spectra for accurate secondary structures.* Proteins, 1999. **35**(3): p. 307-12.

24. Singh, B.R., *In Infrared Analysis of Peptides and Proteins: Principles and Applications.* 2000.

25. Susi, H.B., D. M., *Resolution-enhanced Fourier transform infrared spectroscopy of enzymes.* Methods Enzymol, 1986. **130**: p. 290.

26. Parker, F.S., *Applications of Infrared Spectroscopy in Biochemistry, biology and Medicine.* 1971.

27. Mantsch, H.H.C., D., *Infrared Spectroscopy of Biomolecules.* 1996.

28. Barth, A. and C. Zscherp, *What vibrations tell us about proteins.* Q Rev Biophys, 2002. **35**(4): p. 369-430.

29. Miyazawa, T., *Perturbation Treatment of the Characteristic Vibrations of Polypeptide Chains in Various Configurations.* The Journal of Chemical Physics, 1960. **32**(6): p. 1647-1652.

30. Kirschner, D.A., C. Abraham, and D.J. Selkoe, *X-ray diffraction from intraneuronal paired helical filaments and extraneuronal amyloid fibers in Alzheimer disease indicates cross-beta conformation.* Proceedings of the National Academy of Sciences of the United States of America, 1986. **83**(2): p. 503-507.

31. Astbury, W.T., S. Dickinson, and K. Bailey, *The X-ray interpretation of denaturation and the structure of the seed globulins.* Biochem J, 1935. **29**(10): p. 2351-2360.1.

32. Parker, K.D. and K.M. Rudall, *The Silk of the Egg-Stalk of the Green Lace-Wing Fly: Structure of the Silk of Chrysopa Egg-stalks.* Nature, 1957. **179**(4566): p. 905-906.

33. Geddes, A.J., et al., *"Cross-beta" conformation in proteins.* J Mol Biol, 1968. **32**(2): p. 343-58.

34. Inouye, H., P.E. Fraser, and D.A. Kirschner, *Structure of beta-crystallite assemblies formed by Alzheimer beta-amyloid protein analogues: analysis by x-ray diffraction.* Biophysical Journal, 1993. **64**(2): p. 502-519.

35. Inouye, H. and D.A. Kirschner, *X-ray diffraction analysis of scrapie prion: intermediate and folded structures in a peptide containing two putative alpha-helices.* J Mol Biol, 1997. **268**(2): p. 375-89.

36. Krejchi, M.T., et al., *Crystal Structures of Chain-Folded Antiparallel β-Sheet Assemblies from Sequence-Designed Periodic Polypeptides.* Macromolecules, 1997. **30**(17): p. 5012-5024.

37. Sikorski, P.A., E. D. T.; Serpell, L. C., *Structure and texture of fibrous crystals formed by Alzheimer's abeta(11-25) peptide fragment.* Structure, 2003. **11**: p. 915.

38. Eanes, E.D. and G.G. Glenner, *X-ray diffraction studies on amyloid filaments.* J Histochem Cytochem, 1968. **16**(11): p. 673-7.

39. Mehta, A.K., et al., *Facial Symmetry in Protein Self-Assembly.* Journal of the American Chemical Society, 2008. **130**(30): p. 9829-9835.

40. Childers, W.S., et al., *Templating Molecular Arrays in Amyloid's Cross-β Grooves.* Journal of the American Chemical Society, 2009. **131**(29): p. 10165-10172.

41. Nilsson, M.R., *Techniques to study amyloid fibril formation in vitro.* Methods, 2004. **34**(1): p. 151-60.

42. Paul, C., et al., *Vibrational coupling, isotopic editing, and beta-sheet structure in a membrane-bound polypeptide.* J Am Chem Soc, 2004. **126**(18): p. 5843-50.

43. Cho, S.J., et al., *Combinatorial synthesis of a triphenylmethine library and their application in the development of Surface Enhanced Raman Scattering (SERS) probes.* Chemical Communications, 2010. **46**(5): p. 722-724.

44. Anthony, N.R., et al., *Mapping amyloid-[small beta](16-22) nucleation pathways using fluorescence lifetime imaging microscopy.* Soft Matter, 2014. **10**(23): p. 4162-4172.

Chapter 3: Retro-aldol Activity of Aβ(16-22) Congeners: The Binding Site

Introduction

The parent seven residue peptide discussed in Chapter 2, ^{16}KLVFFA^{22}E, contains the hydrophobic nucleating core of the Aβ peptide of Alzheimer's disease [1-4] and can sample diverse morphologically distinct and environmentally responsive assemblies or phases (Figure 3-1) [5, 6]. Pure cross-β phases predominate under select environmental conditions, and constraints from solid-state NMR, ordered X-ray diffraction, molecular dynamic (MD) simulations [7, 8], and optical signatures of Congo red (CR) binding [9] have enabled the construction of structural models for several assemblies.

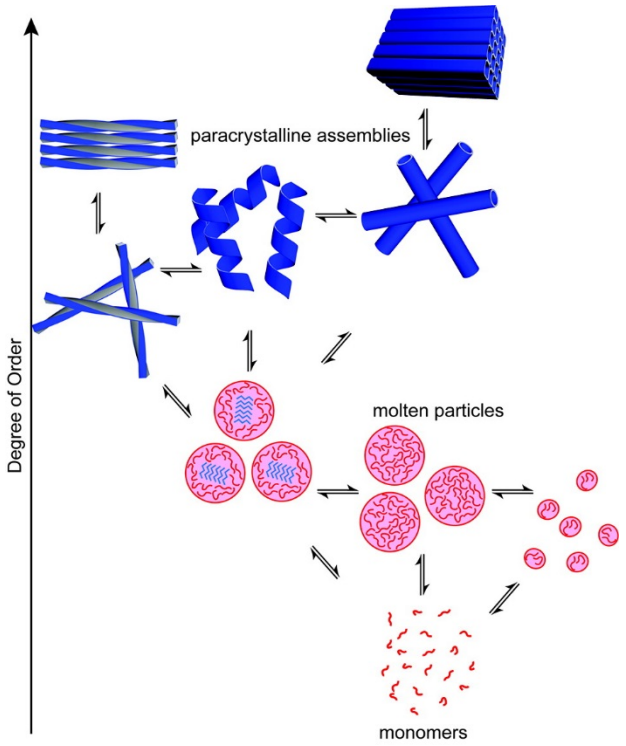

Figure 3-1: *Network diagram indicating observed phase transitions. Each phase exhibits thermodynamic barriers that can be arranged in a dynamic network. Adapted from [5]*

The nanotubes described in Figure 1-8 of Chapter 1 and in Chapter 2 are a distinct phase in this network and the structural implications of a nucleophilic lysine side chain within a hydrophobic groove is reminiscent of the architecture seen in class I aldolases [10]. Although the architecture of the tube surface is similar to type I aldolases, a distinct difference with the peptide assembly surfaces, is the repeating nature and proximity of the residues composing the hydrophobic pocket and reactive side chains on the tube surface. It is possible that these features and the ability to control the exposed residues on the tube surface present the opportunity to create unique catalysts. In chapter 2, I have shown that these nanotubes template imine condensation with 6-amino-2-naphthaldehyde. To expand the catalytic range of these assemblies, we considered (±)-methodol, the product of acetone condensation with 6-methoxy-2-naphthaldehyde and previously used to evaluate retro-aldol catalysis [10, 11], as an initial substrate to characterize the catalytic capability of the peptide nanotubes (Figure 3-2).

The centerpiece of the amine catalyzed reaction is the formation of the enamine intermediate. The enamine based mechanism proceeds in several distinct steps (Figure 3-2), involving acid-base catalysis by either amino acid side chains or water molecules. First, nucleophilic attack by lysine side chain amine on the ketone of the methodol substrate forms a carbinolamine intermediate, which eliminates water to form the imine/iminium species. Carbon-carbon bond cleavage is triggered by the deprotonation of the β-alcohol, with the iminium acting as an electron sink. The resulting enamine can tautomerize to an imine and hydrolyze to release the covalently bound product and free the enzyme for another round of catalysis [12].

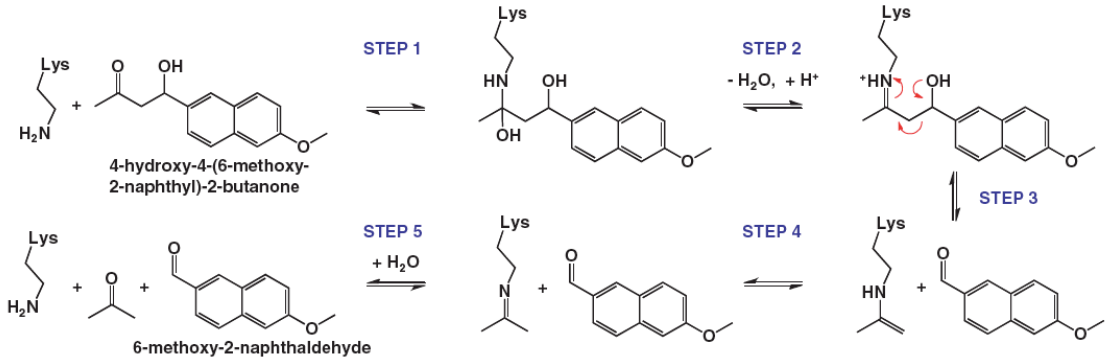

Figure 3-2: *Steps in the amine-catalyzed retro-aldol reaction of 4-hydroxy-4-(6-methoxy-2-naphthyl)-2-butanone to form 6-methoxy-2-naphthaldehyde [12].*

The enamine intermediates in these reactions are typically unstable in water and equilibrium between formation and hydrolysis of an enamine makes direct observation of an enamine within protein crystals difficult [13-15]. However, studies with aldolase and other enzymes [16, 17] have shown that the molecular steps involving the Lysine residue in covalent catalysis are well known steps involved in activating a substrate ketone to an enaminone. As shown in Figure 3-3, this mechanism involves a lysine addition to the carbonyl to form the carbinolamine and subsequently collapses to the iminium ion. The enaminone can be formed via imine tautomerization with β-diketones (2,4-pentanedione, 3-methyl-2,4 pentanedione, 2-acetylcyclopentanone, and 2-acetylcyclohexanone) and this stable product can be quantified spectrophotometrically at 318-335 nm [18-20] (Figure 3-3).

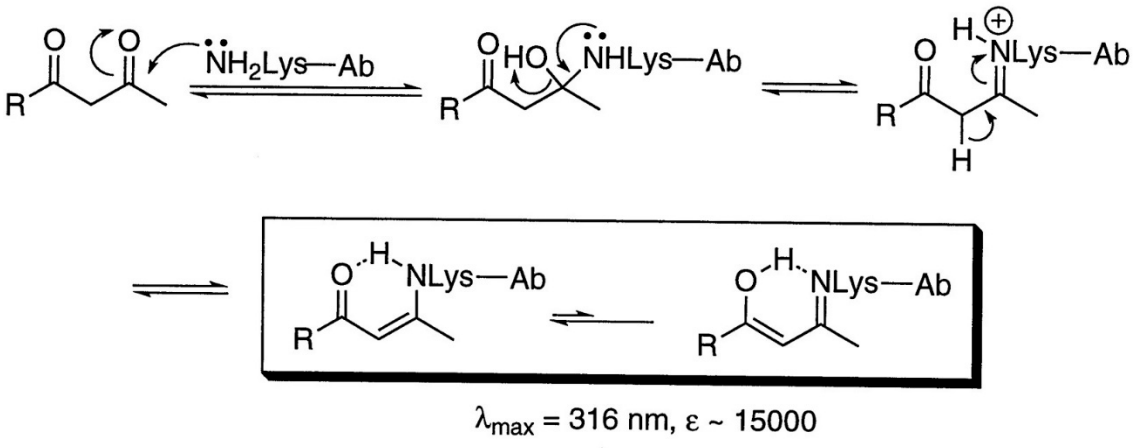

Figure 3-3: *Scheme showing the mechanism of amine reactivity towards diketone to give a stable enaminone [20].*

Mechanistically, retroaldolases exploiting amine catalysis represent the most complex designed enzymes to date [21-23] because they utilize a multistep reaction sequence involving several enzyme- bound Schiff base intermediates. Assays for testing retroaldolase enzymes commonly have been accelerated by using substrates with absorbance and/or fluorescent profiles. Methodol (4-hydroxy-4-(6-methoxy-2-naphthyl)-2- butanone) and related compounds have been extensively used to benchmark a variety of different systems ranging from micelles [24] to small peptides and foldamers [25, 26] to computationally-designed and evolved retroaldolases [21, 23, 27, 28] and antibodies [10, 20, 29].

The basic design for a retroaldolase involve a hydrophobic substrate binding site and a primary amine localized within the binding site [23]. This design allows the pKa of the amine group to be properly modulated to form the iminium intermediate at neutral or near neutral pHs. This simple design is an inherent feature of the peptide nanotubes

assemblies formed from the amyloidogenic seven residue peptide Aβ(16-22) and its variants driving the efforts to explore the ability of cross-β assemblies to catalyze retro-aldol reaction using methodol as a substrate.

Results and Discussion

Evaluation of the Active Sites in the Nanotubes

Given the large numbers of potential active sites along the lamination grooves as modelled in Figure 3-4, we sought a substrate or site-specific inhibitor that would be readily observable using physicochemical methods [30-34]. In addition, estimating the starting peptide concentration is not sufficient as the amount of peptide that is assembled is required to know the number of possible active sites.

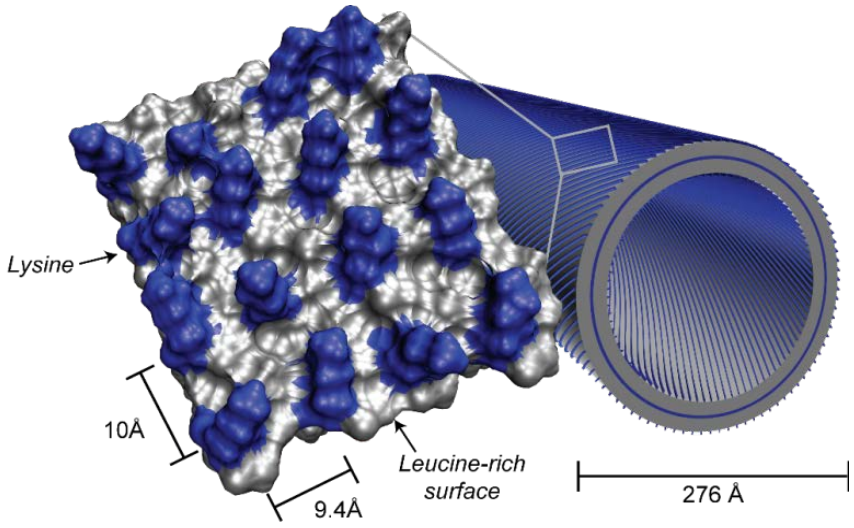

Figure 3-4: *Structural model for the K16 nanotube with a van der Waal surface expansion displaying the lysine (blue) and leucine (grey) residues. The leucines form the hydrophobic binding pockets while half of the lysines are exposed on the tube surface and the other half are in the bilayer. The bilayer is indicated on the tube cartoon by the blue stripe that runs through the middle of the tube wall.*

Since the peptides are assembled in 20% or 40% MeCN/H_2O at acidic or neutral pH, conditions chosen to give the most homogenous population of assemblies, and the reactions are carried out in aqueous buffer with 5% DMSO or 5% MeCN (needed to solubilize the substrate) in order to compare with known enzymes, it is important to know the impact of the assemblies. The protocol for preparing the peptide assemblies for catalysis involves spinning down the assemblies and re-suspending the pellets in water. If all the nanotubes are not pelleted, then the actual concentration of nanotubes will be less than initial concentration. For all these reasons, it is necessary to develop methods to determine the concentration of reactive amines in the nanotubes.

The approach developed to determine the numbers of available amines presented on the peptide assembly surface was based on the capability of lysine side chain to react with 2,4-pentanedione (acetyl acetone) to form enaminone which can be quantified with UV-Vis (Figure 3-3). A solution of 2,4 pentanedione has a maximum absorbance at 275 nm (depending on the solvent) (Figure 3-5A), but when 2,4-pentanedione is reacted with a primary amine, such as lysine, the transition shifts to 318 nm due to the generation of the enaminone (Figure 3-3). The absorbance of the enaminone can be used to estimate both the progress of the reaction and the number of reactive amines. 500 μM nanotubes incubated with 2500 μM 2,4-pentanedione reached equilibrium after about 21 hours (Figure 3-5B)

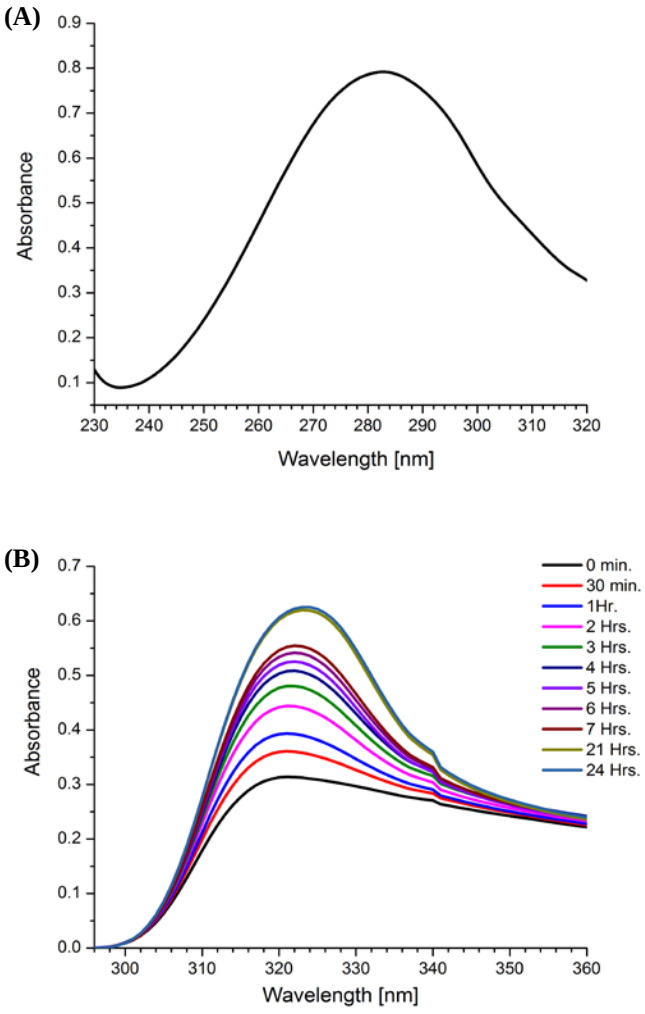

Figure 3-5: *(A) UV-Vis spectra of 2.5 mM of 2,4-pentanedione (acetyl acetone) in buffer. (B) UV-Vis progressive monitoring of reaction of 2500 µM 2,4-pentanedione with 500 µM Ac-KLVFFAL-NH_2 over a period of 24 hours.*

By reacting the nanotubes for 48 hours at room temperature, the resulting concentration of acetyl acetone required to saturate the nanotubes was found to be 240±8 µM (Figure 3-6).

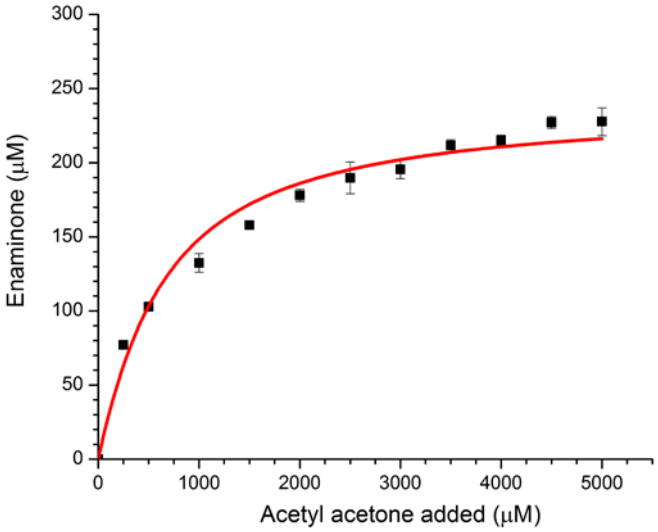

Figure 3-6: Titrating amine accessibility on Ac-KLVFFAL-NH₂ nanotube surface. *Enaminone formation monitored by UV absorbance at 316 nm after 48 hours as a function of 2,4-pentanedione concentration in the presence of 500 μM Ac-KLVFFAL-NH₂ peptide assembled as nanotubes. A fit to the data ($y=240\pm8\ \mu M * (1-e^{-0.0013\pm0.0001*x})$), indicates half of the peptide lysine sidechains (240±8 μM) are solvent accessible, consistent with the nanotube peptide bilayer wall architecture*

This result is also consistent with the nanotube peptide bilayer wall architecture [35], indicating that approximately 50% of the peptide lysine side chains are accessible.

Number of Peptides per Binding Site

Our structural model suggests that the nanotube surface displays an array of hydrophobic pockets placed side by side. The acetyl acetone is expected to react with the primary amine on the nanotubes without the need of a binding site, but the binding of larger molecules such as methodol may be influenced by the hydrophobic surface of the nanotubes. Given the ability to measure the free amine with acetyl acetone, naphthalene was functionalized with the reactive diketone moiety to give 1-(6-methoxy-2-naphthalenyl)-1,3-butanedione (Figure 3-7), the diketone of methodol.

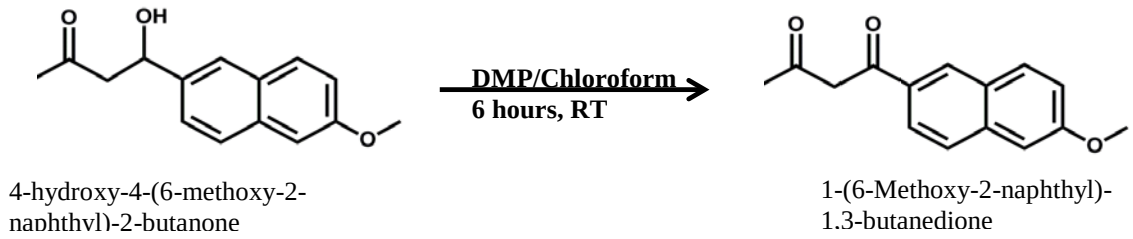

4-hydroxy-4-(6-methoxy-2-naphthyl)-2-butanone

1-(6-Methoxy-2-naphthyl)-1,3-butanedione

Figure 3-7: *Scheme for the synthesis of 1-(6-methoxy-2-naphthalenyl)-1,3-butanedione*

The reaction of 1-(6-methoxy-2-naphthalenyl)-1,3-butanedione with the primary amine should react similarly to 2,4-pentanedione and give the conjugated enaminone (Figure 3-8) with an absorbance at 358 nm [21].

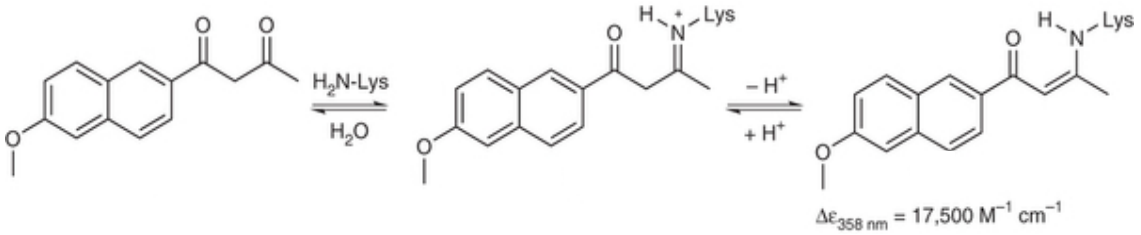

Figure 3-8: *Scheme showing the reaction of Lysine amine with 1-(6-methoxy-2-naphthalenyl)-1,3-butanedione to give a stable enaminone. Adapted from [21]*

As shown in Figure 3-9, the titration of 300 µM Ac-KLVFFAL-NH_2 nanotubes with 1-(6-methoxy-2-naphthalenyl)-1,3-butanedione saturated at 74.1±3.1 µM, giving at least four peptides per 1-(6-methoxy-2-naphthalenyl)-1,3-butanedione binding site establishing that the amine is reactive.

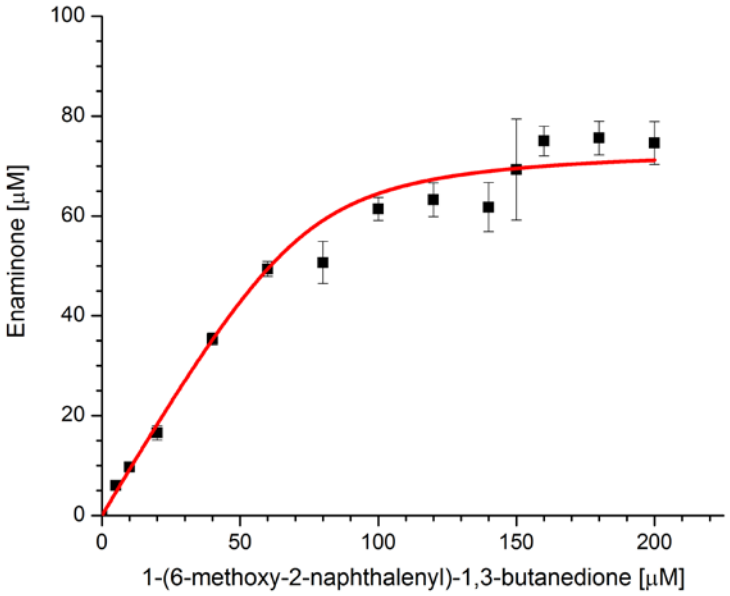

Figure 3-9: Titrating amine accessibility on Ac-KLVFFAL-NH₂ nanotube surface. *Enaminone formation upon addition of 1-(6-methoxy-2-naphthalenyl)-1,3-butanedione to 300μM Ac-KLVFFAL-NH₂ monitored by UV absorbance at 350 nm. A fit to the data ($y=74.1\pm3.1\ \mu M * (1-e^{-0.0013\pm0.0001*x})$) demonstrated reaction with ½ of the available amines and giving 4.0±0.1 peptides per binding site.*

Retro-aldol Reactivity of Peptide Assemblies

To initially explore the catalytic mechanism of the supramolecular lysine rich surfaces of peptide nanotubes, Ac-KLVFFAL-NH_2 and Ac-RLVFFAL-NH_2 peptides, were prepared, allowed to assemble separately, and shown to form morphologically indistinguishable nanotubes by transmission electron microscopy (Chapter 2). 6-methoxy-2-naphthaldehyde, our expected retroaldol product and a structurally similar portion of the cross-β dye Congo red (CR) binds homogeneously along the nanotube assemblies (Figure 3-10A,C). TEM analyses confirm that both Ac-KLVFFAL-NH_2 and Ac-RLVFFAL-NH_2 tube morphology is unchanged by naphthaldehyde binding (Figure

3-10B), but the Ac-KLVFFAL-NH_2 assemblies appear to quench naphthaldehyde fluorescence (Figure 3-10C). To test if the quenching was due to reversible imine formation with the aldehyde carbonyl [36], no obvious fluorescence quenching was observed with Alexa 555 dye (Figure 3-10D).

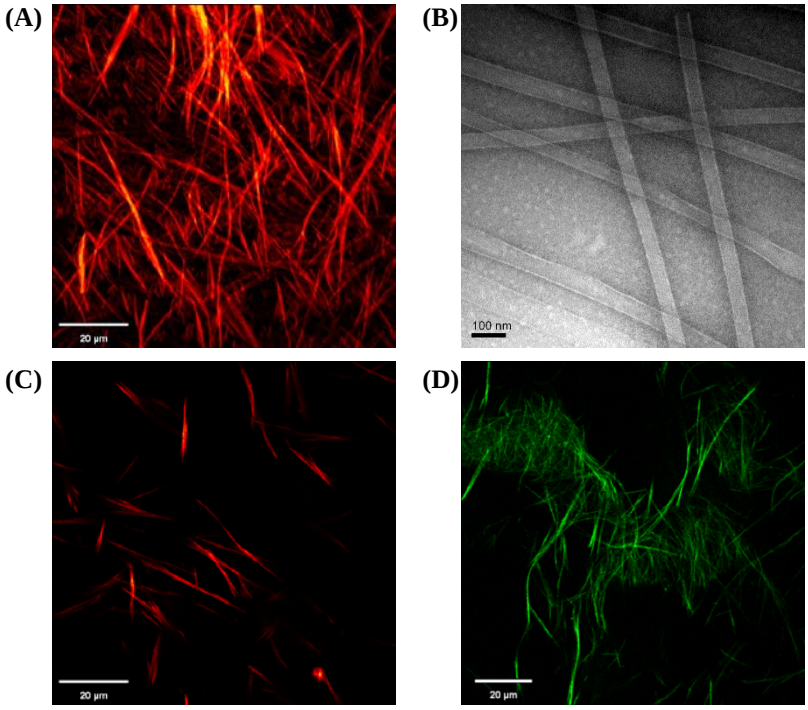

Figure 3-10: *Fluorescence image of (**A**) Ac-RLVFFAL-NH_2 and (**C**) Ac-KLVFFAL-NH_2 nanotubes incubated with 6-methoxy-2-naphthaldehyde. (**B**) TEM image of Ac-KLVFFAL-NH_2 control showing that the nanotubes are still intact under experimental conditions. (**D**) Fluorescence image of Ac-KLVFFAL-NH_2 nanotubes incubated Alexa 555.*

To evaluate the retro-aldol catalytic range of the peptide assemblies, both Ac-KLVFFAL-NH_2 and Ac-RLVFFAL-NH_2 nanotubes were separately incubated with (±)-methodol. The rate of retro-aldol conversion of (±)-methodol (Figure 3-11A) by Ac-KLVFFAL-NH_2 to the reaction product, 6-methoxy-2-naphthaldehyde, is evaluated by

the increase in fluroescence (Figure 3-11B, red line**)**. The arginine nanotubes show no significant florescence (Figure 3-11B, green line**)** over the background (Figure 3-11B, black line**)**. Compared to a lysine (Figure 3-11C), the Ac-KLVFFAL-NH_2 nanotubes gives an initial rate that is $>10^4$ above lysine. The absence of activity for the Ac-RLVFFAL-NH_2 assemblies highlights the importance of the lysine side chain.

(A)

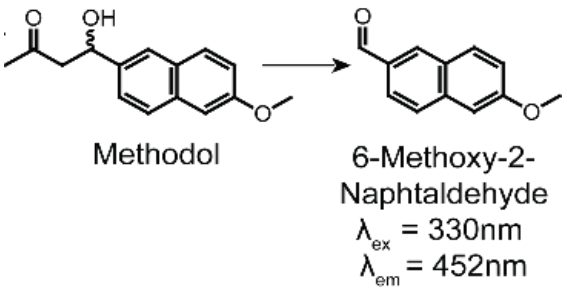

(B)

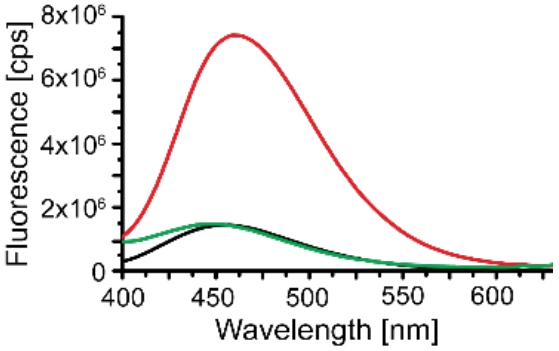

(C)

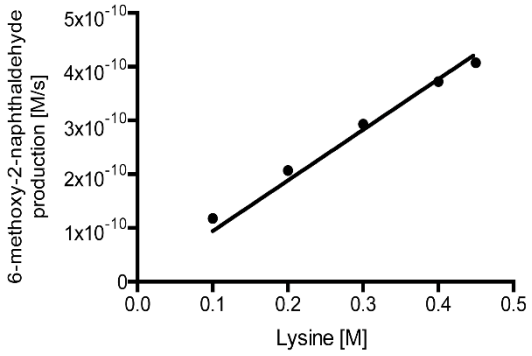

Figure 3-11: *(**A**) Retro-aldol reaction of methodol to generate the fluorescent 6-methoxy-2-naphthaldehyde. (**B**) Fluorescence emission spectra (λ_{ex} = 330 nm, λ_{em} = 452 nm) of 50 μM methodol (black line), 50 μM methodol with 1 mM Ac-KLVFFAL-NH_2 nanotubes (red line), and 50 μM methodol with 1 mM Ac-RLVFFAL-NH_2 nanotubes (green line) incubated in 50 mM sodium phosphate buffer with 300 mM NaCl at pH 7.5 for 36 hours at room temperature. Each sample contains 5% 6-methoxy-2-naphthaldehyde at zero time to establish baseline fluorescence. (**C**) Production of 6-methoxy-2-naphthaldehyde as a function of lysine concentration. Reactions were performed in 50 mM phosphate buffer at 25°C with 300 mM NaCl at pH 7.5 with 400 μM methodol substrate. Line fits yielded a second-order rate constant of 2.36 x 10^{-6} $M^{-1}s^{-1}$, identical to previous measurements.*

Amyloid Structural Control

Catalysis by these assemblies is based on the assumption that substrate binding to the nanotube surface is required. Our growing knowledge of the energetic constraints on assembly is now allowing specific control over the final assembly. For example, the amyloid surfaces are more dramatically altered by assembling Ac-KLVFFAE at neutral pH. Ac-KLVFFAE carries a C-terminal carboxylate, and assembles into fibers with the β-strands arranged in antiparallel in-register due to the formation of a K-E salt bridge [7, 37, 38]. Such cross-strand pairing has also been exploited by replacing valine with a bulkier ter-leucine, where the peptide assembles into nanotubes (Figure 3-12A) independent of pH [7] (Figure 3-12C).

TEM micrograph show that the nanotubes formed by Ac-KL(terL)FFAE-NH_2 peptide are significantly larger (Figure 3-12A), ~180 nm, than the 80 nm nanotubes formed by Ac-KLVFFAE-NH_2. Curiously, the CD spectrum displays a minimum at ~200 nm and a maximum at ~225 nm (Figure 3-12B), almost a mirror image of the CD spectrum of Ac-KLVFFAE-NH_2, when assembled as fibers or tubes. X-ray diffraction studies confirm the amyloid cross-β structure (Figure 3-12D), and amide type I stretching

modes are consistent with an antiparallel out-of-register peptide arrangement (Figure 3-12C).

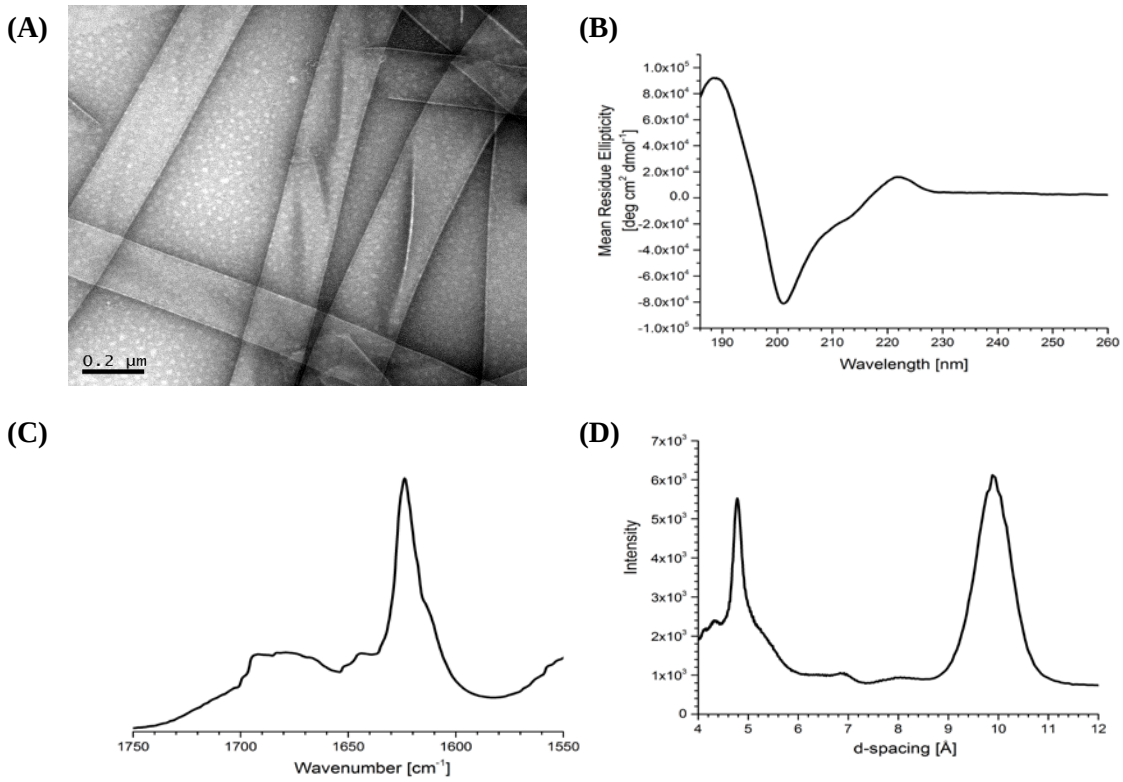

Figure 3-12: *Structural characterization of 2.5 mM Ac-KL(terL)FFAE-NH_2 assembled in 40% MeCN/H_2O, pH 7* ***(A)*** *Uranyl acetate stained TEM micrographs. Scale bar is 200 nm. (B) CD wavelength scans (C) FT-IR and (D) X-ray diffraction.*

Ac-KLVFFAQ-NH_2 peptide was found to assemble in 20% MeCN/H_2O at acidic pH into fibers [39] with parallel in-register strand arrangement as controlled by the Q-Q cross-strand pairing. This peptide is useful as it doubles the concentration of lysine on one face of the fiber. To place the Q in the binding groove, Ac-KL(terL)FFAQ-NH_2 peptide was prepared. The peptide was assembled under the same condition as the Ac-KLVFFAQ-NH_2 peptide. As predicted, the peptides assembled into nanotubes (Figure 3-

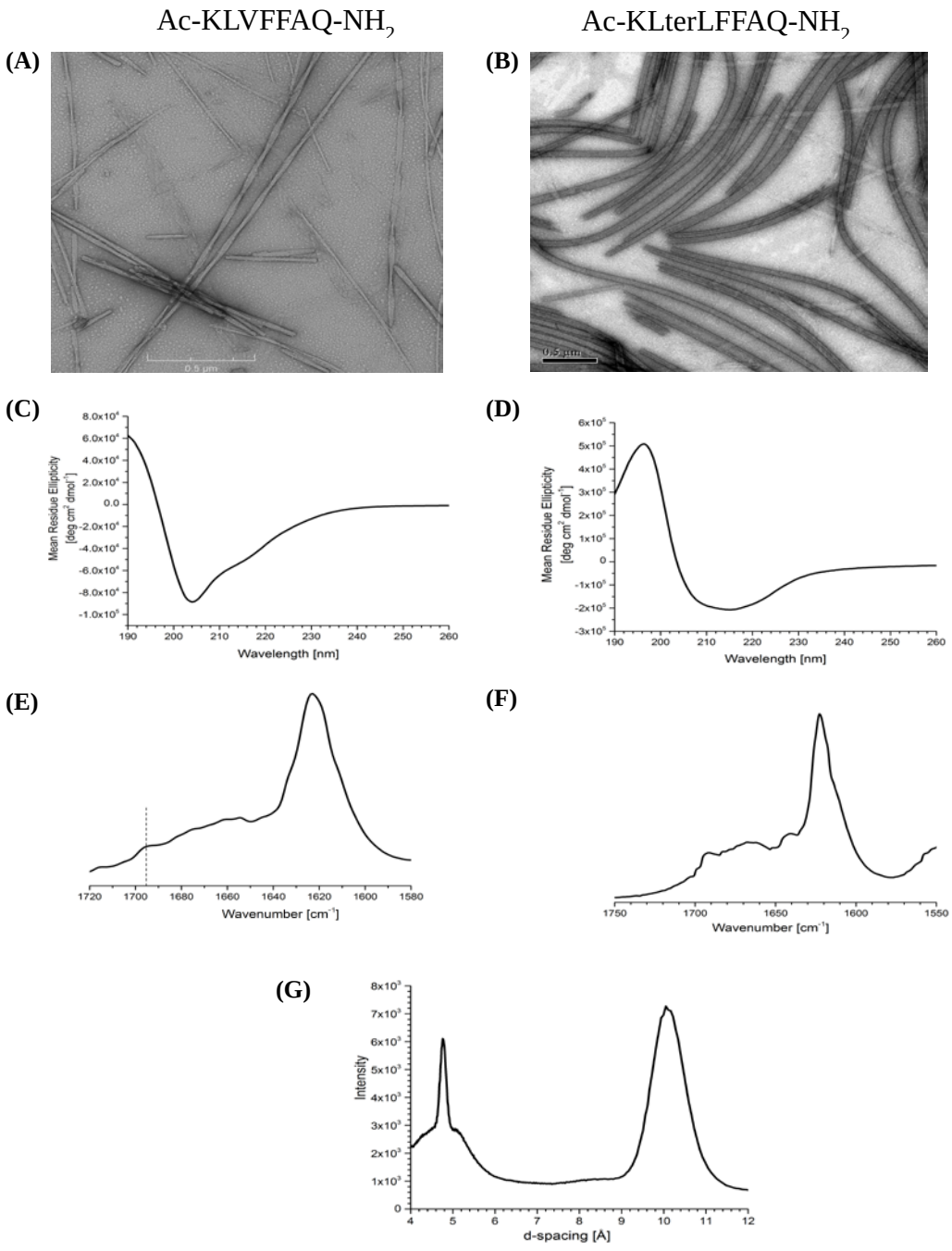

Figure 3-13: *TEM micrographs of (A) Ac-KLVFFAQ-NH₂ (B) Ac-KLterLFFAQ-NH₂. CD spectrum of mature (C) Ac-KLVFFAQ-NH₂ showing a negative ellipticity at 205 nm (D) Ac-KLterLFFAQ-NH₂ nanotubes showing a positive ellipticity at 198 nm and a negative ellipticity at 215 nm. IR of the (E) Ac-KLVFFAQ-NH₂ with a parallel ß-strand orientation. (F) Ac-KLterLFFAQ-NH₂ nanotubes with an antiparallel ß-strand orientation. (G) X-ray diffraction of Ac-KLterLFFAQ-NH₂ showing hydrogen bonding distance of 4.7Å and laminate distance of 10.3Å.*

13B). CD displayed a characteristic β-sheet signature with a maximum at ~198 nm and a minimum at ~215 nm (Figure 3-13D). FT-IR measurement places the amide I stretch vibration at 1624 cm^{-1} and 1693 cm^{-1} indicating an anti-parallel β-strand arrangement [56, 57] (Figure 3-13F). X-ray diffraction studies also confirmed cross-β architecture for the nanotubes.

Lysine Microenvironment is Critical for Catalysis

While Ac-KLVFFAE-NH_2 peptides assemble to a similar degree as Ac-KLVFFAL-NH_2, the anti-parallel in-register β-strand fibers [7, 40] have a less well-defined groove (Figure 3-14). Indeed, this Ac-KLVFFAE-NH_2 fibers does not bind the naphthaldehyde product (Figure 3-15) and no catalytic activity is detected for retro-aldol cleavage of methodol, even at concentrations that approach both the peptide (2 mM) and substrate solubility (~500 μM) limits (Figure 3-16). Recognizing that the side chain carboxylate charge may affect the catalytic availability of the lysine amine in both the free peptide and the supramolecular fiber because of K-E salt bridge, the glutamine congener Ac-KLVFFAQ-NH_2 lacking the charge was evaluated for activity. This Q congener with the shallower groove was inactive (Figure 3-16) even though the lysine density along one fiber face is twice that of the Ac-KLVFFAL-NH_2 assemblies (Figure 3-14). Ac-KL(*ter-L*)FFAE-NH_2 generates nanotubes with surface grooves similar to that of Ac-KLVFFAL-NH_2 but the grooves contain charged glutamic acid residues. This charged surface grooves prevent binding of 6-methoxy-2-naphthaldehyde **(**Figure 3-15) and no catalytic conversion of methodol was observed (Figure 3-16) suggesting that the activity obtained with Ac-KLVFFAL-NH_2 was due to the hydrophobic binding pocket alone and not due to un-assembled peptide that might be present in solution. No catalysis

was observed even when the Q congener (Ac-KL(*ter-L*)FFAQ-NH_2), was assembled into nanotubes, suggesting that the neutral glutamine residue in the binding site also prevent binding. Taking advantage of the ability to differentially regulate the lysine microenvironment by subtle differences in the supra-molecular architecture, these results are consistent with a binding site requirement for catalysis.

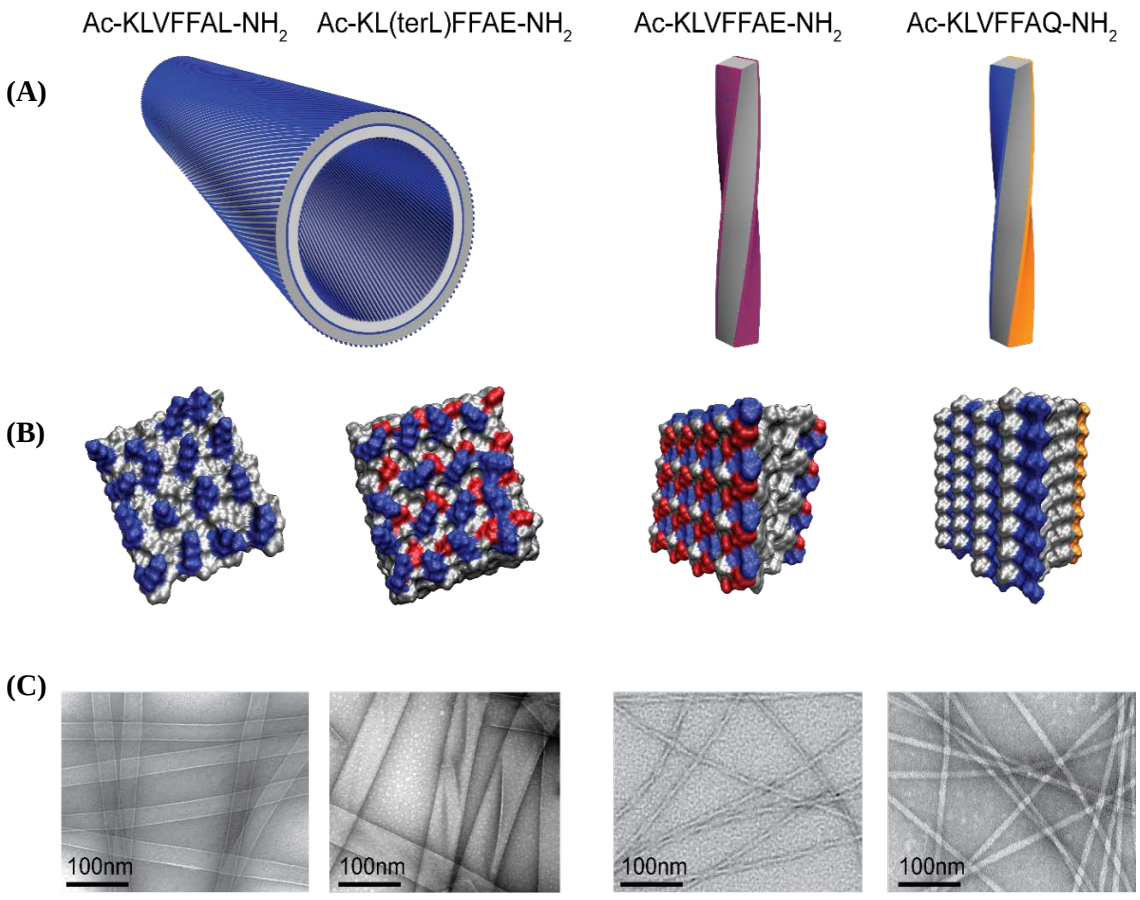

Figure 3-14: *(A) Cartoon of peptide assemblies and (B) solvent exposed surfaces. For the surface renderings, positively charged residues are colored blue, negatively charged residues red, glutamine residues orange and hydrophobic residues grey. (C) Negatively stained transmission electron micrographs of peptide assemblies*

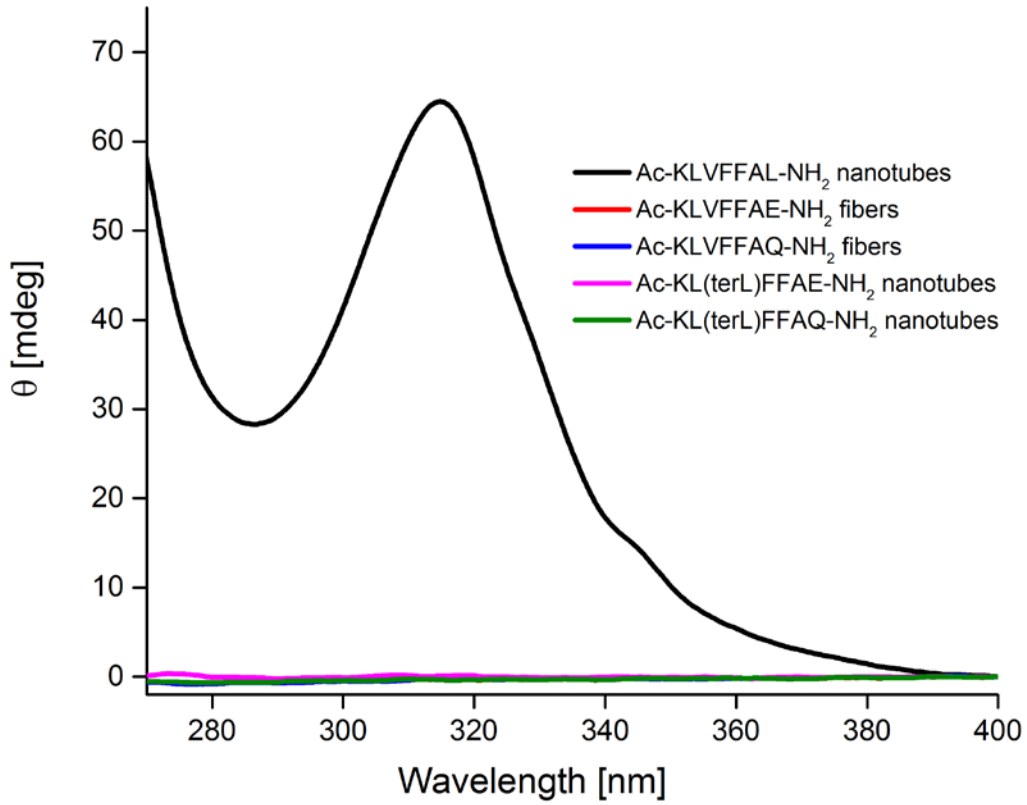

Figure 3-15: Evaluation of 6-methoxy-2-naphthaldehyde binding to peptide assemblies by CD. *Circular Dichroism of 0.1 mM 6-methoxy-2-naphthaldehyde incubated with 0.5 mM of each of the peptide assemblies. A transition centered at 318 nm was observed in the presence of Ac-KLVFFAE-NH_2 nanotubes (black) but not for Ac-KLVFFAE-NH_2 fibers (red), Ac-KLVFFAQ-NH_2 fibers (blue), Ac-KL(terL)FFAE-NH_2 nanotubes (pink) or Ac-KL(terL)FFAQ-NH_2 tubes (green) under these conditions.*

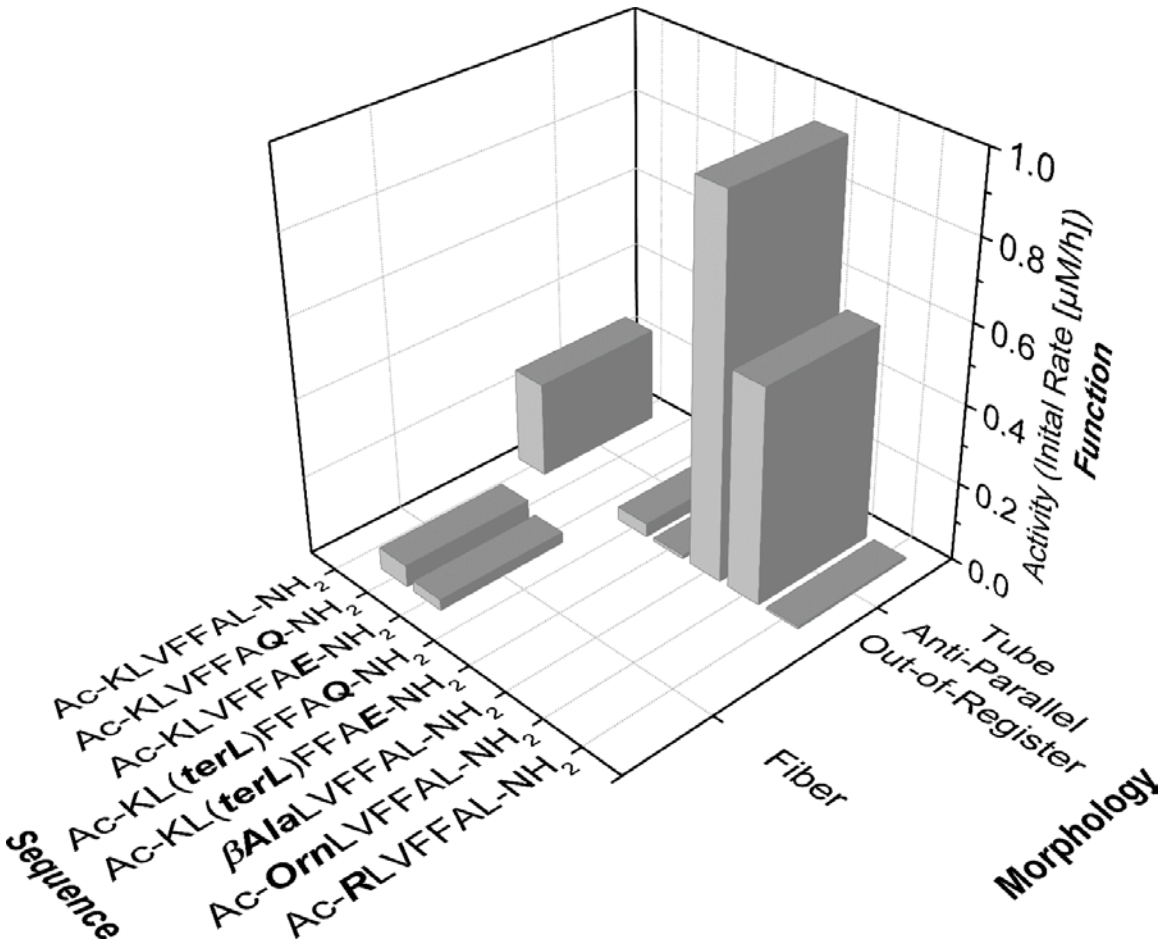

Figure 3-16: *Initial rate of production of 6-methoxy-2-naphthaldehyde by the indicated peptide assembly where the peptide concentration is 500 μM and the starting (±)-methodol concentration is 80 μM.*

A model of the Ac-KLVFFAL-NH_2 nanotube binding site was built to better understand methodol binding to the nanotubes. The model include constraints from solid-state NMR, ordered diffraction, molecular dynamic simulations (MD) [35, 41] and optical signatures of CR binding [42]. Further MD simulations evaluating the conformationally flexible lysine side chain found that it could access >40% of the tube's surface area (Figure 3-17). Substrate docking suggest a range of possible binding modes

(Figure 3-18) and therefore the surface lysine could react with a range of potential methodol binding geometries within the groove that may affect the enantioselectivity of the reaction.

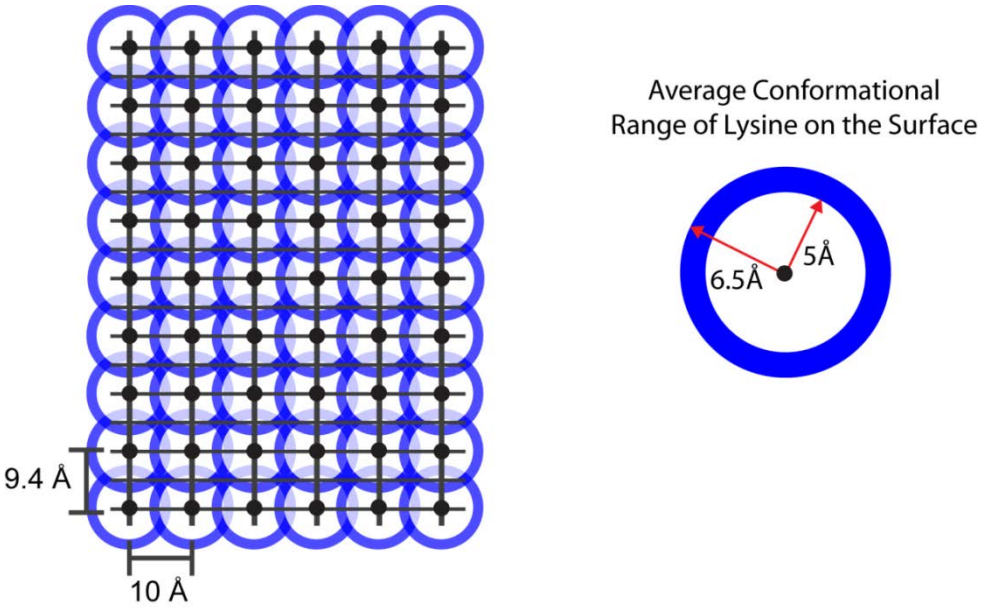

Figure 3-17: Grid view of Ac-KLVFFAL-NH₂ catalytic surface. *Blue circles centered at the N-terminus of the each peptide indicate the average conformational range of the lysine amines along the tube surface.*

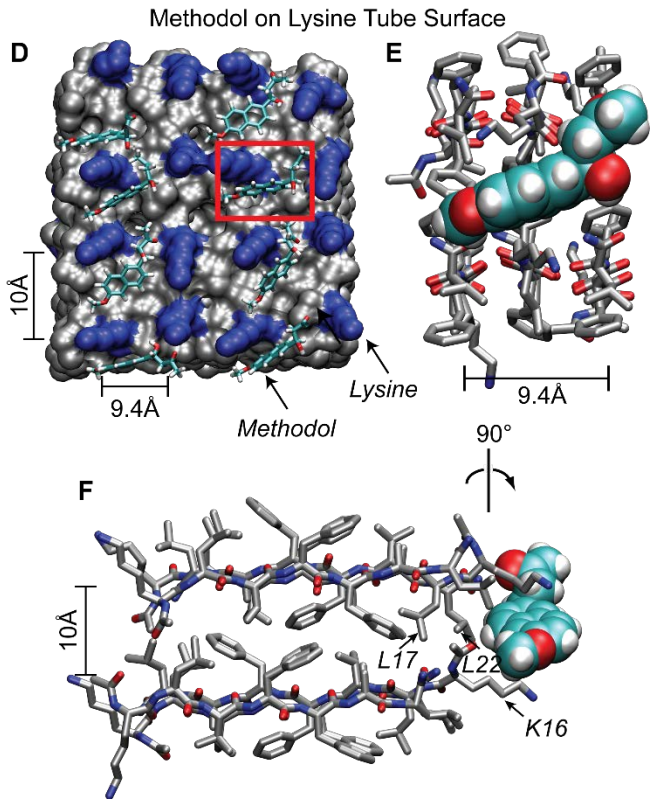

Figure 3-18: *(**D**) 1.2 ns molecular dynamics simulation of (S)-methodol docked onto surface of K1 anti-parallel out-of-register amyloid assembly. In the space filling models the hydrophobic, LVFFAL residues are colored grey, the lysines colored blue and methodol is drawn as sticks with carbons colored green, oxygen red and hydrogen white. (**E**, **F**) Expansions of methodol (space filling) on tube surface with peptides drawn as sticks.*

Enantioselectivity Studies

If the methodol binds the chiral surface of the nanotubes, then the retro-aldol reaction would be expected to show enantioselectivity. To evaluate the effect of methodol binding within the groove, site enantioselectivity using (±)-methodol conversion was analyzed with Chiralpak AD-RH (Daicel) chromatography. When eluted isocratically with 40% MeCN/Water at a flow rate of 0.5 mL/min, the retention times of (R)- and (S)-methodol were 18.6 and 21.3 minutes, respectively (Figure 3-19 Top). (R)- and (S)-

methodol chirality was assigned with aldolase antibody 38C2. Antibody 38C2 has been shown to catalyze both the aldol and retro-aldol reaction enantioselectively and has been shown to resolve racemic methodol to yield only the (R)-methodol with 97% ee [43]. After incubating the aldolase antibody 38C2 with (±)-methodol for 24 hours, the un-consumed enantiomer eluted at t=18.6 minutes and was assigned as [R]-methodol (Figure 3-19).

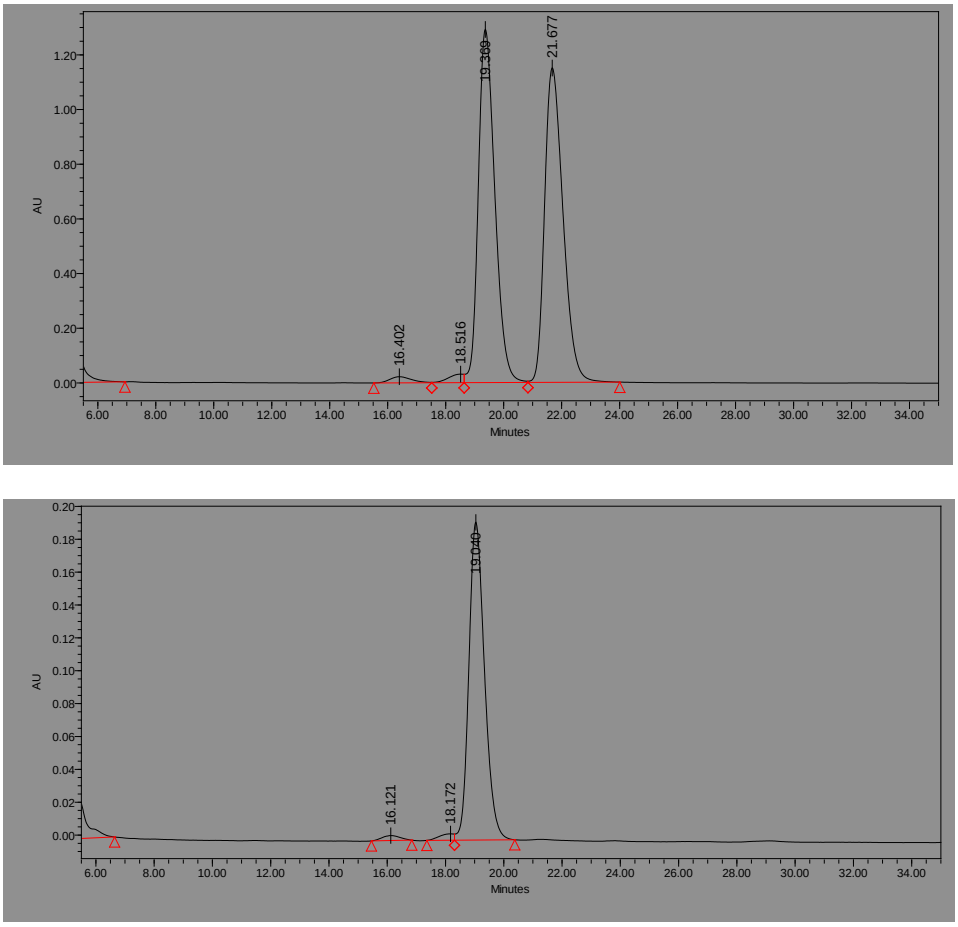

Figure 3-19: *HPLC Chromatogram of Antibody* 38C2 catalyzed retro-aldol cleavage of (±)-methodol. *(Top) immediately after adding antibody* 38C2 and *(Bottom) after 22 hours incubation. The trace was obtained using an isocratic elution with 40% MeCN/H_2O.*

Ac-KLVFFAL-NH_2 nanotubes incubated with (±)-methodol gave an initial velocity ratio S-/R- of 3.41 (Figure 3-20) and a 78% ee after 98% conversion over a period of 192 hours (Figure 3-21).

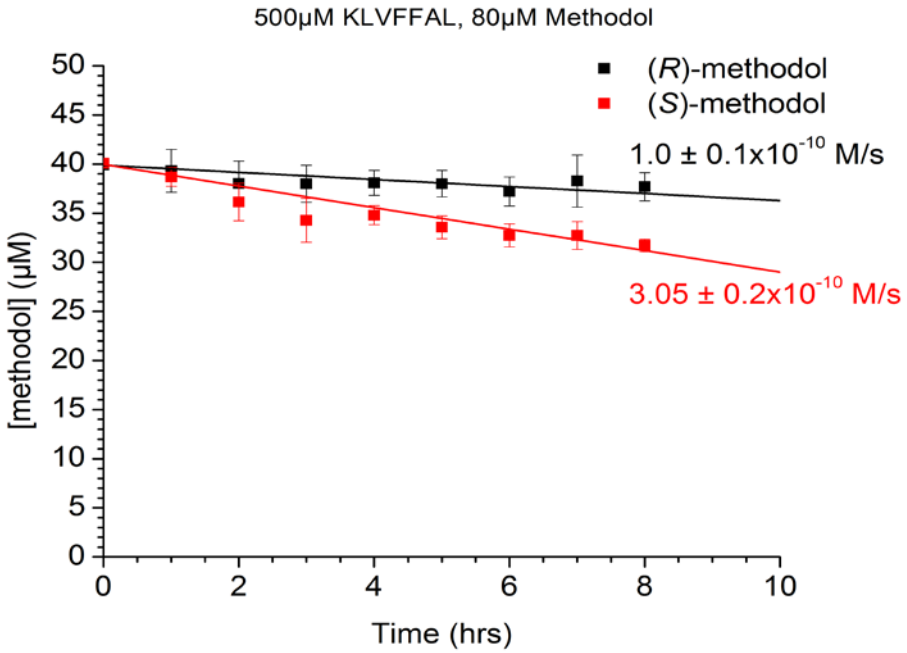

Figure 3-20: *Enantioselectivity of methodol consumption with 500 μM Ac-KLVFFAL-NH_2 catalyst over 8 hours and a starting (±)-methodol concentration of 80 μM methodol. All reactions were performed in 50 mM phosphate buffer at 25℃ with 300 mM NaCl at pH 7.5.*

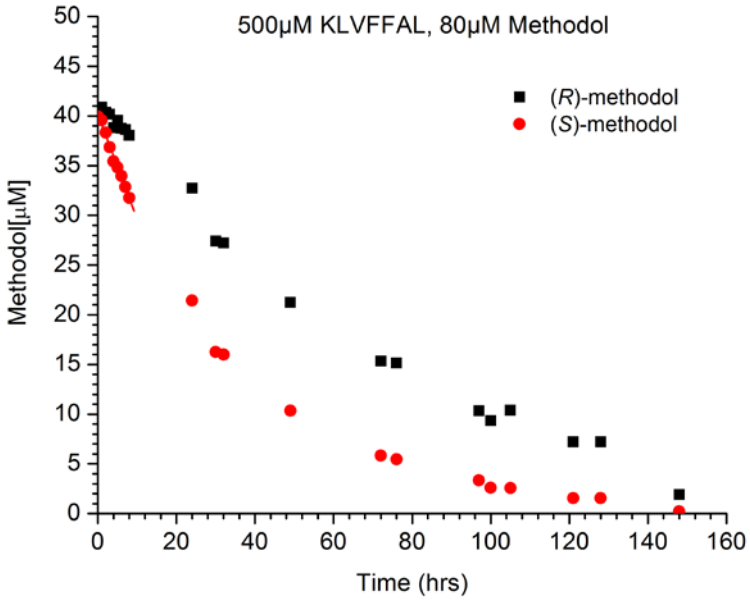

Figure 3-21: *Enantioselectivity of methodol consumption with 500 μM Ac-KLVFFAL-NH_2 catalyst and a starting (±)-methodol concentration of 80 μM methodol. All reactions were performed in 50 mM phosphate buffer at 25℃ with 300 mM NaCl at pH 7.5 containing 5% DMSO.*

To explore the possibility of further controlling this enantioselectivity, homochiral D-Ac-KLVFFAL-NH_2 prepared from all D-amino acids and heterochiral Ac-^{D}KLVFFAL-NH_2 containing only D-Lys were assembled. The D-Ac-KLVFFAL-NH_2 assembles into homogeneous peptide nanotubes (Figure 3-22C) with the similar diameter, 45.0 ± 3.2 nm, as L-Ac-KLVFFAL-NH_2. The CD approximates a mirror image of the all L-Ac-KLVFFAL-NH_2 with a positive band at ~ 225 nm and a negative transition at ~ 198 nm (Figure 3-22A). Heterochiral Ac-^{D}KLVFFAL-NH_2 assembles into homogenous nanotubes (Figure 3-22D) morphologically similar to the all L and all D assemblies with average widths of 46.6 ± 6.2 nm. The CD spectrum (Figure 3-22B) and FT-IR vibrations at 1623 cm^{-1} and 1694 cm^{-1} and X-ray diffraction, are most similar to the all L-Ac-KLVFFAL-NH_2.

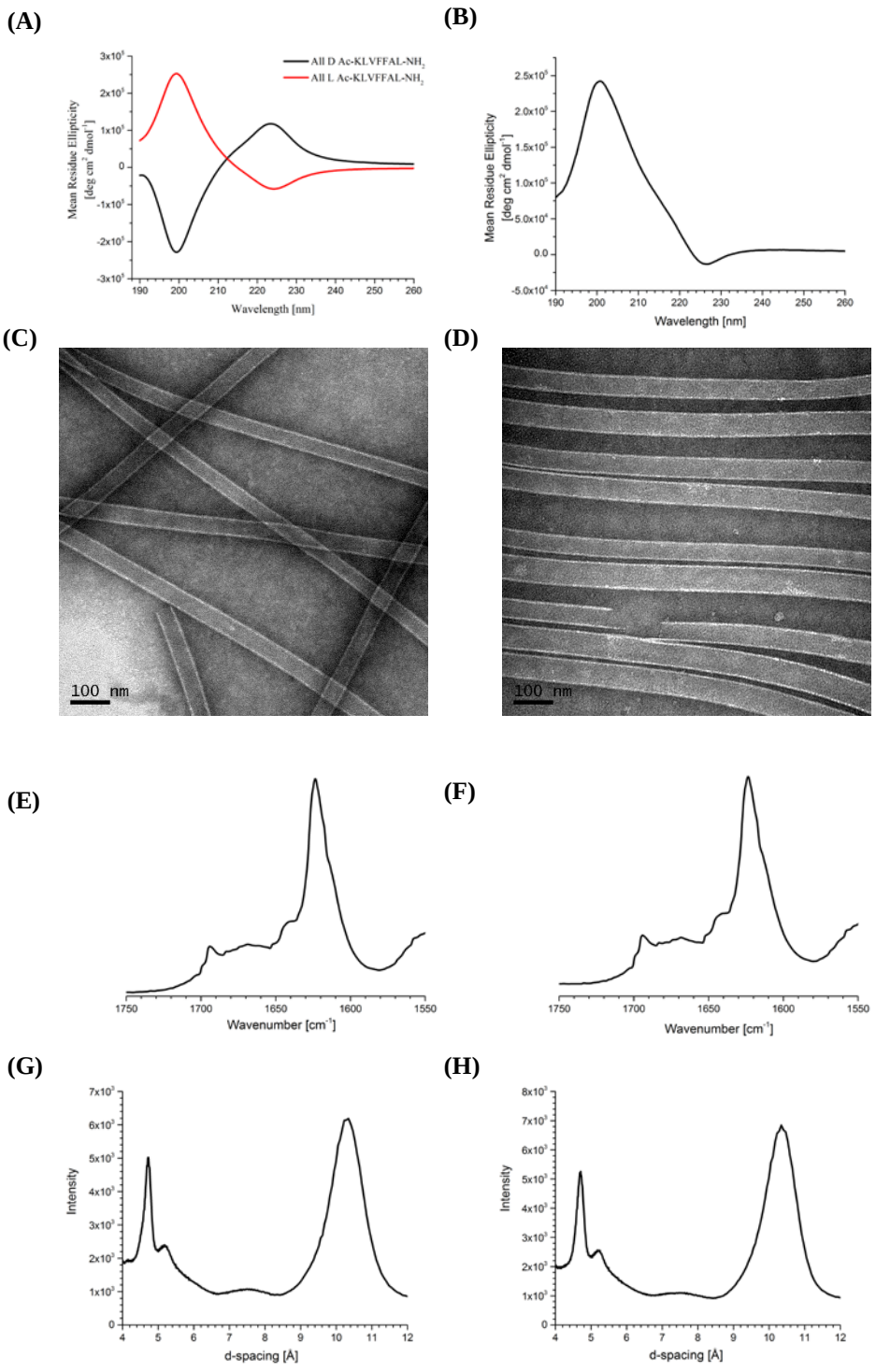

Figure 3-22: *Characterizations of nanotubes assembled by homochiral and heterochiral Ac-KLVFFAL-NH_2. (A) CD spectrum of mature all D Ac-KLVFFAL-NH_2 nanotubes (black) shows a positive transition at 225 nm and a negative one at 200 nm, resembling the mirror image of the all L Ac-KLVFFAL-NH_2 nanotube CD spectrum (red); (B) CD spectrum of mature heterochiral Ac-^{D}KLVFFAL-NH_2 nanotubes*

shows a negative band at 225 nm and a positive band at 200 nm, resembling the CD spectrum of the all L Ac-KLVFFAL-NH_2 nanotube. Uranyl acetate stained TEM images of the (C) homochiral all D Ac-KLVFFAL-NH_2 and (D) heterochiral Ac-^{D}KLVFFAL-NH_2. IR of the (E) homochiral all D Ac-KLVFFAL-NH_2 and (F) heterochiral Ac-^{D}KLVFFAL-NH_2 peptide assemblies show that both peptide assemblies have the same antiparallel β-strand orientation. X-ray diffraction of both peptide assemblies shows the same H-bonding distance of 4.7Å and laminate distance of 10.3Å (G) homochiral all D Ac-KLVFFAL-NH_2 and (H) heterochiral Ac-^{D}KLVFFAL-NH_2 peptide.

Attempts to control the chirality of the binding groove involved substituting C-terminus leucine with D-Leu to give Ac-KLVFFA^{D}L-NH_2. TEM revealed that this peptide assembles as sheets and ribbons, not nanotubes with characteristic β-sheet CD elipticity minimum at ~220 nm and maxima at ~ 190 nm, but these assemblies are not soluble, and are excluded from further study.

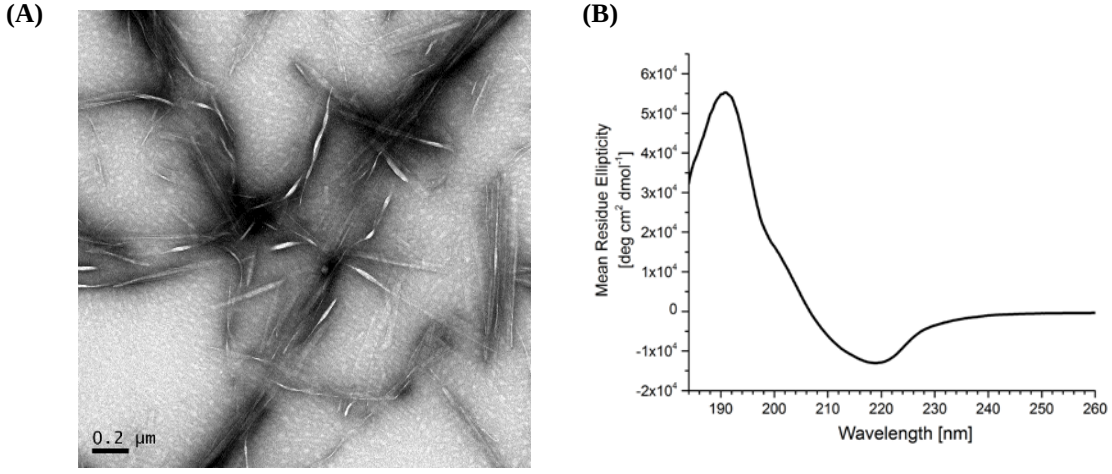

Figure 3-23: *Uranyl acetate stained TEM image of the heterochiral Ac-KLVFFA^{D}L-NH_2 (B) CD spectrum of mature heterochiral Ac-KLVFFA^{D}L-NH_2 nanotubes showed a negative ellipticity at 220 nm and a positive ellipticity at ~190 nm.*

Homochiral (D) and (L) Ac-KLVFFAL-NH_2 peptide nanotubes consume (±) methodol at comparable rates with opposite enantiomeric preferences. However, the

heterochiral Ac-^{D}KLVFFAL-NH_2 peptide assemblies show no enantioselectivity. (Figure 3-24).

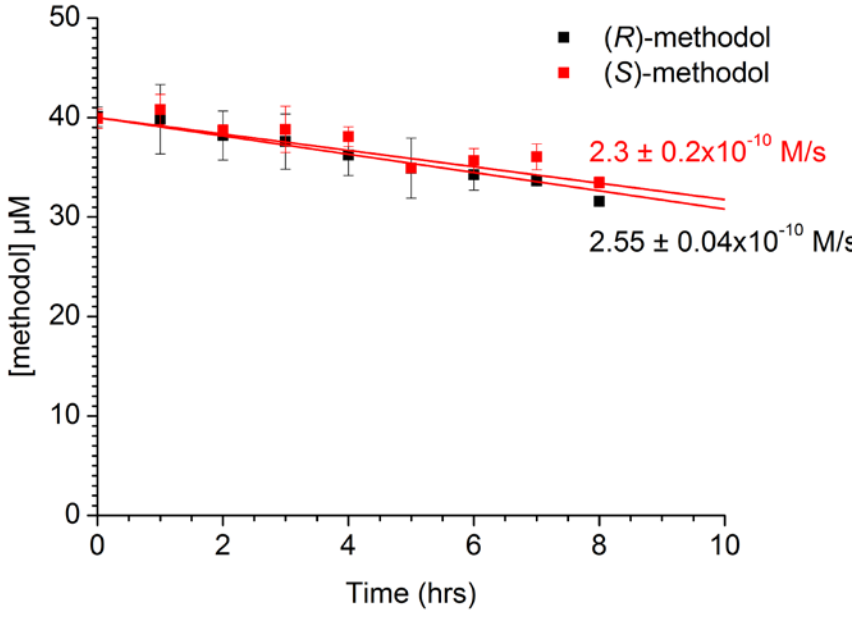

Figure 3-24: *Enantioselectivity of methodol consumption with 500 µM Ac-^{D}KLVFFAL-NH_2 catalyst and a starting (±)-methodol concentration of 80 µM methodol.*

Turnover Frequency

The "turnover frequency (TOF)" is defined as the number of substrate units that a single molecule of catalyst can convert into product per unit of time which directly evaluates the impact of product inhibition on the catalytic system. To determine if the nanotubes binding sites are capable of turnover, the TOF was determined with 10 µM and 50 µM Ac-KLVFFAL-NH_2 nanotubes and 400 µM methodol and the reaction was monitored over time. At a concentration of 10 µM Ac-KLVFFAL-NH_2 nanotubes, almost 20 turnovers are observed over 2000 minutes whereas the higher Ac-KLVFFAL-NH_2 concentrations (50 µM) are more impacted by product inhibition (Figure 3-25).

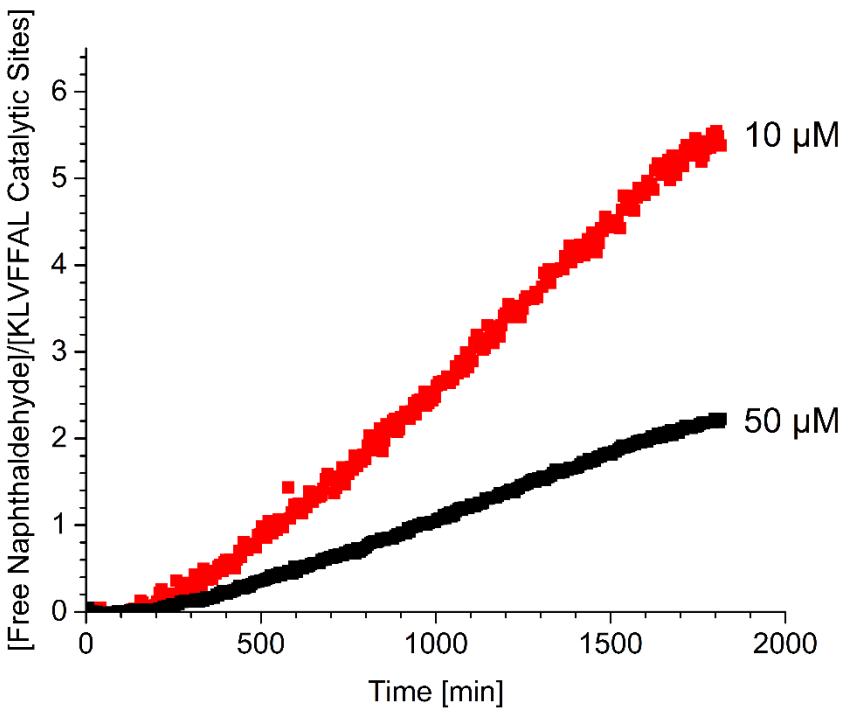

Figure 3-25: *Reaction progress curves over multiple turnovers for Ac-KLVFFAL-NH_2. Methodol substrate (400 μM) was mixed with 10 μM (red) and 50 μM (black) Ac-KLVFFAL-NH_2 peptide assembled as peptide nanotubes. The ratio of free naphthaldehyde to Ac-KLVFFAL-NH_2 catalytic sites (6 peptides/site) was plotted as a function of time. Almost 20 turnovers are observed for 10 μM Ac-KLVFFAL-NH_2 catalyst over 2000 minutes, and higher Ac-KLVFFAL-NH_2 concentrations (50 μM) are more impacted by product inhibition.*

Kinetic Analysis of the Retro-aldol Catalysis.

A minimal Michaelis-Menten kinetic model used for enzyme kinetics [44, 45] was initially explored. This model, requires the substrate concentration to be significantly higher than the catalyst concentration but substrate solubility limited this requirement and necessitated the development of other kinetic models. As shown in Figure 3-26, the model separates out the binding and kinetic steps, but does not attempt to resolve the

expected steps in catalytic conversion. Expression for each enantiomer and the rate of product (P1) release are broken out as separate steps.

$$E+S \underset{k_{forS}*K_{dS}}{\overset{k_{forS}}{\rightleftharpoons}} ES \xrightarrow{k_{catS}} E+P_1+P_2 \quad (1)$$

$$E+R \underset{k_{forR}*K_{dR}}{\overset{k_{forR}}{\rightleftharpoons}} ER \xrightarrow{k_{catR}} E+P_1+P_2 \quad (2)$$

$$EP_1 \underset{k_a}{\overset{k_aK_d}{\rightleftharpoons}} E+P_1 \quad (3)$$

Figure 3-26: *The minimal kinetic scheme developed to resolve the contribution of the peptide assemblies to retro-aldol catalysis where E is binding site, S is S-methodol, ES is the bound complex, P_1 is 6-methoxy-2-naphthaldehyde, P_2 is acetone, R is R-methodol, ER is the bound complex, and EP_1 is the enzyme-6-methoxy-2-naphthaldehyde complex. K_d is the dissociation constant for 6-methoxy-2-naphthaldehyde (Product) from the nanotube surface.*

To test our model in predicting the enzyme activity of Ac-KLVFFAL-NH_2 nanotubes, a range of substrate (methodol) and peptide concentrations that kept the substrate soluble and the peptide assemblies stable are selected. R- and S-methodol consumption is determined by chiral HPLC and the production 6-methoxy-2-naphthaldehye is determined by fluorescence for racemic, R-enriched and S-enriched methodol. The R-enriched and S-enriched methodol means that each enantiomer contained a small percentage of the other enantiomer. Also, the methodol solution contained <5% of the product, 6-amino-2-naphthaldehye, making all the fluorescence data start with non-zero values at 0 time. Results of the substrate consumption and product formation were used to evaluate the parameters in equation (1) to (3) by

minimizing the sum of square error (SSE) between the calculated and experimental values (Figure 3-26) normalized for the number of data points and the scale of the measurements[46]. Latin Hypercube sampling[47] was used to determine suitable initial guesses for the kinetic parameters and the optimization procedure was carried out with the fmincon function in MATLAB 2012a (Mathwork, Inc). The confidence intervals of best fit parameters were estimated based on the singular value decomposition[48] for their covariance matrices[46].

Numbers of peptides per binding sites (n) composed of 1-14 peptides to determine [E] for Ac-KLVFFAL-NH_2 nanotubes were tested to fit the experimental data using the above mechanism. The sum of squared error (SSE), a measure of discrepancy between the experimental data and the estimation model, was determined for each fit using the equation:

$$SSE = \Sigma(\hat{y} - y)^2 \qquad (4)$$

A small SSE indicate a tight fit of the prediction to the experimental data. Therefore, our mechanistic model suggests the number of peptides per binding sites (n) is equal to 6 because the normalized SSE for the Ac-KLVFFAL-NH_2 have the lowest value at 6 while n=14 has the highest value (Figure 3-27). I propose that the number defines the length along the cross-β groove, as defined by Congo red [49], with a length of 4.5 peptides x 4.7Å apart = 21Å which reflects the sum of the total accessible poses that impact catalysis. The number of peptides per binding site from the model (n=6) encompasses a larger area than the determined value (n=4) from saturation binding with 1-(6-methoxy-2-

naphthalenyl)-1,3-butanedione of 4 peptides/enaminone suggesting that only a subset of the binding modes are catalytically competent.

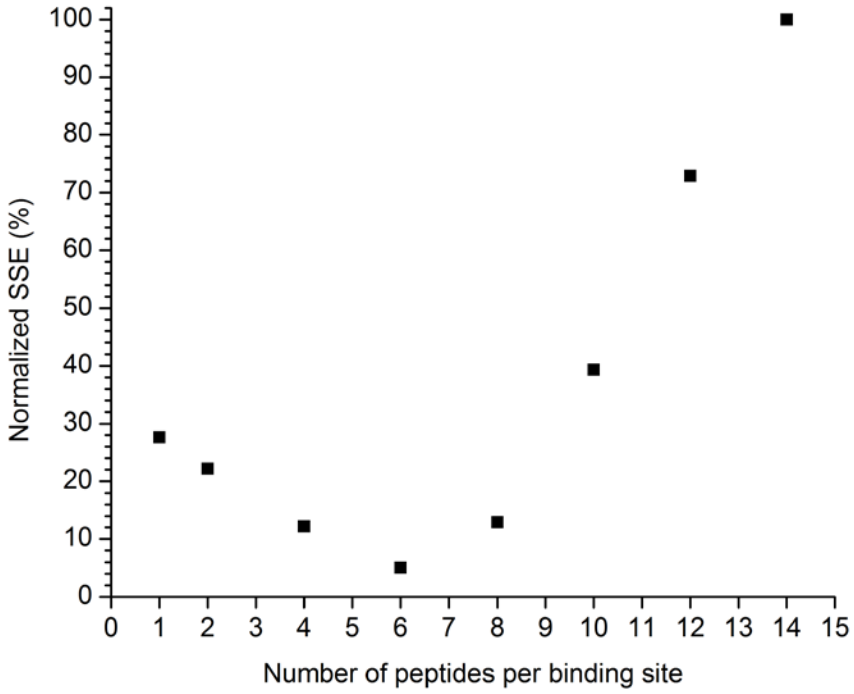

Figure 3-27: *Normalized sum of square error (SSE) for R- and S-methodol consumption on Ac-KLVFFAL-NH_2*

As shown in Figure 3-28, the binding constant (K_d) was determined by titrating a solution of 5.8 μM 6-methoxy-2-naphthaldehyde with 5-500 μM peptide nanotubes given that the product, 6-methoxy-2-naphthaldehyde, also forms a Schiff base complex with lysine, resulting in loss of fluorescence [11]. Using the number of peptide per binding site of n=6, a K_d of 5.91μM was determined for Ac-KLVFFAL-NH_2.

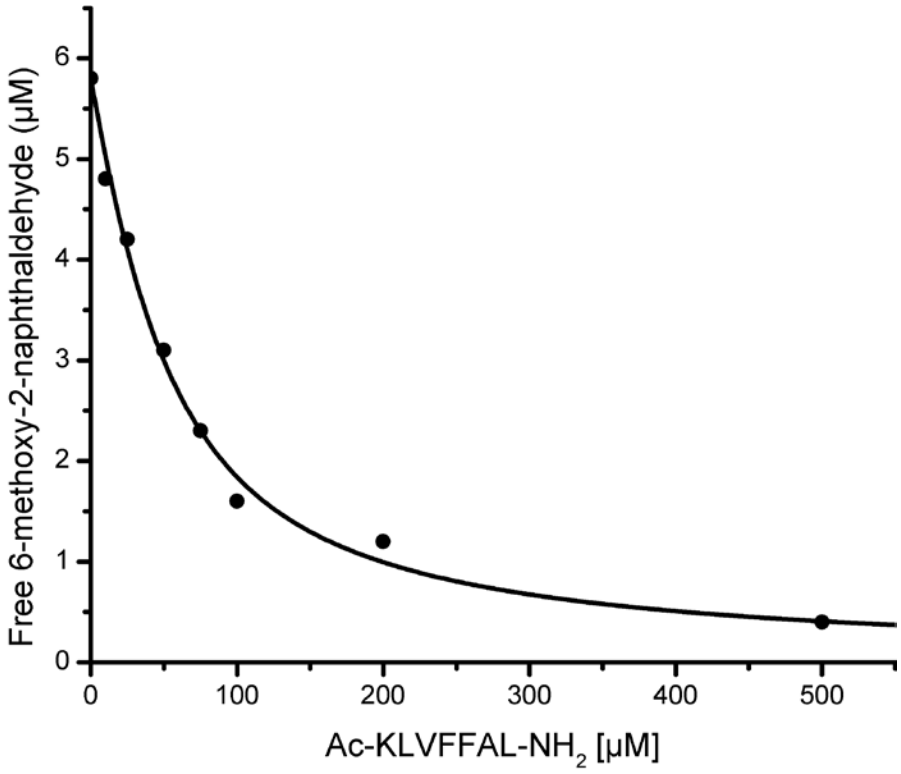

Figure 3-28: *Measurement of free 6-methoxy-2-naphthaldehyde (MNA) as a function of peptide assembly (peptide concentration) by titrating 5.8 μM 6-methoxy-2-naphthaldehyde with peptide assemblies over 5-500 μM peptide concentration. The fluorescence data was fit to* $MNA_{free} = 1/2*([MNA]_{Tot}-K_d-[Peptide]+sqrt(4*[MNA]_{Tot}*K+(-[MNA]_{Tot}+K+[Peptide])^2))$ *using 6 peptides per napthaldehyde binding site to yield a* K_d *of 5.91μM for Ac-KLVFFAL-*NH_2

The mechanistic model based on equations 1-3 fits the substrate consumption for Ac-KLVFFAL-NH_2 (Figure 3-29A) nanotubes reasonably well, together with the product accumulation (Figure 3-29B), over the first 8 hours given 500 μM peptides and 80 μM substrates. As shown in Figure 3-29C, D with doubled substrate concentration (160 μM), the joint model fits follow the decrease of R- and S- methodol concentrations for up to 128 hours. These long-term joint fits are consistent with the tubes remaining stable for the entire time of measurement, maintaining a constant number of catalytic sites, and following the same mechanism (equations 1-3) through the course of the reaction.

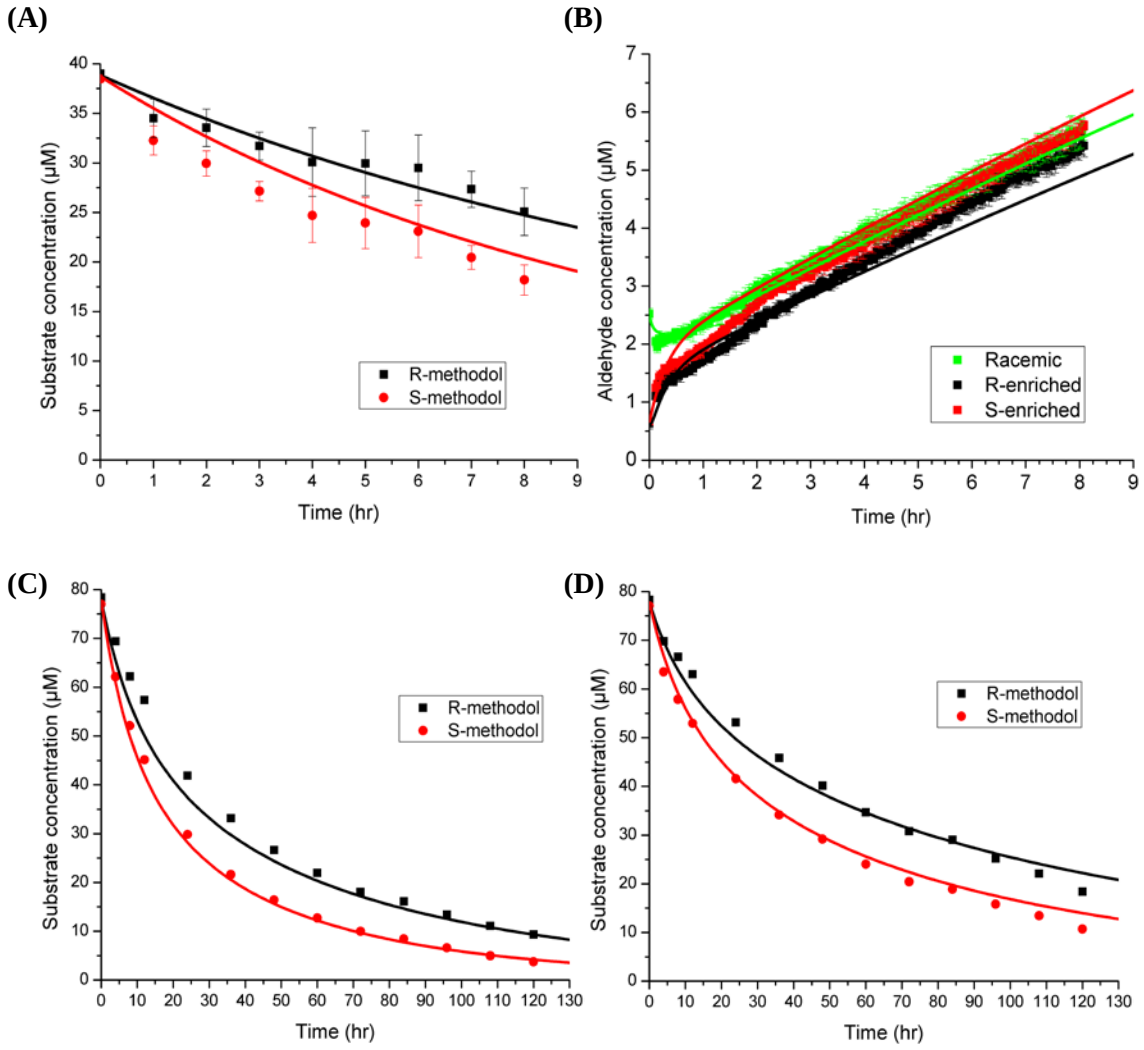

Figure 3-29: Best fits of Ac-KLVFFAL-NH₂ retro-aldol catalysis with 6 peptides per binding site. *(**A**) Chrial HPLC of 500 μM peptide and 76.7 μM (±)-methodol. (**B**) Naphthaldehyde fluorescence of 500 μM peptides with 76.7 μM (±)-methodol (green), 79.2 μM R-enriched methodol (black) and 79.1 μM S-enriched methodol (red). (**C**) Chrial HPLC of 500 μM peptide and 155.3 μM (±)-methodol. (**D**) Chrial HPLC of 300 μM peptide and 155.4 μM (±)-methodol. Solid lines are best fits using equations 1 to 3. **(A)** Initial concentrations are: [E] = 83.3 μM, [S] = 38.3 μM, [R] = 38.5 μM, [P_1] = 3.1 μM. **(B)** The initial concentrations of the racemic solution are: [E] = 83.3 μM, [S] = 38.3 μM, [R] = 38.5 μM, [P_1] = 3.1 μM. The initial concentrations of the R-enriched substrate are: [E] = 83.3 μM, [S] = 11.9 μM, [R] = 67.3 μM, [P_1] = 0.77 μM. The initial concentrations of the S-enriched substrate are: [E] = 83.3 μM, [S] = 67.2 μM, [R] = 11.9 μM, [P_1] = 0.95 μM. **(C)** The initial concentrations are: [E] = 83.3 μM, [S] = 77.0 μM, [R] = 78.4 μM, [P_1] = 4.6 μM. **(D)** The initial concentrations are: [E] = 50 μM, [S] = 77.0 μM, [R] = 78.4 μM, [P_1] = 4.6 μM.*

As shown in Figure 3-30, simulation of the enzyme-substrate complex concentrations (*ER* and *ES)* without the chemical step ($k_{catR} = k_{catS} = 0$) suggests that the substrate-binding to the nanotubes reaches equilibrium within 30 minutes. When included in the simulation, the chemical step takes longer to finish (Figure 3-31), indicating that the chemical step is rate-limiting. Due to limited substrate solubility, [*ER*] and [*ES*] do not remain constant, and our model does not allow Michaelis-Menten's k_{cat}/K_M calculations by equation (5) below. In addition to limitations of substrate solubility, product binding also makes the kinetics deviate from Michaelis-Menten kinetics early in the initial rates. Thus, equation (5) cannot be directly applied and k_{cat}/K_M calculated from this mechanism will not accurately reflect catalyst efficiency.

$$\frac{dP}{dt} = \frac{k_{cat}[\mathrm{E}]_{tot}[\mathrm{S}]}{K_m + [\mathrm{S}]} \qquad (5)$$

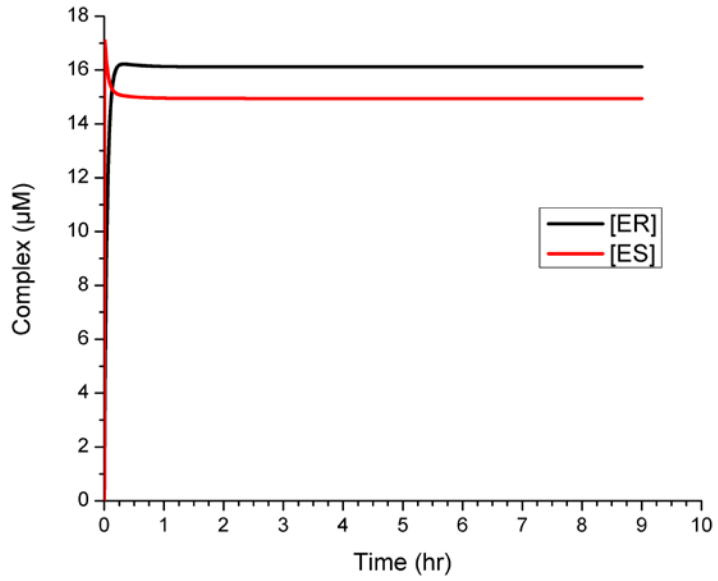

Figure 3-30: *Simulation of complex formation with 6 peptides per binding site of S- and R-substrates "without" the carbon-carbon bond formation step (k_{catR} and k_{catS}) on the Ac-KLVFFAL-NH_2 nanotubes. The initial concentrations are: [E] = 83.3 μM, [S] = 38.3 μM, [R] = 38.5 μM, [P_1] = 3.1 μM.*

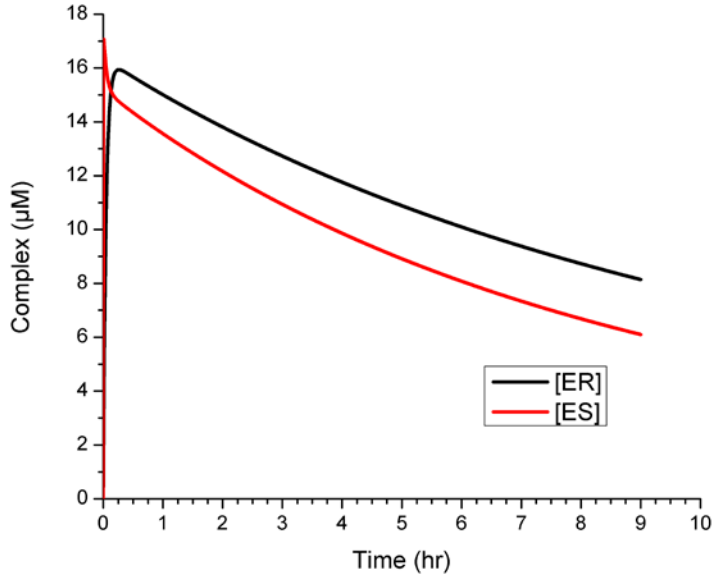

Figure 3-31: *Simulation of complex formation with 6 peptides per binding site of S- and R-substrates "with" the carbon-carbon bond formation step (k_{catR} and k_{catS}) on the Ac-KLVFFAL-NH_2 nanotubes. The initial concentrations are: [E] = 83.3 μM, [S] = 38.3 μM, [R] = 38.5 μM, [P_1] = 3.1 μM.*

According to Table 3-1, the substrate dissociation constants, K_{dR} and K_{dS}, suggest that Ac-KLVFFAL-NH_2 nanotubes show higher binding affinity for R-methodol. This is consistent with carbon-carbon bond cleavage determining S-methodol enantioselectivity even when the tubes prefer R-methodol upon binding.

k_{forR}	3.98(5.60) $\times 10^{-5}$ $sec^{-1}\mu M^{-1}$
k_{forS}	9.18(45.0) $\times 10^{-4}$ $sec^{-1}\mu M^{-1}$
k_{catR}	4.08(1.26) $\times 10^{-5}$ sec^{-1}
k_{catS}	6.20(2.39) $\times 10^{-5}$ sec^{-1}
k_a	1.60(0.07) $\times 10^{-5}$ $sec^{-1}\mu M^{-1}$
K_{dR}	7.02(3.05) $\times 10^{1}$ sec^{-1}
K_{dS}	7.96(4.33) $\times 10^{1}$ sec^{-1}
K_d	5.91 μM

Table 3-1: *Dissociation constants of R- and S-methodol with Ac-KLVFFAL-NH_2 nanotubes.*

Parameter estimation for equations 1 to 3 were carried out by setting either equal chemical step constants ($k_{catR} = k_{catS}$) or equal substrate dissociation constants ($K_{dR} = K_{dS}$) for Ac-KLVFFAL-NH_2 nanotubes (Table 3-2). The goodness of these limiting models is compared to the non-restricted model by Akaike information criterion (AIC) [50, 51] and the Akaike weight [52]. AIC provides a means for model selection by estimating the quality of each model relative to each of the other models. It measures the consistency of the models by rewarding the model with the lower SSE or the smaller number of parameters, and is calculated by:

$$\mathrm{AIC} = N_d \ln\left(\frac{SSE}{N_d}\right) + 2N_p \qquad (6)$$

where N_d is the number of data points, N_p is the number of parameters, and SSE is the sum of squares error. The Akaike weights are the weight of evidence in favor of a model being the actual best model for a particular situation. It can be interpreted as the estimated probability that model *i* is the best model for the data at hand, given the set of models considered and calculated by:

$$\text{Akaike weight} = \frac{\exp\left(-\frac{1}{2}\Delta_i(\mathrm{AIC})\right)}{\sum_{j=1}^{N_M}\exp\left(-\frac{1}{2}\Delta_j(\mathrm{AIC})\right)} \qquad (7)$$

where N_M is the total number of models for comparison and $\Delta_i(\mathrm{AIC})$ is the difference between the AIC of model *i* and the minimal AIC from the model set. The Akaike weights for all models combined should add up to 1.

As shown in Tables 3-2, the non-restricted model has the lowest AIC value and the greatest Akaike weight (92.83%), which means the model is more consistent with unequal dissociation constants and chemical steps for R- and S- methodol. However, the restriction on the chemical step constants ($k_{catR} = k_{catS}$) has the greatest SSE and the lowest Akaike weight suggesting a 0% probability of this model matching the experimental data. In addition, the $k_{catR} = k_{catS}$ model has a stronger impact on the enantioselective consumption for Ac-KLVFFAL-NH_2 nanotubes, consistent with the nanotubes' stronger binding affinity toward R-methodol but stronger chemical activity toward S-methodol when the tubes prefer to break S-methodol selectively.

Restriction	N_d	**SSE**	N_p	**AIC**	**Akaike weight(%)**
No restriction	793	7.94×10^1	7	-1810.80	92.83
$k_{catR} = k_{catS}$	793	2.00×10^2	6	-1079.94	0.00
$K_{dR} = K_{dS}$	793	8.01×10^1	6	-1805.68	7.17

Table 3-2: AIC analysis of best fits for equations 1 to 3. *Listed are fits to the concentrations from HPLC and fluorescence in Figure 3-28 with and without restrictions, where N_d is the number of data points, and N_p is the number of parameters.*

Conclusion

In this chapter, the retro-aldol cleavage of methodol is used as a reaction to explore the catalytic competence of the cross-β assemblies. We take advantage of subtle changes in peptide sequence and assembly conditions to explore catalyst efficiency. Peptides containing a single amino acid substitution in the surface grooves allowed great control of the binding site so also nanotubes that lack hydrophobic amino acids in the surface grooves. Peptide assemblies are dynamic systems in which a given fraction of free peptides could remain in solution in equilibrium with the assembled phase. The fact that the fibers and nanotubes lacking hydrophobic amino acids in the surface grooves are not catalytic support a model in which reaction occurs in the grooves and not just from free peptides in solution.

With a high density of catalytic sites on the nanotubes surface and a chiral microenvironment for substrate binding, the enantioselective retro-aldol cleavage of methodol was catalyzed by Ac-KLVFFAL-NH_2 with a preference for S-Methodol. To study how chirality will govern the performance of peptide assemblies as catalyst, homochiral and heterochiral peptide assembly was also synthesized and characterized. While the all D peptide sequences assemble into morphologically identical nanotubes as the all L amino acids peptide sequences, the self-assembling behavior of heterochiral peptide sequences was found to depend on the location of the substituted amino acids within the sequence as well as the peptide sequence itself. Catalytic studies show the same rate of catalysis are observed with the nanotubes irrespective of chirality but different enatioselectivity are observed. While all L Ac-KLVFFAL-NH_2 and all D Ac-KLVFFAL-NH_2 show opposite enantioselctivity for (±)-methodol, total loss of

enantioselctivity was observed with the heterochiral peptide nanotubes demonstrating the chirality of the constituent amino acids in the peptide nanotubes play an important role in the enantioselectivity of the retrol-aldol reaction.

A kinetic model was developed to better define the catalytic mechanism. Based on the model, the number of peptides per binding site in the nanotubes was estimated as n=6 which encompasses a larger area than the determined value (n=4) from saturation binding with 1-(6-methoxy-2-naphthalenyl)-1,3-butanedione of 4 peptides/enaminone suggesting that only a subset of the binding modes are catalytically competent. The kinetic simulation suggests that the chemical step is rate limiting and the C-C bond cleavage step determines the enantioselectivity. Even though the Ac-KLVFFAL nanotubes show substrate turnover, the next question is are there ways to improve the catalytic rates of the nanotubes?

Materials and Methods

Synthesis of Methodol.

Racemic 4-hydroxy-4-(6-methoxy-2-naphthyl)-2-butanone was prepared following published procedures [10, 36] via condensation of acetone with 6-methoxy-2-napthaldehyde (Sigma-Aldrich). Acetone (196 μl, 2.50eq) in THF was added drop wise to a freshly prepared solution of LDA maintained at −78°C. After stirring at this temperature for 30 min, 6-methoxy-2-naphthaldehyde (100 mg, 1.07 mmol) in 5 ml THF was added drop wise over a period of 1 minute. The mixture was stirred for 30 minutes at −78°C, and then quenched with saturated NH_4Cl, allowed to warm to room temperature, extracted with ethyl acetate, and the organic layer dried with $MgSO_4$. The solution was

decanted, taken to dryness *in vacuo*, and the crude product flash purified (SiO_2, ethyl acetate/hexane) to give an off-white solid with yields and spectral data consistent with those previously reported.

(R)-Methodol: Acetone (100 ml) was changed with 6-methoxy-2-naphthaldehyde (887 mg, 4.76 mmol) and L-proline (248 mg, 0.40eq) and stirred at room temperature for 5 hours or until complete by TCL. The mixture was dried down in vacuo, re-suspended in 40 ml vinyl acetate and treated with *P.cepacia* (1.32 g, 245 mg/mmol substrate), a spoon of 4Å molecular sieve was added. Reaction proceeded at room temperature under N_2 protection overnight. The reaction crude was filtered and applied to flash column (EA: hexane=1:2) to give white product 674 mg (92% yield). ^{1}H NMR (600 MHz, CDCl3): δ7.75 (m, 1H); δ7.73 (q, 2H); δ7.43 (dd, 1H); δ7.16 (dd, 1H); δ7.13 (d, 1H); δ5.30 (m, 1H), δ3.92 (s, 3H), δ3.34 (s, 1H), δ2.95 (m, 2H), δ2.21 (s, 3H).

(S)-Methodol: 6-methoxy-2-naphthaldehyde (500 mg, 2.68 mmol) and D-proline (124 mg, 0.40eq) were suspended in 60 ml acetone at room temperature and TLC indicated completion after three hours. Remove solid by filtration, filtrate was dried down under vacuum and applied to flash column directly (EA: Hexane=1:2) to give white solid 355 mg (86% yield). ^{1}H NMR (600 MHz, CDCl3): δ7.74 (m, 1H); δ7.73 (m, 2H); δ7.43 (dd, 1H); δ7.16 (dd, 1H); δ7.13 (d, 1H); δ5.29 (m, 1H), δ3.92 (s, 3H), δ3.36 (s, 1H), δ2.95 (m, 2H), δ2.21 (s, 3H).

Synthesis of 1-(6-methoxy-2-naphthalenyl)-1,3-butanedione

244 mg of 4-hydroxy-4-(6-methoxy-2-naphthyl)-2-butanone was dissolved in 10

mls chloroform and the solution was incubated with 1.5 equivalents of Dess-Martin periodinane in chloroform at room temperature overnight. The oxidized product was purified by silica gel chromatography in hexanes/ethyl acetate. The product was verified by MS (positive ion m/z = 243.1) and 1H NMR (400 MHz, CDCl3: δ = 2.25 (s, 3H); δ = 3.83 (s, 3H); δ = 6.30 (s, 2H); δ = 7.34 (m, 2H); δ = 7.81(m, 3H); δ = 8.39 (s, 1H).

Computational Modeling

Methodol docking was performed manually with energy minimization (Macromodel - (Schrodinger, Inc. Portland, OR) [53]) to remove van der Waals clashes. To define lysine accessibility across the tube surface, a 1 ns molecular dynamics (MD) run (Desmond) [54] at 300K with SPC explicit water model [55] and the OPLS2005 all atom force field [56] was completed starting with 8 H-bonded peptides × 5 laminates of KLVFFAL peptides solvated in SPC water. Initial structures were allowed to relax for 100ps before the production run. Boundary conditions were set to create infinite H-bonded β-sheets and infinite β-sheet stacking.

Models of naphthaldehyde bound to Ac-KLVFFAL-NH_2.

6-methoxy-2-napthaldehyde was placed on the tube surface and energy minimized with Macromodel and using a constant dielectric of 4 with the OPLS all-atom force field. To minimize edge-effects from the energy minimization, the system was then solvated in a box of SPC water with the box size set to ensure periodic boundary conditions to simulate infinite H-bonded β-sheets and laminated β-sheets. The system was energy minimized first with the solute restrained, followed by energy minimization without restraints. The system was relaxed with a molecular dynamics simulation in the

NVT ensemble using a Berendsen thermostat for 12ps at 10K with a fast temperature relaxation constant and velocity resampling every 1ps with non-hydrogen solute atoms restrained. Followed by MD in the NPT ensemble using a Berendsen thermostat and a Berendsen barostat for 12ps at 10K and a pressure of 1 atm with a fast temperature relaxation constant, a slow pressure relaxation constant, velocity resampling every 1ps and non-hydrogen solute atoms restrained. MD for 24ps at 300K and 1 atm in the NPT ensemble using a Berendsen thermostat and a Berendsen barostat with a fast temperature relaxation constant, a slow pressure relaxation constant, velocity resampling every 1ps and non-hydrogen solute atoms restrained. Finally MD simulations for 24ps at 300K and 1 atm in the NPT ensemble using a Berendsen thermostat and a Berendsen barostat with a fast temperature relaxation constant and a normal pressure relaxation constant and no atom restraints.

Reaction of Ac-KLVFFAL-NH_2 nanotube assemblies with 2,4-pentanedione (Acetyl acetone).

Ac-KLVFFAL-NH_2 (500 µM) was assembled completely into nanotubes and allowed to react with 250 to 5000 µM acetyl acetone in 5% DMSO, 50 mM Phosphate Buffer, 300 mM NaCl, pH 7.5 for 48 hours. Changes in absorbance were observed in 96 well plates on a Synergy HT Multidetection microplate reader to convert enaminone (λ_{max} =316 nm, ε = extinction coefficient of 15,000 $M^{-1}cm^{-1}$) product to titrate available amine concentration.

Reaction of Ac-KLVFFAL-NH_2 nanotube assemblies with* 1-(6-methoxy-2-naphthalenyl)-*1,3-butanedione.

Ac-KLVFFAL-NH_2 (300 μM) was assembled completely as nanotubes and allowed to react with 5 to 250 μM 1-(6-methoxy-2-naphthalenyl)-1,3-butanedione in 5% Acetonitrile, 25 mM HEPES Buffer, 150 mM NaCl, pH 7.5 for 18 hours. Changes in absorbance were observed in 96 well plates on a Synergy HT Multidetection microplate reader to convert enaminone (λ_{max} =350 nm, ε = extinction coefficient of 17,500 $M^{-1}cm^{-1}$) product to titrate available amine concentration.

Retro-Aldol Kinetic Analyses.

Prior to kinetic analysis, peptide assemblies were centrifuged at 13,800 g for 60 minutes and suspended in distilled water. Immediately before kinetic analysis, solution was buffered to pH 7.5 with 50 mM phosphate and brought to final concentrations of 300 mM NaCl and 5 % DMSO to enhance the solubility of methodol. Fluorescence measurements for retro-aldol kinetics were collected on a Synergy HT Multi-detection microplate reader. Triplicate samples consisted of 200 μL reaction volumes with excitation at 360 nm and fluorescence emission observed at 460 nm at a sensitivity level of 50. Time point measurements were collected every 45 s, and plates were shaken for 20 revolutions per sec at an intensity level of 3. Catalytic efficiencies were measured at a fixed peptide concentration, for example 500 μM at varying methodol concentrations to obtain initial rates.

Product enantiomeric excess was determined by chiral HPLC analysis using a Chiralpak AD-RH (Daicel) column. When eluted isocratically with 40% MeCN/Water at

a flow rate of 0.5 mL/min, the retention times of (R)- and (S)-methodol were 18.6 and 21.3 minutes, respectively. Detection was at 230 nm. (R)- and (S)-methodol chirality was assigned with aldolase antibody 38C2. A stock solution of aldolase antibody 38C2 (molecular weight ~ 150,000 g/mol) (Aldrich) was prepared by adding 2 mL of ASTM Type II water (Harleco) to 10 mg lyophilized powder and gently mixed by slowly pipetting the solution up and down until the antibody was dissolved. Antibody concentration of stock solution was determined by measuring the absorbance at 280 nm (ε_{280} =1.35 mL mg^{-1} cm^{-1}) of 100 μL of antibody solution to 700 μL of 50 mM phosphate buffered saline, pH = 7.4.

Antibody 38C2 has been shown to resolve racemic methodol to yield only the (R)-methodol with 97% ee [43]. 1.5 μM of antibody 38C2 was added to 50 μM methodol in 50 mM PBS buffer, 300 mM NaCl, pH 7.4. The reaction was injected at zero time on HPLC using a Chiralpak AD-RH (Daicel) column and run isocratically with 40% MeCN/Water at a flow rate of 0.5 mL/min to resolve two enantiomers with retention times 18.6 minutes and 21.3 minutes. The reaction was then allowed to incubate for 22 hours and resolved by HPLC. The un-consumed enantiomer eluted at t=18.6 minutes and this was assigned as [R]-methodol.

References

1. Hilbich, C., et al., *Substitutions of hydrophobic amino acids reduce the amyloidogenicity of Alzheimer's disease βA4 peptides.* Journal of Molecular Biology, 1992. **228**(2): p. 460-473.

2. Wood, S.J., et al., *Prolines and Aamyloidogenicity in Fragments of the Alzheimer's Peptide .beta./A4.* Biochemistry, 1995. **34**(3): p. 724-730.

3. Williams, A.D., et al., *Mapping abeta amyloid fibril secondary structure using scanning proline mutagenesis.* J Mol Biol, 2004. **335**(3): p. 833-42.

4. Williams, A.D., S. Shivaprasad, and R. Wetzel, *Alanine scanning mutagenesis of Abeta(1-40) amyloid fibril stability.* J Mol Biol, 2006. **357**(4): p. 1283-94.

5. Childers, W.S., et al., *Phase Networks of Cross-β Peptide Assemblies.* Langmuir, 2012. **28**(15): p. 6386-6395.

6. Ni, R., et al., *Remodeling Cross-β Nanotube Surfaces with Peptide/Lipid Chimeras.* Angewandte Chemie International Edition, 2012. **51**(27): p. 6635-6638.

7. Mehta, A.K., et al., *Facial Symmetry in Protein Self-Assembly.* Journal of the American Chemical Society, 2008. **130**(30): p. 9829-9835.

8. Childers, W.S., et al., *Peptides organized as bilayer membranes.* Angewandte Chemie International Edition, 2010. **49**(24): p. 4104-7.

9. Childers, W.S., et al., *Templating Molecular Arrays in Amyloid's Cross-β Grooves.* Journal of the American Chemical Society, 2009. **131**(29): p. 10165-72.

10. List, B., C.F. Barbas, and R.A. Lerner, *Aldol sensors for the rapid generation of tunable fluorescence by antibody catalysis.* Proceedings of the National Academy of Sciences of the United States of America, 1998. **95**(26): p. 15351-15355.

11. Lassila, J.K., D. Baker, and D. Herschlag, *Origins of catalysis by computationally designed retroaldolase enzymes.* Proc Natl Acad Sci U S A, 2010. **107**(11): p. 4937-42.

12. Jiang, L., et al., *De Novo Computational Design of Retro-Aldol Enzymes.* Science, 2008. **319**(5868): p. 1387-1391.

13. Heine, A., et al., *Observation of Covalent Intermediates in an Enzyme Mechanism at Atomic Resolution.* Science, 2001. **294**(5541): p. 369-374.

14. Allard, J., P. Grochulski, and J. Sygusch, *Covalent intermediate trapped in 2-keto-3-deoxy-6- phosphogluconate (KDPG) aldolase structure at 1.95-Å resolution.* Proceedings of the National Academy of Sciences of the United States of America, 2001. **98**(7): p. 3679-3684.

15. St-Jean, M. and J. Sygusch, *Stereospecific Proton Transfer by a Mobile Catalyst in Mammalian Fructose-1,6-bisphosphate Aldolase.* Journal of Biological Chemistry, 2007. **282**(42): p. 31028-31037.

16. Keinan, E., *Catalytic Antibodies.* 2006: Wiley.

17. Spector, L.B., *Covalent Catalysis by Enzymes.* 2011: Springer New York.

18. Wagner, J., R.A. Lerner, and C.F. Barbas, III, *Efficient Aldolase Catalytic Antibodies That Use the Enamine Mechanism of Natural Enzymes.* Science, 1995. **270**(5243): p. 1797-1800.

19. Björnestedt, R., et al., *Copying Nature's Mechanism for the Decarboxylation of β-Keto Acids into Catalytic Antibodies by Reactive Immunization.* Journal of the American Chemical Society, 1996. **118**(47): p. 11720-11724.

20. Barbas, C.F., III, et al., *Immune Versus Natural Selection: Antibody Aldolases with Enzymic Rates But Broader Scope.* Science, 1997. **278**(5346): p. 2085-2092.

21. Giger, L., et al., *Evolution of a designed retro-aldolase leads to complete active site remodeling.* Nat Chem Biol, 2013. **9**(8): p. 494-8.

22. Bjelic, S., et al., *Exploration of Alternate Catalytic Mechanisms and Optimization Strategies for Retroaldolase Design.* Journal of Molecular Biology, 2014. **426**(1): p. 256-271.

23. Jiang, L., et al., *De novo computational design of retro-aldol enzymes.* Science, 2008. **319**(5868): p. 1387-91.

24. Schmidt, J., et al., *The effect of the hydrophobic environment on the retro-aldol reaction: comparison to a computationally-designed enzyme.* Organic & Biomolecular Chemistry, 2013. **11**(48): p. 8419-8425.

25. Muller, M.M., et al., *A rationally designed aldolase foldamer.* Angew Chem Int Ed Engl, 2009. **48**(5): p. 922-5.

26. Tanaka, F., R. Fuller, and C.F. Barbas, 3rd, *Development of small designer aldolase enzymes: catalytic activity, folding, and substrate specificity.* Biochemistry, 2005. **44**(20): p. 7583-92.

27. Bjelic, S., et al., *Computational design of enone-binding proteins with catalytic activity for the Morita-Baylis-Hillman reaction.* ACS Chem Biol, 2013. **8**(4): p. 749-57.

28. Althoff, E.A., et al., *Robust design and optimization of retroaldol enzymes.* Protein Science, 2012. **21**(5): p. 717-726.

29. Hilvert, D., *Critical analysis of antibody catalysis.* Annu Rev Biochem, 2000. **69**: p. 751-93.

30. Brocklehurst, K., M. Resmini, and C.M. Topham, *Kinetic and titration methods for determination of active site contents of enzyme and catalytic antibody preparations.* Methods, 2001. **24**(2): p. 153-67.

31. Resmini, M., et al., *A general kinetic approach to investigation of active-site availability in macromolecular catalysts.* Biochemical Journal, 2000. **346**(Pt 1): p. 117-125.

32. Topham, C.M., et al., *The Kinetic Basis of a General Method for the Investigation of Active Site Content of Enzymes and Catalytic Antibodies: First-Order Behaviour under Single-turnover and Cycling Conditions.* Journal of Theoretical Biology, 2000. **204**(2): p. 239-256.

33. Ray, W.J. and D.E. Koshland, *An All-or-None Assay for Assessing the Role of Amino Acid Residues in Enzyme Action--Application to Phosphoglucomutase.* Journal of the American Chemical Society, 1963. **85**(13): p. 1977-1983.

34. Ray, W.J. and G.A. Roscelli, *The Use of an All-or-None Assay for Measuring Enzyme-activator Dissociation Constants.* Journal of Biological Chemistry, 1966. **241**(4): p. 1012-1015.

35. Childers, W.S., et al., *Peptides Organized as Bilayer Membranes.* Angewandte Chemie International Edition, 2010. **49**(24): p. 4104-4107.

36. Lassila, J.K., D. Baker, and D. Herschlag, *Origins of catalysis by computationally designed retroaldolase enzymes.* Proceedings of the National Academy of Sciences of the United States of America, 2010. **107**(11): p. 4937-4942.

37. Lu, K., et al., *Exploiting Amyloid Fibril Lamination for Nanotube Self-Assembly.* Journal of the American Chemical Society, 2003. **125**(21): p. 6391-6393.

38. Balbach, J.J., et al., *Amyloid Fibril Formation by Aβ16-22, a Seven-Residue Fragment of the Alzheimer's β-Amyloid Peptide, and Structural Characterization by Solid State NMR†.* Biochemistry, 2000. **39**(45): p. 13748-13759.

39. Liang, C., et al., *Kinetic Intermediates in Amyloid Assembly.* Journal of the American Chemical Society, 2014. **136**(43): p. 15146-15149.

40. Liang, Y., et al., *Cross-Strand Pairing and Amyloid Assembly.* Biochemistry, 2008. **47**(38): p. 10018-10026.

41. Mehta, A.K., et al., *Facial Symmetry in Protein Self-Assembly.* J. Am. Chem. Soc., 2008. **130**(30): p. 9829-9835.

42. Childers, W.S., et al., *Templating Molecular Arrays in Amyloid's Cross-Beta Grooves.* J Am Chem Soc, 2009. **131**(29): p. 10165-10172.

43. Turner, J.M., et al., *An Efficient Benchtop System for Multigram-Scale Kinetic Resolutions Using Aldolase Antibodies.* Chemistry – A European Journal, 2000. **6**(15): p. 2772-2774.

44. Michaelis, L. and M.L. Menten, *Die Kinetik der Invertinwirkung.* Biochemische Zeitschrift, 1913. **49**: p. 333–369.

45. Chen, W.W., M. Niepel, and P.K. Sorger, *Classic and contemporary approaches to modeling biochemical reactions.* Genes & Development, 2010. **24**(17): p. 1861-1875.

46. Miller, S.M. and J.B. Rawlings, *Model identification and control strategies for batch cooling crystallizers.* AIChE Journal, 1994. **40**(8): p. 1312-1327.

47. McKay, M.D., R.J. Beckman, and W.J. Conover, *A Comparison of Three Methods for Selecting Values of Input Variables in the Analysis of Output from a Computer Code.* Technometrics, 1979. **21**(2): p. 239-245.

48. Press, W.H., *Numerical recipes in C : the art of scientific computing*. 1988, Cambridge [Cambridgeshire] ; New York: Cambridge Cambridgeshire ; New York : Cambridge University Press.

49. Childers, W.S., et al., *Templating Molecular Arrays in Amyloid's Cross-β Grooves.* Journal of the American Chemical Society, 2009. **131**(29): p. 10165-10172.

50. Xue, W.-F., S.W. Homans, and S.E. Radford, *Systematic analysis of nucleation-dependent polymerization reveals new insights into the mechanism of amyloid self-assembly.* Proceedings of the National Academy of Sciences, 2008. **105**(26): p. 8926-8931.

51. Hurvich, C.M. and C.L. Tsai, *Regression and time series model selection in small samples.* Biometrika, 1989. **76**(2): p. 297-307.

52. Wagenmakers, E.-J. and S. Farrell, *AIC model selection using Akaike weights.* Psychonomic Bulletin & Review, 2004. **11**(1): p. 192-196.

53. Mohamadi, F., et al., *Macromodel - an Integrated Software System for Modeling Organic and Bioorganic Molecules Using Molecular Mechanics.* Journal of Computational Chemistry, 1990. **11**(4): p. 440-467.

54. Bowers, K.J., et al. *Scalable algorithms for molecular dynamics simulations on commodity clusters*. in *SC 2006 Conference, Proceedings of the ACM/IEEE*. 2006. IEEE.

55. Berendsen, H., et al., *Interaction models for water in relation to protein hydration.* Intermolecular forces, 1981. **11**(1): p. 331-342.

56. Kaminski, G.A., et al., *Evaluation and Reparametrization of the OPLS-AA Force Field for Proteins via Comparison with Accurate Quantum Chemical Calculations on Peptides†*. The Journal of Physical Chemistry B, 2001. **105**(28): p. 6474-6487.

Chapter 4: Retro-aldol activity of Aβ(16-22) congeners: The Active Site Amine

Introduction

In chapter 3, the Ac-KLVFFAL-NH_2 nanotubes are shown to selectively catalyze the retro-aldol cleavage of (±)-methodol. These data are most consistent with covalent catalysis much as seen in aldolase and other lysine catalysts. This chapter explores the role of the amine in catalysis by varying the position of the amine in the hydrophobic grooves of the nanotubes.

Results and Discussion

Modification of the Position of the Catalytic Amine

The results from chapter 3 suggest that the observed catalytic cleavage of methodol is taking place in the hydrophobic grooves on the nanotubes. Bringing the amine closer into the hydrophobic grooves could impact the rate either through proximity to the substrate or through modulation of the pKa [1-4]. To test this possibility, the amine tether of lysine was shortened by replacing lysine in Ac-KLVFFAL-NH_2 with ornithine (minus one methylene group), diaminobutyric acid (minus two methylene groups), diaminopropionic acid (minus three methylene groups) and β-alanine (minus three methylene groups) (Figure 4-1).

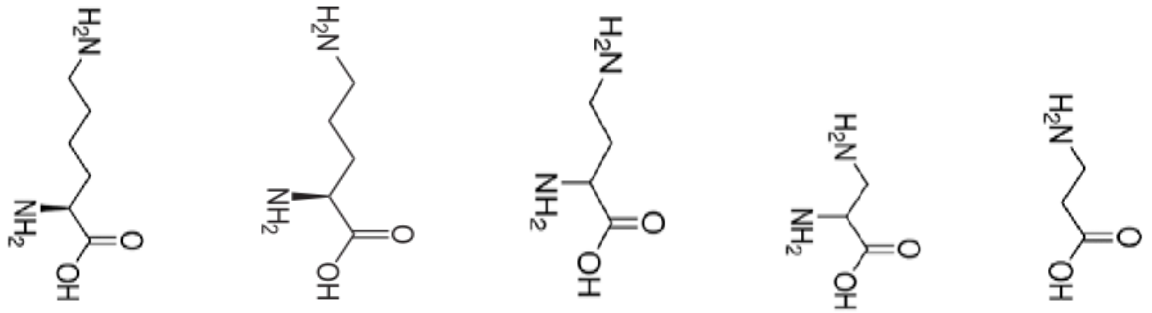

(A) **(B)** **(C)** **(D)** **(E)**

Figure 4-1: *Amino acid structure of (A) Lysine (B) Ornithine (C) Diaminobutyric acid (D) Diaminopropionic acid and (E) β-alanine*

Structural analysis of these substitutions reinforce the argument that the N-terminal position can accommodate a wide range of substitutions. The CD spectra of assembly prepared with 0.5 mM K16Orn, K16βAla, K16Dab and K16Dap are virtually identical with β-sheet minima at 225 nm and strong positive ellipticity at 200 nm (Figure 4-2). TEM micrographs of these K16 modified peptides are morphologically similar to the Ac-KLVFFAL-NH_2 nanotubes, but with slightly different diameters. Ac-(Orn)LVFFAL-NH_2 nanotubes maintain an average tube widths of 41.7±2.6 nm, 48.2±5.2 nm for NH_2-(βAla)LVFFAL-NH_2, 39.5±5.4 nm for Ac-(Dab)LVFFAL-NH_2 and 40.3±5.9 nm for Ac-(Dap)LVFFAL-NH_2 (Figure 4-4) while Ac-KLVFFAL-NH_2 is 44.2±3.6 nm.

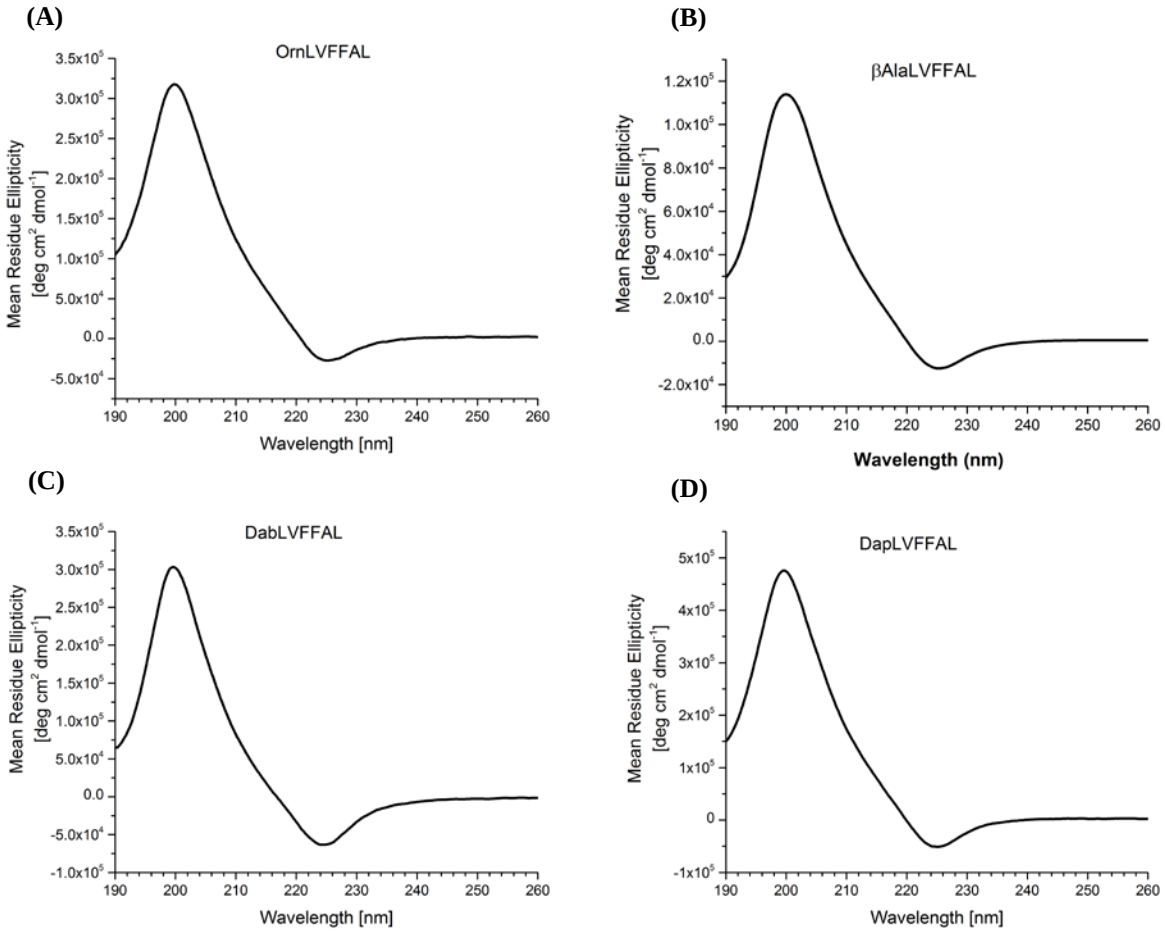

Figure 4-2: *CD Wavelength scans of (A) 0.5 mM Ac-(Orn)LVFFAL-NH_2 (B) 0.5 mM NH_2-(ßAla)LVFFAL-NH_2 and (C) 0.5 mM Ac-(Dab)LVFFAL-NH_2 and (D) 0.5 mM Ac-(Dap)LVFFAL-NH_2. All samples were assembled in 40% MeCN/H_2O with 0.1% TFA at 4ºC except NH_2-ßAlaLVFFAL-NH_2 which was assembled at RT.*

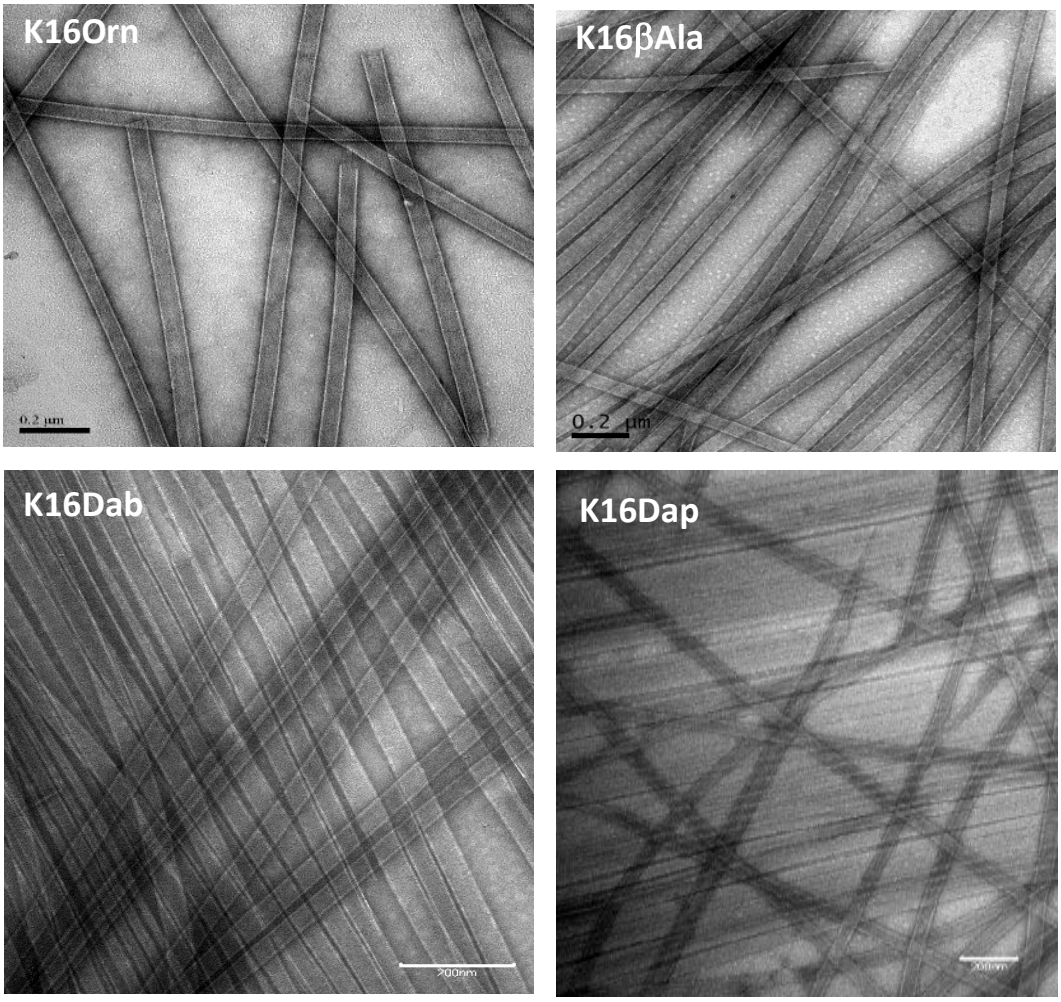

Figure 4-3: *Uranyl acetate stained TEM images of the 2.5 mM K16 modified peptide assemblies. (A) Ac-(Orn)LVFFAL-NH_2 (B) NH_2-(βAla)LVFFAL-NH_2 and (C) Ac-(Dab)LVFFAL-NH_2 and (D) Ac-(Dap)LVFFAL-NH_2. Scale bar is 200 nm.*

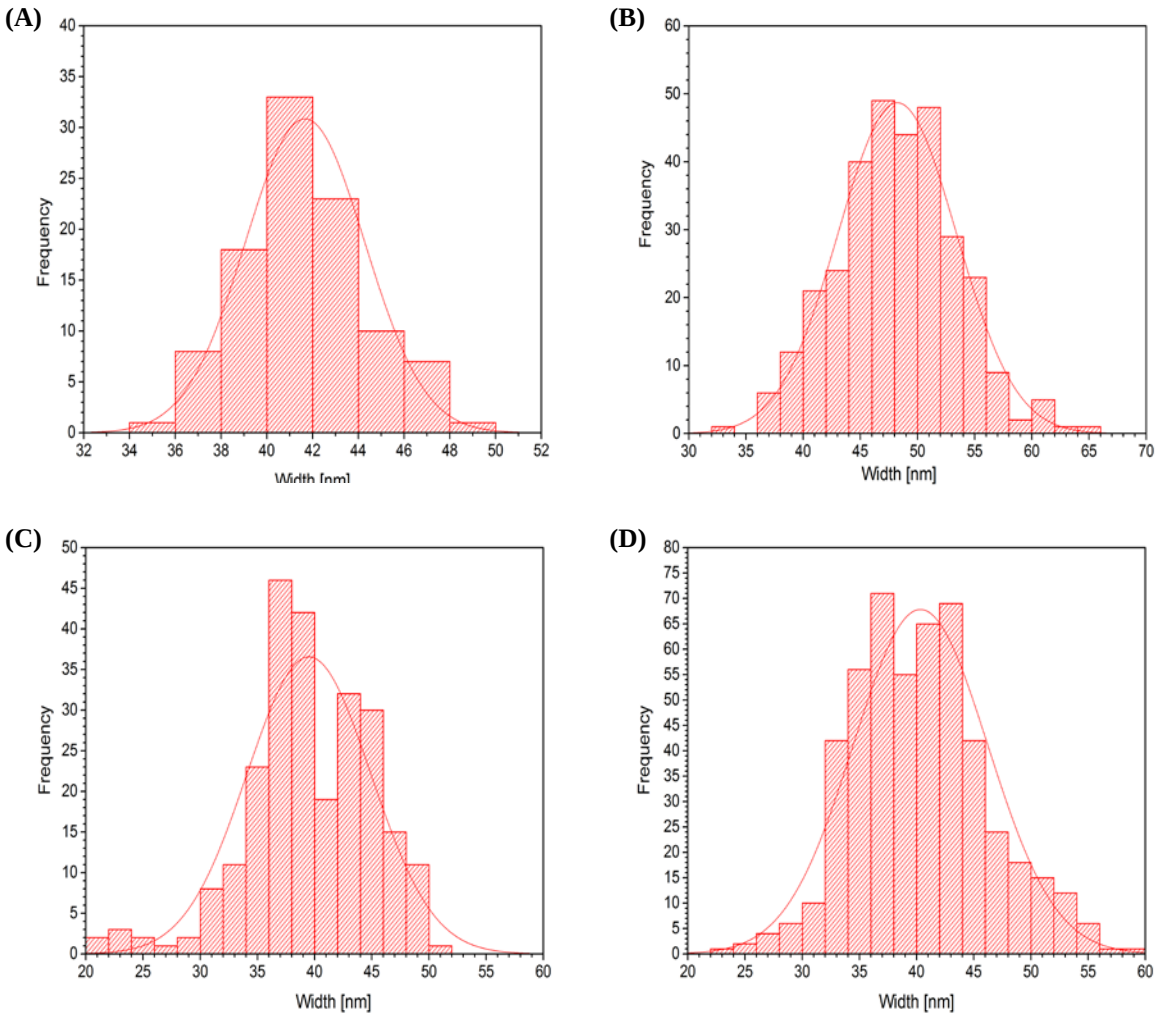

Figure 4-4: *Tube width measurements from TEM image of (A) K16Orn, (B) K16βAla, (C) K16Dab and (D) K16Dap. 150-300 measurements were taken and the frequency was plotted against widths and fit to Gaussian distributions with the center width of 41.7 ± 2.6 nm for K16Orn, 48.2 ± 5.2 nm for K16ßAla, 39.5 ± 5.4 nm for K16Dab and 40.3 ± 5.9 nm for K16Dap.*

The backbone amide stretching modes provide even greater insight into the structure of the analogs. As shown in Figure 4-5, the FT-IR amide I stretch vibrations of all the peptide nanotubes assemblies have a maximum absorption at 1623 cm^{-1} and a

weaker one at 1694 cm^{-1}, consistent with anti-parallel β-sheet architecture similar to Ac-KLVFFAL-NH_2 nanotubes.

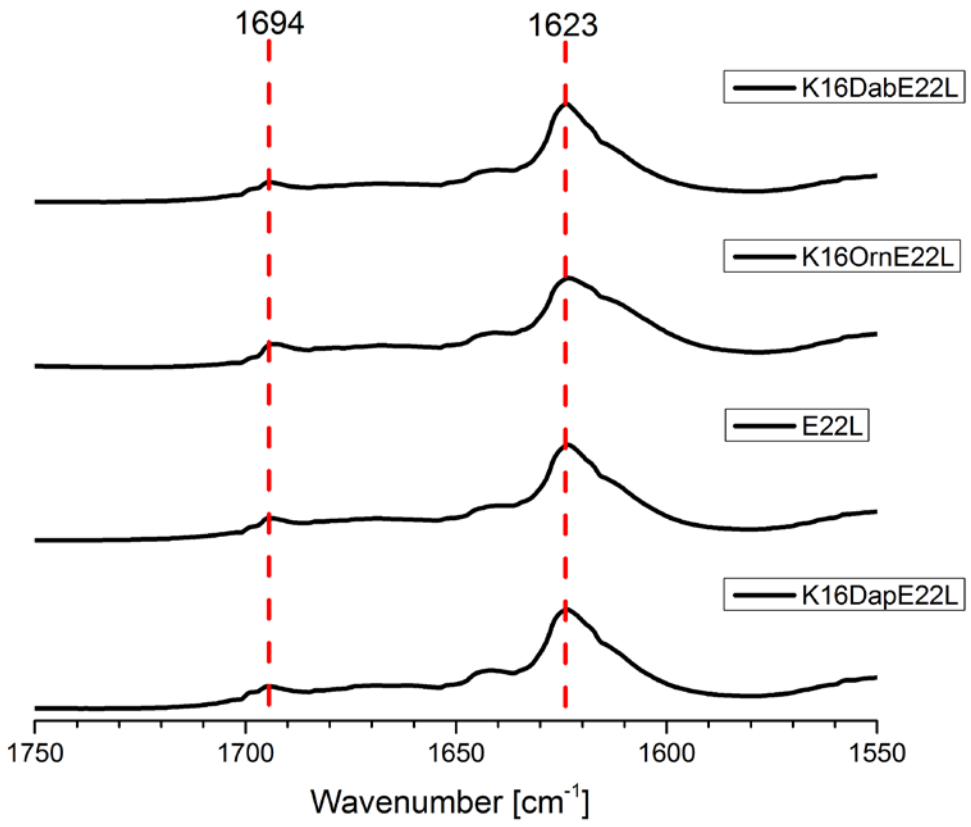

Figure 4-5: *FT-IR of the K16 modified peptide assemblies shows that all the four peptide assemblies have the same antiparallel ß-strand orientation.*

Enriching ^{13}C at the F19 carbonyl position, [1-^{13}C]F19, allows better resolution of the delocalized normal modes along the β-sheet. The FT-IR signal of the peptide secondary structure is split into ^{12}C and ^{13}C amide I stretches which is brought about by the perturbation of the ^{12}C carbonyl oscillator coupling network by ^{13}C enrichment. The magnitude of the observed splitting and wavenumber shift depends on the extended

hydrogen-bonded oscillator network [5, 6] and all these [1-^{13}C]F19 enriched peptide assemblies absorb at 1637 cm^{-1} and 1595 cm^{-1} (Figure 4-6), virtually identical to the Ac-KLVFFAL-NH_2 nanotubes. The precise registry of the Ac-KLVFFAL-NH_2 nanotubes have been confirmed by solid-state NMR as antiparallel, out-of-register β-sheet [7].

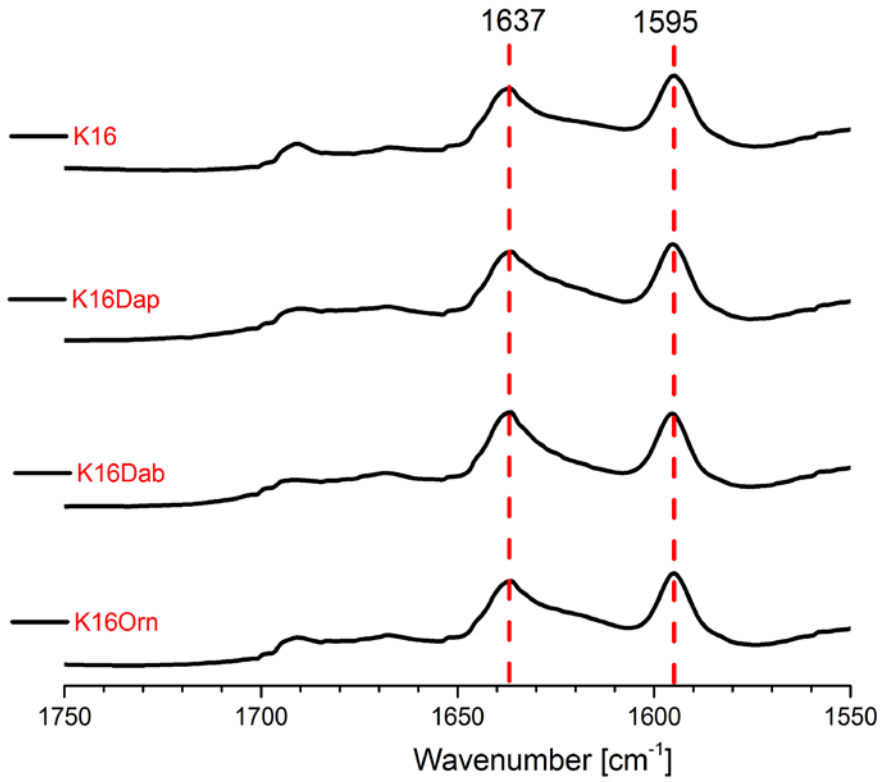

Figure 4-6: *Isotope edited FT-IR of the K16 modified peptide assemblies incubated in 40% MeCN/H_2O at pH 2.0. The spectrum shows the splitting between the ^{12}C and ^{13}C peaks of ~ 35 cm^{-1} with the ^{13}C shifting to a lower frequency at 1595 cm^{-1} and ^{12}C at 1637 cm^{-1}.*

X-ray diffraction further confirms the long range order of the nanotubes. The classic cross-β assembly of amyloid with distinct d-spacings of 4.7Å representing the

distances between the hydrogen bonded β-strands and the d-spacings of ~10.2Å correlated to the laminate distances separating the β-sheets.

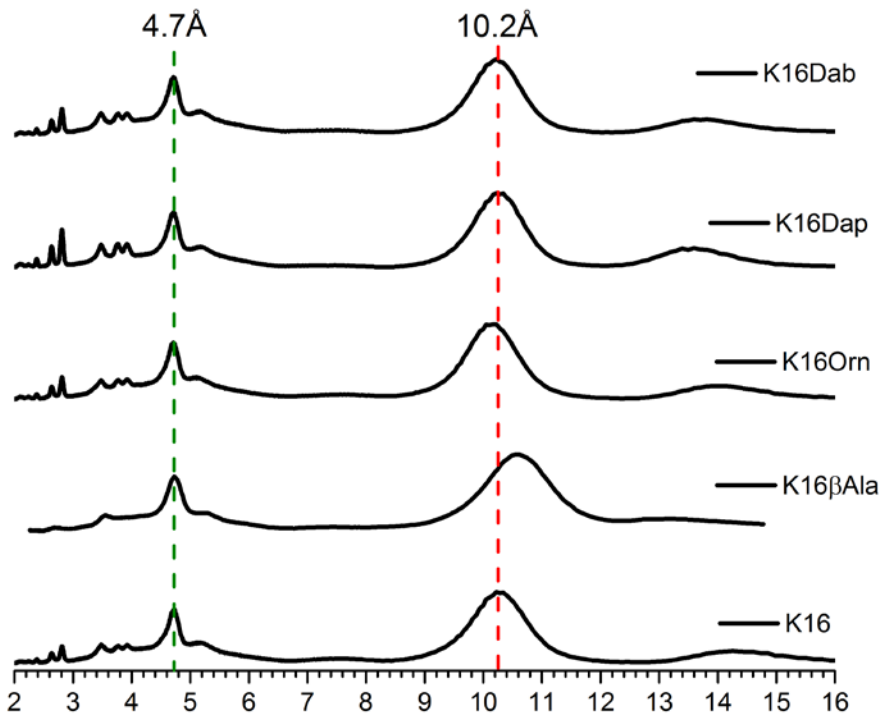

***Figure 4-7**: X-ray diffraction of the K16 modified peptide assemblies shows that all the four peptide assemblies have the same hydrogen bonding distance of 4.7Å as Ac-KLVFFAL-NH_2 and while Ac-(Orn)LVFFAL-NH_2, Ac-(Dab)LVFFAL-NH_2 and Ac-(Dap)LVFFAL-NH_2 nanotubes have laminate distances of 10.2Å, NH_2-(βAla)LVFFAL-NH_2 have laminate distance of 10.5Å. All the nanotubes were bundled with SO_4^{2-} salt before diffraction except NH_2-(βAla)LVFFAL-NH_2. The diffraction peaks below 4Å are due to salts from bundling the tubes, they are absent from un-bundled NH_2-(βAla)LVFFAL-NH_2.*

Taken together, CD, TEM, FTIR and X-ray diffraction all indicate that replacing the lysine in Ac-KLVFFAL-NH_2 with ornithine, β-Alanine, diaminobutyric acid and diaminopropionic acid did not drastically impact overall nanotube structure.

More dramatic repositioning of the amine was explored by substituting the leucine residues making up the grooves (L17 or L22) with lysine. K16LL22K, Ac-LLVFFAK-NH_2, also assembles into homogenous nanotubes at pH 2 (Figure 4-8A), and at pH 7, into mixed ribbons and nanotubes (Figure 4-8B). As shown in Figure 4-8C, both the pH 2 and pH 7 peptide assemblies display characteristic β-sheet CD spectra with a negative ellipticity at 218 nm and a positive cotton effect at ~200 nm. FT-IR spectra also display amide I stretching modes consistent with anti-parallel β-sheet architecture (Figure 4-8D) and X-ray diffraction confirm the cross-β structure (Figure 4-8E). Unlike K16LL22K, the transposition K16LL17K (Ac-LKVFFAL) assemble into thin ribbons at pH 2 (Figure 4-9A) and a mixture of thin ribbons and sheets at pH 7 (Figure 4-9B). The CD spectra of the peptide assemblies at pH 2 display very weak negative ellipticity at ~230 nm and a weak positive ellipticity at ~215 nm (Figure 4-9C), while at pH 7 the assemblies display a more intense minima at ~220 nm and a maxima at ~190 nm with a shoulder at ~200 nm (Figure 4-9D). FT-IR amide I stretch vibrations of the peptide assemblies have absorptions at 1623 cm^{-1} and 1694 cm^{-1} consistent with antiparallel β-sheet secondary structure (Figure 4-9E). X-ray diffraction analysis show d-spacing at 4.7Å and a broader d-spacing at ~11.2Å. These less well defined structures unfortunately complicate any specific arguments about catalysis.

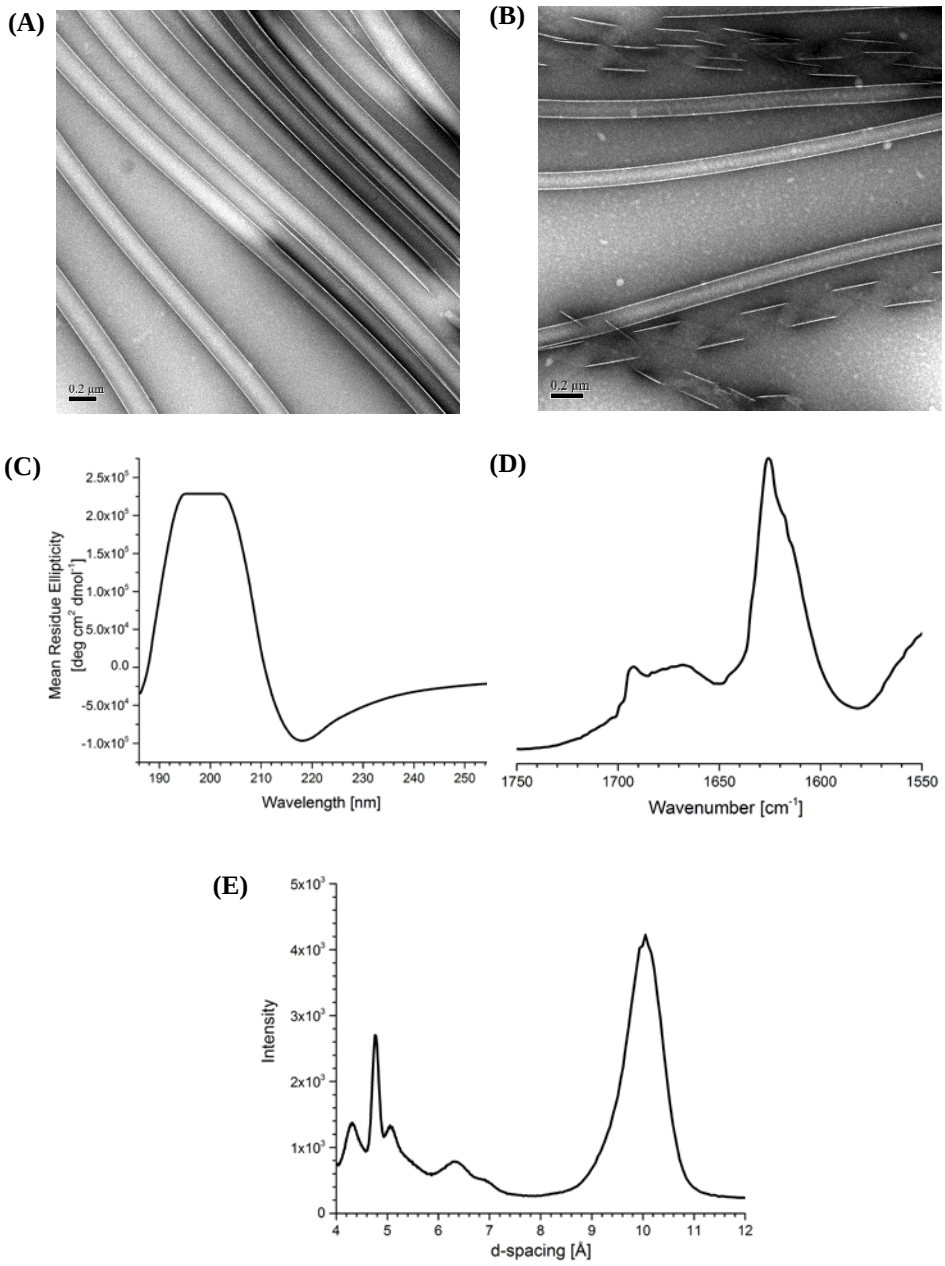

Figure 4-8: *Structural Characterization of Ac-LLVFFAK (A) Uranyl acetate stained TEM images at pH 2 (B) Uranyl acetate stained TEM images at pH 7. (C) CD spectra (D) IR spectra showing antiparallel ß-strand orientation and (E) X-ray diffraction showing the hydrogen bonding distance of 4.7Å and laminate distances of 10.1Å.*

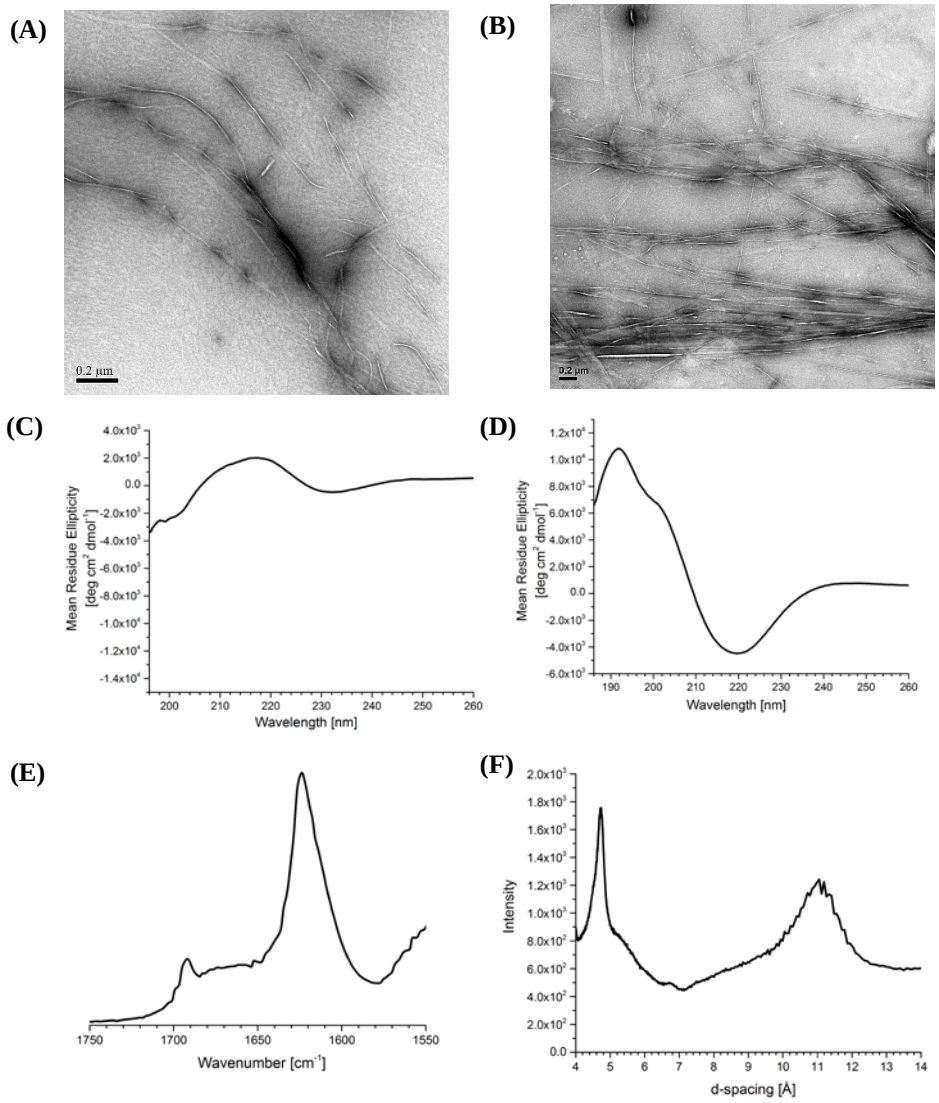

Figure 4-9: *Structural Characterization of Ac-LKVFFAL (A) Uranyl acetate stained TEM images at pH 2 (B) Uranyl acetate stained TEM images at pH 7. (C) CD spectra at pH 2 (D) CD spectra at pH 7 (E) IR spectra showing antiparallel ß-strand orientation and (F) X-ray diffraction showing the hydrogen bonding distance of 4.7Å and laminate distances of 11.2Å.*

Evaluation of the Retro-aldol Activity

Initial test of the reactivity of these assemblies is the reaction with 2,4-pentanedione. For example, titration of 500 μM Ac-(Orn)LVFFAL-NH_2 nanotubes with 2,4-pentanedione saturated 251±7.4 μM (Figure 4-10), consistent with the same ~50% of the peptide amine side chains available. However, a striking increase in methodol initial rates of conversion is observed following the order βAla > Orn > Lys (Figure 3.6 of Chapter 3). By TEM, the K16Orn nanotubes remain intact even after several days under the reaction condition (Figure 4-11A), but the K16βAla nanotubes unravel to ribbons.

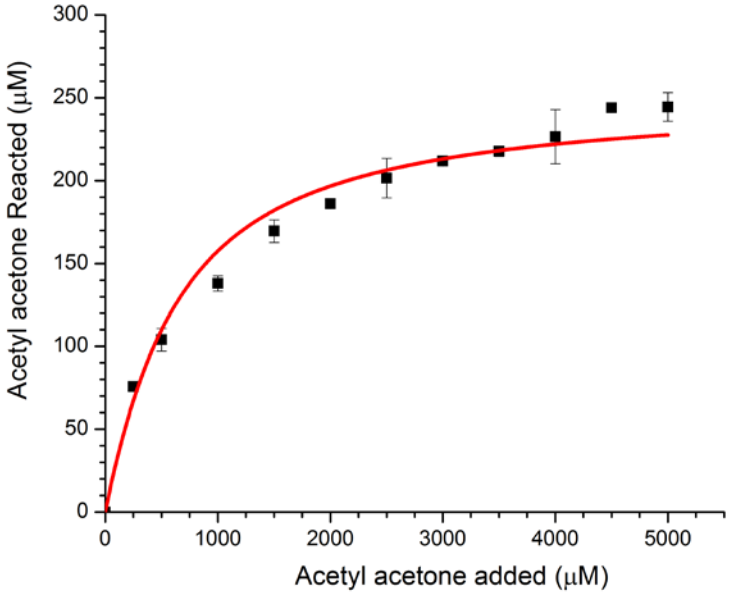

Figure 4-10: Titrating amine accessibility on Ac-(Orn)LVFFAL-NH_2 nanotube surface. *Enaminone formation monitored by UV absorbance at 316 nm followed as a function of 2,4-pentanedione concentration in the presence of 500 μM Ac-(Orn)LVFFAL-NH_2 nanotubes. A fit to the data ($y=251\pm7.4\ \mu M * (1-e^{-0.0013\pm0.0001*x})$), indicates half of the peptide lysine side chains are solvent accessible, consistent with the nanotube peptide bilayer wall architecture*

Stock solutions of the K16βAla nanotubes in water show disassembly without added substrate (Figure 4-11B), suggesting that K16βAla nanotubes are unstable in water. Hence, further catalytic studies on the K16βAla nanotubes were discontinued and the remaining studies focused on K16Orn, K16Dab and K16Dap assemblies.

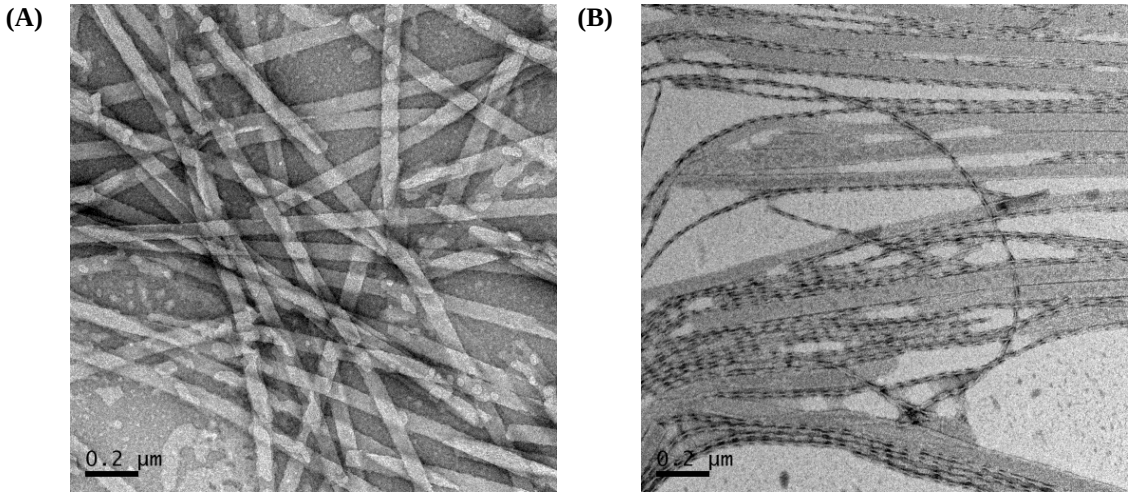

Figure 4-11: *TEM image of (**A**) K16Orn and (**B**) K16βAla incubated with methodol for a week under the reaction conditions.*

Compared with Ac-KLVFFAL-NH_2, K16Orn, K16Dab and K16Dap nanotubes all showed significantly increased initial rates of methodol conversion with K16Dap showing ~16 times more product formed after 1 hour (Figure 4-12). Placing the amine at different positions, at the C-terminus, Ac-LLVFFAK-NH_2 or adjacent to the N-terminus, Ac-LKVFFAL-NH_2 eliminates activity (Figure 4-12). It is possible that the lysine is buried in the groove and inaccessible for the catalysis, reconsidering the result of the Ac-KL(terL)FFAE-NH_2 nanotubes in chapter 3, the reduced hydrophobicity of the groove could also prevent binding.

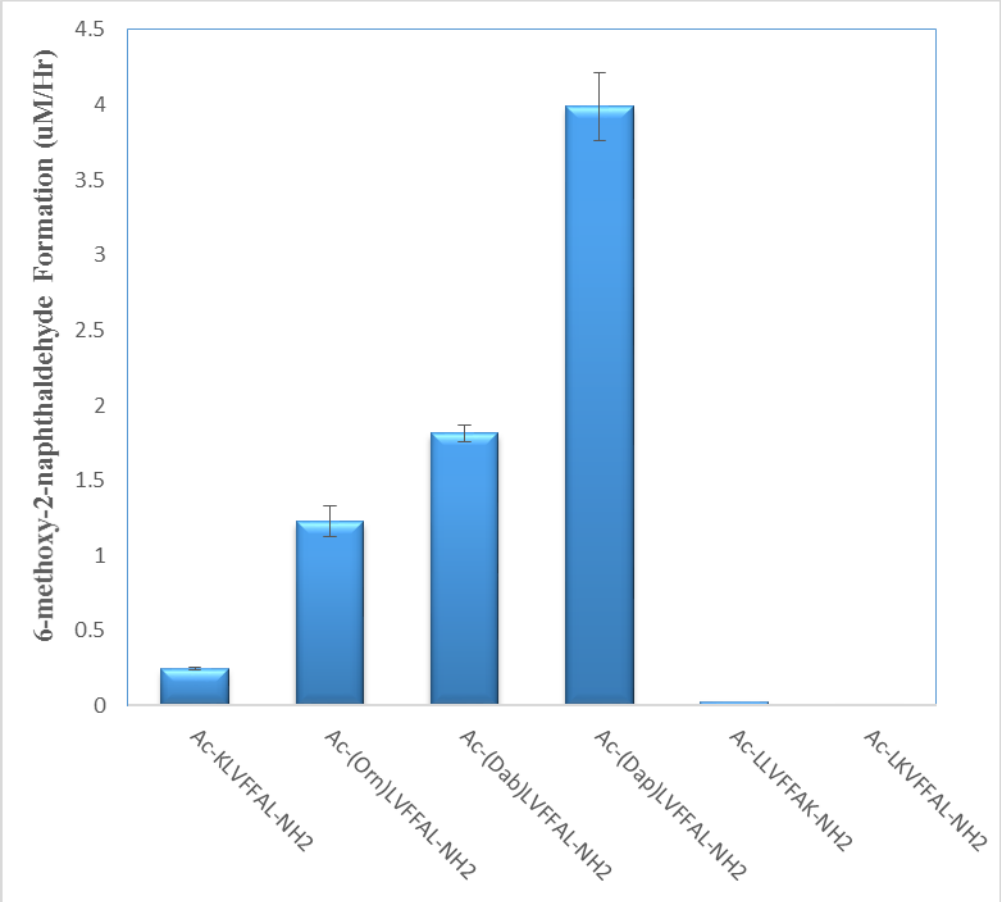

Figure 4-12: *Initial rate of production of 6-methoxy-2-naphthaldehyde by the indicated peptide assembly where the peptide concentration is 500 µM and the starting (±)-methodol concentration is 80 µM.*

The rate of naphthaldehyde formation catalyzed by K16Orn, K16Dab and K16Dap nanotubes are monitored over 8 hours and the K16Dab nanotubes reach a plateau at ~ 7 hours (Figure 4-13). The same trend is observed for K16Orn nanotubes, but with K16Dap nanotubes, product increase linearly the first 2 hours and plateaus after ~ 3 hours (Figure 4-14). Product inhibition has been reported by Lassila et al. with their computationally designed retroaldolase [3], which is also expected for the nanotubes.

From this series, it appears that the closer the amines are to the binding groove, the higher the catalytic rates and the more pronounced the product inhibition.

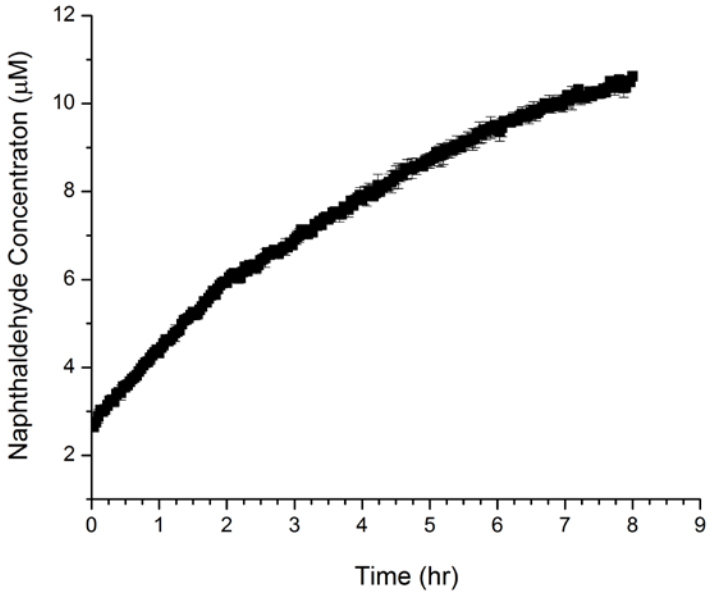

Figure 4-13: *Naphthaldehyde fluorescence for 80 μM racemic methodol in the presence of 500 μM Ac-(Dab)LVFFAL-NH_2 nanotubes.*

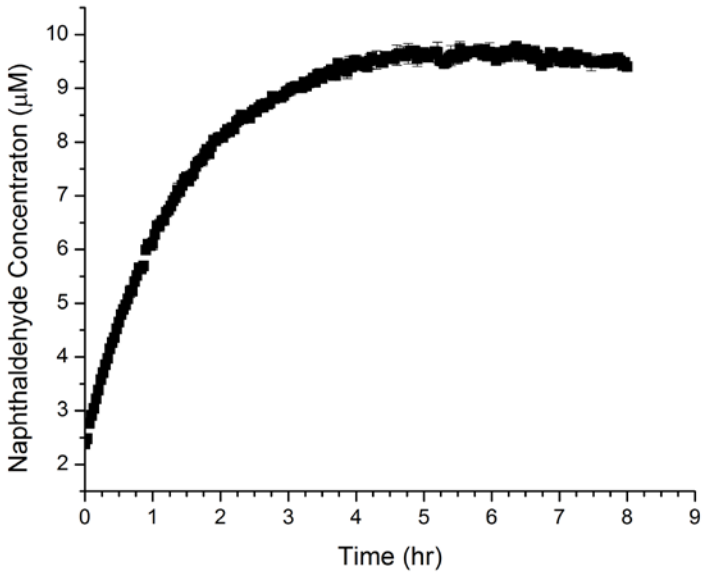

Figure 4-14: *Naphthaldehyde fluorescence for 80 μM racemic methodol in the presence of 500 μM Ac-(Dap)LVFFAL-NH_2 nanotubes.*

Like Ac-KLVFFAL-NH_2, K16Orn nanotubes prefer S-methodol (Figure 4-15). In contrast, there no enantioselectivity with either K16Dab or K16Dap nanotubes under these conditions (Figure 4-16 and 4.17), and the reasons are not yet clear.

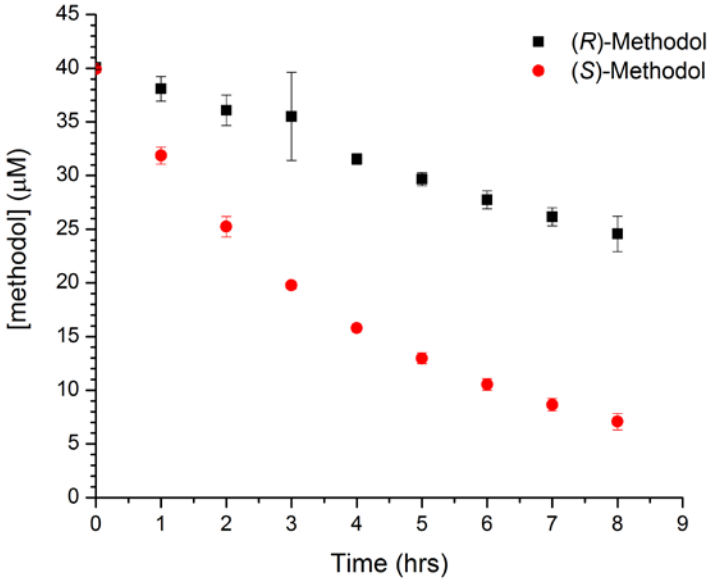

Figure 4-15: *(±)-Methodol (80 µM) consumption in the presence of 500 µM Ac-(Orn)LVFFAL-NH_2 nanotubes shows a preference for S-methodol.*

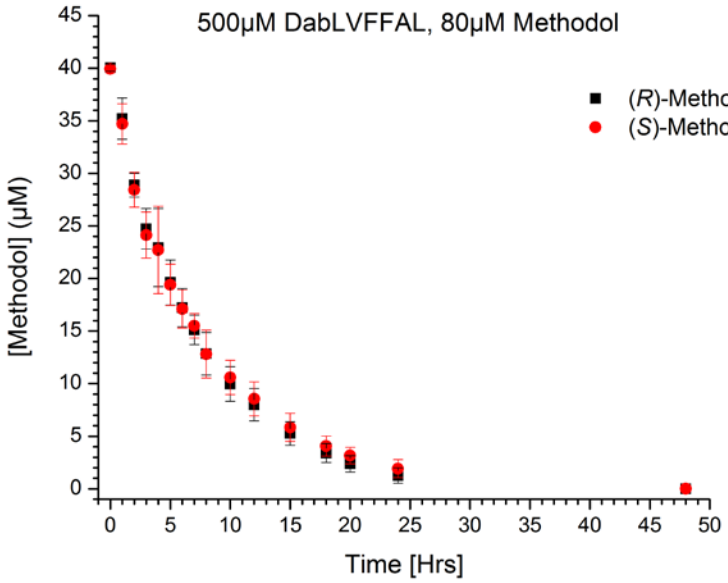

Figure 4-16: *Progressive monitoring of (±)-Methodol (80 µM) consumption in the presence of 500 µM Ac-(Dab)LVFFAL-NH_2 nanotubes over 48 hours shows no preference for either R- or S- Methodol.*

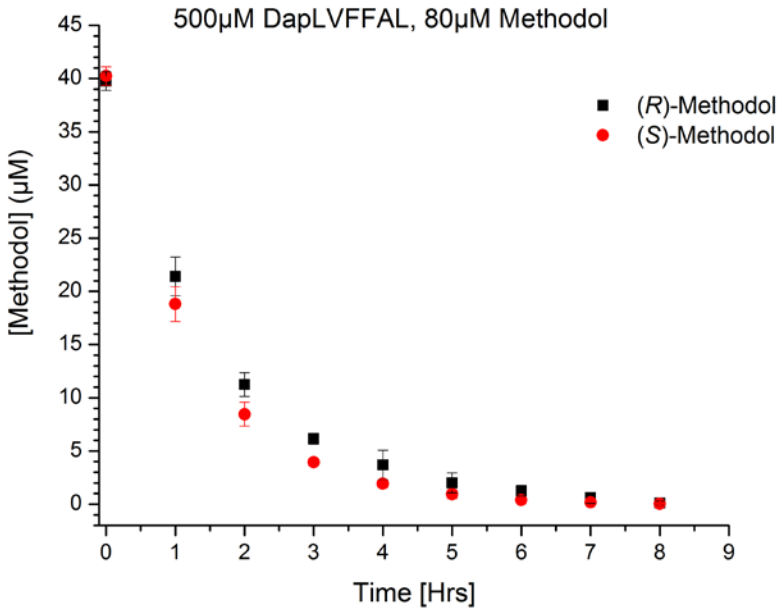

Figure 4-17: *Progressive monitoring of (±)-Methodol (80 μM) consumption in the presence of 500 μM Ac-(Dap)LVFFAL-NH_2 nanotubes over 8 hours shows little to no enantioselectivity.*

Kinetic Evaluation of Catalysis

The same mechanistic model described in chapter 3 is used to fit the substrate consumption and product accumulation by Ac-(Orn)LVFFAL-NH_2, Ac-(Dab)LVFFAL-NH_2 and Ac-(Dap)LVFFAL-NH_2 nanotubes. As shown in Figure 4-18A-C, the normalized sum of square errors (SSE) for Ac-(Orn)LVFFAL-NH_2, Ac-(Dab)LVFFAL-NH_2 and Ac-(Dap)LVFFAL-NH_2 nanotubes are lowest at n=6, the same as determined for the Ac-KLVFFAL-NH_2 nanotubes in chapter 3.

Using n=6, titrating a solution of 5.8 μM 6-methoxy-2-naphthaldehyde with 5-500 μM peptide nanotubes gives K_d of 6.49 μM, 4.19 μM and 2.28 μM for Ac-

(Orn)LVFFAL-NH_2, Ac-(Dab)LVFFAL-NH_2 and Ac-(Dap)LVFFAL-NH_2 respectively (Figure 4-19), consistent with the product inhibition observed with the peptide nanotubes and confirming that Ac-(Dap)LVFFAL-NH_2 binds the naphthaldehyde product most tightly.

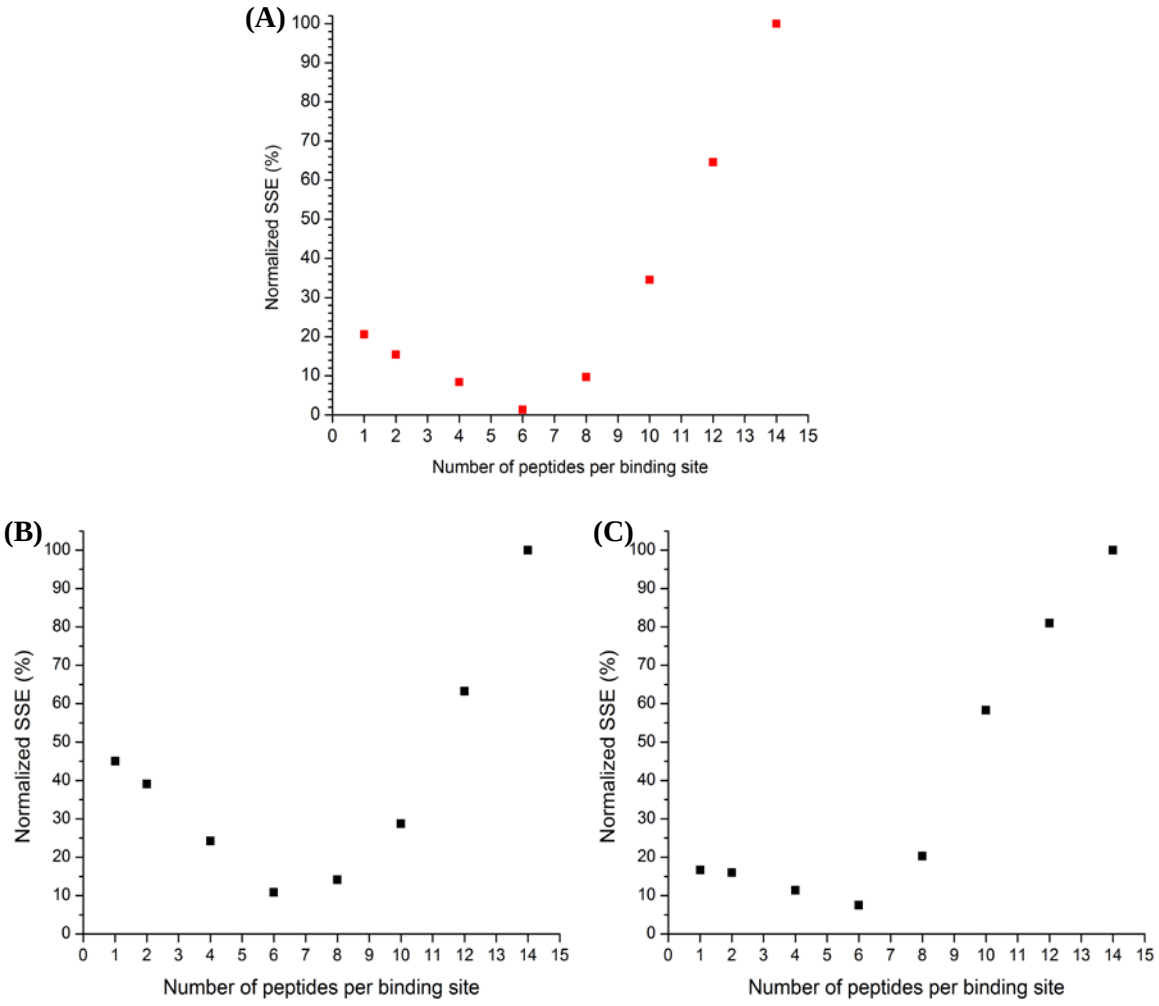

Figure 4-18: *Normalized sum of square error (SSE) for R- and S-methodol consumption on* ***(A)*** *Ac-(Orn)LVFFAL-NH_2,* ***(B)*** *Ac-(Dab)LVFFAL-NH_2 and* ***(C)*** *Ac-(Dap)LVFFAL-NH_2 nanotubes.*

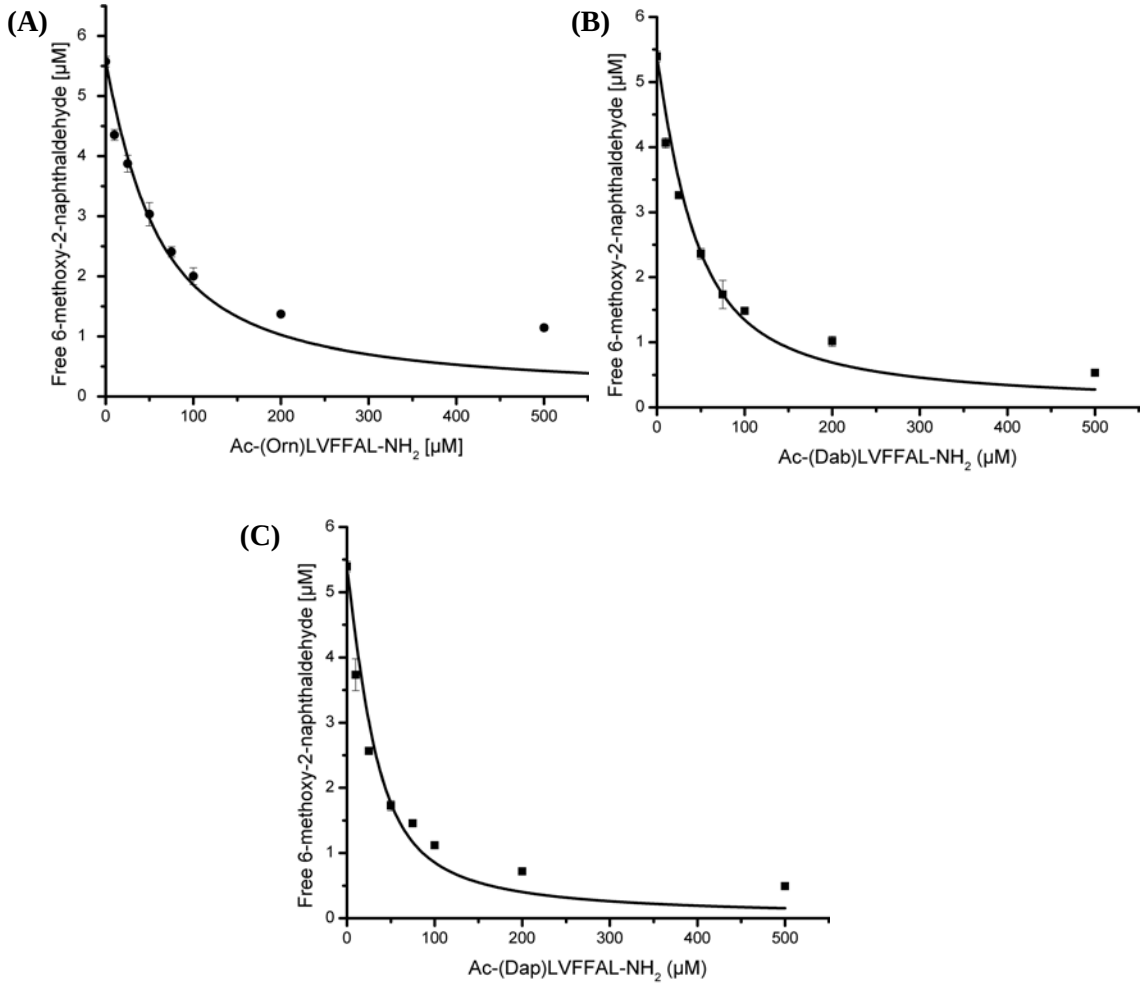

Figure 4-19: *Measurement of free 6-methoxy-2-naphthaldehyde (MNA) as a function of peptide assembly (peptide concentration) by titrating 5.8 µM 6-methoxy-2-naphthaldehyde with peptide assemblies over 5-500 µM peptide concentration. The fluorescence data was fit to* $MNA_{free} = 1/2*([MNA]_{Tot}-K_d-[Peptide]+sqrt(4*[MNA]_{Tot}*K+(-[MNA]_{Tot}+K+[Peptide])^2))$ *using 6 peptides per napthaldehyde binding site to yield a* K_d *of (A) 6.49 µM for Ac-(Orn)LVFFAL-*NH_2 *(B) 4.19 µM for Ac-(Dab)LVFFAL-*NH_2 *and (C) 2.28 µM for Ac-(Dap)LVFFAL-*NH_2

The fits for methodol conversion by the Ac-(Orn)LVFFAL-NH_2, Ac-(Dab)LVFFAL-NH_2 and Ac-(Dap)LVFFAL-NH_2 nanotubes are shown in Figure 4-20, 4.21 and 4.22 respectively. Like Ac-KLVFFAL-NH_2, Ac-(Orn)LVFFAL-NH_2 (K_{dR} = 1.21 $\times 10^1$ μM and K_{dS} = 2.51 $\times 10^1$ μM) and Ac-(Dab)LVFFAL-NH_2 (K_{dR} = 3.85 $\times 10^0$ μM and K_{dS} = 5.89 $\times 10^0$ μM) show a higher binding affinity for R-methodol whereas Ac-(Dap)LVFFAL-NH_2 (K_{dR} = 1.46 $\times 10^0$ μM and K_{dS} = 1.05 $\times 10^0$ μM) show a slightly higher binding affinity for S-methodol (Tables 4.1 and 4.2), but the closer amine groups in both Ac-(Dab)LVFFAL-NH_2 and Ac-(Dap)LVFFAL-NH_2 weaken the enantioselectivity of the peptide nanotubes and consume R- and S- methodol equally. The faster rate observed for Ac-(Dap)LVFFAL-NH_2 could be due to a more optimal placement of the amine to stabilize the transition state when the amine linker was shortened. Although we do not have data to support, it is possible that the pKa of the amine is modulated optimally by placing it in a more hydrophobic environment in Ac-(Dap)LVFFAL-NH_2.

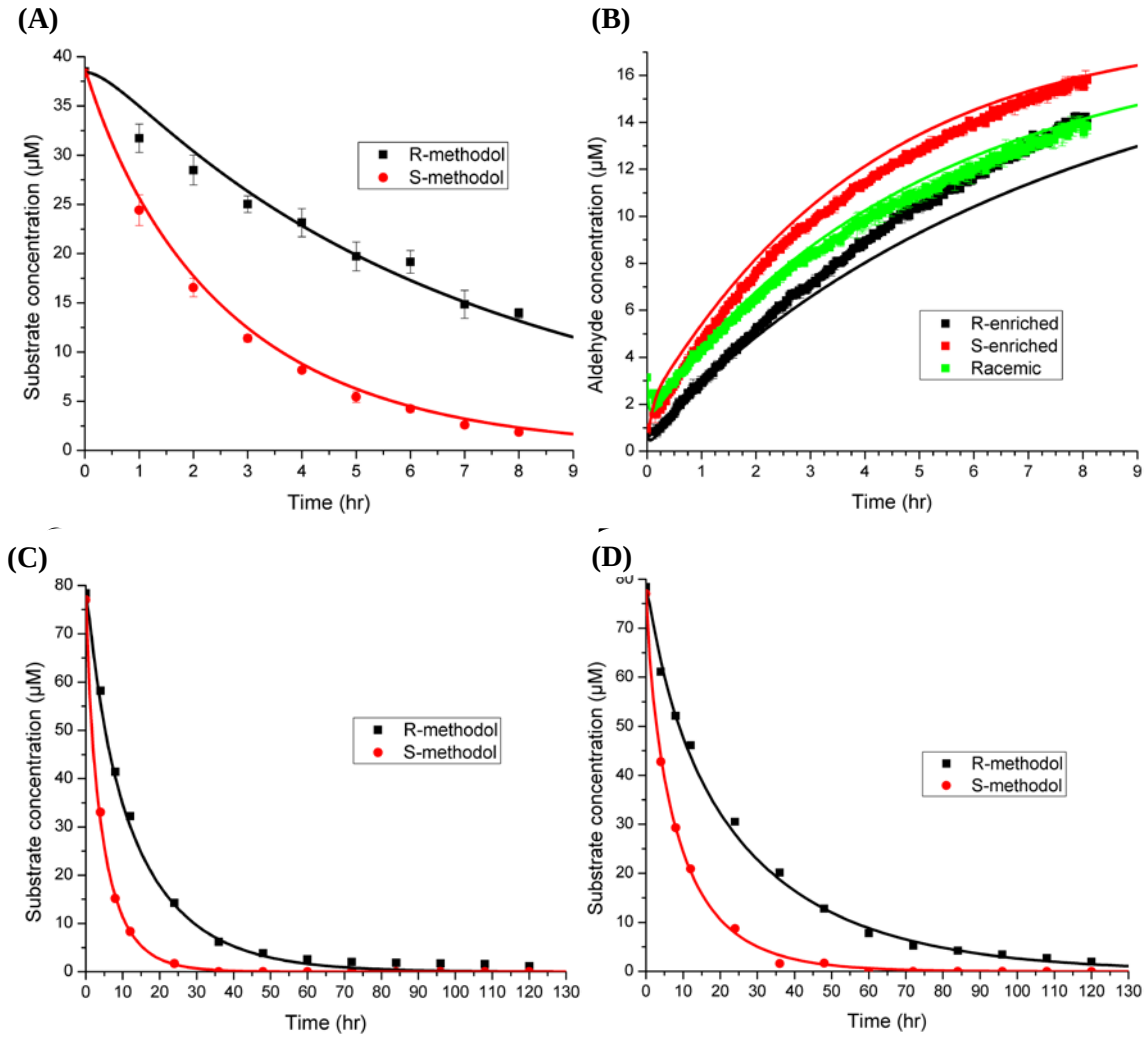

Figure 4-20: Best fits of Ac-(Orn)LVFFAL-NH₂ retro-aldol catalysis with 6 peptides per binding site. *(**A**) Chiral HPLC of 500 μM peptide and 76.7 μM (±)-methodol. (**B**) Naphthaldehyde fluorescence of 500 μM peptides with 76.7 μM (±)-methodol (green), 79.2 μM R-enriched methodol (black) and 79.1 μM S-enriched methodol (red). (**C**) Chiral HPLC of 500 μM peptide and 155.3 μM (±)-methodol. (**D**) Chiral HPLC of 300 μM peptide and 155.4 μM (±)-methodol. Solid lines are best fits using equations 1 to 3 with **(A)** initial concentrations [E] = 83.3 μM, [S] = 38.3 μM, [R] = 38.5 μM, [P_1] = 3.1 μM. **(B)** Initial concentrations of the racemic solution (green) [E] = 83.3 μM, [S] = 38.3 μM, [R] = 38.5 μM, [P_1] = 3.1 μM, for R-enriched substrate (black) [E] = 83.3 μM, [S] = 11.9 μM, [R] = 67.3 μM, [P_1] = 0.77 μM and initial concentrations of the S-enriched substrate (red) [E] = 83.3 μM, [S] = 67.2 μM, [R] = 11.9 μM, [P_1] = 0.95 μM. **(C)** The initial concentrations are: [E] = 83.3 μM, [S] = 77.0 μM, [R] = 78.4 μM, [P_1] = 4.6 μM. **(D)** The initial concentrations are: [E] = 50 μM, [S] = 77.0 μM, [R] = 78.4 μM, [P_1] = 4.6 μM.*

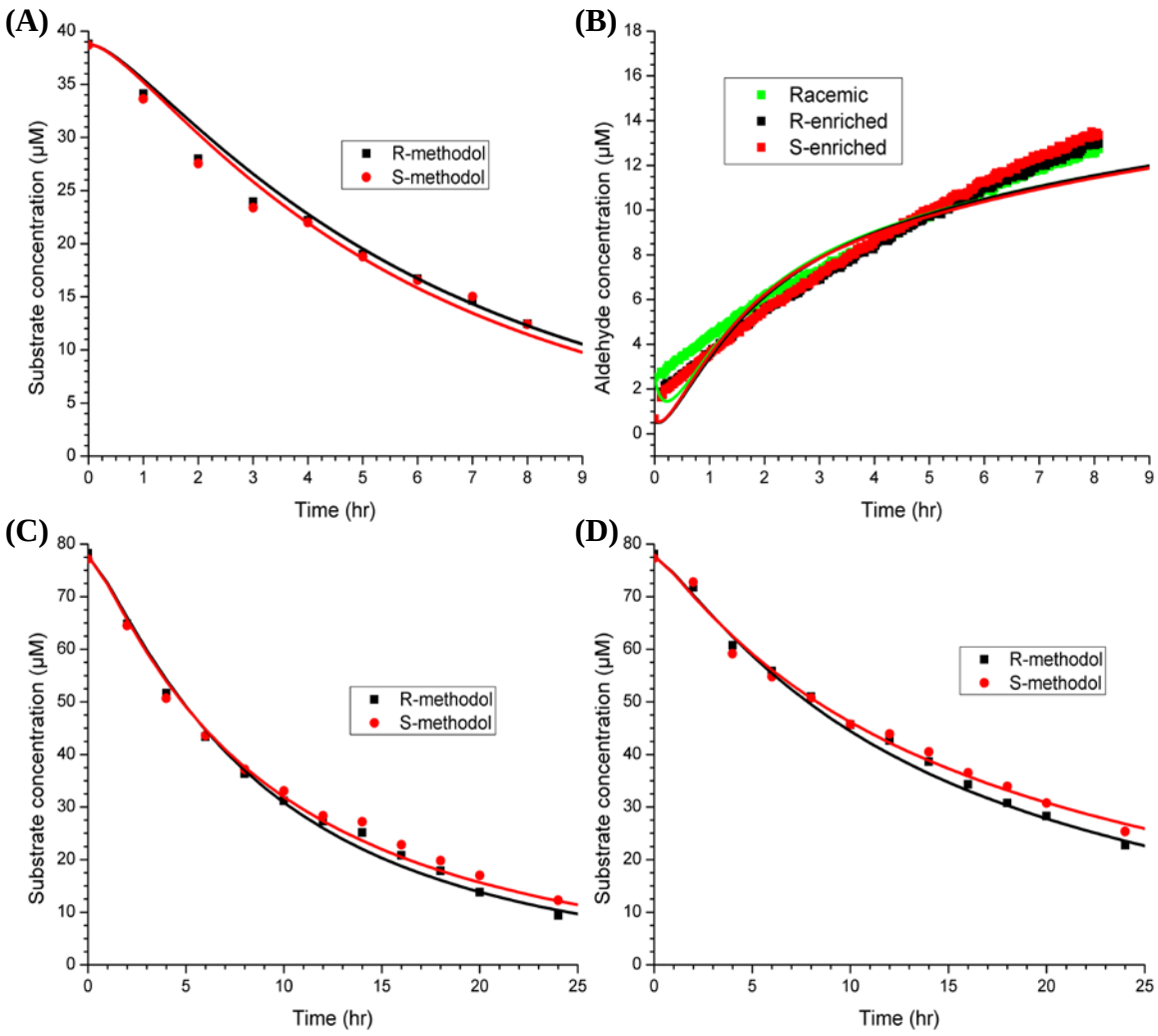

Figure 4-21: Best joint fits with 6 Ac-(Dab)LVFFAL-NH₂ peptides per binding site. *Equation (1) to (3) for (A, C, D) the methodol concentrations from chiral HPLC are used to fit (B) concentration of 6-amino 2-naphthaldehye measured from fluorescence.* ***(A)*** *The initial concentrations are: [E] = 83.3 μM, [S] = 38.7 μM, [R] = 38.8 μM, [P_1] = 2.5 μM.* ***(B)*** *The initial concentrations of the racemic solution are: [E] = 83.3 μM, [S] = 38.7 μM, [R] = 38.8 μM, [P_1] = 2.5 μM. The initial concentrations of the R-enriched substrate are: [E] = 83.3 μM, [S] = 11.9 μM, [R] = 67.5 μM, [P_1] = 0.63 μM. The initial concentrations of the S-enriched substrate are: [E] = 83.3 μM, [S] = 67.4 μM, [R] = 11.9 μM, [P_1] = 0.67 μM.* ***(C)*** *The initial concentrations are: [E] = 83.3 μM, [S] = 77.1 μM, [R] = 78.2 μM, [P_1] = 4.7 μM.* ***(D)*** *The initial concentrations are: [E] = 50 μM, [S] = 77.2 μM, [R] = 78.1 μM, [P_1] = 4.7 μM.*

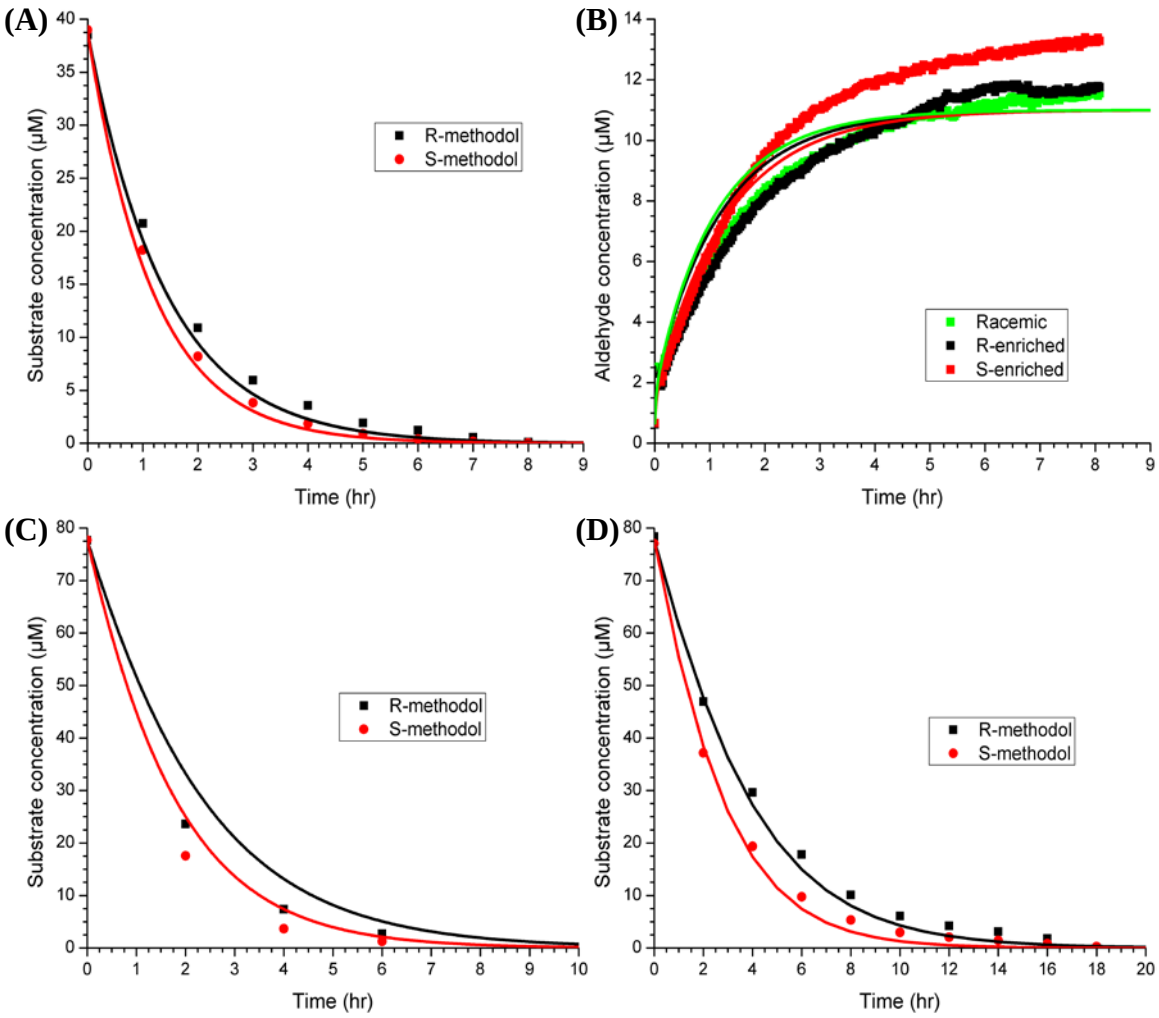

Figure 4-22: Best joint fits with 6 Ac-(Dap)LVFFAL-NH₂ peptides per binding site. *Equation (1) to (3) for (A, C, D) the methodol concentrations from chiral HPLC are used to fit (B) concentration of 6-amino 2-naphthaldehye measured from fluorescence.* ***(A)*** *The initial concentrations are: [E] = 83.3 μM, [S] = 38.7 μM, [R] = 38.8 μM, [P_1] = 2.5 μM.* ***(B)*** *The initial concentrations of the racemic solution are: [E] = 83.3 μM, [S] = 38.7 μM, [R] = 38.8 μM, [P_1] = 2.5 μM. The initial concentrations of the R-enriched substrate are: [E] = 83.3 μM, [S] = 11.9 μM, [R] = 67.5 μM, [P_1] = 0.63 μM. The initial concentrations of the S-enriched substrate are: [E] = 83.3 μM, [S] = 67.4 μM, [R] = 11.9 μM, [P_1] = 0.67 μM.* ***(C)*** *The initial concentrations are: [E] = 83.3 μM, [S] = 77.7 μM, [R] = 77.7 μM, [P_1] = 4.6 μM.* ***(D)*** *The initial concentrations are: [E] = 50 μM, [S] = 77.0 μM, [R] = 78.3 μM, [P_1] = 4.7 μM.*

	Ac-(Orn)LVFFAL	**Ac-(Dab)LVFFAL**	**Ac-(Dap)LVFFAL**
k_{forR}	9.94 (1.62) $\times 10^{-6}$ $sec^{-1}\mu M^{-1}$	7.54 $\times 10^{-6}$ $sec^{-1}\mu M^{-1}$	3.16$\times 10^{-3}$ $sec^{-1}\mu M^{-1}$
k_{forS}	1.17 (0.25) $\times 10^{-4}$ $sec^{-1}\mu M^{-1}$	6.82 $\times 10^{-6}$ $sec^{-1}\mu M^{-1}$	3.01$\times 10^{-3}$ $sec^{-1}\mu M^{-1}$
k_{catR}	6.00 (0.69) $\times 10^{-5}$ sec^{-1}	5.31 $\times 10^{-5}$ sec^{-1}	2.17$\times 10^{-4}$ sec^{-1}
k_{catS}	1.90 (0.35) $\times 10^{-4}$ sec^{-1}	6.22 $\times 10^{-5}$ sec^{-1}	2.53$\times 10^{-4}$ sec^{-1}
k_a	7.47 (0.20) $\times 10^{-5}$ $sec^{-1}\mu M^{-1}$	1.80 $\times 10^{-5}$ $sec^{-1}\mu M^{-1}$	7.07$\times 10^{-4}$ $sec^{-1}\mu M^{-1}$
K_{dR}	1.21 (0.35) $\times 10^{1}$ μM	3.85 $\times 10^{0}$ μM	1.46$\times 10^{0}$ μM
K_{dS}	2.51 (0.86) $\times 10^{1}$ μM	5.89 $\times 10^{0}$ μM	1.05$\times 10^{0}$ μM
K_d	6.49 μM	4.19 μM	2.28 μM

Table 4-1: *Parameters for the best fits of Ac-(Orn)LVFFAL-NH_2, Ac-(Dab)LVFFAL-NH_2 and Ac-(Dap)LVFFAL-NH_2 nanotubes.*

Testing how the change of amine position may affect either the binding step or the chemical step by the Akaike weight (Tables 4-3, 4-4 and 4-5) show that none of the models with additional restrictions has a higher Akaike weight than the non-restricted model. Hence, similar to the Ac-KLVFFAL-NH_2 nanotubes, the Ac-(Orn)LVFFAL-NH_2 nanotubes, Ac-(Dab)LVFFAL-NH_2 and Ac-(Dap)LVFFAL-NH_2 nanotubes still have different binding and chemical activities towards the methodol substrates and aldehyde products.

Restriction	N_d	**SSE**	N_p	**AIC**	**Akaike weight(%)**
No restriction	793	2.83×10^1	7	-2629.40	100.00
$k_{catR} = k_{catS}$	793	1.07×10^2	6	-1573.16	0.00
$K_{dR} = K_{dS}$	793	4.07×10^1	6	-2343.13	0.00

Table 4-2: *AIC analysis of best fits for equations 1 to 3 fitting to the concentrations from HPLC and fluorescence in Figure 4-20 (for Ac-(Orn)LVFFAL-NH₂) with and without restrictions, where N_d is the number of data points, and N_p is the number of parameters.*

Restriction	N_d	**SSE**	N_p	**AIC**	**Akaike weight(%)**
No restriction	793	1.36×10^2	7	-1384.78	92.32
$k_{catR} = k_{catS}$	793	1.37×10^2	6	-1379.57	6.85
$K_{dR} = K_{dS}$	793	1.38×10^2	6	-1375.36	0.83

Table 4-3: *AIC analysis of best fits for equation (1) to (3) fitting to the concentrations from HPLC and fluorescence in Figure 4-21 for Ac-(Dab)LVFFAL-NH₂ with and without restrictions, where N_d is the number of data points, and N_p is the number of parameters.*

Restriction	N_d	**SSE**	N_p	**AIC**	**Akaike weight(%)**
No restriction	793	1.33×10^2	7	-1402.36	100
$k_{catR} = k_{catS}$	793	1.40×10^2	6	-1365.42	0.00
$K_{dR} = K_{dS}$	793	2.02×10^2	6	-1074.12	0.00

Table 4-4: *AIC analysis of best fits for equation (1) to (3) fitting to the concentrations from HPLC and fluorescence in Figure 4-22 for Ac-(Dap)LVFFAL-NH₂ with and without restrictions, where N_d is the number of data points, and N_p is the number of parameters.*

The results so far showcase that apart from the position of the primary amine, the hydrophobicity of the nanotubes binding groove is also important for substrate binding.

The next section describes the effect of changing the hydrophobicity of the grooves on peptide assembly and catalysis. Increasing the hydrophobicity of the grooves might be good at increasing substrate binding but might increase product binding as well leading to product inhibition. Also decreasing the hydrophobicity might have the opposite effect, decrease both substrate and product binding.

Manipulating the Hydrophobic Groove

Peptides were designed to replace the leucine residues in the hydrophobic binding grooves on the tube surface with other hydrophobic amino acids:

1. L17L22 to Alanine: Ac-KLVFFAL-NH_2 was mutated to Ac-KAVFFAA-NH_2 and the synthesized peptide assembled at 40% MeCN/H_2O at pH 2 and pH 7 for 1 month. By TEM, Ac-KAVFFAA-NH_2 assemble into particles at pH 2 and remain as particles even after several months (Figure 4-23A) while at pH 7, the peptide assembles into a mixture of particles and fibers (Figure 4-23B).

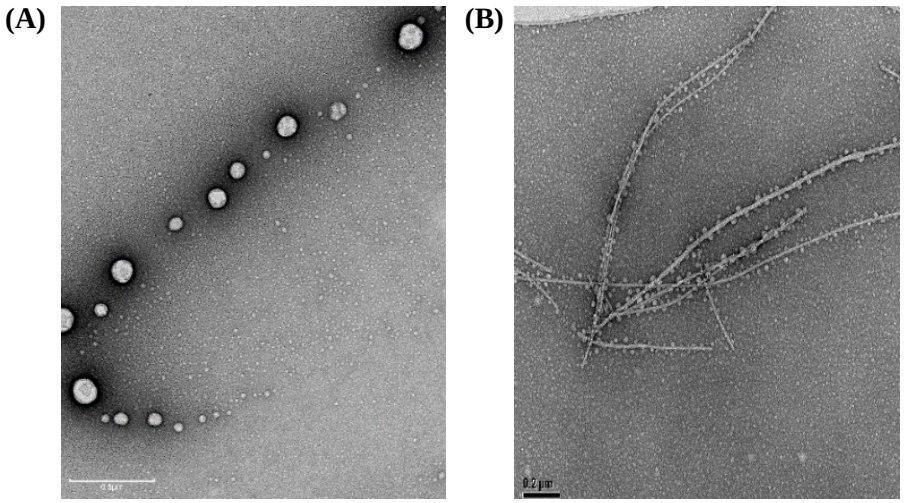

Figure 4-23: *TEM micrographs of Ac-KAVFFAA-NH_2 at (A) pH 2 and (B) pH 7. Scale bar is 200 nm.*

CD spectrum of the pH 2 assemblies show a double minimum at ~200 nm and 230 nm and a maximum at ~220 nm while the pH 7 assemblies display a maximum at ~196 nm and a double minimum at 204 nm and 230 nm. The CD spectra are most likely due to a mixture of conformations (random coils and β-sheets) in the samples.

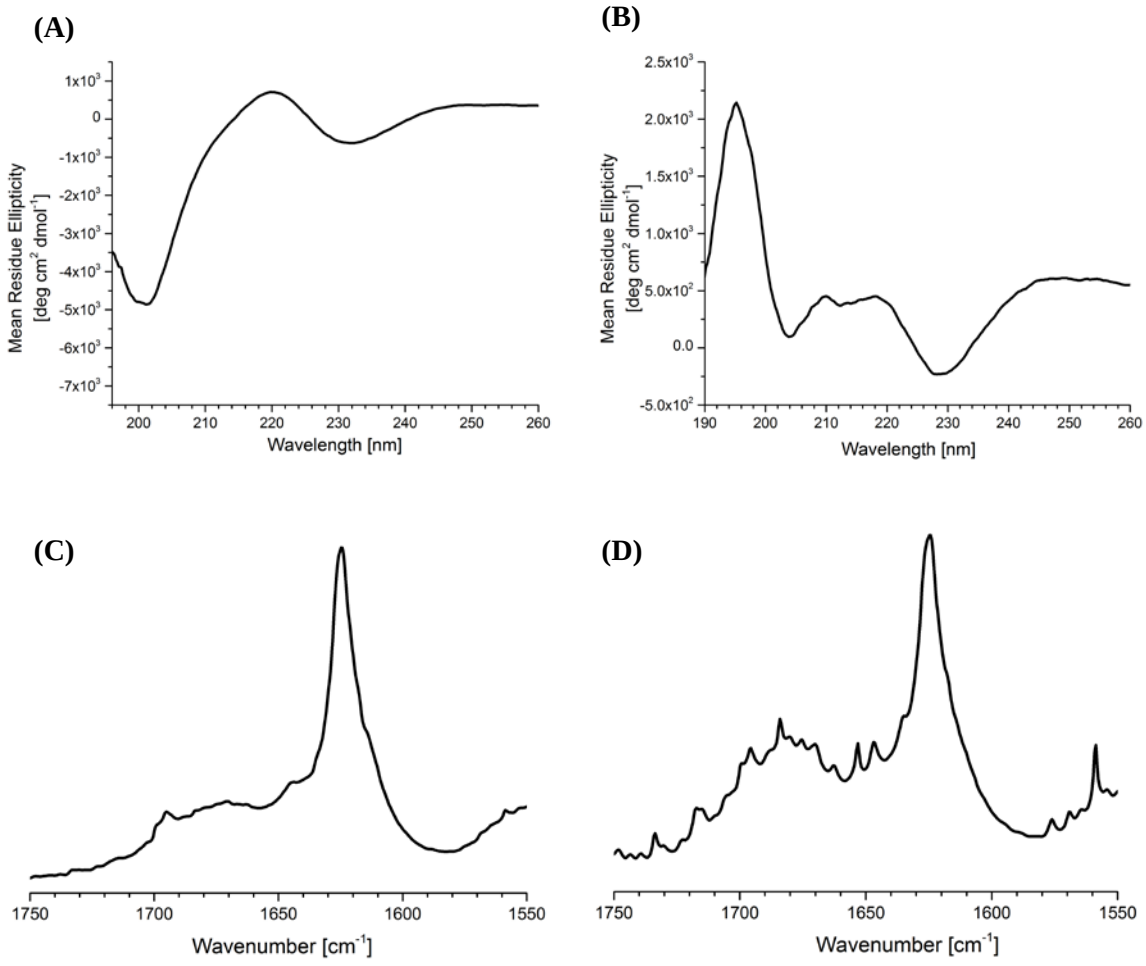

Figure 4-24: *CD spectrum of Ac-KAVFFAA-NH_2 at (A) pH 2 (B) pH 7 and FT-IR of Ac-KAVFFAA-NH_2 (C) at pH 2 with an anti-parallel ß-strand orientation. (D) at pH 7*

FT-IR analysis show an intense amide I band at 1625 cm^{-1} for both the pH 2 and pH 7 assemblies suggesting that the assemblies are mainly composed of β-sheets. At pH 2, the peak at 1693 cm^{-1} is distinct for an antiparallel β-strand arrangement but the assemblies at pH 7 had several small peaks between 1640 and 1750 cm^{-1} including at 1693 cm^{-1} likely due to the non-homogeneity of the sample. Formation of antiparallel β-strand arrangement is more favored to maintain the V-A cross-strand pairing as discussed in Chapter 1. Because Ac-KAVFFAA-NH_2 did not assemble with obvious grooves, it was not further considered.

2. L17L22 to Isoleucine: Ac-KLVFFAL-NH_2 was mutated to Ac-KIVFFAI-NH_2 and incubated at pH 2 and pH 7 into fibers of different morphologies (Figure 4-25A and B). At pH 2, the assemblies are mostly long fiber dimers while at pH 7, they are mixtures of short fiber dimers and twisted fibers. It is interesting that only a slight difference between leucine and isoleucine could have such a dramatic effect on the peptide assembly morphology. As shown in Figure 4-25C, the CD spectrum of Ac-KIVFFAI-NH_2 display a maximum at ~200 nm and a negative ellipticity at ~235 nm, significantly shifted relative to the 225 nm minimum observed for Ac-KLVFFAL-NH_2. The FT-IR spectra show a strong amide I band at ~1625 cm^{-1} and a weak band at ~1673 cm^{-1} (Figure 4-25D) while the 1693 cm^{-1} band is not observed suggesting that the β-strands might be arranged parallel. X-ray diffraction of Ac-KIVFFAI-NH_2 shows a hydrogen bonding distance at 4.7Å and laminate distance at 9.7Å supporting the cross-β structure. Hence, the isoleucine side chain may be playing a critical role in the self-assembly and further structural investigation by ss-NMR might be needed to solve the structure.

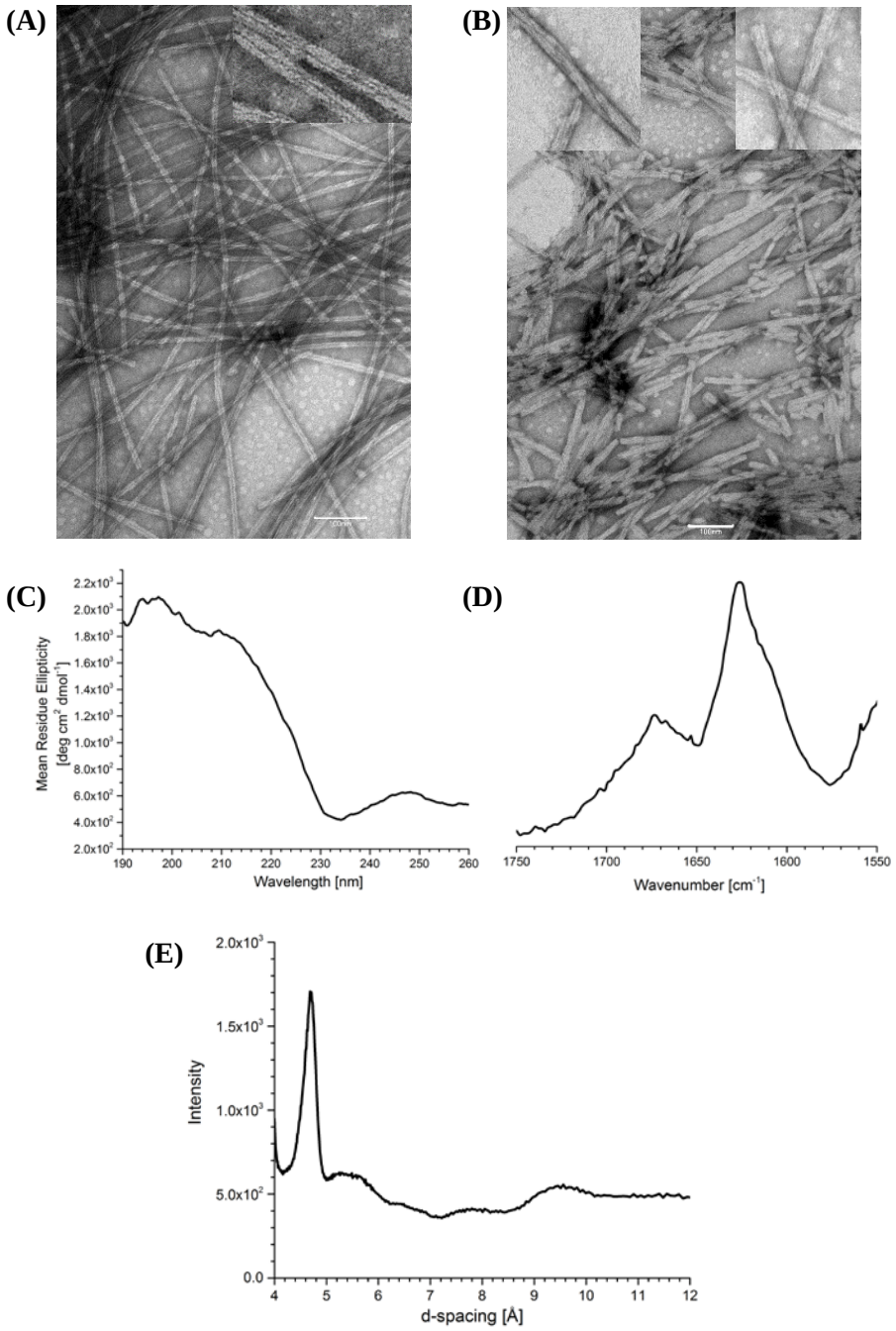

Figure 4-25: *TEM micrographs of Ac-KIVFFAI-NH_2 at (A) pH 2 and (B) pH 7. Scale bar is 100 nm. (C) CD spectrum of mature Ac-KIVFFAI-NH_2 showing a negative ellipticity at ~235 nm and a positive ellipticity at 195 nm with a shoulder peak at 210 nm. (D) IR of Ac-KIVFFAI-NH_2 with a parallel ß-strand orientation. (E) X-ray diffraction of Ac-KIVFFAI-NH_2 showing hydrogen bonding distance of 4.7Å and laminate distance of 9.7Å.*

3. L17L22 to Valine: Ac-KLVFFAL-NH_2 was mutated to Ac-KVVFFAV-NH_2 and assembled at pH 2 and pH 7 to mixed nanotubes and ribbons. As shown in Figure 4-26, the assemblies at pH 2 are largely nanotubes while the pH 7 assemblies are predominantly ribbons with a few nanotubes and fibers.

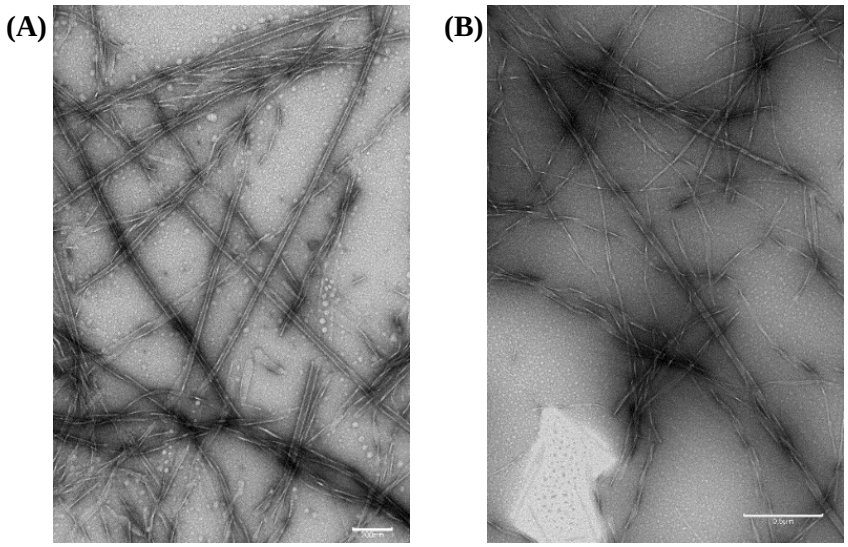

Figure 4-26: *TEM micrographs of Ac-KVVFFAV-NH_2 at (A) pH 2 and (B) pH 7. Scale bar is 100 nm.*

The CD spectrum of Ac-KVVFFAV-NH_2 assemblies display the classic β-sheet signature with a maximum at ~195 nm and 200 nm and a negative ellipticity at ~208 nm and 220 nm at pH 2 and pH 7 respectively. The FT-IR spectra show a strong amide I band at ~1625 cm^{-1} and a weak band at ~1677 cm^{-1} but the 1693 cm^{-1} peak is not observed. X-ray diffraction of Ac-KVVFFAV-NH_2 shows a hydrogen bonding distance at 4.7Å and laminate distance at ~11.5Å providing evidence for the cross-β structure. It is possible that the β-strands are shifted out of register so that the V22 cross-strand pair with A21 such that the V-A cross-strand pairing will still direct the assembly.

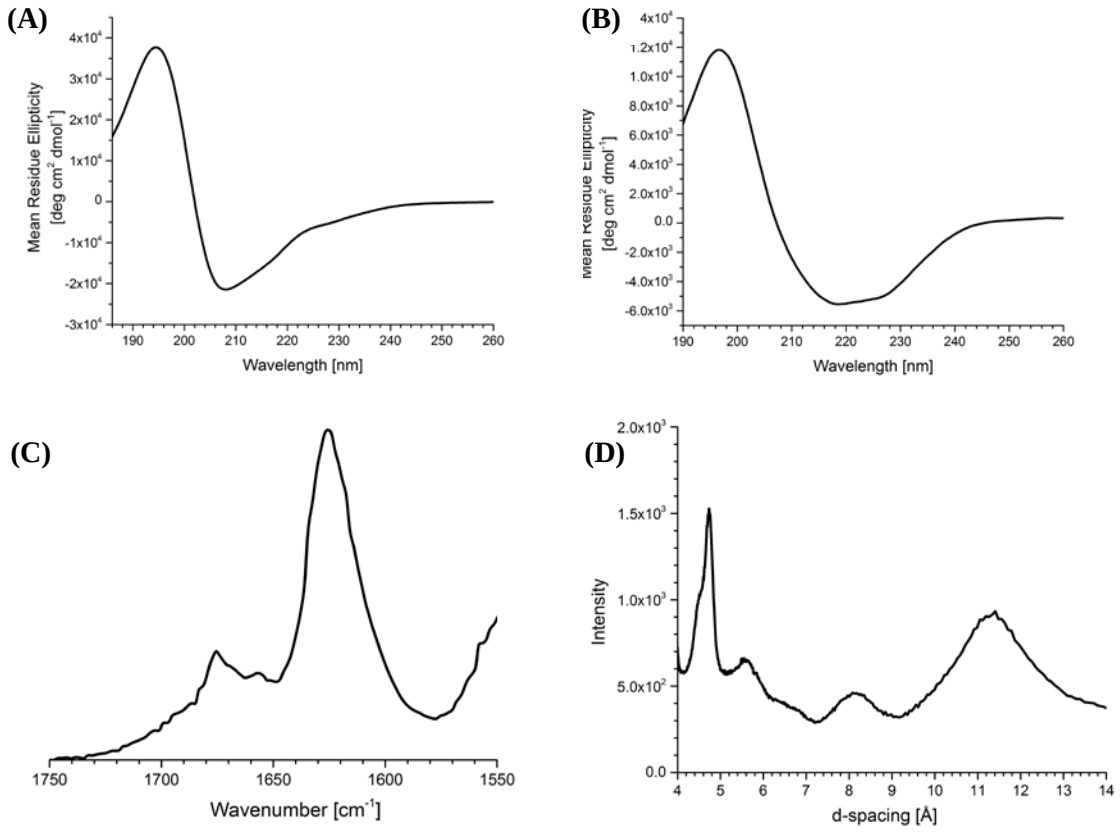

Figure 4-27: Structural characterization of Ac-KVVFFAV-NH₂ *(A) CD spectrum at pH 2 showing a negative ellipticity at ~208 nm and a positive ellipticity at 195 nm. (B) CD spectrum at pH 7 showing a negative ellipticity at ~220 nm and a positive ellipticity at ~200 nm. (C) IR of spectra indicative of a parallel ß-strand orientation. (D) X-ray diffraction showing hydrogen bonding distance of 4.7Å and laminate distance of ~11.5Å.*

4. L17 to Valine: Ac-KLVFFAL-NH_2 was mutated to Ac-KVVFFAL-NH_2 to explore how mixing hydrophobic amino acids in the binding groove will affect peptide assembly and catalysis. As shown in Figure 4-28A, the peptide assembles into fiber dimers at both pH 2 and 7. The CD spectrum display a maximum at ~195 nm and a minimum at ~215 nm (Figure 4-28B) typical of β-sheet secondary structure, and FT-IR spectra display a strong amide I absorption at ~1625 cm^{-1} and a weak band at ~1673 cm^{-1}. X-ray

diffraction confirm an amyloid cross-β structure with shows a hydrogen bonding distance at 4.7Å and laminate distance at 10.2Å (Figure 4-28D). The data suggest that V-A cross-strand pairing does not play a role in the peptide assembly.

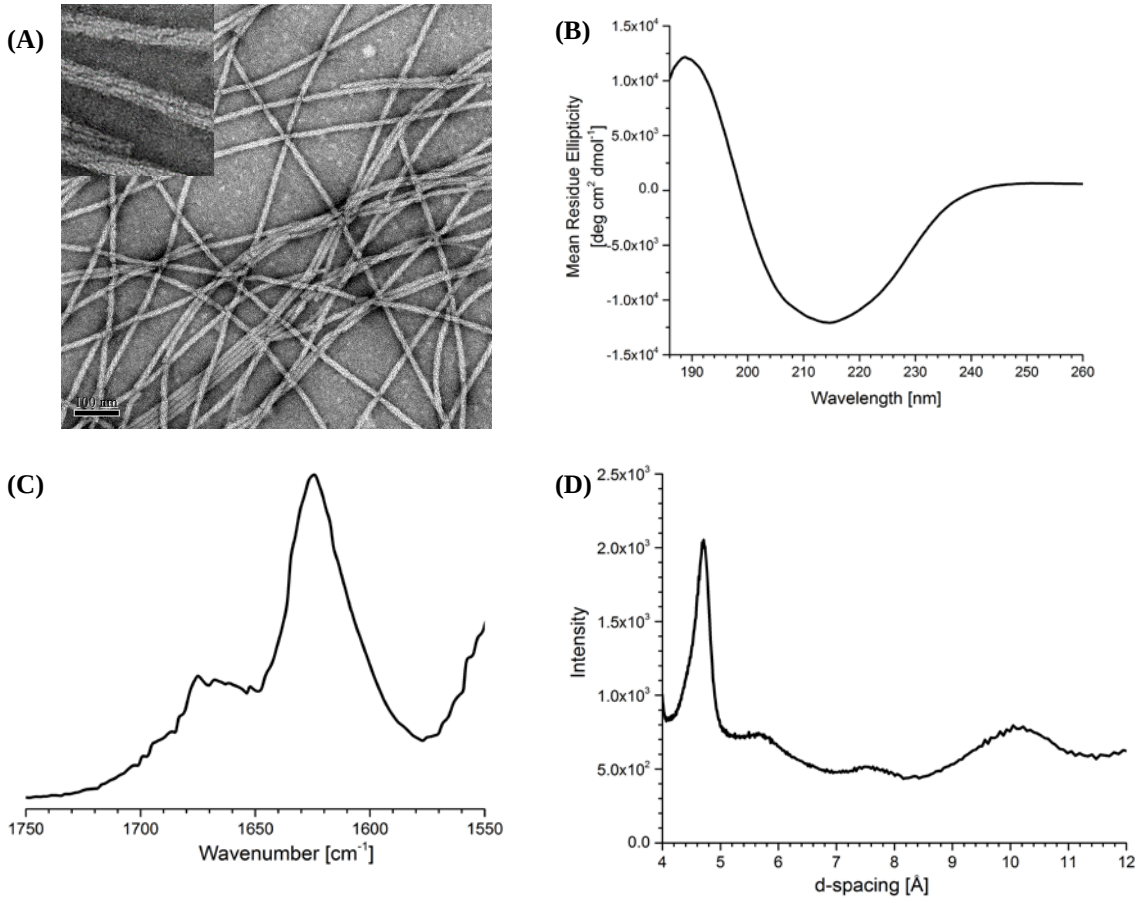

Figure 4-28: Structural characterization of Ac-KVVFFAL-NH₂ *(A) TEM micrograph of fiber dimers, scale bar is 100 nm (B) CD spectrum showing a negative ellipticity at ~215 nm and a positive ellipticity at ~190 nm. (C) IR of spectra indicative of a parallel ß-strand orientation. (D) X-ray diffraction showing hydrogen bonding distance of 4.7Å and laminate distance of ~10.2Å.*

5. L17 to terL: As shown in Figure 4-29, Ac-K(terL)VFFAL-NH_2 appear to form fiber trimers (three individual fiber bundled together) at both pH 2 and 7. The CD spectrum display a characteristic β-sheet signature with a positive and negative ellipticity at ~202 nm and ~218 nm respectively. The IR spectrum provide evidence for antiparallel β-sheet arrangements with an intense amide I absorption at ~1625 cm^{-1} and a weaker one at ~1694 cm^{-1} (Figure 4-29C). X-ray diffraction have d-spacings at 4.7Å and 10.4Å for hydrogen bonding distance and laminate distance respectively.

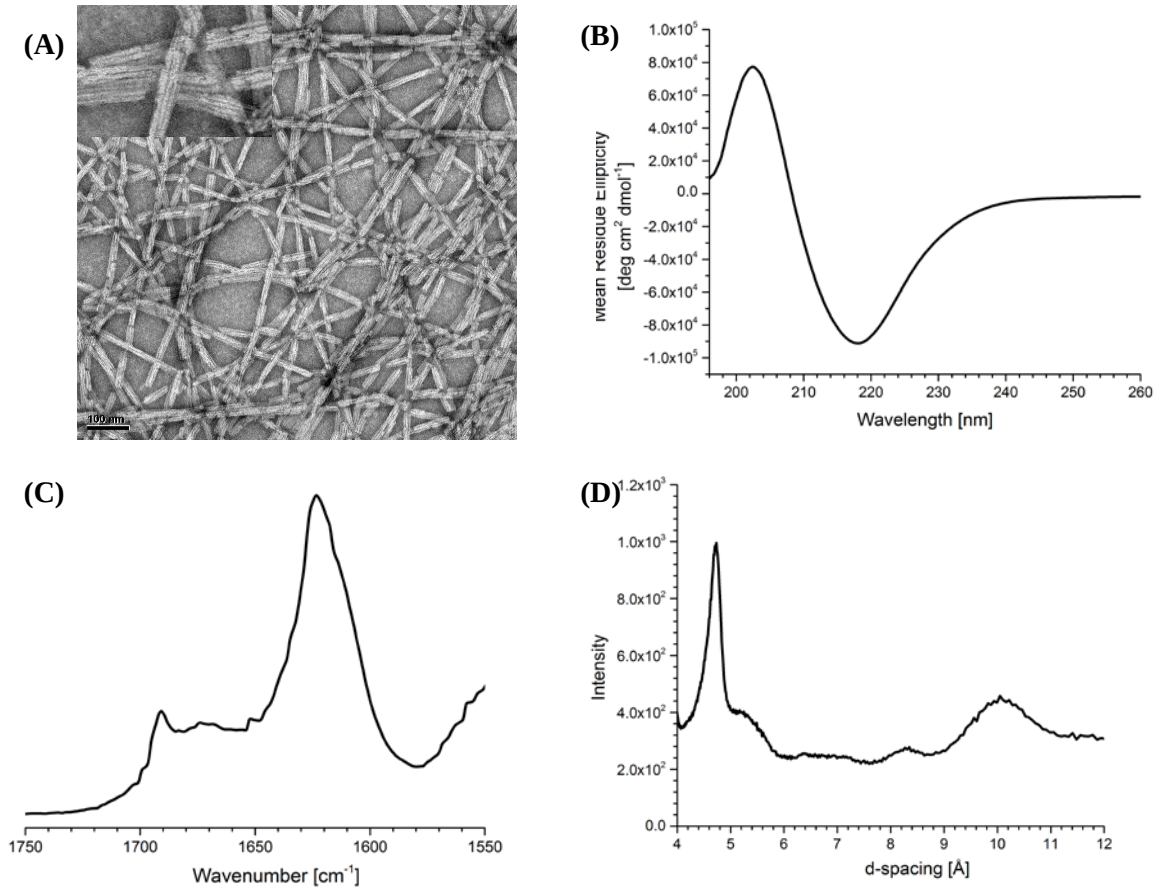

Figure 4-29: Structural characterization of Ac-K(terL)VFFAL-NH₂ *(A) TEM micrograph of fiber trimers (B) CD spectrum showing a negative ellipticity at ~215 nm and a positive ellipticity at ~190 nm. (C) IR of spectra indicates an anti-parallel ß-strand orientation. (D) X-ray diffraction showing hydrogen bonding distance of 4.7Å and laminate distance of ~10.4Å.*

Ac-KLVFFAL-NH₂ to Ac-KVLFFAV-NH₂ Substitution: Ac-KVLFFAV-NH_2 assemble into sheets at pH 2 and bundled fibers at pH 7. The CD spectra display a characteristic β-sheet signature with a maximum at ~195 nm and a negative ellipticity at ~220 nm for the sheets while the fibers have a negative ellipticity at ~225 nm. The IR spectra of both pH 2 and pH 7 assemblies have a strong amide I band at ~1625 cm^{-1} and a band at ~1694 cm^{-1} suggesting antiparallel β-sheets structure but the pH 7 assemblies have an extra band at 1677 cm^{-1}. V17-A21 cross-strand pairing is likely responsible for the β-strand orientation to produce in-register peptides. X-ray diffraction shows a hydrogen bonding distance at 4.7Å and laminate distance at 10.4Å confirming a cross-β structure.

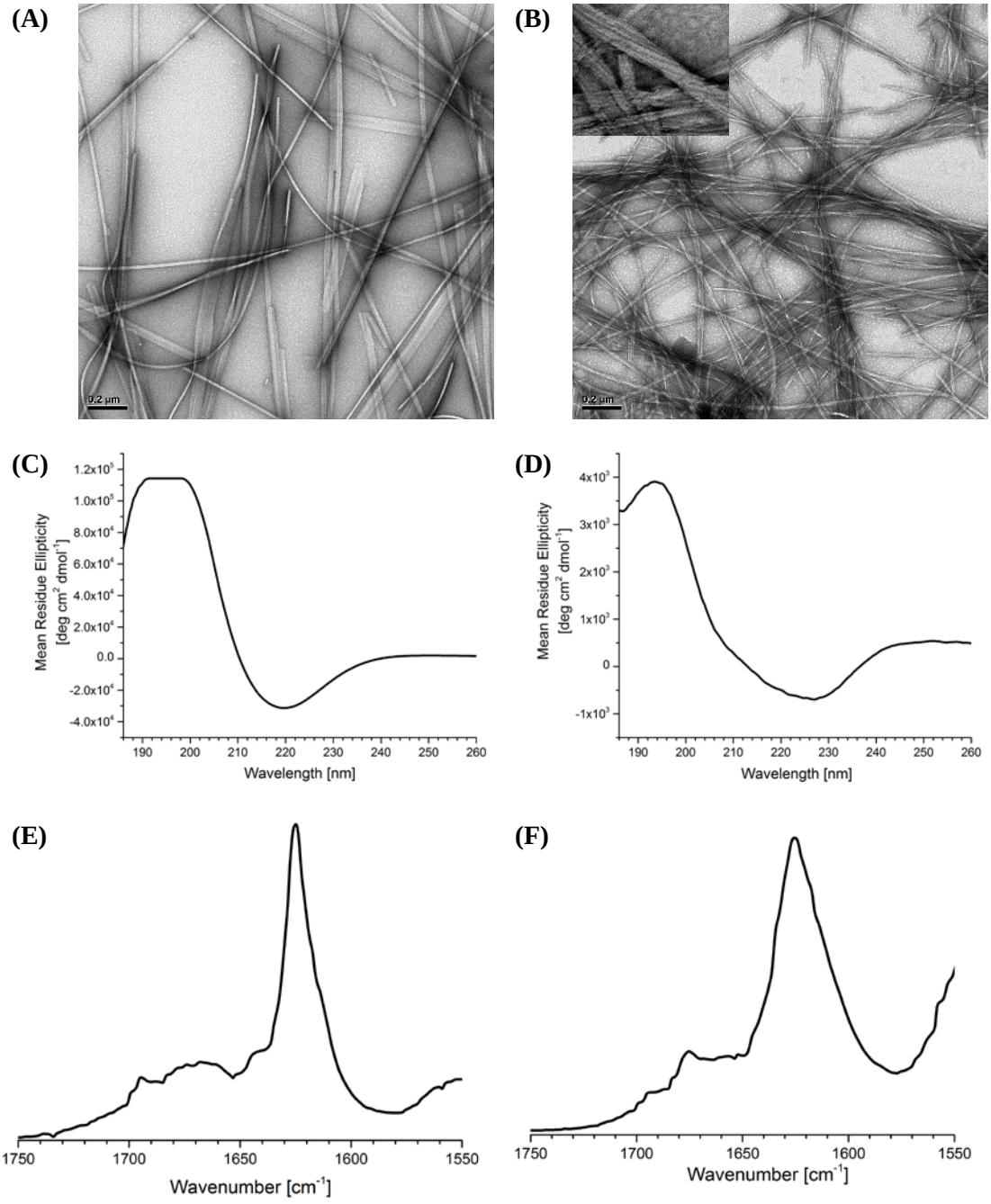

Figure 4-30: Structural characterization of Ac-KVLFFAV-NH₂ *(A) TEM micrograph of sheets assembled at pH 2 (B) TEM micrograph of bundled fibers assembled at pH 7 (C) CD spectrum at pH 2 showing a negative ellipticity at ~220 nm and a positive ellipticity at ~195 nm. (D) CD spectrum at pH 7 showing a negative ellipticity at ~225 nm and a positive ellipticity at ~195 nm. (E) FT-IR spectrum indicates an anti-parallel ß-strand orientation at pH 2. (F) FT-IR spectrum suggests a parallel ß-strand orientation at pH 7*

Ac-KLVFFAL-NH$_2$ to Ac-KLVFFAV-NH$_2$ Substitution: By TEM, Ac-KLVFFAV-NH$_2$ assembles into nanotubes independent of pH, with average tube widths of 350 nm about 8 times the size of Ac-KLVFFAL-NH$_2$ nanotubes. The CD spectrum is almost a mirror image of the spectrum for Ac-KLVFFAL-NH$_2$ with a minimum at ~200 nm and a maximum at ~ 220 nm (Figure 4-31B). This CD result suggests that the nanotubes formed by Ac-KLVFFAV-NH$_2$ might be structurally different from those formed by Ac-KLVFFAL-NH$_2$. As shown in Figure 4-31C, the FT-IR spectrum display an intense amide I stretch at 1625 cm^{-1} and the band at 1693 cm^{-1} consistent with an antiparallel β-sheet structure. Further evaluation of the β-sheets with X-ray diffraction show that the nanotubes maintain the cross-β assembly of amyloid with d-spacing of 4.7Å for hydrogen bonding distances and a broad d-spacing at ~11Å representing the laminate distance.

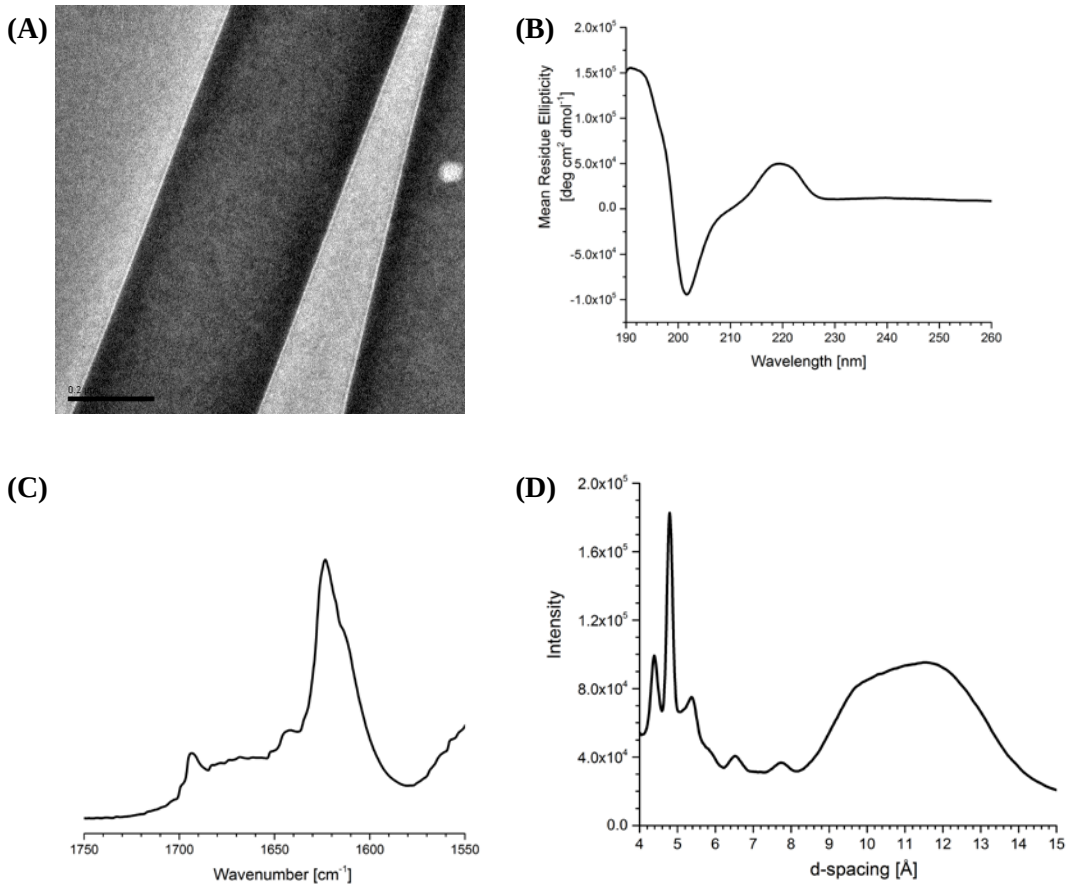

Figure 4-31: Structural characterization of Ac-KLVFFAV-NH₂ *(A) TEM micrograph of nanotubes assembled at pH. Scale bar is 200 nm (B) CD spectrum show a negative ellipticity at ~202 nm and a positive ellipticity at ~220 nm. (C) FT-IR spectrum indicates an anti-parallel ß-strand orientation (D) X-ray diffraction display showing hydrogen bonding distance of 4.7Å and a very broad peak at ~11Å representing the laminate distance.*

To test how Ac-KLVFFAV-NH_2 responds to chiral substitutions, all D-Ac-KLVFFAV-NH_2, was prepared as well as heterochiral Ac-^{D}KLVFFAV-NH_2. Like Ac-KLVFFAL-NH_2, all D Ac-KLVFFAV-NH_2 assembles into homogenous nanotubes of similar size (Figure 4-32B) as the all L Ac-KLVFFAV-NH_2. The CD spectrum is also a mirror image (Figure 4-32D) of the CD spectra of the all L-Ac-KLVFFAV-NH_2.

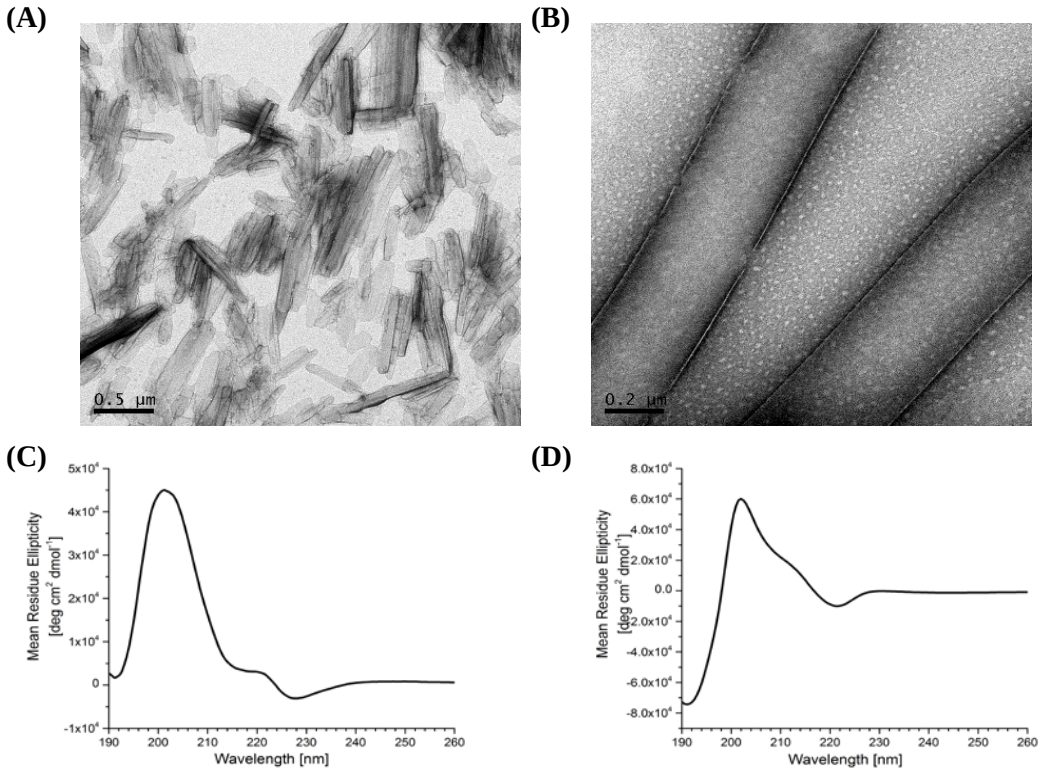

Figure 4-32: Top. *Uranyl acetate negatively stained TEM images of the (A) heterochiral Ac-^{D}KLVFFAV-NH_2 (B) homochiral all D Ac-KLVFFAV-NH_2.* ***Bottom.*** *CD spectrum of mature (C) heterochiral Ac-^{D}KLVFFAV-NH_2 nanotubes and (D) all D Ac-KLVFFAV-NH_2 nanotubes. Both spectra showed a positive ellipticity at 200 nm and a negative ellipticity at ~225 nm with a shoulder at ~218 nm. The spectra resemble the mirror image of the all L Ac-KLVFFAV-NH_2 nanotube CD spectrum.*

The heterochiral Ac-^{D}KLVFFAV-NH_2, did not assemble into nanotubes as seen in the heterochiral Ac-^{D}KLVFFAL-NH_2. The peptide assembles into sheets of various lengths and widths (Figure 4-32A). Another difference between heterochiral Ac-^{D}KLVFFAL-NH_2 assemblies and heterochiral Ac-^{D}KLVFFAL-NH_2 assemblies is that the CD spectrum is a mirror image of the all L-Ac-KLVFFAV-NH_2 (Figure 4-32C). These results further support the structural difference between the Ac-KLVFFAL-NH_2 and Ac-KLVFFAV-NH_2 assemblies.

Retro-aldol Activities of L17 and L22 Congeners

Most of the congener peptides formed particles, fibers and sheets, but Ac-KLVFFAV-NH_2 (large diameter tubes) and Ac-KVVFFAV-NH_2 (mixture of tubes and ribbons) assembled as structures that appear capable of forming grooves for catalysis. The evidence in Chapter 3 suggested that these grooves are critical for retro-aldol activity. Indeed, Ac-KterLVFFAL-NH_2 assemblies with 80 μM (±)-methodol did not show any activity as expected. Ac-KVVFFAV-NH_2 ribbons/nanotubes showed some activity but not as catalytic as the Ac-KLVFFAL-NH_2 (Figure 4-33). Since the Ac-KVVFFAV-NH_2 contained a mixture of nanotubes and ribbons, it is difficult to conclude that replacing the L17 and L22 with valine did not improve activity because there is no evidence that the ribbons are catalytic or not. Interestingly, Ac-KLVFFAV-NH_2 nanotubes which contain a mixture of leucine and valine in the binding groove show increased activity to about 3 fold relative to Ac-KLVFFAL-NH_2 nanotubes (Figure 4-33). Measurement of the product binding to Ac-KLVFFAV-NH_2 nanotubes reveal a decrease in binding affinity of the product to the Ac-KLVFFAV-NH_2 nanotubes with a K_d of 25.6 μM (Table 4-5) that is almost 5 times the K_d of Ac-KLVFFAL-NH_2 nanotubes. It is possible that improved catalytic activity observed with Ac-KLVFFAV-NH_2 nanotubes could be due to decreased product inhibition. As shown in Figure 4-34, enantioselectivity measurements of the Ac-KLVFFAV-NH_2 nanotubes display a preference for S-methodol, similar to Ac-KLVFFAL-NH_2 and Ac-(Orn)LVFFAL-NH_2.

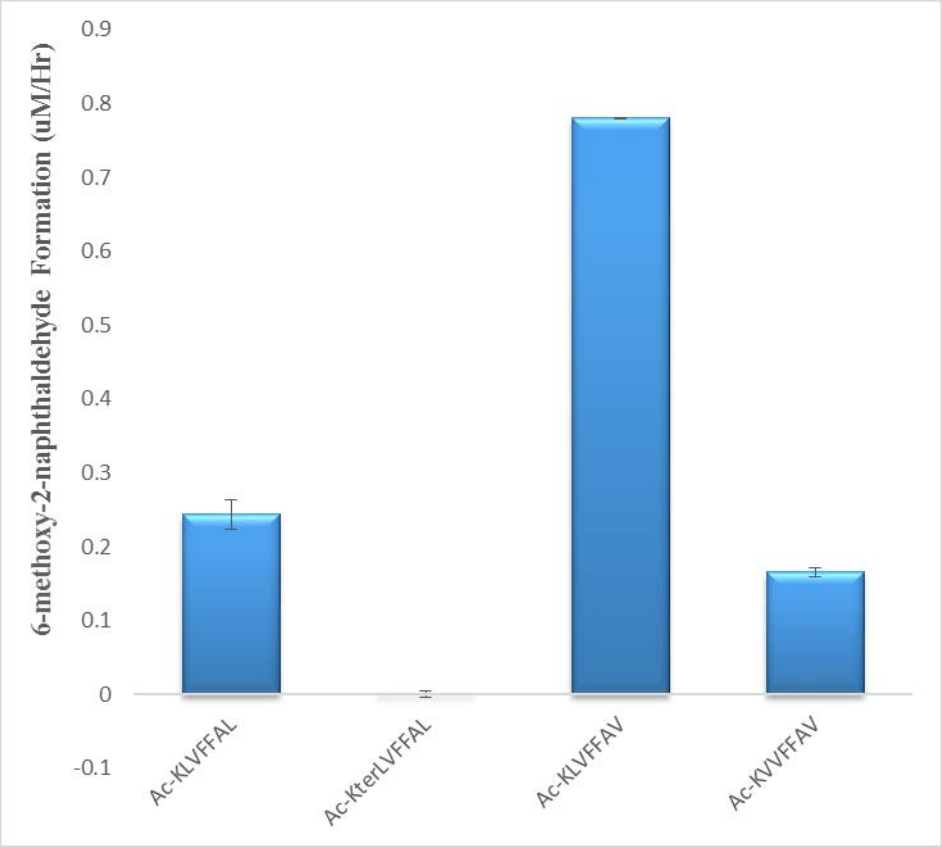

Figure 4-33: *Initial rate of production of 6-methoxy-2-naphthaldehyde by the indicated peptide at peptide concentration of 500 µM and 80 µM (±)-methodol concentration.*

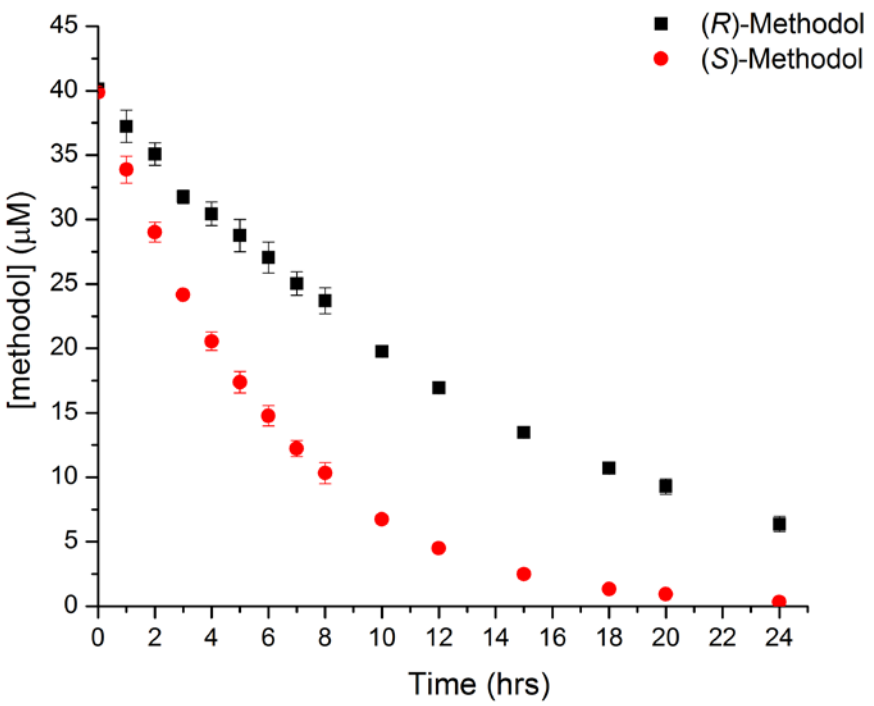

Figure 4-34: *Monitoring of (±)-Methodol (80 μM) consumption in the presence of 500 μM Ac-KLVFFAV-NH_2 nanotubes over 24 hours shows preference for S-methodol.*

CD suggests that the structure of Ac-KLVFFAV-NH_2 nanotubes might be different. The 6-methoxy-2-naphthaldehyde product also binds less tightly to the Ac-KLVFFAV-NH_2 nanotubes suggesting the binding site might be different. Therefore, numbers of peptides per binding sites (n) was determined for Ac-KLVFFAV-NH_2 nanotubes as described in chapter 3. The result suggests that the number of peptides per binding sites (n) is equal to 4 because the normalized SSE for the Ac-KLVFFAV-NH_2 have the lowest value at 4 (Figure 4-35). This result further supports the difference in the structure of Ac-KLVFFAV-NH_2 nanotubes relative to Ac-KLVFFAL-NH_2 nanotubes.

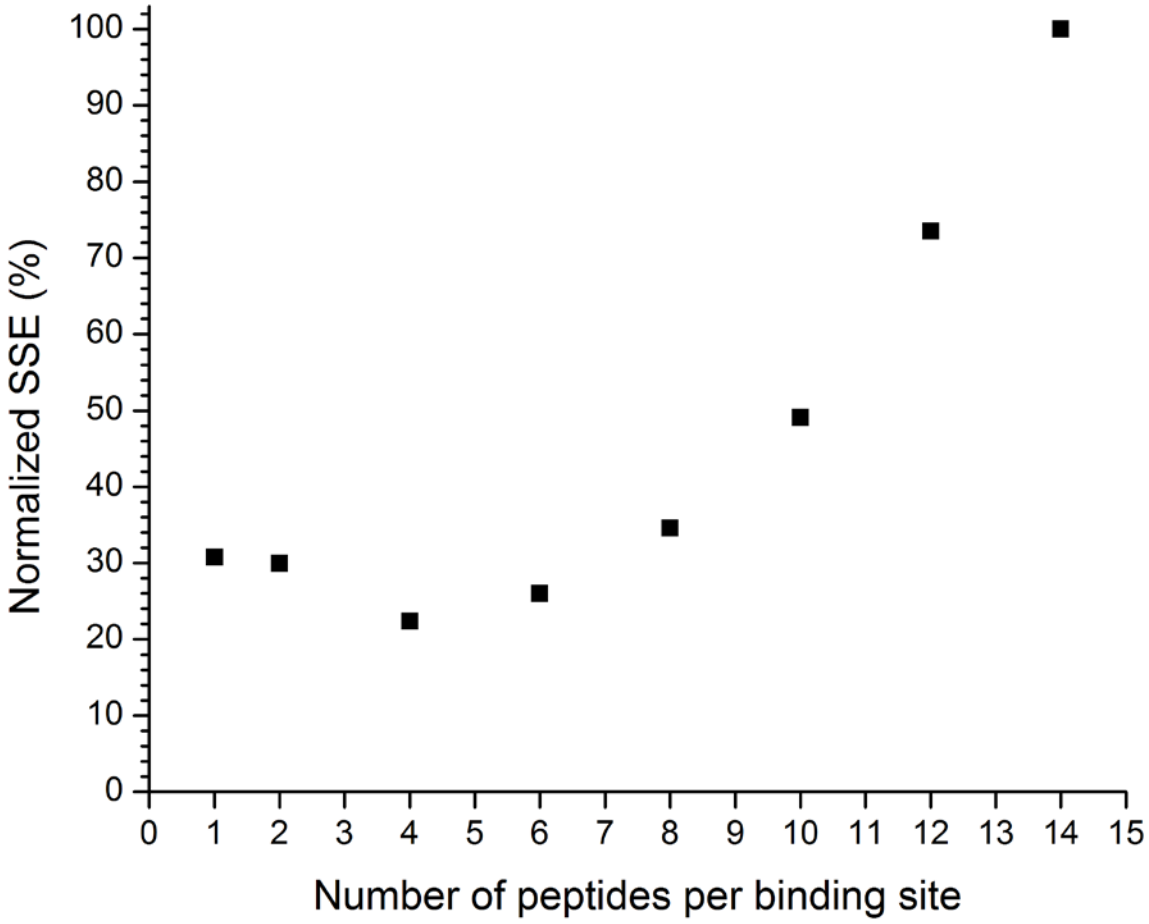

Figure 4-35: *Normalized sum of square error (SSE) for R- and S-methodol consumption on Ac-K LVFFAV-NH_2 nanotubes.*

Using the same number of peptides per binding site (n = 4), the joint fits for the Ac-KLVFFAV-NH_2 shows satisfying consistency with the experimental data (Figure 4-35). By this analysis, Ac-KLVFFAV-NH_2 nanotubes show a higher binding affinity for R-methodol but prefers S-methodol, similar to other catalytic nanotubes.

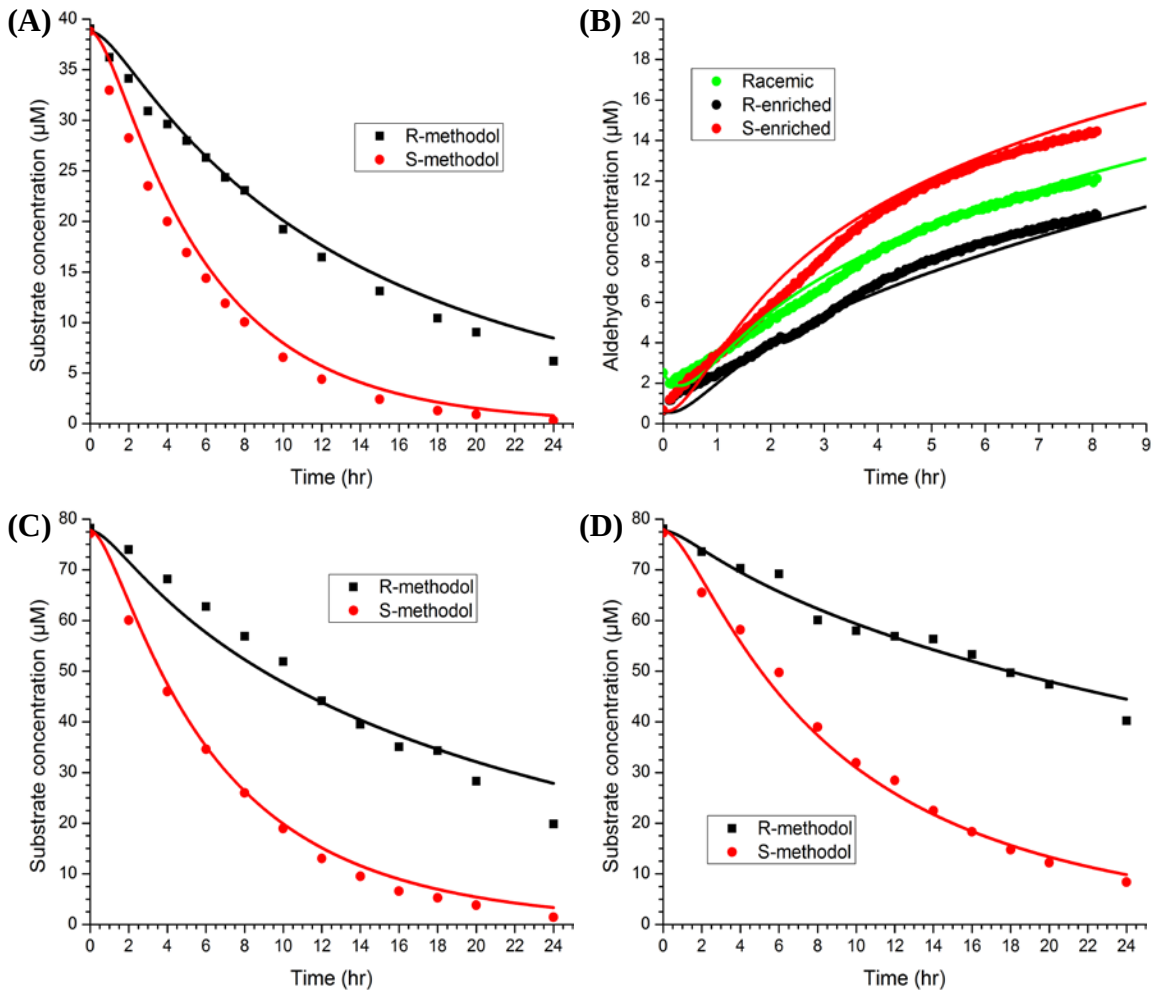

Figure 4-36: Best joint fits with 4 Ac-KLVFFAV-NH₂ peptides per binding site. *Equation (1) to (3) for (A, C, D) the methodol concentrations from chiral HPLC are used to fit (B) concentration of 6-amino 2-naphthaldehye measured from fluorescence.* ***(A)*** *The initial concentrations are: [E] =125 μM, [S] = 38.8 μM, [R] = 39.0 μM, [P_1] = 2.5 μM.* ***(B)*** *The initial concentrations of the racemic solution are: [E] = 125 μM, [S] = 38.8 μM, [R] = 39.0 μM, [P_1] = 2.5 μM. The initial concentrations of the R-enriched substrate are: [E] = 125 μM, [S] = 11.9 μM, [R] = 67.5 μM, [P_1] = 0.63 μM. The initial concentrations of the S-enriched substrate are: [E] = 125 μM, [S] = 67.4 μM, [R] = 11.9 μM, [P_1] = 0.67 μM.* ***(C)*** *The initial concentrations are: [E] = 125 μM, [S] = 77.1 μM, [R] = 78.2 μM, [P_1] = 4.7 μM.* ***(D)*** *The initial concentrations are: [E] = 75 μM, [S] = 77.2 μM, [R] = 78.1 μM, [P_1] = 4.7 μM.*

	Ac-KLVFFAV-NH_2 (n = 4)
k_{forR}	2.26×10^{-7} $sec^{-1}\mu M^{-1}$
k_{forS}	2.04×10^{-6} $sec^{-1}\mu M^{-1}$
k_{catR}	2.59×10^{-4} sec^{-1}
k_{catS}	7.20×10^{-5} sec^{-1}
k_a	4.54×10^{-6} $sec^{-1}\mu M^{-1}$
K_{dR}	2.19×10^{0} μM
K_{dS}	3.16×10^{1} μM
K_d	25.6 μM

Table 4-5: *Parameters for the best fits of Ac-KLVFFAV-NH_2 nanotubes.*

Conclusion

In this chapter, I have synthesized and characterized peptide congeners of Ac-KLVFFAL-NH_2 peptide and found that the assembly is sequence dependent. Shortening of the N-terminal Lys side chain with Orn, Dab, Dap and β-Ala did not impart the self-assembly behavior of the peptides. However, when the lysine was made part of the groove, the assembly behavior changed. While K16LL22K assembled into homogenous nanotubes at pH 2, K16LL17K assemble into thin ribbons. Replacing Lys with Orn, Dab, Dap and β-ala accelerate the retro-aldol reaction of methodol with ~ 16 folds increase observed with K16Dap nanotubes relative K16 nanotubes. The more catalytic the nanotubes are, the more pronounced the product inhibition. Both K16Orn and K16β-Ala show preference for S-methodol but K16Dab and K16Dap did not show any enantioselectivity towards methodol. Overall, subtle difference in the amine shielding can result in dramatic differences in the catalytic activity and enantioselectivity.

Natural protein folding is driven by the hydrophobic collapse, which results in an aggregation of hydrophobic residues at the protein core, while hydrophilic and charged residues are found near the surface [8-11]. For the peptide assemblies, hydrophobic effects is one of the main driving force for self-assembly. In the peptide nanotubes catalyzed imine condensation reactions presented in Chapter 2 and the retro-aldol catalysis in Chapter 3, it is clear that the hydrophobic effect was also the driving force for the approach of the substrates to the catalytic center. Hydrophobicity of the surface binding grooves was varied by replacing L17 and L22 with other hydrophobic amino acids. The variations resulted into morphology change ranging from particles to fibers to ribbons and larger sized nanotubes. Ac-KLVFFAV-NH_2 peptide nanotubes show increased catalytic activity while maintaining enantioselectivity relative to Ac-KLVFFAL-NH_2 peptide nanotubes. This is attributed to the structural difference between the Ac-KLVFFAV-NH_2 peptide nanotubes and the Ac-KLVFFAL-NH_2 peptide nanotubes. With this finding, further peptide design could include shortening the lysine side chain and at the same changing the hydrophobicity of the binding groove. Such peptide assemblies like Ac-(Orn)LVFFAV-NH_2 or Ac-(Dap)LVFFAV-NH_2 might be a way of making better catalytic nanotubes.

Methods

FMOC Protection of Isotopically Enriched Amino Acids

Isotopically labeled amino acids were obtained from Cambridge Isotope Laboratories. Prior to use in solid-phase peptide synthesis, isotopically enriched amino acids (Ala, Val, Leu, Phe, Ile, or Gly) were FMOC protected as described previously

[12]. Briefly, 2.25 mmol of isotopically labeled amino acid in 10% (w/v) Na_2CO_3 was added dropwise to a solution of 2.5 mmol Fmoc-O-succinimide in 5 mL of dioxane. The reaction was continuously stirred for 24 hours at room temperature, and reaction completion was monitored by TLC using 10:1 toluene:acetic acid as an eluting solvent (ninhydrin staining was used to monitor amino acid that was not FMOC protected). If reaction was incomplete an additional 0.88 mmol of Fmoc-O-succinimide in 2 mL dioxane was added and allowed to react for an additional 24 hours at room temperature.

After reaction completion, the reaction mixture was diluted with 30 mL of water and impurities were extracted 3 times with diethyl ether. The water layer containing FMOC labeled amino acids was titrated to pH 2 using HCl, then the FMOC labeled amino acid was extracted 3 times using ethyl acetate. The ethyl acetate washes were collected and washed twice with 1N HCl, then once with distilled water. Anhydrous $MgSO_4$ was added to dry the ethyl acetate layers for 60 minutes. Filtered ethyl acetate solutions were then rotovaped to remove ethyl acetate and dried in a desiccator overnight [12].

Microwave Assisted Solid-Phase Peptide Synthesis

Peptides were synthesized on a Liberty CEM Microwave Automated Peptide Synthesizer (NC, USA) utilizing a FMOC-Rink Amide MBHA Resin (AnaSpec, CA, USA). All FMOC protected amino acids were purchased from Anaspec, and remaining chemicals from Sigma-Aldrich. Each peptide synthesis was performed at 0.1 mmol using a 30 mL reaction vessel at a scale of 0.1 mmol. FMOC-Rink Amide MBHA Resin was initially swollen using ~7 mL dimethylformamide for 15 minutes. FMOC deprotection

was achieved by addition of 20% piperidine 0.1 M N-Hydroxybenzotriazole (HOBt) in dimethylformamide with microwave power set to maintain temperature between 45-55°C for 180 seconds, followed by 3X flushing with dimethylformamide. Each coupling step was performed using 0.1M FMOC protected amino acid, and activated with 0.1 M 2-(1H-Benzotriazole-1-yl)-1,1,3,3-tetramethyluronium hexafluorophosphate (HBTU), and 0.2M N,N –Diisopropylethylamine (DIEA) in DMF. Coupling temperatures were maintained between 75-82°C by optimizing microwave power for 300 seconds. After coupling, the resin was rinsed with three aliquots of dimethylformamide. At the end of coupling steps, 20% acetic anhydride in dimethylformamide was added to acetylate the N-terminus of the peptides. The capping reaction was allowed to proceed for 3 hours at room temperature. Resin was filtered and washed with dichloromethane and allowed to air dry. Peptides were cleaved from the resin using trifluoroacetic acid/thioanisole/1,2-ethanedithiol/anisole (90:5:3:2, v/v/v/v) at room temperature for 3 hours. The cleaved peptide-TFA solution was filtered, and precipitated by dropwise addition of cold (-20°C) diethyl ether. Precipitated product was centrifuged at 3500 rpm for 10 minutes, and the pellet was subjected to 3 additional rounds of washing with cold diethyl ether. Precipitated product was desiccated overnight.

Dried peptides were dissolved in minimal volume of 40% acetonitrile + 0.1% trifluoroacetic acid and purified by RP-HPLC using a C18-reverse phase column with an acetonitrile-water gradient. Samples eluted from HPLC (10 μL) were mixed with 2,5-dihydroxybenzoic acid (10 μL), and 3x2 μL drops were placed as spots on a MALDI plate and allow to dry in desiccator prior to analysis.

Peptide assembly

Peptides (2.5 mM) were dissolved in 40% CH_3CN/H_2O with 0.1% TFA except for Ac-KLVFFAE-NH_2 and Ac-KLVFFAQ-NH_2 peptides. Ac-KLVFFAQ-NH_2 peptide was dissolved in 20% CH_3CN/H_2O with 0.1% TFA and for fibril assemblies Ac-KLVFFAE-NH_2 peptide was dissolved in 40% CH_3CN/H_2O, solution was slowly titrated by drop-wise addition of 200 mM NaOH until solution became viscous (pH 6 as measured by pH paper). Dissolution was assisted by ~2 minutes of continuous vortex, followed by ~15 minutes of sonication until solution became clear. Peptides were allowed to assemble for approximately 2 weeks at 4 °C until mature as monitored by CD β-sheet signature and homogenous population either tubes or fibers as visualized by TEM. Prior to kinetic analysis, peptide assemblies were centrifuged at 13,800g for 60 minutes and resuspended in distilled water prior to being buffered for reaction.

Circular Dichroism

Samples (18 µl) were placed into a quartz cuvette with a 0.1 mm path length (Starna Cells). Each spectra was obtained by scanning wavelength from 300 nm to 185 nm at a scanning rate of 100 nm/min with a resolution of 0.2 nm using Jasco J-810 spectropolarimeter. For each CD run temperature was controlled at 22°C, unless otherwise stated. Prior to recording the presented final wavelength scan CD at 225 nm was recorded for approximately 15-minute period to ensure sample had stabilized at the CD measurement conditions. Three successive wavelength scans were averaged for each sample. Buffer control spectra were averaged and subtracted from the sample spectra. The ellipticity ($[\theta]_{obs}$ mdeg) was converted to mean residue ellipticity ([θ],

deg·cm^2·dmol^{-1}) with the equation $[\theta]=[\theta]_{obs}/(10\times n\times C\times l)$, in which, n is the number of peptide bonds, C is the concentration (mol/L) and l is the path length of the cell (cm).

Fourier-Transform Infrared Spectroscopy

Sample aliquots (15 µL) were dried as thin films on an ATR diamond cell. The IR spectra were acquired using a Jasco FT-IR 4100 ATR with a diamond crystal at room temperature and averaging 400 scans with 2 cm^{-1} resolution. Background spectra were acquired immediately before each sample and were subtracted from each sample spectrum. Data was imported into OriginPro for graphing and analysis.

Transmission Electron Microscopy

10 µL of 2.5 mM peptide assemblies diluted 1:9 was added to TEM grids (200 mesh copper grids with a thin carbon film support – Electron Microscopy Sciences, Hatfield, PA). Peptide assemblies were allowed to adsorb on the grid for 1 min before excess peptide solution was wicked away with filter paper. 10 µL of freshly prepared 2-wt % uranyl acetate solutions were added to TEM grids and incubated for 1-2 minutes for fibers and 4-5 minutes for nanotubes, before wicking away excess stain and then the grids were placed in a vacuum desiccator overnight or until imaging to remove any residual solvents. All staining solutions were prepared fresh and filtered prior to staining to minimize artifacts. TEM micrographs were recorded with a Hitachi 7500 TEM at magnifications ranging from 2000x to 200,000x with a Tungsten filament at an accelerating voltage of 75 kV. Widths measured from TEM were converted into

diameters by setting 2 x width = the tube circumference and solving for the diameter. The standard deviations of the width measurements were converted into error bars.

References:

1. Giger, L., et al., *Evolution of a designed retro-aldolase leads to complete active site remodeling.* Nat Chem Biol, 2013. **9**(8): p. 494-8.

2. Wang, L., et al., *Structural Analyses of Covalent Enzyme–Substrate Analog Complexes Reveal Strengths and Limitations of De Novo Enzyme Design.* Journal of Molecular Biology, 2012. **415**(3): p. 615-625.

3. Lassila, J.K., D. Baker, and D. Herschlag, *Origins of catalysis by computationally designed retroaldolase enzymes.* Proc Natl Acad Sci U S A, 2010. **107**(11): p. 4937-42.

4. Ishikita, H., *Origin of the pKa shift of the catalytic lysine in acetoacetate decarboxylase.* FEBS Lett, 2010. **584**(15): p. 3464-3468.

5. Petty, S.a. and S.M. Decatur, *Experimental evidence for the reorganization of β-strands within aggregates of the Aβ(16-22) peptide.* Journal of the American Chemical Society, 2005. **127**(39): p. 13488-9.

6. Decatur, S.M., *Elucidation of residue-level structure and dynamics of polypeptides via isotope-edited infrared spectroscopy.* Accounts of chemical research, 2006. **39**(3): p. 169-75.

7. Mehta, A.K., et al., *Facial Symmetry in Protein Self-Assembly.* Journal of the American Chemical Society, 2008. **130**(30): p. 9829-9835.

8. Zhou, R., et al., *Hydrophobic collapse in multidomain protein folding.* Science, 2004. **305**(5690): p. 1605-9.

9. Pratt, L.R. and A. Pohorille, *Hydrophobic effects and modeling of biophysical aqueous solution interfaces.* Chem Rev, 2002. **102**(8): p. 2671-92.

10. Schneider, J.P. and J.W. Kelly, *Templates That Induce .alpha.-Helical, .beta.-Sheet, and Loop Conformations.* Chemical Reviews, 1995. **95**(6): p. 2169-2187.

11. Gerstman, B.S. and P.P. Chapagain, *Self-organization in protein folding and the hydrophobic interaction.* The Journal of Chemical Physics, 2005. **123**(5): p. 054901.

12. Samuel-Landtiser M, et al., *Current Protocol Protein Science*. 2007.

Chapter 5: Peptide Nanotubes as Aldol Catalyst

Introduction

Chapter 2 summarizes the data on the ability of the peptide nanotubes to template and catalyze imine condensation. Chapters 3 and 4 discuss in greater detail the hydrolytic retro-aldol reaction. In this chapter, these mechanisms are combined to explore aldol condensation with the possibility of using these nanotubes templates to catalyze aldol polymerization. From the principle of microscopic reversibility [1, 2], the aldol and retro-aldol reaction most likely would proceed through the same transition state, therefore, I anticipate that the peptide nanotubes would also accelerate the aldol reaction.

The aldol reaction is a versatile transformation in organic chemistry for the construction of carbon-carbon bonds. The product, a β-hydroxy-ketone, creates a new chiral center bearing a hydroxyl group that can be further transformed. The close proximity of functional groups of the aldehyde (*ald*) and the alcohol (*ol*) in the product give rise to the name "*aldol"*. In nature, these aldol structural motifs are found in many important naturally occurring compounds including polyketides from which many pharmaceuticals compounds with potent biological activity such as immunosuppressants (FK506), antibiotics (tetracycline) and antifungals (amphotericin B) are derived [3]. If the reaction occurs between two molecules of the same structure, the reaction is called *homo-aldol* otherwise it is a *cross-aldol*.

Enzymes catalyzing this reaction are classified by their mechanism. In Class I aldolases, the active site lysine forms a Schiff base with the carbonyl group of the substrate. The imine formed tautomerises to the enamine to set up formation of the

carbon-carbon bond (Figure 5-1). In Class II aldolases, this process uses Zn^{2+} in Lewis acid catalysis that facilitate enolate formation as shown in Figure 5-3.

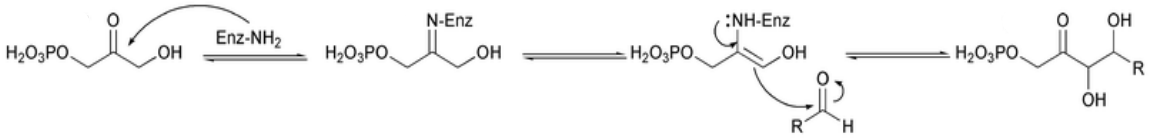

Figure 5-1*: Mechanism of Class I aldolase. Adapted from [4]*

In some cases, the aldol formed can further undergo a hydration reaction into α,β-unsaturated ketone (Figure 5-2).

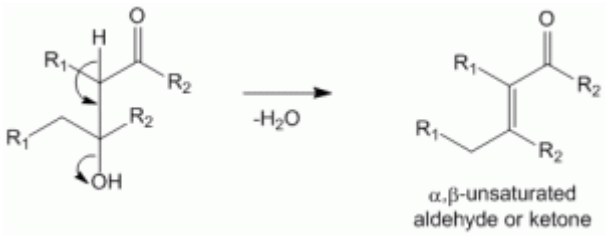

Figure 5-2: *Dehydration of β-hydroxyketone leads to α,β-unsaturted ketone.*

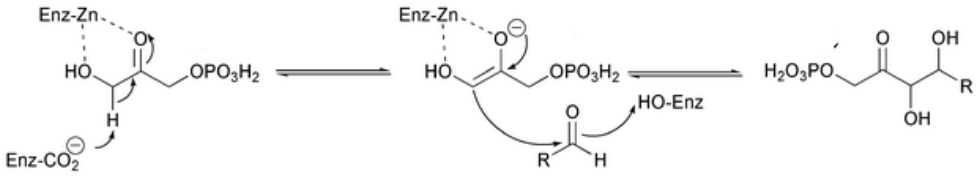

Figure 5-3*: Mechanism of Class II aldolase. Adapted from [4]*

Aldol reactions are generally thermally neutral, but on a template surface, it may be possible to extend the degree of condensation. Here I highlight the remarkable potential of self-assembling Aβ peptide assemblies to catalyze aldol condensation.

Results and Discussion

Peptide Nanotubes as Catalyst for Aldol Reaction

To exploit the nanotubes for catalyzing aldol reaction, 2-acetonaphthone (**8**) and 6-methoxy-2-naphthaldehyde (**9)** (Figure 5-4) were chosen as the substrates creating the possibility that the ketone and aldehyde functionanlities on the substrates will react and add to make an aldol product.

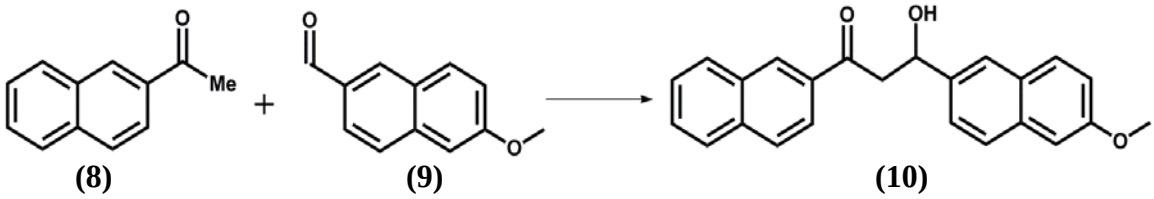

Figure 5-4: *Scheme for the proposed Aldol reactions of 2-acetonaphthone (8) and 6-methoxy-2-naphthaldehyde (9) to give aldol (10)*

The limitation to the substrate selection is there are several ways the substrates can bind in the tube surface grooves. One substrate or the other may bind preferentially (Figure 5-5A), or bind too far apart for reaction (Figure 5-5B), or bind in an orientation incompatible with condensation (Figure 5-5C). For the aldol reaction to occur, the substrates must bind as shown in Figure 5-5D. The aldol product was synthesized (Figure 5-6) on the bench to serve as a positive control for the identification of the product formed.

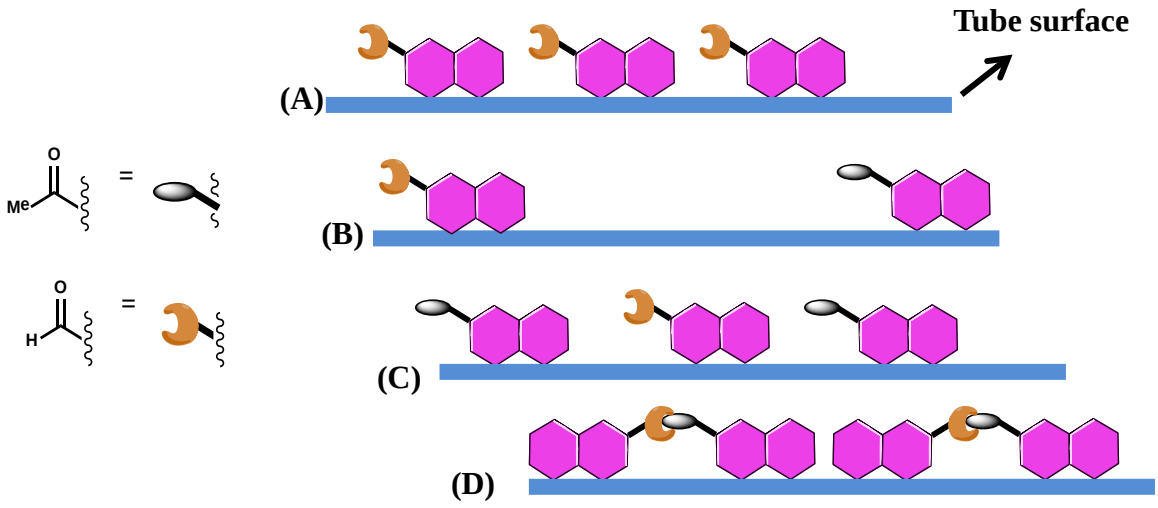

Figure 5-5: *Possible binding orientations of substrates(8) and (9) on nanotube surface grooves.*

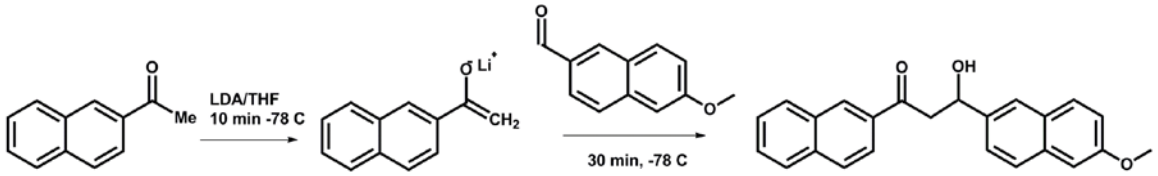

Figure 5-6: *Scheme for the synthesis of the Aldol product (10) from 2-acetonaphthone (8) and 6-methoxy-2-naphthaldehyde (9).*

The UV-vis spectra of the two substrates and the aldol product were taken to check the possibility of monitoring product formation with UV-vis. As shown in Figure 5-7, the UV-Vis spectra of the starting substrate and products were too similar to provide reliable data. Also the product does not have an intense UV-vis signal at the experimental working concentration, only at high concentration did the product give a reliable UV-vis spectra. Hence, product formation was monitored by HPLC.

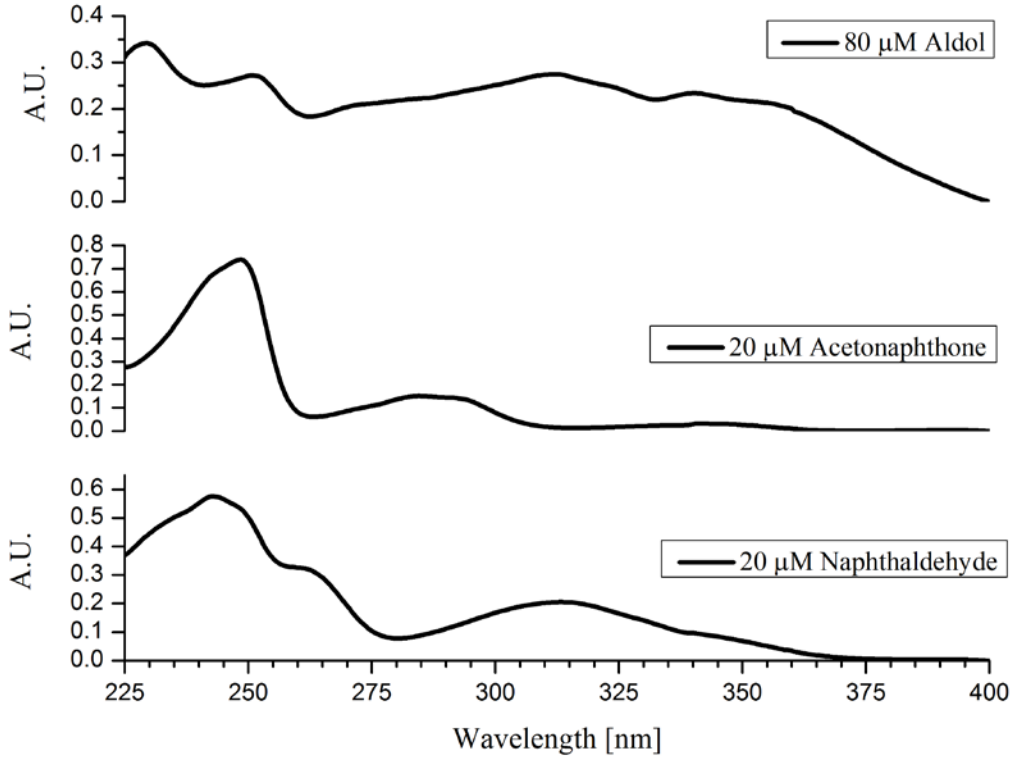

Figure 5-7: *UV-vis spectra of the substrates for aldol reaction and the aldol product formed.*

The HPLC gradient that I found that works and could effectively separate the product from the substrates still resulted in the two substrates having retention times that were too close. Although it was difficult to separate the two substrates, this would not be a problem if we are only interested in the product formed. Figure 5-8 shows the HPLC separation when both 2-acetonaphthone and 6-methoxy-2-naphthaldehyde elute at the same time (t_R = 25 minutes) while the aldol product elute at 36 minutes.

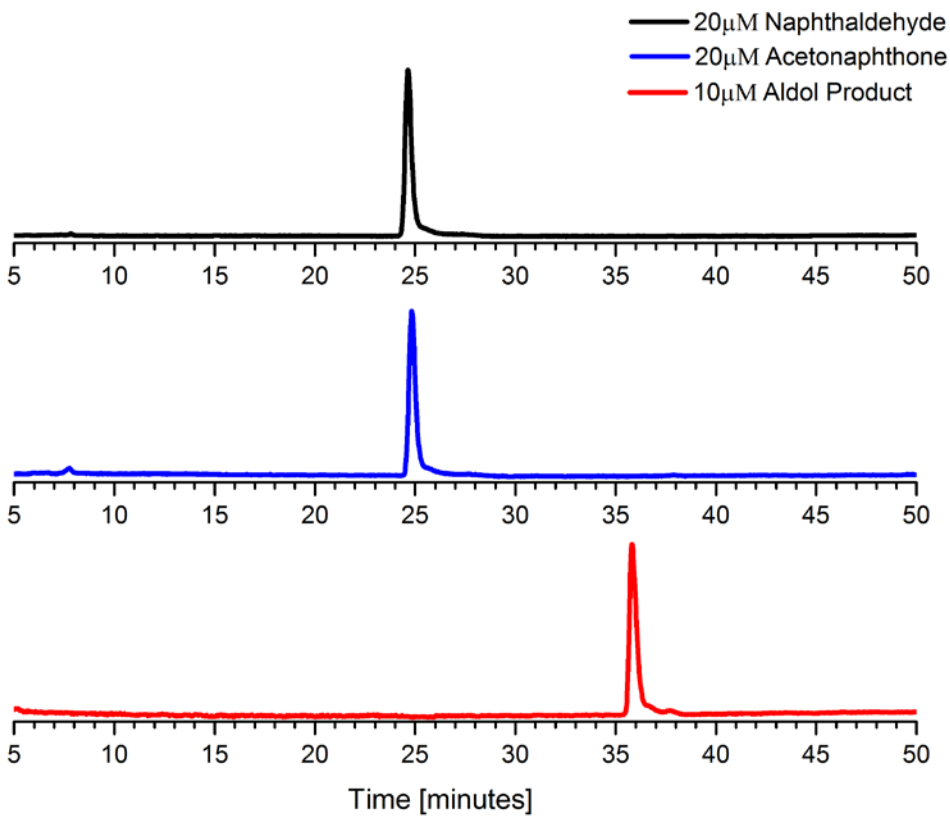

Figure 5-8: *HPLC Chromatogram showing the retention times of the substrates (8) at ~25 minutes and (9) at ~25 minutes and product (10) at ~36 minutes monitored at 254 nm.*

To have accurate HPLC results, reproducibility of injections was taken into consideration and this could be normalized using an internal standard as a reference line to normalize the product areas by the area of the internal standard hence increasing the reproducibility of the results. Methyl-4-nitrobenzoate was investigated as an internal standard because of its strong chromophore. Even though the ester is expected to be reactive with nucleophilic amine, when 10 μM of methyl-4-nitrobenzoate was incubated at room temperature with 500 μM Ac-KLVFFAL-NH_2 nanotubes alone, the intensity by HPLC remained unchanged for 24 hours (Figure 5-9) even when incubated with the

substrates and aldol product (Figure 5-10). It is possible that the concentration of methyl-4-nitrobenzoate used is too low for significant binding to the tubes which further strengthens my argument that binding of substrates to the nanotubes is important for reaction to take place.

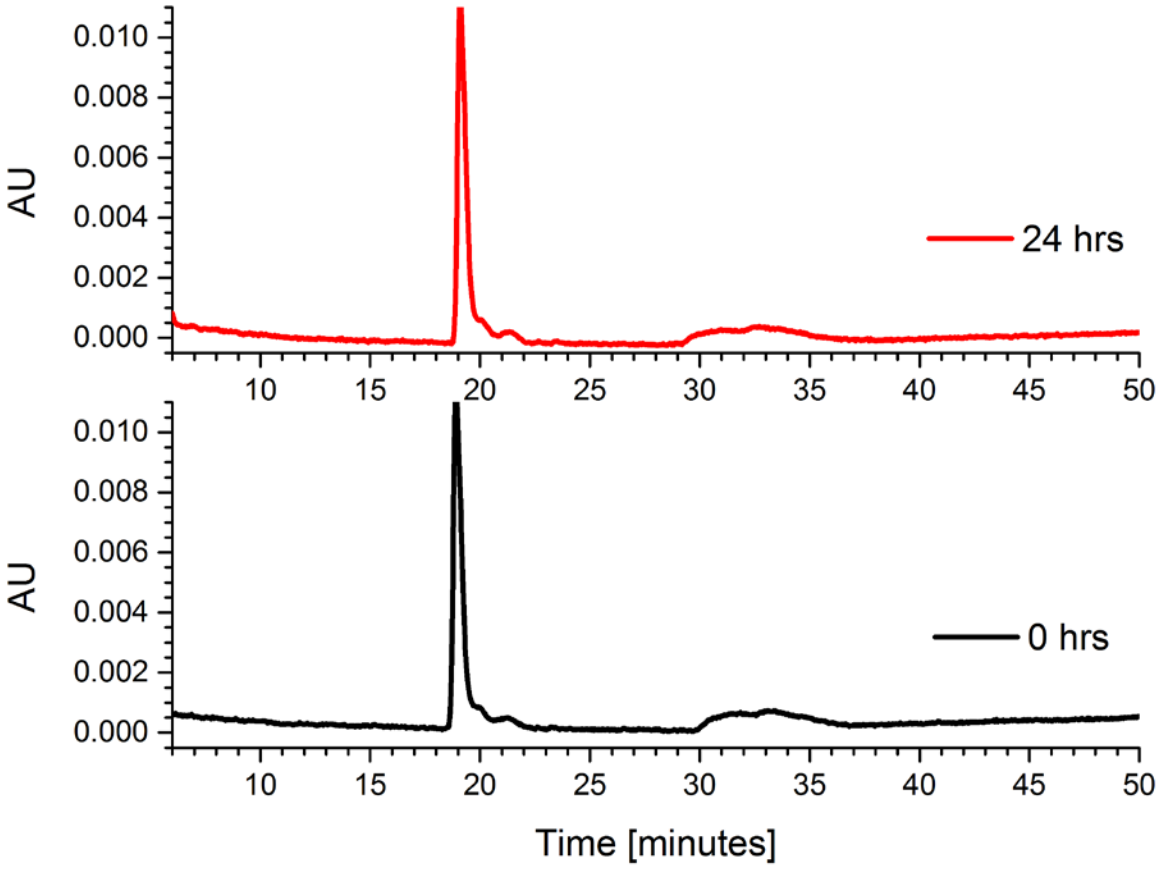

Figure 5-9: *HPLC Chromatogram showing the internal standard (t_R =19 minutes) added to 500 µM Ac-KLVFFAL-NH_2 nanotubes at time zero (black) and 24 hours after incubation (red).*

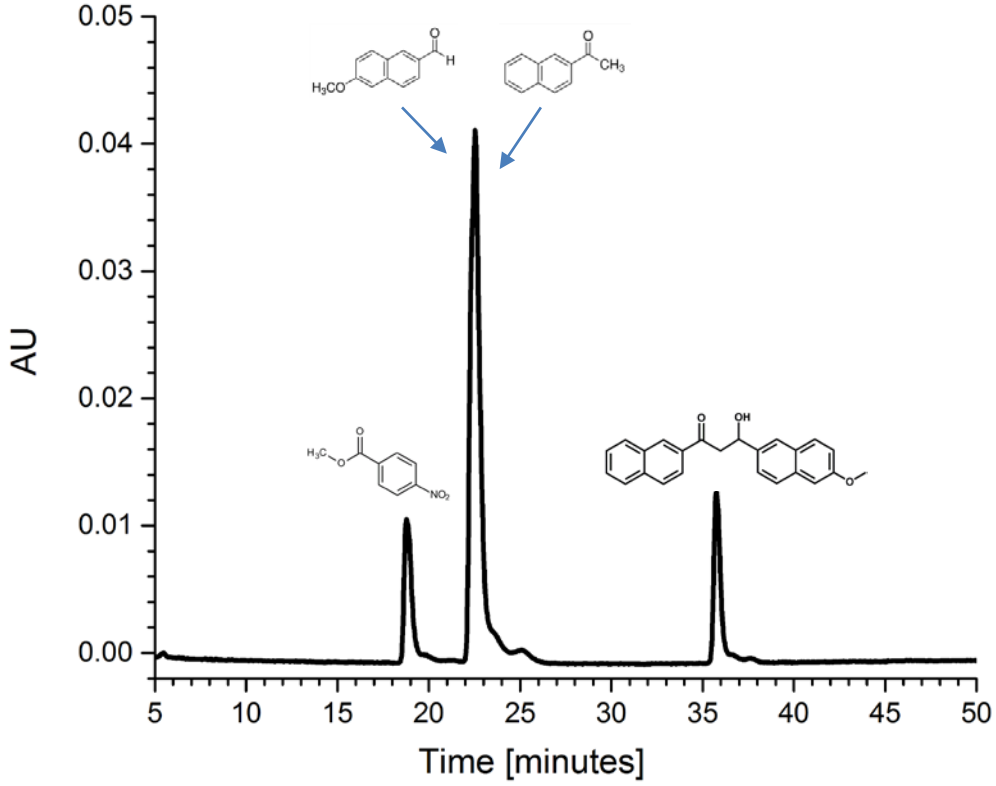

Figure 5-10: *HPLC Chromatogram showing the internal standard (t_R =19 minutes), substrates (t_R =23 minutes) and product 10 (t_R =36 minutes) after 24 hours of incubation.*

Upon incubation of 2-acetonaphthone (8) and 6-methoxy-2-naphthaldehyde (9) in the presence of Ac-KLVFFAL-NH_2 in buffer, HPLC trace showed the formation of a new peak after 1 hour (Figure 5-11). Formation of (10) was confirmed from ESI-MS (Figure 5-12).

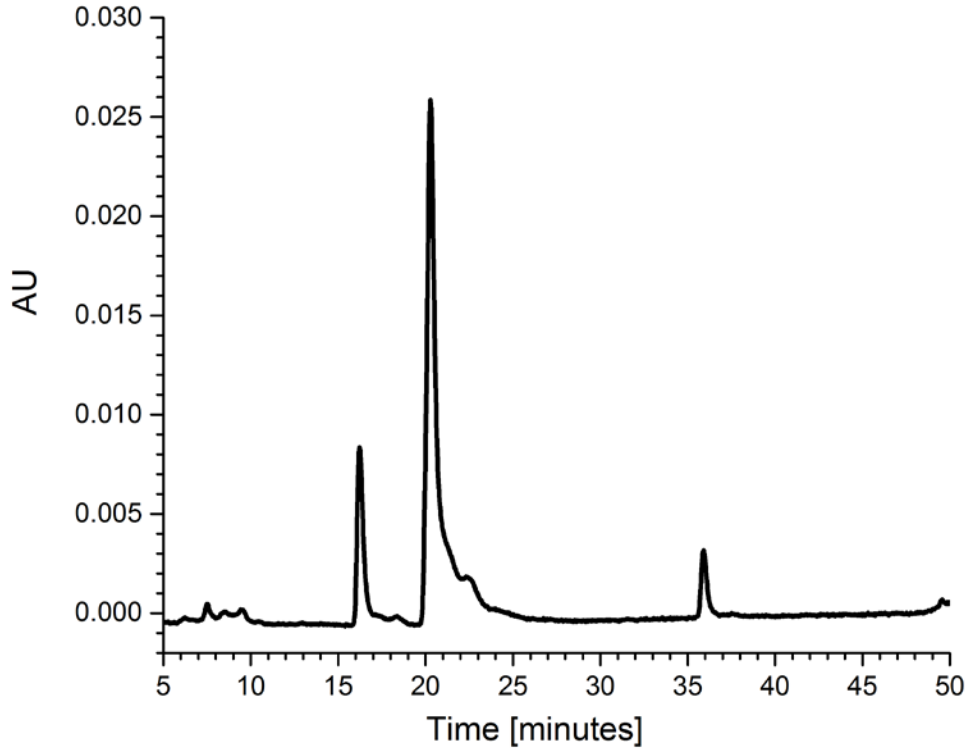

***Figure 5-11**: HPLC trace of aldol reaction with 500 µM Ac-KLVFFAL-NH_2 nanotubes with 20 µM 2-acetonaphthone (8) and 6-methoxy-2-naphthaldehyde (9). Formation of the aldol product (t_R= 36 minutes) was observed after 1 hour.*

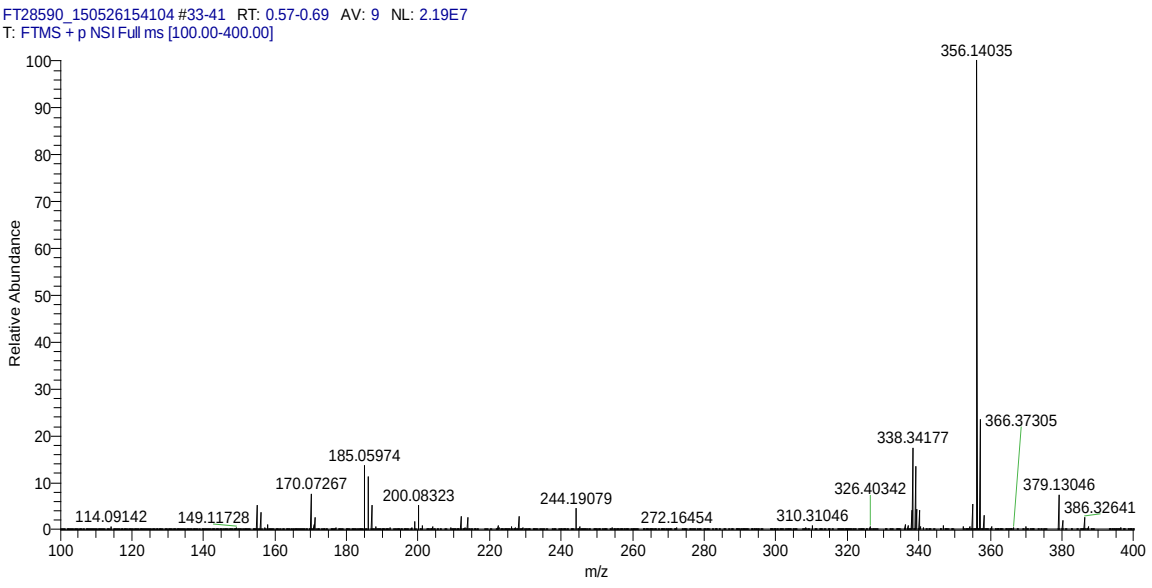

***Figure 5-12**: Elemental composition search of the product from the aldol reaction of 500 µM Ac-KLVFFAL-NH_2 nanotubes with 20 µM 2-acetonaphthone (8) and 6-methoxy-2-naphthaldehyde (9) gives a peak consistent with the mass of the expected aldol product ($[M+H]^+$: 356.141).*

To check if the substrate ratio is important the K16 nanotubes were used to catalyze different ratios of the substrates concentration and the reaction analyzed after 2 hours of incubation. As shown in Table 5-1, irrespective of the ratio of 8:9 tested, same amount of product was formed. Therefore, rest of the study was carried out at substrates ratio of 1:1.

Acetonapthone : Naphthaldehyde	**Aldol (µM)**
1:1	5.08
2:1	5.01
3:1	5.03
5:1	5.08
10:1	5.06

***Table 5-1**: 500 µM Ac-KLVFFAL-NH_2 incubated with varying ratios of 2-acetonaphthone (8) to 6-methoxy-2-naphthaldehyde (9). Samples were incubated for 2 hours and analyzed by HPLC.*

Three different substrates concentrations (10 µM, 20 µM and 40 µM) were also tested, and the results indicate that there is no linear increase in aldol formed with increase in substrate concentration. Only ~17% increase in product formation was observed from substrate concentration of 20 µM to 40 µM (Table 5-2) even at longer

times suggesting that equilibrium is being reached at those concentrations. Henceforth, the rest of the reactions was done with 40 µM substrates concentration.

Acetonapthone /Naphthaldehyde	Aldol (µM)
10 µM	5.08
20 µM	5.75
40 µM	5.94

Table 5-2*: 500 µM Ac-KLVFFAL-NH_2 incubated with 10 µM, 20 µM and 40 µM substrates (**8** and **9**). Samples were incubated for 2 hours and analyzed by HPLC.*

A common issue with the use of HPLC for monitoring reactions is the use of quenching to stop the reaction progress so as to enable kinetic analysis. Usually, another chemical compound would have to be added which can in turn affect the reaction solution and undergo side reactions. The duration of the HPLC method for monitoring the aldol reaction is 59 minutes and the reaction seemed to reach equilibrium between 2-4 hours. As a result it is necessary to quench the reaction to obtain kinetic data. Several quenching methods were tried, but none of them were successful, therefore, it was decided to avoid the use of quenching and just analyze the end-point data.

Alteration of the lysine basic structure by shortening the side chain length to derive Ac-OrnLVFFAL (K16Orn), Ac-DabLVFFAL (K16Dab) and Ac-DapLVFFAL (K16Dap) was discussed in the previous chapter as well as replacing the lysine with arginine (K16R) and histidine (K16H). Interestingly, the rate of the aldol reaction

catalyzed by these K16 congeners was greatly affected (Table 5-3). K16R and K16H nanotubes were not able to catalyze the aldol reaction, suggesting that amine functionality on the lysine is necessary for the reaction to occur. With K16 nanotubes, there was no reaction observed at 0 hour, however, with K16Orn, K16Dab and K16Dap, the reaction was fast enough for product formation to be seen at 0 hour and K16Dap having almost 3 times product formed compared to K16Orn and K16Dab. After 1 hour, K16Orn assemblies achieved 18% product conversion with a slight increase to 21% after 4 hours. With K16Dab, product conversion was 41% at 1 hour and increased to 43% after 4 hours. K16Dap had the highest conversion rate with 69% of the substrate converted after 1 hour but interestingly, there was a decrease in the product formed to 62% after 4 hours. Overall, the shorter the lysine side chain length, the closer to the binding groove and the better the rate of catalysis.

Nanotubes	**Aldol (μM)** **0 Hour**	**Aldol (μM)** **1 Hour**	**Aldol (μM)** **4 Hours**
K16	-	5.77	6.07
K16Orn	5.46	7.11	8.35
K16Dab	5.49	16.48	17.04
K16Dap	13.42	27.42	24.62

Table 5-3*: 500 μM K16, K16Orn, K16Dab and K16Dap separately incubated 40μM substrates (**8** and **9**). Samples were incubated for 2 hours and analyzed by HPLC.*

One complication in aldol condensation reaction is the occurrence of side-reaction taking place at the same time that can greatly reduce the yield of the reaction. This may be as a result of dehydro-condensation of the two starting materials rather than their addition or aldol products itself undergoing dehydration to form conjugated carbonyl molecules (Figure 5-13). It has also been reported that the aldehyde component can undergo aldol reaction as well as condensation with itself [5].

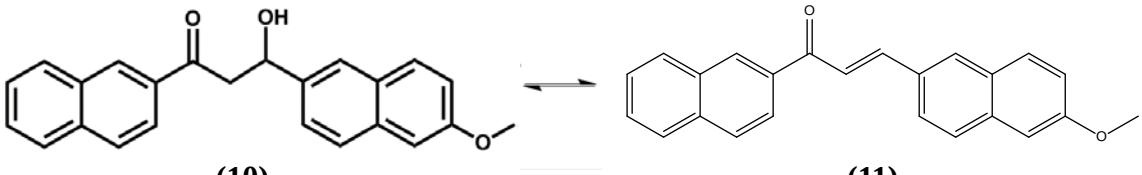

(10) **(11)**

Figure 5-13: *Aldol condensation product (11)*

Reaction of K16 and K16Orn with the substrates did not lead to formation of side products but both K16Dab and K16Dap catalyzed the formation of a side product (Figure 5-14), confirmed by ESI-MS analysis to be the dehydrated aldol product (Figure 5-15). This formation of side product could be a plausible explanation for the decrease in the amount of aldol formed by K16Dap from 1 hour to 4 hours although a decrease is not noticeable in K16Dab reaction. The K16Dap might be catalyzing both the substrates and the aldol product conversion to the dehydrated aldol product whereas the K16Dab is only catalyzing the substrates conversion to the dehydrated aldol product. Another reason for the decrease observed with K16Dap from 1 hour to 4 hours might be product inhibition as a result of product rebinding to the tube surface. Given that the concentration of aldol formed is 5 times higher than the corresponding amount of the side product formed

within the time frame the reaction was monitored, the side-reaction does not appreciably affect the efficiency of the catalyst.

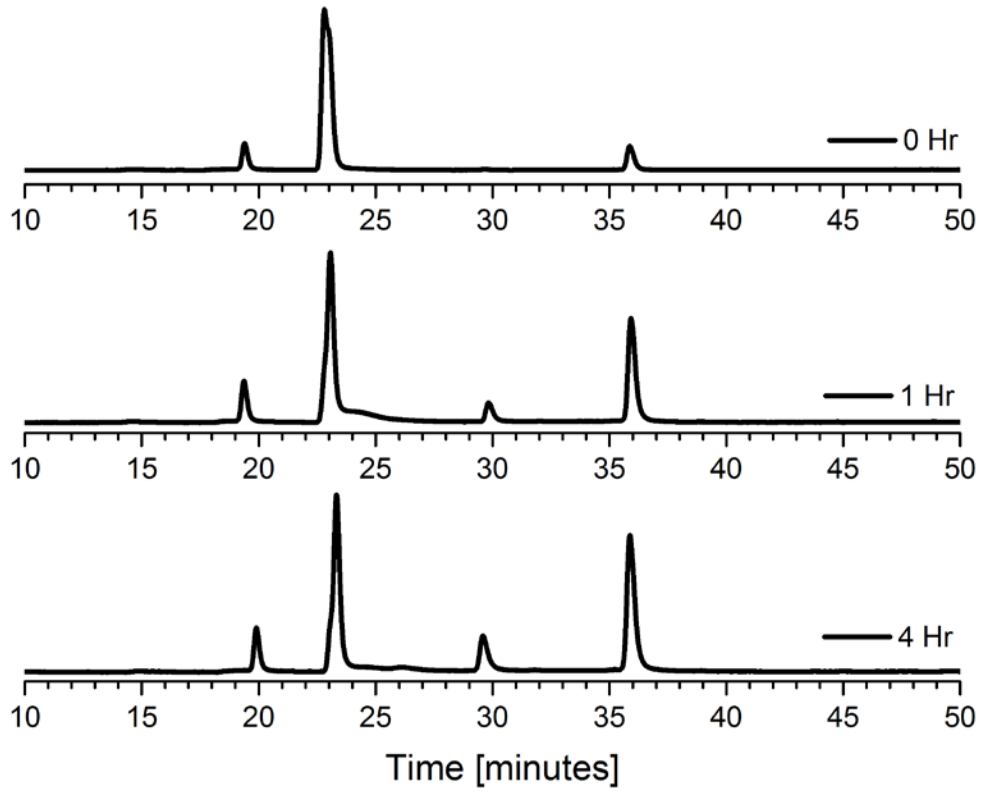

Figure 5-14: *HPLC trace of aldol reaction with 500 µM Ac-DapLVFFAL nanotubes with 40 µM (8) and (9). Formation of the aldol side product (t= 30 minutes) was observed after 1 hour.*

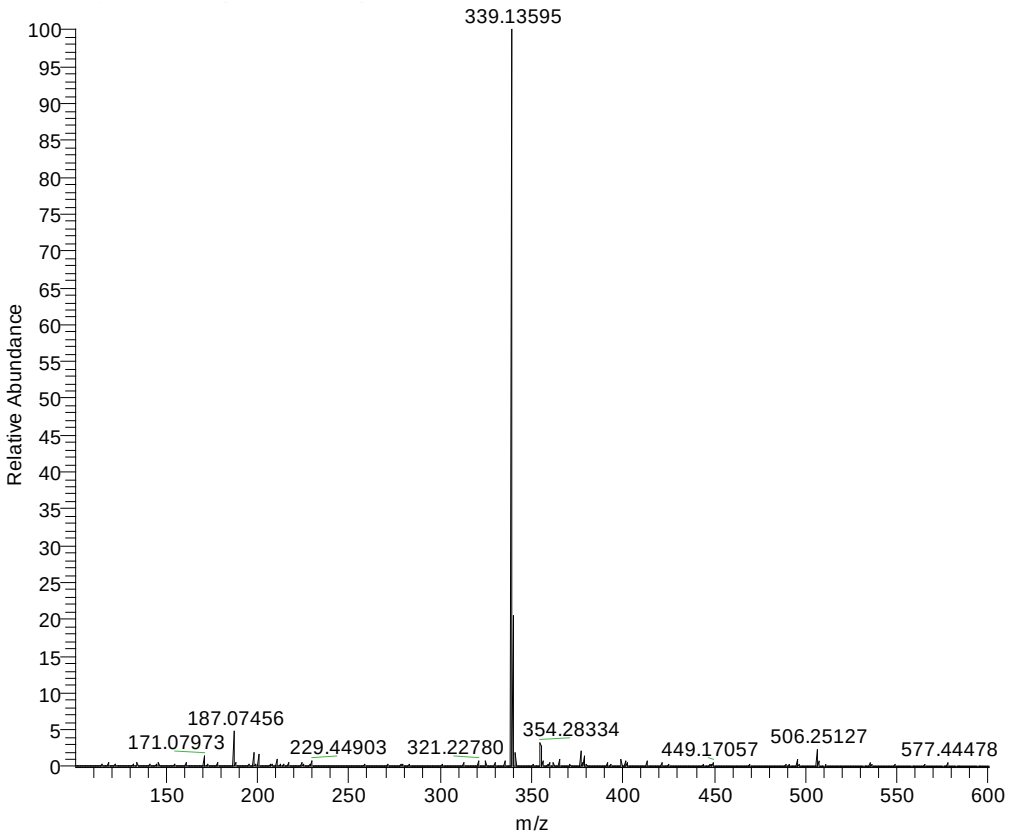

Figure 5-15*: Elemental composition search of the side product gives a peak consistent with the mass of the dehydrated aldol product ([M+H]⁺: 339.135).*

Product Rebinding

With all the catalytic nanotubes studied, there little or no increase in product formation after 4 hours, even though there were still substrates left in the reaction. One possible reason for this observation might be that the nanotubes are falling apart under the reaction condition, it is also possible that the product may be binding to the tube surface preventing more substrates from binding or the system reaching equilibrium whereby the products are binding and getting converted back to the substrates. To ensure that the nanotubes are still intact under the reaction conditions, the reaction mixture

containing the nanotubes were spotted on a TEM grid for microscopy. The result showed that the nanotubes remain intact even after several days under the reaction condition (Figure 5-16) which rules out reason 1.

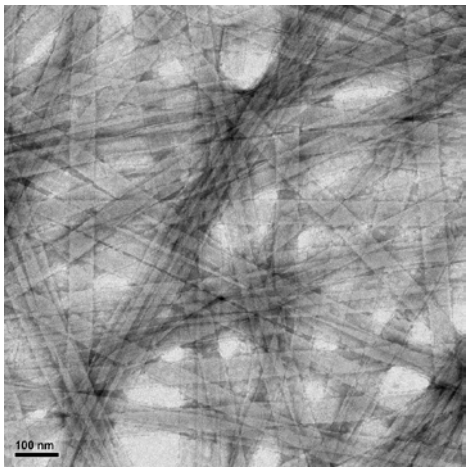

Figure 5-16: *TEM image of K16Dap incubated with the aldol substrates for a week under the reaction conditions.*

To analyze product binding, the reaction was pelleted at 16,100g for 30 minutes, and the supernantant was sampled and the composition compared to that of the resuspended pellets (nanotubes) composition. The result showed that almost all the aldol products were spun down with the nanotubes (Figure 5-17, red chromatogram) while the supernatant did not have any traceable amount of the product (Figure 5-17, red chromatogram). This results suggests that the aldol products are bound to the nanotubes.

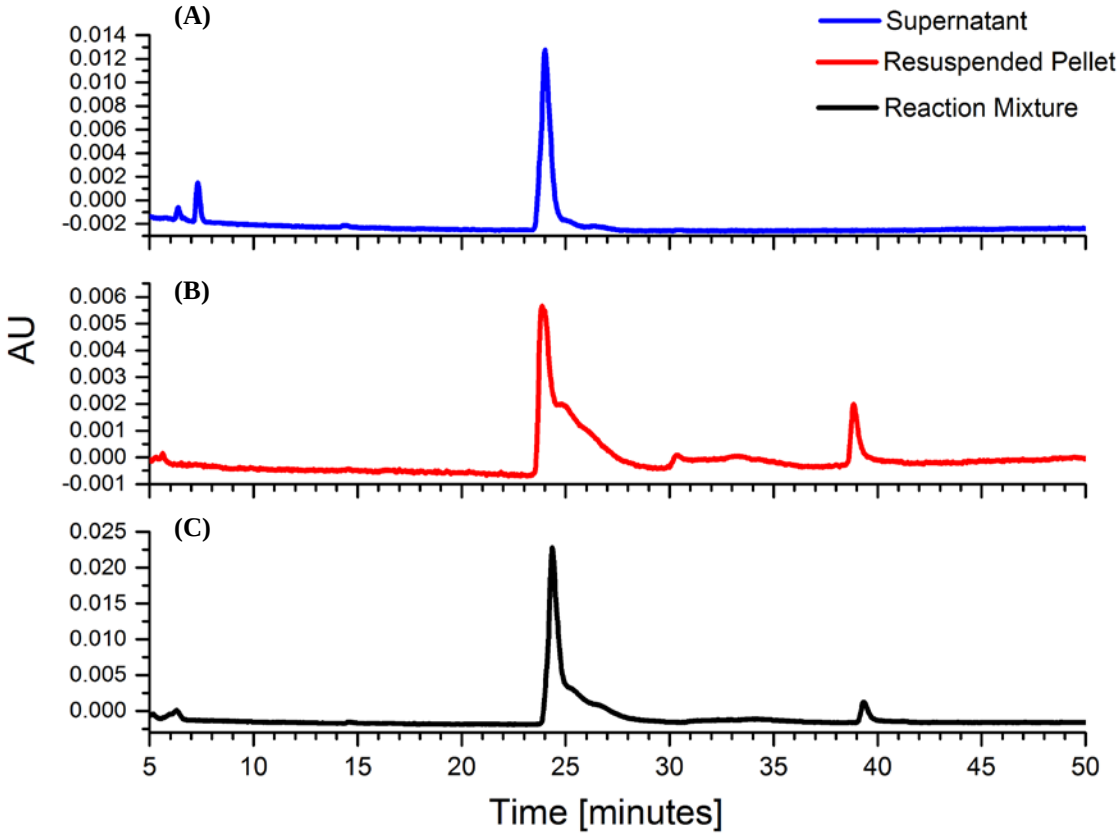

Figure 5-17: *HPLC trace of the reaction mixture containing 500 µM K16 incubated with 40 µM substrates. After 24 hours, the nanotubes were pelleted. The pellet was resuspended in buffer and both supernatant and resuspended pellets were analyzed by HPLC. (A) Chromatogram of the supernatant. (B) Chromatogram of the resuspended pellet and (C) Chromatogram of the reaction mixture before spin down.*

To test for retroaldol activity, 10 µM of the aldol product was added to E22L nanotubes. As shown in Figure 5-18, after 24 hours the concentration of aldol product in the buffer control remained constant (Figure 5-18B, red chromatogram). However, the concentration of the aldol product in the presence of the nanotubes had changed significantly. Appearance of substrates peak could be detected after 24 hours (Figure 5-18D, green chromatogram) which is an indication that the retro-aldol reaction is

occurring albeit, at a very slow rate compared to the aldol reaction. All the other catalytic nanotubes studied displayed the ability to catalyze the retro-aldol reaction.

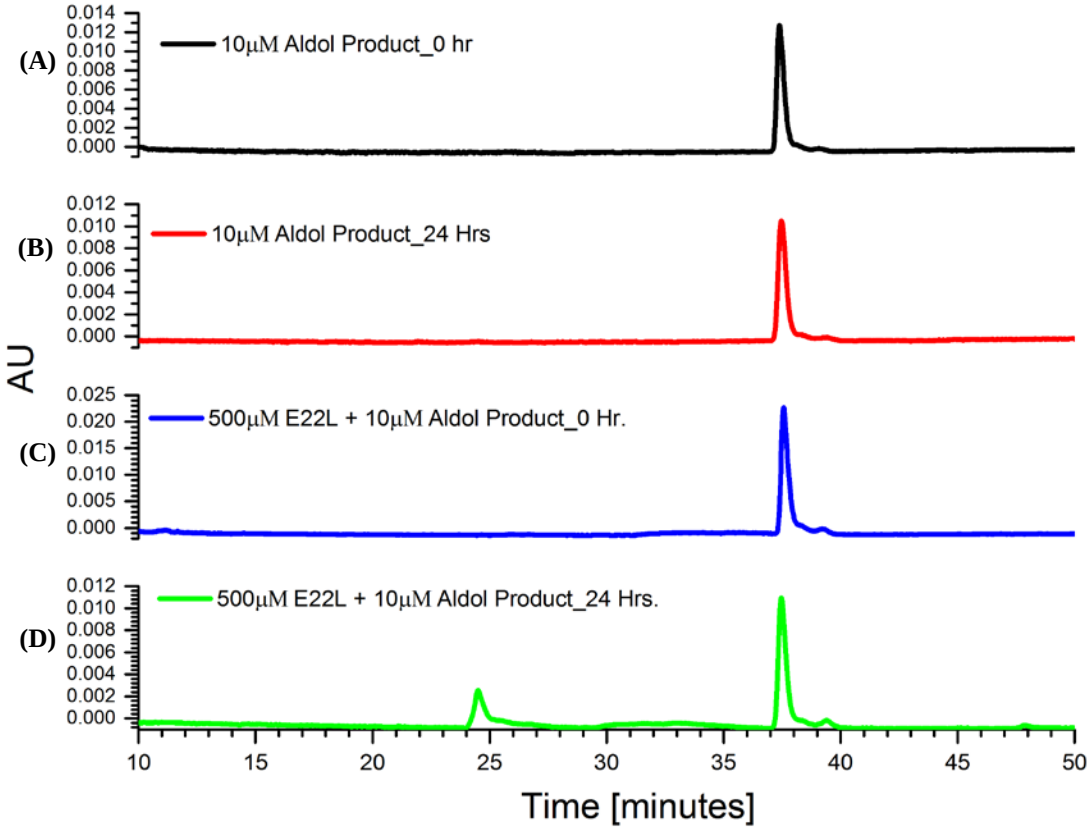

Figure 5-18: *HPLC trace of 10 μM Aldol in buffer without nanotubes at (A) t = 0 hours. (B) t = 24 hours; and the reaction mixture containing 500 μM K16 nanotubes incubated with 10 μM Aldol at (C) t = 0 hours and (D) t = 24 hours. At the initial time t = 0 and after 24 hours, the reaction mixtures were analyzed by HPLC on a C18 RP column.*

Enantiospecificity of Aldol reaction

The designation for the aldol enantiomers could not be determined at the moment because the synthetic aldol could not be made in large enough quantity to satisfy the requirement for polarimetry. Therefore, the first aldol enantiomer to elute by HPLC is

designated *"Enantiomer 1"* and the second enantiomer to elute *"Enantiomer 2"*. After incubating the aldol substrates with the nanotubes for 24 hours, the reaction was extracted with hexane to yield the aldol, the hexane was evaporated off and the aldol re-dissolved in acetonitrile before analysis by a chiral-phase HPLC. Remarkably all the nanotubes displayed excellent enantiospecificity, preferentially catalyzing the formation of the *Enantiomer 1* (Figure 5-19).

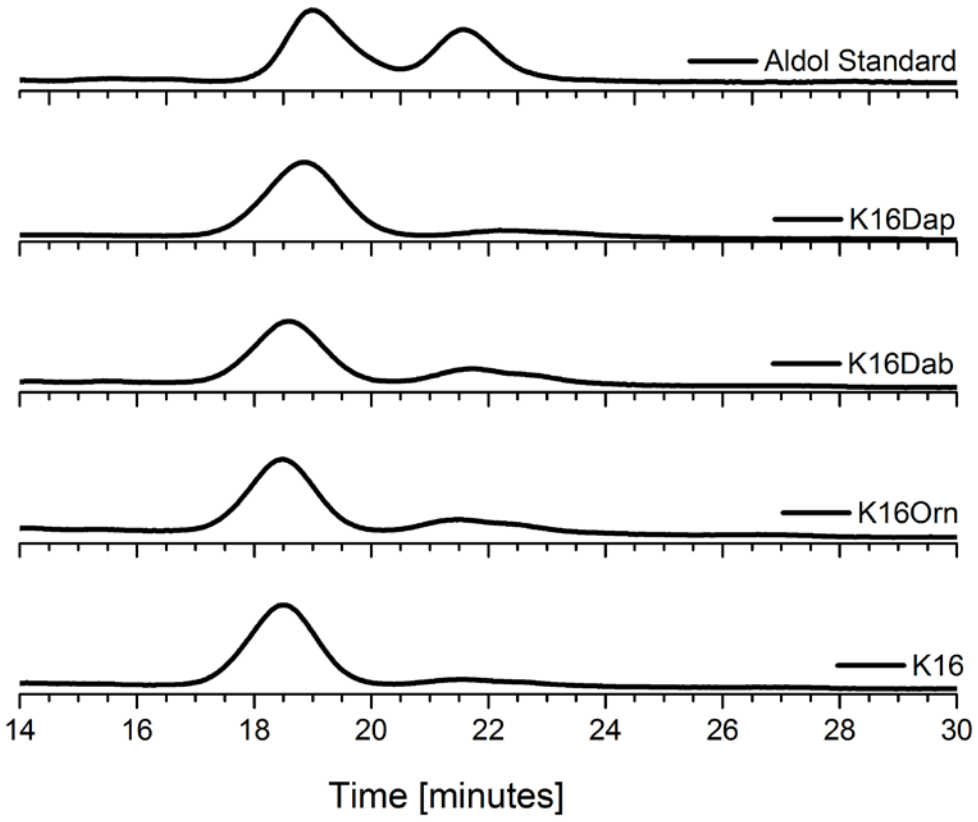

Figure 5-19: *HPLC trace of the racemic mixture of the aldol product (top layers). The other layers are the trace of the indicated nanotubes incubated with 40 μM substrates for 24 hours and analyzed after extraction of the product. Elution was done using an isocratic method with 72% MeCN/H_2O at 0.5 ml/min on a Chiralpak AD-RH column.*

The enantiomeric excess was K16 = 93.5±1.4%, K16Orn = 84.9±0.7%, K16Dab = 80.6±1.0% and K16Dap = 92.3±1.1%. Although the enantiospecificity displayed by the nanotubes are close, the reason for the slight difference is not known at the moment but might be related to the position of the amine from the binding groove.

Checking the enantioselectivity of the consumption of the aldol product for the retro-aldol study, interestingly, all the four nanotubes displayed different enantioselectivity. As shown in Figure 5-20, K16 was not enantioselective while both K16Orn and K16Dab prefer same "*Enantiomer 1*" with 8±4% and 5±0% enantioselectivity respectively. K16Dap on the other hand, have a preference for the "*Enantiomer 2*" with 5±2% enantioselectivity.

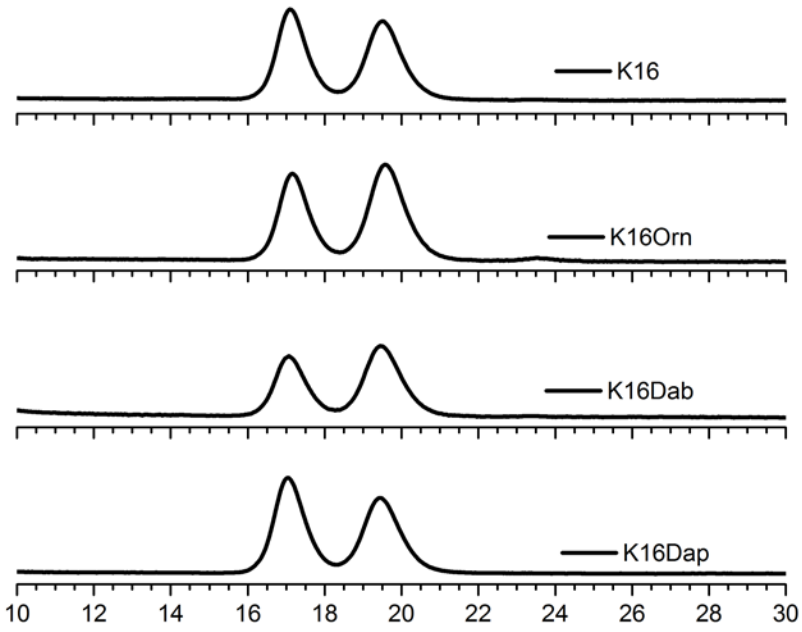

Figure 5-20: *HPLC trace of the indicated nanotubes incubated with 10 μM Aldol for 24 hours and analyzed by HPLC with an isocratic method of 72% MeCN/H_2O at 0.5 ml/min on a Chiralpak AD-RH column.*

The enantioselectivity of the retro-aldol reaction is really low compared to the aldol reaction and this could be because the reaction itself is very slow and very little substrate has been consumed to reflect the enantioselectivity.

Conclusion

I shown in previous chapters the ability of peptide nanotubes to catalyze both imine and retro-aldol reactions. A possible limitation to obtaining higher oligomers with the imine condensation could be the rigidity of the imine bonds in the dimers. To increase flexibility in the product so that it can bind to the tubes to achieve polymerization, I considered exploiting the nanotubes for the aldol C-C formation reaction. The peptide nanotubes were able to generate an enhanced local stoichiometry of the reactants by bringing the two different reactants in close proximity in the right orientation for the reaction to occur. The aldol reactions are significantly accelerated on the Ac-KLVFFAL-NH_2 nanotubes surface with product formation observed after 1 hour of incubation. By adjusting the catalytic residues at the surface, from lysine to ornithine to diaminobutyric acid and diaminopropionic acd, it was possible to optimize the chemistry in the order K16Dap > K16Dab > K16Orn > Lys. It is possible that shortening the lysine side chain provides a more optimal positioning of the amine functionality resulting in the enhanced activity. This result is consistent with the retro-aldol catalysis described in Chapter 4. In addition, both K16Dab and K16Dap nanotubes catalyzed the formation of the dehydrated aldol product. As expected, K16R and K16H nanotubes did not catalyze the aldol reaction reiterating the importance of the amine functionality for the reaction. All the

catalytic nanotubes studied preferentially catalyzed the formation of “Enantiomer 1” of the aldol product. Product binding studies show that the nanotubes bind the aldol product as effectively as reactants fulfilling our criteria for polymerization. Based on these results, we are now poised to explore the polymerization. Next steps would require slight modification of the substrates by bis-functionalizing with aldehyde and/or ketone to achieve polymerization.

One of the main characteristics of enzymes is their high specificity. This specificity for a particular reaction and poor acceptance of a range of substrates may not necessarily be desirable in the application of natural enzymes for synthesis. Based on my discoveries from previous chapters and this chapter, the peptide nanotubes can use various substrates and catalyze three reactions so far. This could be an advantage in large scale organic synthesis since the same nanotubes could be used as catalysts for a variety of reactions.

Materials and Methods

Aldol Reaction

Prior to the aldol reaction, peptide assemblies were centrifuged at 13,800g for 60 minutes and pellets suspended in distilled water. Substrates and synthetic aldol were dissolved in acetonitrile. Dissolving the synthetic aldol in DMSO leads to the formation of the dehydrated aldol. For the reaction, the solution was buffered to pH 7.5 with 50 mM HEPES and 300 mM NaCl and brought to final concentrations of 500 μM peptide assembly in 25 mM HEPES, 150 mM NaCl and 5 % MeCN. For analysis, the reaction

solution was injected on a C18 RP analytical column with a gradient of 33-80% MeCN/H_2O at a flow rate of 1 mL/min.

Product enantiomeric excess was determined by chiral HPLC analysis using a Chiralpak AD-RH (Daicel) column. When eluted isocratically with 72% MeCN/ H_2O at a flow rate of 0.5 mL/min, the retention times of (R)- and (S)-methodol were 17.2 and 19.5 minutes, respectively. Detection was at 254 nm.

Synthesis of Aldol Product

A solution of n-BuLi in hexane (2.5 M, 4.8 ml, 12.0 mmol) was added dropwise to a stirred solution of dry i-Pr_2NH (1.72 ml, 12.2 mmol) in anhydrous THF (20 ml) at -78°C. The resulting mixture was stirred for 10 min, and a solution of acetophenone (1.22 g, 10 mmol) in THF (5 ml) was added dropwise. The mixture was stirred for 10 min at -78°C. Neat benzaldehyde (1.28 ml, 12 mmol) was added, and stirring was continued for 30 min at -78°C. The cold reaction mixture was poured into a separatory funnel with EtOAc and saturated aqueous NH_4Cl. The organic layer was separated and the aqueous layer was extracted with EtOAc. The combined organic phases were washed with brine, dried over $MgSO_4$, filtered, and concentrated. Preparative column chromatography on silica gel (hexane–EtOAc 5:1 as eluent) afforded 3-hydroxy-1,3-diphenylpropan-1-one as a yellowish oil.

Electron Microscopy

10 µL of 2.5 mM peptide assemblies diluted 1:9 with water containing 0.1% TFA was added to TEM grids (200 mesh copper grids with a thin carbon film support –

Electron Microscopy Sciences, Hatfield, PA). Peptide assemblies were allowed to adsorb on the grid for 1 minute before excess peptide solution was wicked away with filter paper. Freshly prepared 2-wt % uranyl acetate solutions were added to TEM grids and incubated for 4-5 minutes before wicking away excess stain and then the grids were placed in a vacuum desiccator overnight or until imaging to remove any residual solvents. All staining solutions were prepared fresh and filtered prior to staining to minimize artifacts. TEM micrographs were recorded with a Philips 410 TEM at magnifications ranging from 40,000X to 100,000X with a Tungsten filament at an accelerating voltage of 75 kV.

UV-Vis Absorption Measurements

UV-vis absorption spectra were recorded with a Jasco V-530 UV spectrophotometer using a 2-10 mm cuvette path length. UV spectra were background subtracted to minimize scattering effects.

References:

1. Tolman, R.C., *The Principle of Microscopic Reversibility.* Proc Natl Acad Sci U S A, 1925. **11**(7): p. 436-9.

2. Blackmond, D.G., *"If pigs could fly" chemistry: a tutorial on the principle of microscopic reversibility.* Angew Chem Int Ed Engl, 2009. **48**(15): p. 2648-54.

3. Schetter, B. and R. Mahrwald, *Modern Aldol Methods for the Total Synthesis of Polyketides.* Angewandte Chemie International Edition, 2006. **45**(45): p. 7506-7525.

4. Sukumaran, J. and U. Hanefeld, *Enantioselective C-C bond synthesis catalysed by enzymes.* Chemical Society Reviews, 2005. **34**(6): p. 530-542.

5. Trost, B.M. and C.S. Brindle, *The direct catalytic asymmetric aldol reaction.* Chemical Society Reviews, 2010. **39**(5): p. 1600-1632.

Chapter 6: Amyloids as a Rogue Enzyme

Introduction

Metal ions play an important role in biological systems, essential for both catalytic and structural functions in enzymes and proteins. To perform these functions, complex machinery is used to control the metabolism of metal ions which includes selection, transporting, sensing and storing. The mammalian brain is the most aerobically active organ, accounting for 2% of total body mass and yet consuming 20% of total oxygen in a resting individual. Neurodegenerative diseases have been associated with oxidative stress, and in Alzheimer's disease (AD), the roles of metal ions in both aggregation of amyloidogenic peptides and the generation of Reactive Oxygen Species (ROS) have been proposed. [1-7]

The major components of amyloid deposits are the 39–42 amino acid peptides derived from amyloid precursor protein known as the amyloid-β peptide (Aβ) [8, 9]. It is believed that Aβ fibrils and other aggregates contribute directly to neuronal cell loss [10]. The redox active metal ions, iron and copper are also both found in AD plaques [11-13], providing a source of ROS generation [5]. In fact, studies have shown that in vitro incubation of an Aβ-Cu(II) mixture with electron donors under aerobic condition produce hydrogen peroxide [14-16]. Abnormal concentrations of zinc have been found in the amyloid plaques of Alzheimer's disease [17] and Zn^{2+} triggers the rapid and extensive aggregation of Aβ peptide in canine cerebrospinal fluid [18]. All these metal ions play important roles in amyloid aggregation, neurotoxicity and Alzheimer's disease. Therefore, there is need for the accurate determination of redox potentials of metal

complexes of the Aβ peptides to unravel their roles in oxidative stress.

The fact that amyloid assemblies appear to share many common structural features of well folded enzymes including buried ions [19], metal binding sites [20-22], and substrate binding sites [23], makes me hypothesize that amyloid assemblies with metal ions can be viewed as metalloenzymes whose catalytic activities are responsible for its toxicity in amyloid related diseases. This toxicity might not be due to ROS generation alone but might be in parallel with other reactions being catalyzed by Aβ-metal complex in the brain. One of such reactions could be an aldol condensation reaction which could result in altered metabolism in the brain.

Results and Discussion

Structural Characterization of Aβ assemblies in the presence of Cu^{2+}

Due to the difficulty in gaining insights on the pathway and structures of Aβ aggregation and the effect of metal binding, studies with shorter and simpler model peptides have been explored initially. The model peptide, Aβ(13-21), and its congeners K16A and H14A [20, 21] contain the His-13/His-14 dyad that have been previously implicated in metal binding [22, 24, 25]. These peptides also contain the core hydrophobic sequence, LVFFA [26, 27], that has proven to be so crucial for assembly. This short peptide self-assembles *in vitro* into typical amyloid fibrils that are morphologically similar to the full-length Aβ peptide [21].

The TEM of fibers assembled from Ac-Aβ(13-21)H14A are shown in Figure 6-1A, and appear as a mixture of twisted and non-twisted fibers that are slightly bundled.

When assembled in the presence of Cu^{2+}, little twisting is observed (Figure 6-1C). The significant increase in the β-sheet signature in the presence of Cu^{2+} suggests that the Cu^{2+} stabilizes fiber formation (Figure 6-1B). The blue shift in the Cu^{2+} wavelength to ~661 nm (Figure 6-1D) is consistent with the Cu^{2+} being incorporated in the fiber assembly. Extended X-ray absorption fine structure (EXFAS) spectroscopy places the Cu^{2+} in the fiber as bridging two His-13 residues between paprallel hydrogen-bonded β-strands in a His-Cu^{2+}-His chelated structure [28] as shown in Figure 6-2B.

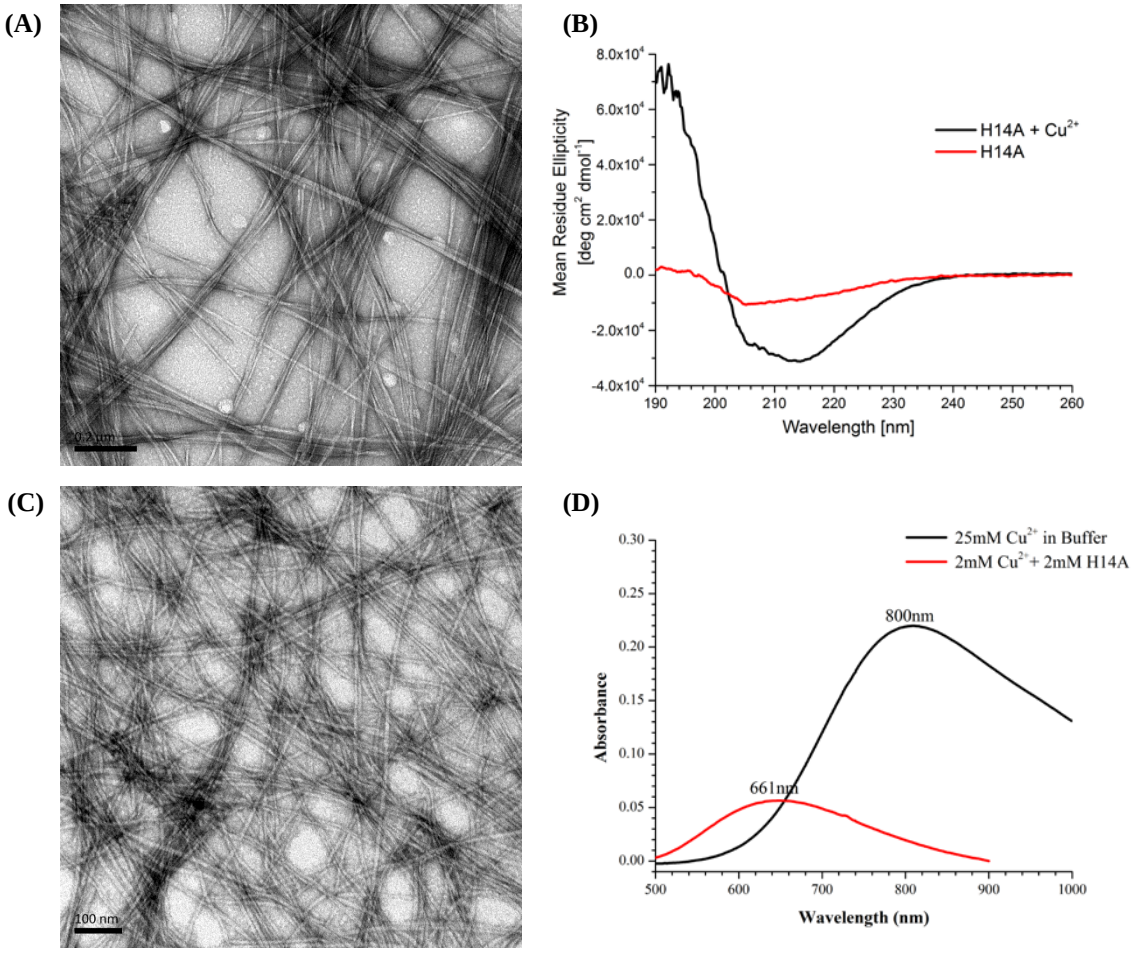

Figure 6-1: *(A) TEM micrograph of Ac-Aβ(13-21)H14A without Cu^{2+}. Scale bar 200 nm and (C) TEM micrograph of Ac-Aβ(13-21)H14A with Cu^{2+}. Scale bar 100 nm. (B) CD spectrum of Ac-Aβ(13-21)H14A (red) without Cu^{2+} and (black) with Cu^{2+} and (D) UV-vis spectrum of Cu^{2+}-Aβ(13-21)H14A. All assemblies were at 2 mM Ac-Aβ(13-21)H14A (with 1:1 Cu^{2+}ratio) in 25 mM HEPES, pH 7.2.*

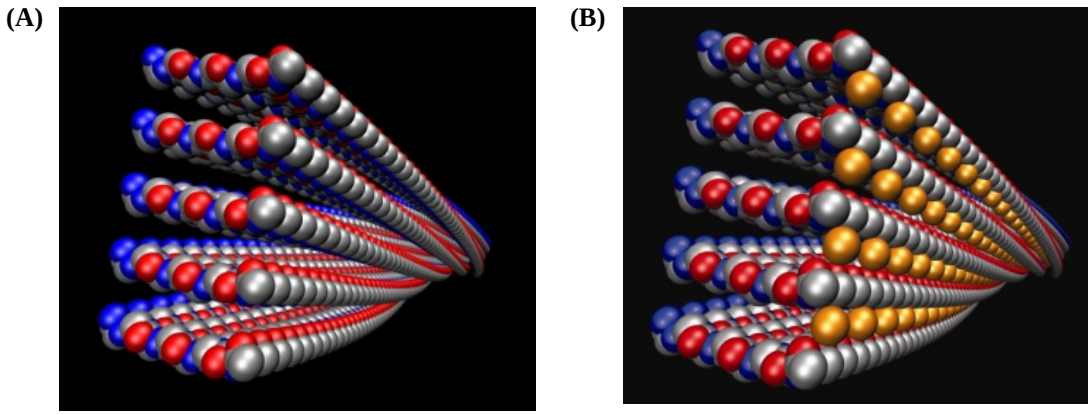

Figure 6-2: *Structural model of Ac-Aβ(13-21)H14A fiber assembly (A) without metal and (B) with* Cu^{2+}*. Grey represents the histidine residues and yellow represents the* Cu^{2+}*.*

When incubated in 25 mM MES buffer at pH 5.6, NH_2-Aβ(13-21)K16A develops β-sheet secondary structure, showing an increase in mean residue molar ellipticity (MRME) by circular dichroism (CD) at 212 nm (Figure 6-3B). TEM reveals that Aβ(13-21)K16A assembles into twisted fibril dimmers (Figure 6-3A).

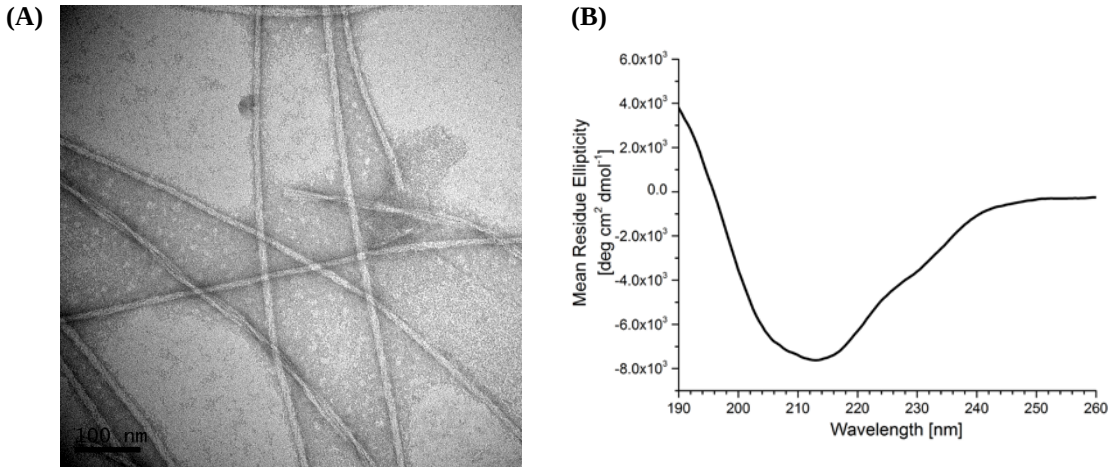

Figure 6-3: *(A) TEM micrograph of 2 mM Aβ(13-21)K16A. Scale bar 100 nm and (B) CD spectrum of Aβ(13-21)K16A.*

Inhibitory effect of Cu^{2+} on NH_2-Aβ(13-21)K16A has been reported [20]. A blue shift of the Cu^{2+} λ_{max} upon addition to K16A was observed by UV, suggesting that the Cu^{2+} is bound to the peptide but there was no fiber formation observed by TEM and no secondary structure could be determined by CD suggesting no β-sheet formation. It was concluded that the Cu^{2+}-bound NH_2-Aβ(13-21)K16A remain as soluble dimers in solution (Figure 6-4A). However, my observation was quite different from what was reported. I observed that the Cu^{2+} did not inhibit fiber formation but slowed it down considerably.

Initially, upon addition of Cu^{2+} to NH_2-Aβ(13-21)K16A, I observed the same UV spectrum with Cu^{2+} λ_{max} shifted to 602 nm (Figure 6-4C). CD measurement at 4 days of incubation displayed a minimum at ~198 nm, indicative of random coil structure and TEM taken at the same time showed only particle formation (Figure 6-4D). Interestingly, after 1 of month incubation, the Cu^{2+} λ_{max} shifted to ~565 nm (Figure 6-4D), indicating that the Cu^{2+} environment has changed. Instead of the minimum at 198 nm initially observed, the CD spectrum now displays a maximum ~200 nm and a minimum at 216 nm characteristic of a β-sheet structure (Figure 6-4B). The CD signal continued to increase over 3 months. Upon sampling for TEM, amazingly, Cu^{2+}-NH_2-Aβ(13-21)K16A had transitioned from amorphous dimers to well defined nanoribbons (Figure 6-4F). Increasing the incubation time further did not have any impact on the assembly nor did incubating the Cu^{2+}-NH_2-Aβ(13-21)K16A at different temperatures (4ºC, 25 ºC and 37 ºC). The final morphology of the assembly is maintained at the temperature range studied.

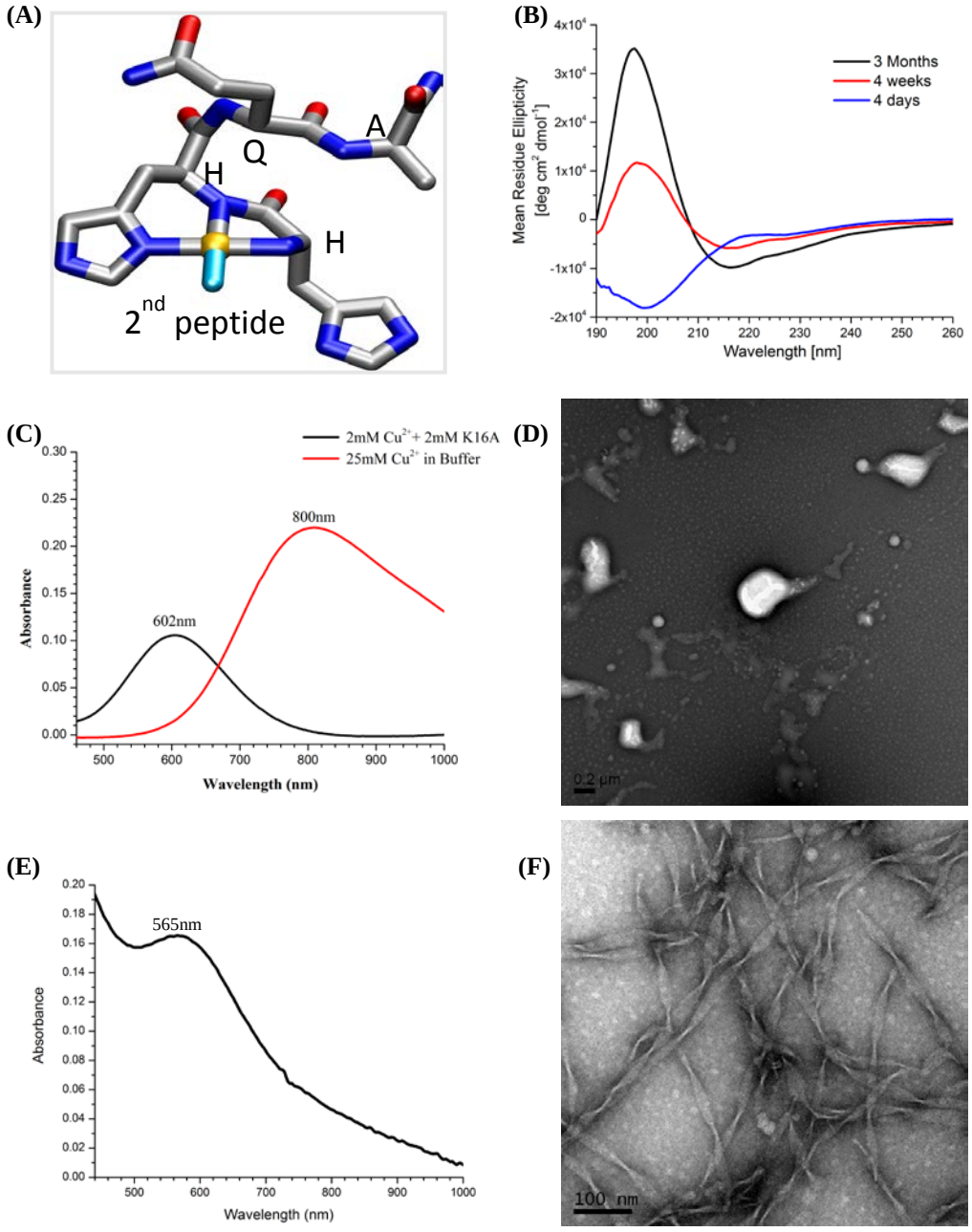

Figure 6-4: *Characterization of Cu^{2+}-NH_2-Aβ(13-21)K16A assemblies (A) Proposed model for Cu^{2+} coordination with NH_2-Aβ(13-21)K16A (B) Time dependent CD spectrum of Cu^{2+}-NH_2-Aβ(13-21)K16A. (C) UV-vis absorbance of Cu^{2+}-NH_2-Aβ(13-21)K16A incubated for 4 days. (D) TEM micrograph of Cu^{2+}-NH_2-Aβ(13-21)K16A incubated for 4 days. Scale bar 200 nm (E) UV-vis absorbance of Cu^{2+}-NH_2-Aβ(13-21)K16A incubated for 4 weeks. (F) TEM micrograph of Cu^{2+}-NH_2-Aβ(13-21)K16A incubated for 4 weeks. Scale bar 100 nm. All assemblies were at 2 mM NH_2-Aβ(13-21)K16A (with 1:1 Cu^{2+}ratio) in 25 mM MES, pH 5.6.*

Determination of Redox Potentials of Cu-Aβ complexes

Some enzymes in nature bind copper (cupro-enzymes) to catalyze key redox reactions essential to metabolic processes such as mitochondrial respiration [29]. However, these enzymes also offer some protection against the toxic effects of copper. The redox cycling of the copper ion in Cu-Aβ complex has been proposed as the basis of the generation of ROS, therefore determination of Cu^{2+} redox potential in this complex is crucial. Values from different studies have been reported in the literature. One report proposes a quasi-reversible redox process at a high potential ($E_{1/2}$ = 0.8 V vs. NHE) [14]. Other studies found lower redox potentials at $E_{1/2}$ = 0.5 V and 0.3 V vs. NHE, associated to irreversible [30] and reversible processes [31], respectively. There are lots of discrepancies in the results which may be linked to variations in the working conditions such as different working electrodes used and/or different buffering conditions. As a result, there is still no real consensus about the redox potential of the Cu-Aβ complex, therefore, more studies are required to investigate the redox potential of Cu-Aβ complex. Ac-Aβ(13-21)H14A, when bound to Cu^{2+} has been shown to be as toxic as full-length Aβ found in Alzheimer's patient plaques (Figure 6-5) whereas NH_2-Aβ(13-21)K16A is not [20].

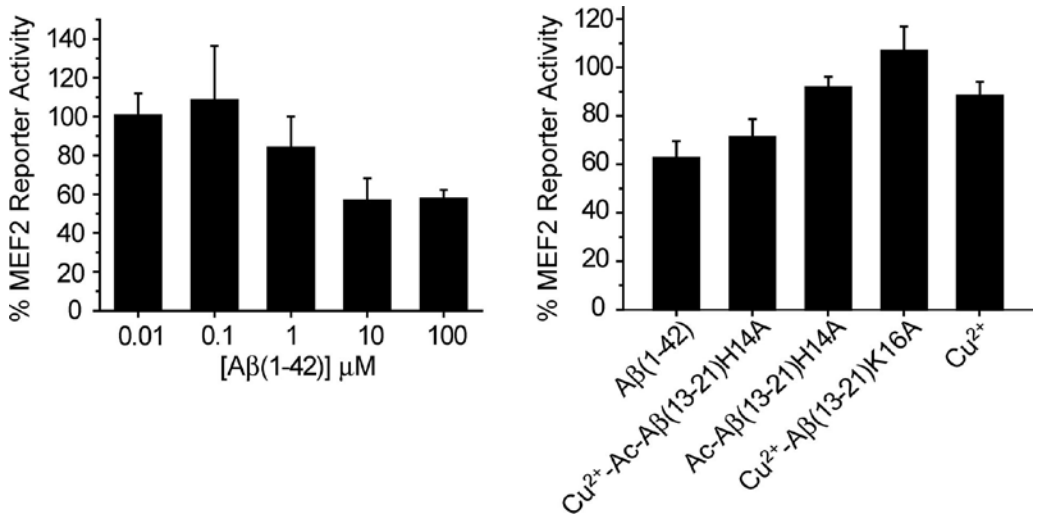

Figure 6-5: *MEF2 luciferase reporter gene assay. (Left) Aβ(1–42) dose-dependent response. (Right) Cu^{2+}–Ac-Aβ(13–21) H14A fibrils are as toxic as Aβ(1–42) and Aβ(10–35) fibrils and Cu^{2+}–Aβ (13–21) K16A complex is nontoxic. Peptide concentration is 10 μM. Adapted from [20].*

To expand upon this finding, I determined the reduction-oxidation potential of Cu^{2+}-Ac-Aβ(13-21)H14A and Cu^{2+}-NH_2-Aβ(13-21)K16A using cyclic voltammetry and then correlated this redox potential to their ability to generate reactive oxygen species (ROS). The hypothesis is that the toxic Cu^{2+}-Ac-Aβ(13-21)H14A should have a redox potential similar or close to that of Cu-Aβ(1-42) and the non-toxic Cu-Aβ(13-21)K16A should have a redox potential lower than Cu^{2+}-Ac-Aβ(13-21)H14A. Given that a key issue in understanding the toxicity of the Aβ peptides to neurons is related to the production of ROS [2, 3, 32], I hypothesize that Cu^{2+}-Ac-Aβ(13-21)H14A should generate more ROS than Cu^{2+}-NH_2-Aβ(13-21)K16A.

Electrochemical methods can be used to accurately and directly determine the potentials of redox-active biomolecules. This can be achieved by carefully choosing the electrode materials and electrolyte system for facile electron transfer at the electrode/solution interface. Cyclic voltammetry is a widely used technique for acquiring

qualitative electrochemical information about metal-containing complexes and can report on their chemical reactivity. The diagram for the experimental set-up is shown in Figure 6-6. The set-up contain a small volume cell with a three electrode system (working electrode, auxillary electrode and reference electrode).

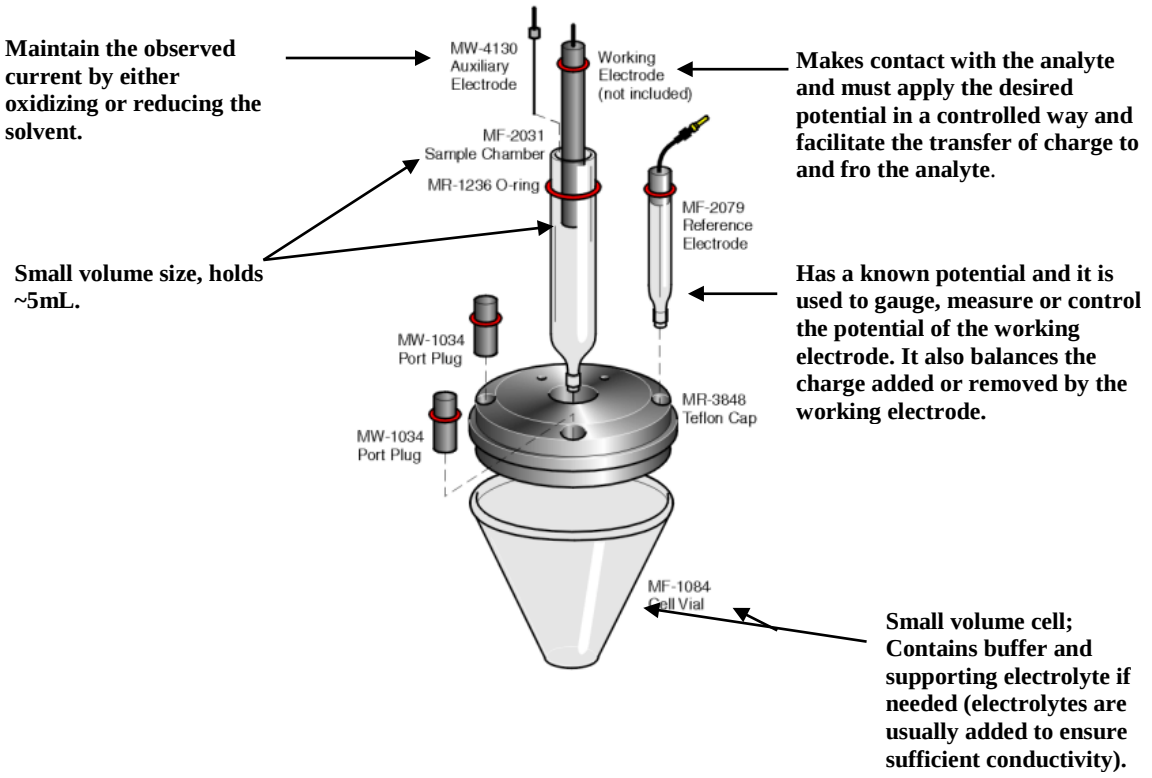

Figure 6-6: *Experimental set-up for cyclic voltammetry (https://www.basinc.com/products/ec/lvc-c3.php)*

The formal reduction potential E° is given as $E° = [E_{pa} + E_{pc}]/2$, where E_{pa} is the anodic or oxidation peak and the E_{pc} is the cathodic or reduction peak. A reversible voltammogram characteristic of fast electron exchange exhibits a $\Delta E°$ of about 59 mV.

To determine the redox potential and be able to compare our measurements to other measurements, it is necessary to obtain a control voltammogram with $K_3Fe^{III}(CN)_6$

(potassium ferrocyanide) under the same experimental conditions I will be working with. The control was run each time a cyclic voltammetry experiment was done. For the result presented, the calculated E°' was 0.17 V versus Ag/AgCl reference electrode. Considering that our working conditions is different from others, 0.17 V was an appropriate approximation of E° for $Fe^{III}(CN)_6^{3-}/Fe^{II}(CN)_6^{4-}$ system, given the resulting reversible voltammogram obtained (Figure 6-7). Comparison to the literature value of 0.36 V versus NHE for $Fe^{III}(CN)_6^{3-}/Fe^{II}(CN)_6^{4-}$ [33], indicates a +0.15 V difference with respect to the experimental E° calculated here. Therefore, using $Fe^{III}(CN)_6^{3-}/Fe^{II}(CN)_6^{4-}$ system as a reference, a value of 0.19 V is added to the E°' values obtained here versus Ag/AgCl .

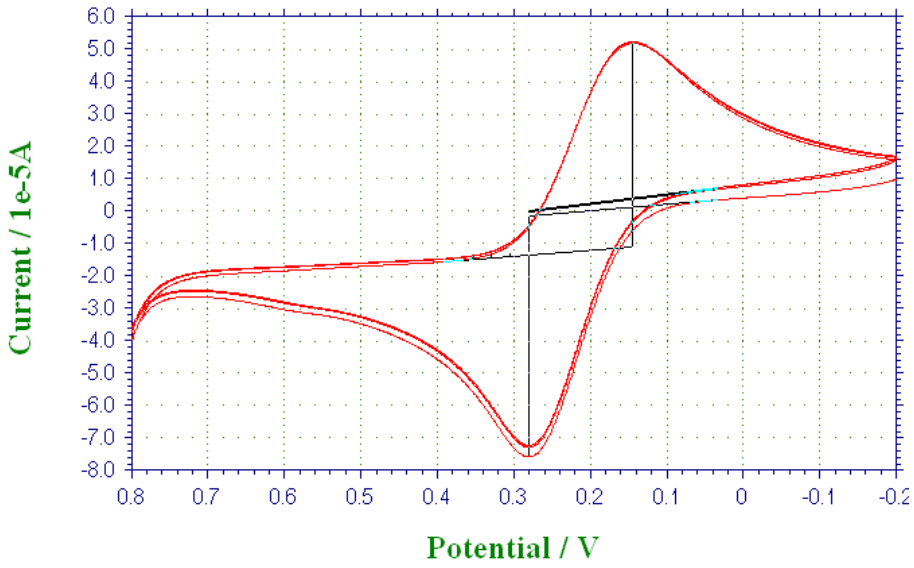

Figure 6-7: *Cyclic voltammogram recorded at scan rates of 100 mV/s for* $Fe^{III}(CN)_6^{3-}/Fe^{II}(CN)_6^{4-}$

The redox potential for the reduction of copper center in Cu^{2+}-Aβ(13-21)H14A was determined to be 0.10±0.02 V vs Ag/AgCl (0.29 V versus NHE) (Figure 6-8A). This is

similar to the redox potential previously reported for the complexes of Aβ(1-16), Aβ(1-28) and Aβ(1-42) with Cu(II) which was 0.08 V vs Ag/AgCl (0.28 V versus NHE) [31, 34]. The cyclic voltammogram exhibit a quasi-reversible ΔE°=84 mV characteristic of a slow electron exchange. The redox potential of Cu^{2+}-Aβ(13-21)K16A is 0.26±0.02 V vs Ag/AgCl (0.45 V versus NHE), this is higher than the redox potential of Cu^{2+}-Aβ(13-21)

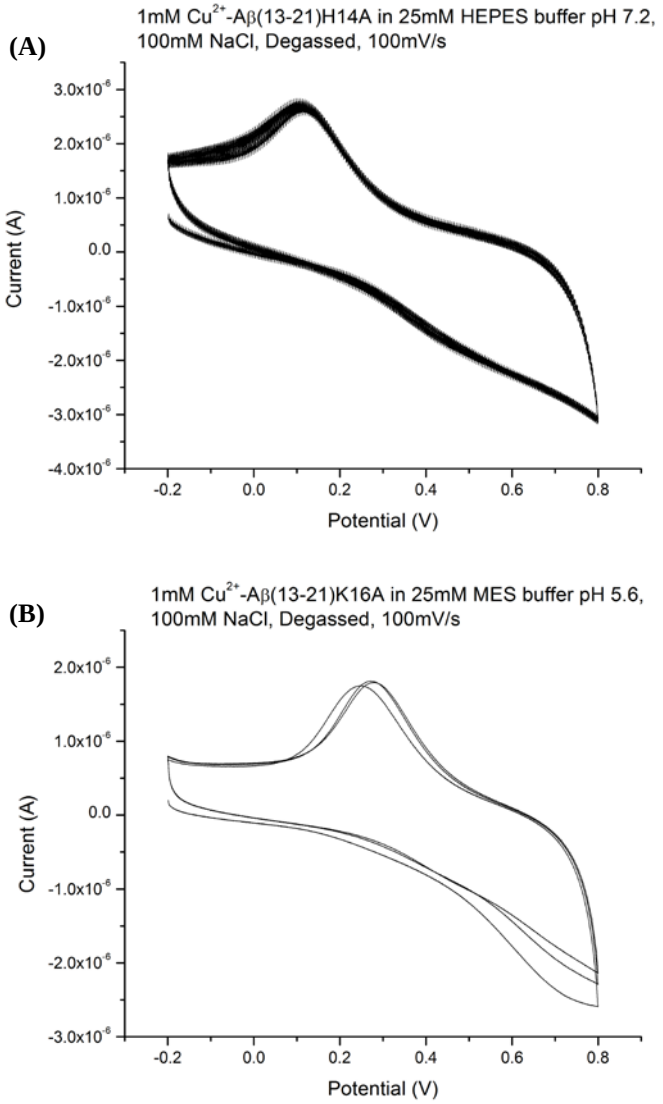

Figure 6-8*: Cyclic voltammogram recorded at scan rates of 100 mV/s for (A) 2 mM Cu^{2+}-2 mM Aβ(13-21)H14A, $E_{1/2}$ = 0.29 V versus NHE, 0.09 V vs Ag/AgCl (B) 2 mM Cu^{2+}-2 mM Aβ(13-21)K16A, $E_{1/2}$ = 0.45 V versus NHE, 0.26 V vs Ag/AgCl.*

H14A. The more positive potential for Cu^{2+}-Aβ(13-21)K16A compared to that of Cu^{2+}-Aβ(13-21)H14A indicates the ease of reduction in Cu^{2+}-Aβ(13-21)K16A which means it favored the Cu(I) reduced state much more than Cu^{2+}-Aβ(13-21)H14A. The voltammetric response for Cu^{2+}-Aβ(13-21)K16A also shows a quasi-reversible electron transfer, ΔE°=113 mV characteristic of a slow electron exchange, even slower than that of Cu^{2+}-Aβ(13-21)H14A . Therefore, redox cycling is likely to be more difficult for Cu^{2+}-Aβ(13-21)K16A than Cu^{2+}-Aβ(13-21)H14A. The reason for this might be that upon redox reaction, the Cu^{2+}-Aβ(13-21)K16A undergoes a small conformational change and once in that conformation, the re-oxidation is more difficult because of the new geometry. For oxidation to occur, the copper center needs to migrate back to its initial site, hence the larger ΔEº compared to Cu^{2+}-Aβ(13-21)H14A. There is need for more structural studies to fully understand this phenomenon.

Determination of H_2O_2 Production by Cu^{2+}-Aβ complexes

To further exploit the catalytic range of Cu^{2+}-Aβ, the ability to generate ROS was studied. To achieve ROS generation, the redox potential of Aβ-Cu^{2+} complexes has to be higher than that of the reductant, for example, ascorbate with a redox potential of 0.052 V vs NHE [35]. Also the redox potential of Aβ-Cu^{2+} has to be lower than that of the O_2/H_2O_2 redox couple of 0.296 V vs NHE [36]. Generally, H_2O_2 reduction is obtained at potentials of about +0.1 to -0.05 V vs. Ag|AgCl [37, 38]. When the Aβ-Cu^{2+} is reduced, the Aβ-Cu^{+} produced could subsequently reduce oxygen to form hydrogen peroxide via a catalytic cycle (Figure 6-9).

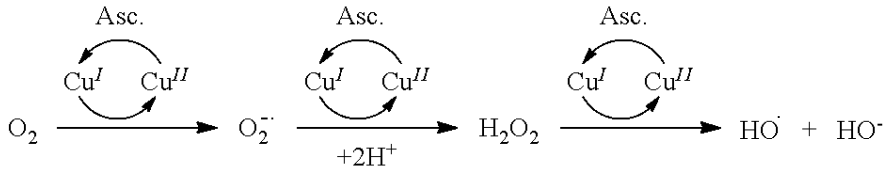

Figure 6-9*: Oxygen reduction by copper redox cycling in the presence of ascorbate.*

Both Cu^{2+}-Aβ(13-21)H14A and Cu^{2+}-Aβ(13-21)K16A have redox potentials higher than that of ascorbate so thermodynamically, they can both be reduced by ascorbate. Comparing the redox potential of Cu^{2+}-Aβ(13-21)H14A and Cu^{2+}-Aβ(13-21)K16A to that of O_2/H_2O_2 redox couple, it is clear that O_2 should be incapable of oxidizing Cu^{+}-Aβ(13-21)K16A because of its higher redox potential. In contrast, Cu^{2+}-Aβ(13-21)H14A with a lower redox potential that O_2/H_2O_2 redox couple should be easily oxidized. Because redox cycling of copper is the underlying mechanism to produce reactive oxygen species (ROS), it seems reasonable that Cu^{2+}-Aβ(13-21)H14A should generate higher quantities of H_2O_2.

The catalytic activity of the Cu^{2+}-bound assemblies to generate H_2O_2 was initially studied with dichlorofluorescein diacetate assay but there was too much background fluorescence from the MES buffer control for Cu^{2+}-Aβ(13-21)K16A. Instead, the Amplex Red Hydrogen Peroxide/Peroxidase Assay kit was used. This assay uses the Amplex Red reagent (10-acetyl-3,7-dihydroxyphenoxazine) in combination with horseradish peroxidase (HRP), to detect hydrogen peroxide released from biological samples, including cells or generated in enzyme-coupled reactions. The Ample Red reagent reacts with H_2O_2 in a 1:1 stoichiometry to produce the red-fluorescent oxidation product,

resorufin which has λ_{ex} and λ_{em} of ~ 571 nm and 585 nm respectively. The assay can be performed fluorometrically or spectrophotometrically.

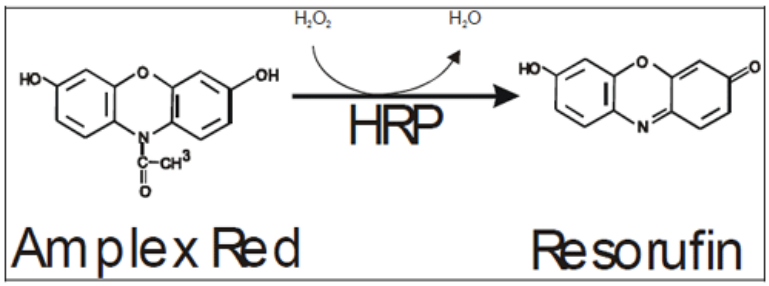

Figure 6-10*: Scheme for Amplex Red Hydrogen Peroxide/Peroxidase Assay.*

In the presence of stoichiometric ratio of Cu^{2+} to Aβ (100 μM), the rate of H_2O_2 generated increases gradually with time (Fig 6-11). After 3 hours of reaction, the amount of H_2O_2 generated in the presence of Cu^{2+}-Aβ and free Cu^{2+} is shown in Figure 6-12. The amount of H_2O_2 detected was in the order of Cu^{2+}-Aβ(13-21)K16A > Cu^{2+}-Aβ(13-21)H14A > free Cu^{2+}. Both Cu^{2+}-Aβ(13-21)H14A and Cu^{2+}-Aβ(13-21)K16A generated more H_2O_2 that free Cu^{2+} which agrees with previous studies [16, 39]. At a lower concentration of Cu^{2+} to Aβ of 10 μM, Cu^{2+}-Aβ(13-21)K16A still produced the highest amount of H_2O_2 but the order of production is now different Cu^{2+}-Aβ(13-21)K16A > Cu^{2+}-Aβ(13-21)H14A ≤ free Cu^{2+}. That much more H_2O_2 was generated by the Cu^{2+}-Aβ(13-21)K16A suggests that several other factors may be involved in the process. In contrast to the H_2O_2 generation measurements, the redox potential was measured in the absence of oxygen and reductant. It is possible that the presence of oxygen and other components in the amplex red assay could influence the redox potential of Cu^{2+}-Aβ(13-21)K16A to an acceptable value for H_2O_2 generation. Another factor might be the pH and buffer difference, the redox potential values of Cu^{2+}-Aβ(13-21)K16A and Cu^{2+}-Aβ(13-

21)H14A were determined with 25 mM MES buffer at pH 5.6 and 25 mM HEPES buffer at pH 7.2 respectively. In contrast, the amplex red assay for H_2O_2 generation was done in the supplied reaction buffer in the kit which was 50 mM sodium phosphate at pH 7.4.

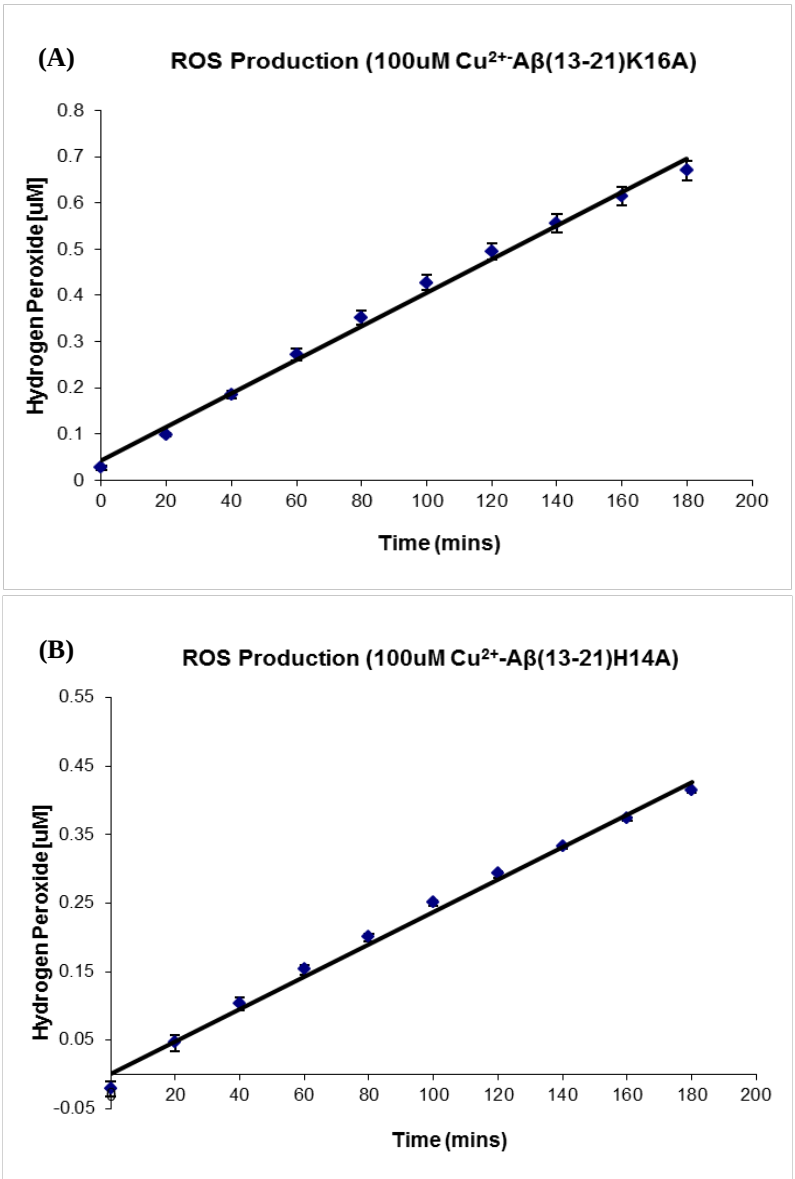

***Figure 6-11**: Rate of H_2O_2 production in the presence of (**A**) Cu^{2+}-Aβ(13-21)K16A and (**B**) Cu^{2+}-Aβ(13-21)H14A. The rates were measured at room temperature with [Aβ−Cu(II)] = 100 μM. Each data point is the average of at least three replicate measurements.*

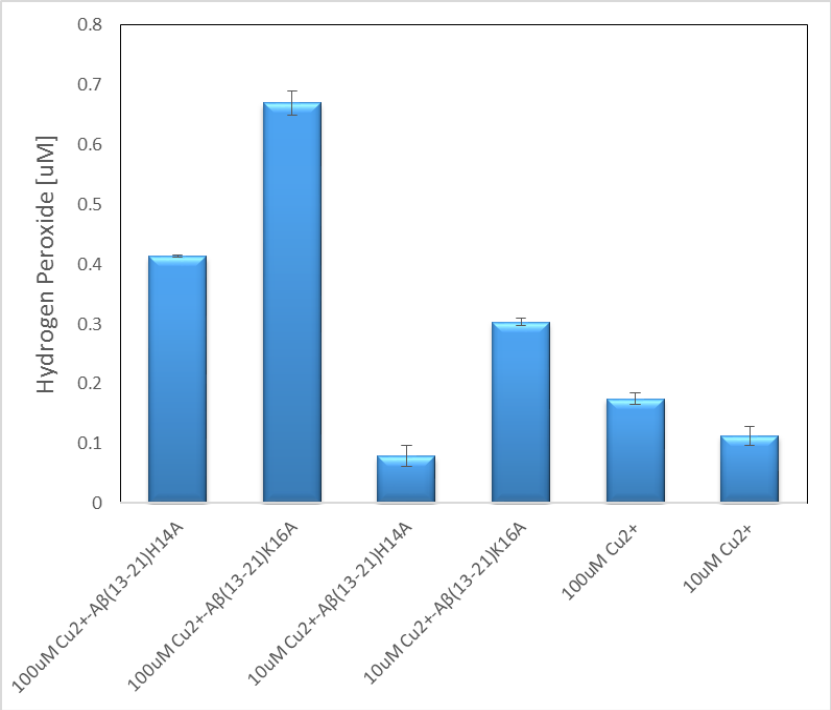

***Figure 6-12**: Catalytic H_2O_2 production by 100 µM and 10 µM of Aβ-Cu^{2+} and free Cu^{2+} after 3 hours of incubation.*

It is possible that the phosphate buffer could have altered the redox potential of Cu^{2+}-Aβ(13-21)K16A making H_2O_2 generation more feasible. In fact, it has been found that increasing the pH of a solution makes the redox potential more negative and vice versa [40-42].

Structural Characterization of Aβ assemblies in the presence of Zn^{2+}

Mutagenesis and pH dependence studies on human Aβ peptide self-assembly in the presence of Zn^{2+} show that His13 is crucial for the Zn^{2+} binding [25, 43]. Therefore, in order to simplify the Zn^{2+} binding modes of Aβ peptide, several truncated Aβ peptides, such as Aβ(10-21) and NH_2-Aβ(13-21)K16A and Ac-Aβ(13-21)H14A, have been

investigated in our lab [21, 22]. These studies have shown that Zn^{2+} will facilitate the self-assembly of Aβ(10-21) to induce amyloid fibril formation. Also, *in vitro*, Zn^{2+} accelerates the self-assembly of NH_2-Aβ(13-21)K16A and induces the formation of ribbons while the peptide without Zn^{2+} assembled into fibers [21]. To further this research, I have studied the effect of temperature on the self-assembly of NH_2-Aβ(13-21)K16A.

It is well documented that external stimuli, such as pH, temperature, and ionic strength, can control the protein folding and peptide self-assembly by changing the driving force [44-46]. From my temperature studies on assembly of NH_2-Aβ(13-21)K16A in the presence of Zn^{2+}, the results show that NH_2-Aβ(13-21)K16A can self-assemble into different morphologies incubated with Zn^{2+} at different temperatures. At higher temperature, circular dichroism (CD) reveal that the self-assembly of Zn^{2+}-NH_2-Aβ(13-21)K16A results in increased β-sheet signature with an increase in mean residue molar ellipticity (MRE) at 199 nm and 224 nm. The CD minimum at 224 nm and maximum at 199 nm is much more pronounced in the 37ºC sample followed by the 25ºC sample while the 4ºC sample exhibited the least β-sheet signature (Figure 6-13A).

TEM images show that NH_2-Aβ(13-21)K16A self-assembles into different morphologies at different temperatures in the presence of Zn^{2+} (Figure 6-13B,C,D). At 4ºC, Zn^{2+}-NH_2-Aβ(13-21)K16A assemble into two types of ribbons (Figure 6-13B), with the average widths of 30 nm and 110 nm. At 25ºC, Zn^{2+}-NH_2-Aβ(13-21)K16A self-assemble into the mixture of ribbons and nanotubes. The widths of ribbons ranges from 170-282 nm while the average width of nanotube was 221 nm. When the peptides were incubated at 37ºC, all the Zn^{2+}-NH_2-Aβ(13-21)K16A self-assemble into nanotubes of

varying sizes, with the most encountered widths of 180 nm, 242 nm and 287 nm. Evidently, increasing the incubation temperature can increase the sheets lamination during the self-assembly process. There is no clear explanation for this behavior. The nanotubes formed are very stable and they do not revert back to ribbons if the temperature is lowered.

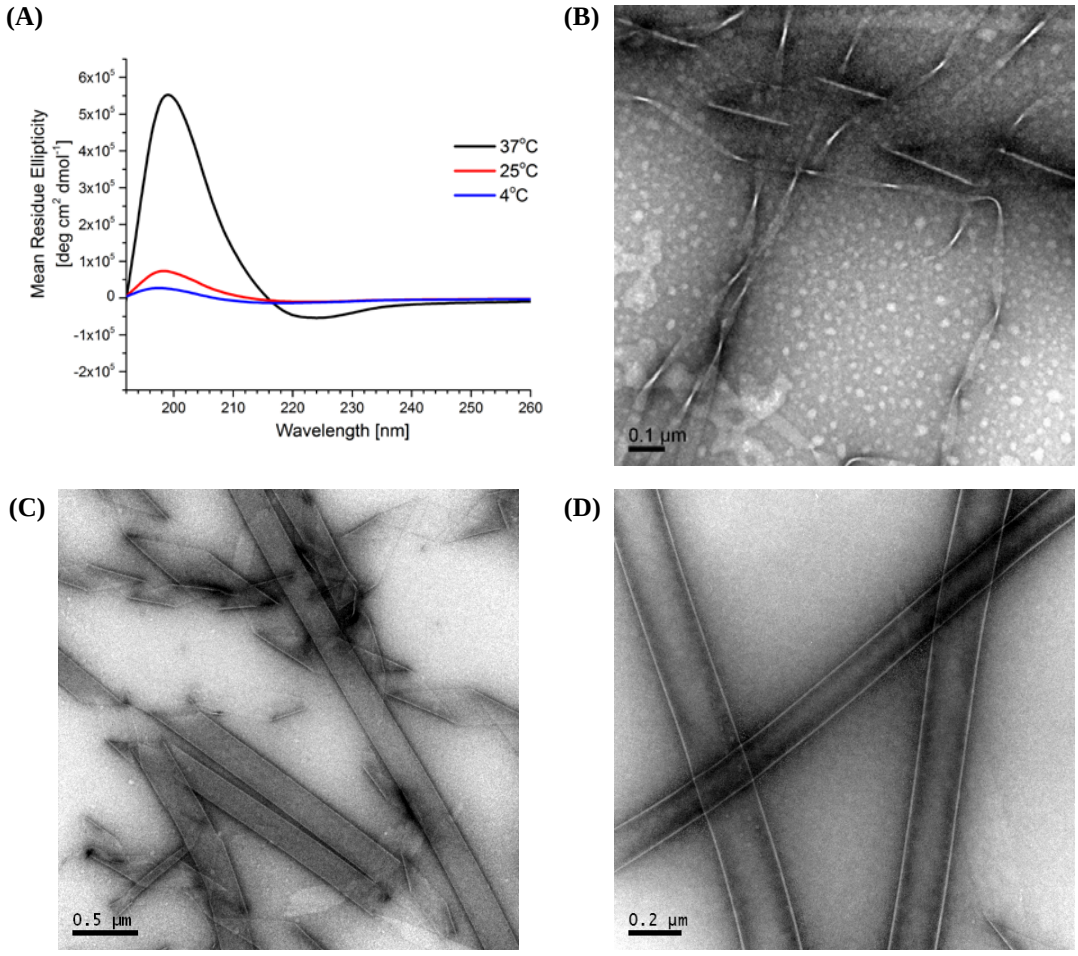

***Figure 6-13**: Temperature-dependent (A) CD spectra of 0.5 mM Aβ(13-21)K16A in 25 mM MES buffer at pH 5.6 in the presence of 0.5 mM Zn^{2+} after three days at the indicated temperatures and TEM images of 0.5 mM Aβ(13-21)K16A in 25 mM MES buffer at pH 5.6 in the presence of 0.5 mM Zn^{2+}at (**B**) 4ºC (**C**) 25ºC and (**D**) 37ºC.*

In the presence of Zn^{2+}, Ac-Aβ(13-21)H14A peptides self-assemble into fibers in solution (Figure 6-14A). The fibers formed are morphologically similar to the fibers formed by the peptide without Zn^{2+}. CD measurement showed an increase in the β-sheet signature when Ac-Aβ(13-21)H14A was incubated with Zn^{2+} (Figure 6-14B) confirming that Zn^{2+} does accelerate the self-assembly of Ac-Aβ(13-21)H14A. Temperature studies was also carried out on Zn^{2+}-Ac-Aβ(13-21)H14A and there is no morphological change observed when the Zn^{2+}-Ac-Aβ(13-21)H14A was incubated at a different temperature.

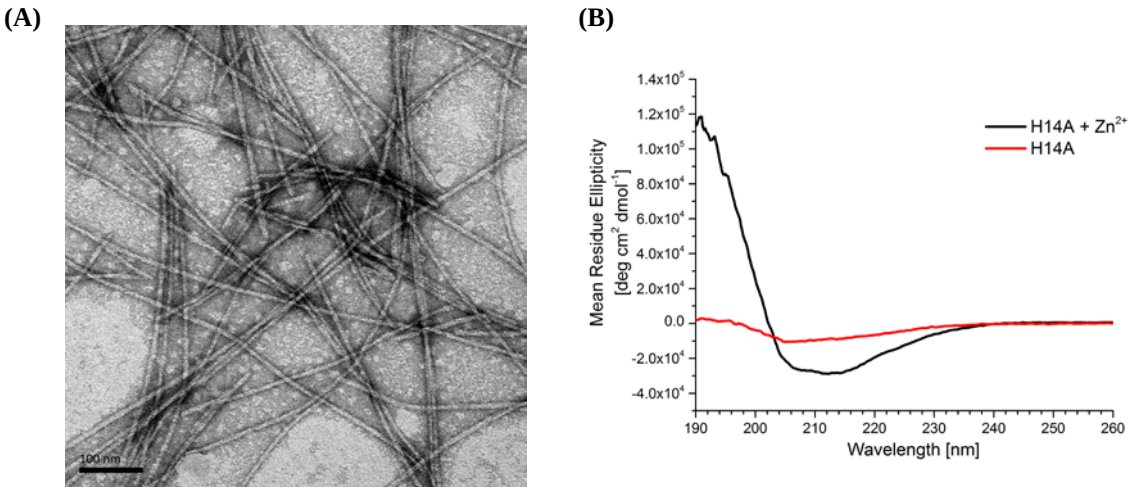

***Figure 6-14**: (**A**) TEM images of 0.5 mM Aβ(13-21)H14A in 25 mM HEPES buffer at pH 7.2 in the presence of 0.5 mM Zn^{2+} and (**B**) CD spectra of 0.5 mM Aβ(13-21)H14A and 0.5 mM Zn^{2+}-Aβ(13-21)H14A*

X-ray absorption spectroscopy (XAS) studies done on the ribbons formed at 25ºC by Zn^{2+}-NH_2-Aβ(13-21)K16A and the fibers formed by Zn^{2+}-Ac-Aβ(13-21)H14A revealed that the Zn^{2+} chelates two His residues in both fibers and ribbons with a distinct inter-sheet His-Zn^{2+}-His coordination modes between His 13 and His 14 in Zn^{2+}-NH_2-Aβ(13-21)K16A (Figure 6-15). However, elimination of inter-sheet metal binding in

H14A results in two His 13s on one face of the β-sheet chelating Zn^{2+} in an intra-sheet His-Zn^{2+}-His chelation [21].

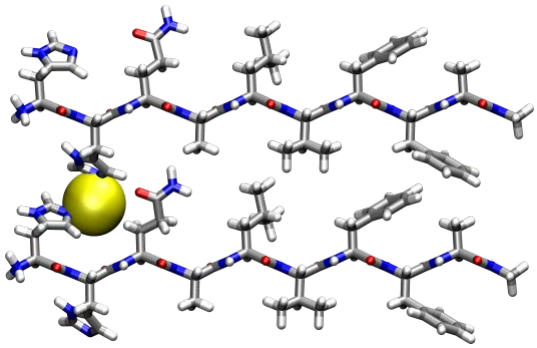

Figure 6-15: *Structural model of NH_2-Aβ(13-21)K16A ribbon assembly with Zn^{2+} showing inter-sheet His 13-Zn^{2+}-His 14 chelation. Yellow ball represents the Zn^{2+}.*

Structural Characterization of Aβ assemblies in the presence of Co^{2+} and Ni^{2+}

Although Co^{2+} and Ni^{2+} are not implicated in AD, the binding of Aβ to Co^{2+} and Ni^{2+} was studied to further understand the interaction of Aβ with other metals and to study the catalytic activities of metal-bound assemblies in the latter part of this chapter.

Ac-Aβ(13-21)H14A was incubated with equimolar amounts of Ni^{2+} and Co^{2+}, CD measurement after 3 days showed an increase in the β-sheet signature in the presence of Ni^{2+} indicating that the Ni^{2+} accelerates fiber formation (Figure 6-16A). In the presence of Co^{2+}, the β-sheet signature was not increased compared to the Ac-Aβ(13-21)H14A alone, this means that the Co^{2+} might bind to the Ac-Aβ(13-21)H14A but not necessarily accelerating the self-assembly process.

By TEM Co^{2+}-Ac-Aβ(13-21)H14A assemble into single fibers (Figure 6-16B)

that are morphologically similar to their Cu^{2+}-bound counterparts (Figure 6-1C), whereas the fibers formed by the Ni^{2+}-Ac-Aβ(13-21)H14A peptide are mostly dimers (Figure 6-16C) and closely resemble the fibers formed by Ac-Aβ(13-21)H14A without metals (Figure 6-1A). This shows that the metal binding site in the Ac-Aβ(13-21)H14A is flexible enough to accommodate different kinds of metals.

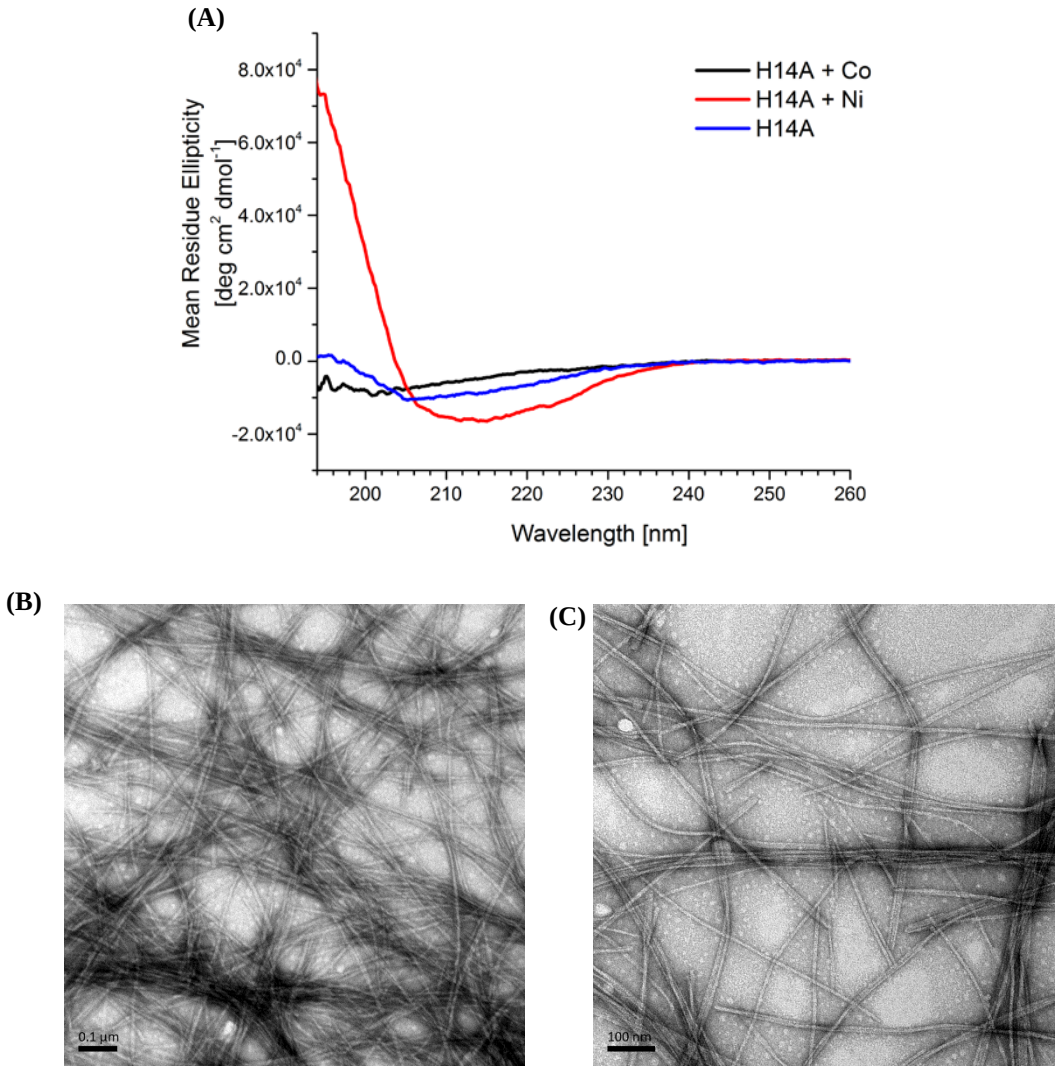

Figure 6-16: *Characterization of $Co^{2+}$and Ni^{2+}bound Ac-Aβ(13-21)H14A assemblies (A) CD spectrum of M^{2+}-Ac-Aβ(13-21)H14A and TEM micrograph of (B) Co^{2+}-Ac-Aβ(13-21)H14A. (C) Ni^{2+}-Ac-Aβ(13-21)H14A. Scale bar is 100 nm. All assemblies were at 2 mM Ac-Aβ(13-21)H14A (with 1:1 M^{2+}ratio) in 25 mM HEPES, pH 7.2*

NH_2-Aβ(13-21)K16A peptide was also incubated with equimolar amounts of Ni^{2+} and Co^{2+}. The CD spectrum of NH_2-Aβ(13-21)K16A in the presence of Ni^{2+} showed a minimum at ~220 nm indicating β-sheet formation (Figure 6-17A). This wavelength is red shifted compared to the NH_2-Aβ(13-21)K16A peptide alone. However, in the presence of Co^{2+}, the CD minimum was at ~210 nm (Figure 6-17B) close to what was observed for the NH_2-Aβ(13-21)K16A peptide alone. When the UV measurement was carried out, a blue shift of the Ni^{2+} λ_{max} to ~609 nm (Figure 6-17E) was observed upon addition to NH_2-Aβ(13-21)K16A suggesting that the Ni^{2+} is bound to the peptide. The same observation was also made for the Co^{2+}-NH_2-Aβ(13-21)K16A with a blue shift to ~380 nm (Figure 6-17F). These indicate that the peptides are bound to the peptides.

TEM analysis show that the Ni^{2+}-NH_2-Aβ(13-21)K16A assemble into nanoribbons (Figure 6-17C) that closely resemble the nanoribbons formed by the Cu^{2+}-NH_2-Aβ(13-21)K16A. The Co^{2+}-NH_2-Aβ(13-21)K16A assembly behaved differently, in that it did not assemble into nanoribbons but instead into clumps of very thin fiber-like morphology (Figure 6-17C). There was no morphology change even after several months of incubation. Incubating both the Co^{2+}-NH_2-Aβ(13-21)K16A and Ni^{2+}-NH_2-Aβ(13-21)K16A at different temperatures (4 ºC, 25 ºC and 37 ºC) did alter the final morphology of the assemblies.

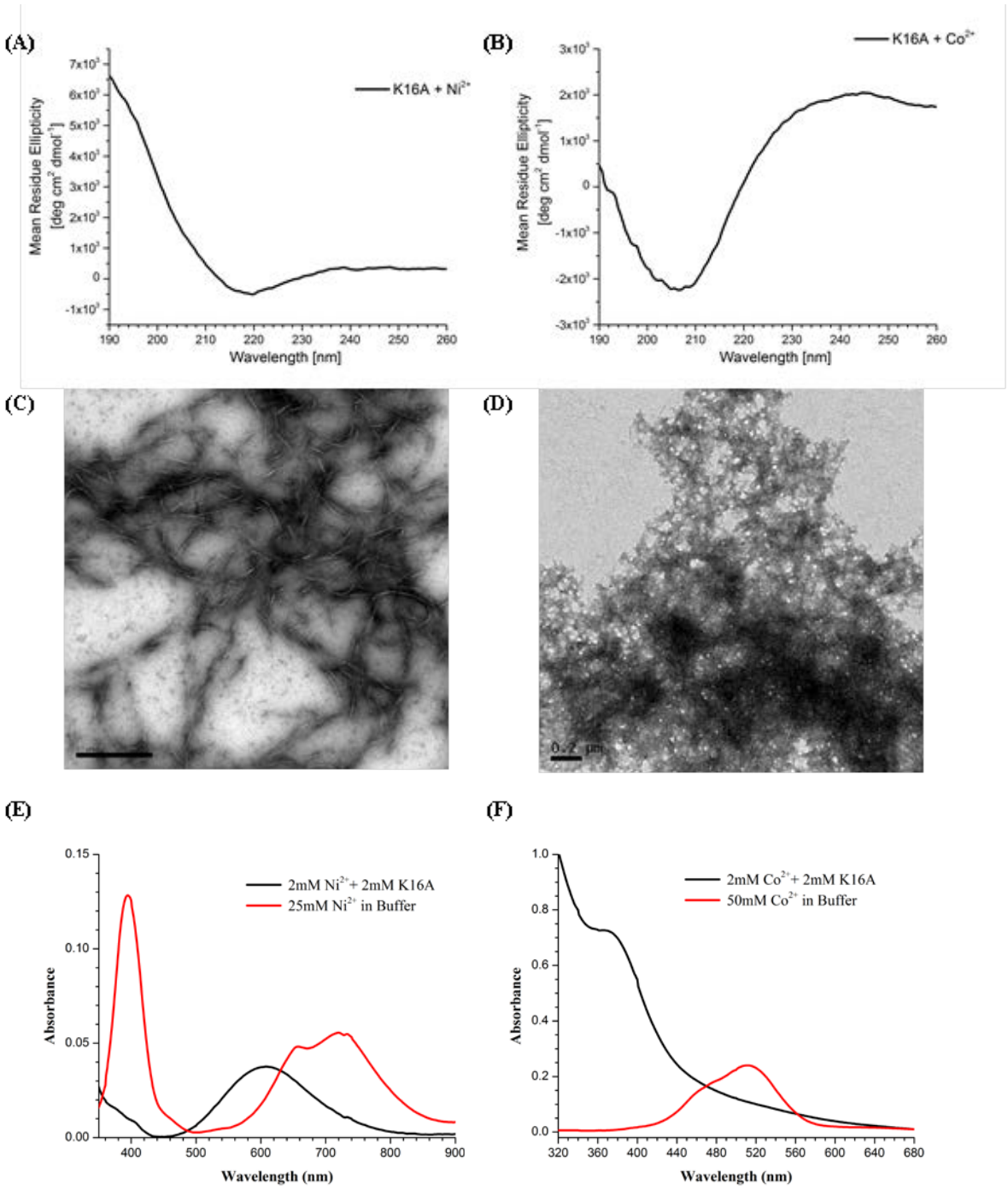

Figure 6-17: *Characterization of $Co^{2+}$and Ni^{2+}bound NH_2-Aβ(13-21)K16A assemblies (A) CD spectrum of Ni^{2+}-NH_2-Aβ(13-21)K16A. (B) CD spectrum of Co^{2+}-NH_2-Aβ(13-21)K16A (C) TEM micrograph of Ni^{2+}-NH_2-Aβ(13-21)K16A. Scale bar 500 nm (D) TEM micrograph of Co^{2+}-NH_2-Aβ(13-21)K16A. Scale bar 200 nm (E) UV-vis absorbance of Ni^{2+}-NH_2-Aβ(13-21)K16A. (F) UV-vis absorbance of Co^{2+}-NH_2-Aβ(13-21)K16A. All assemblies were at 2 mM NH_2-Aβ(13-21)K16A (with 1:1 M^{2+}ratio) in 25 mM MES, pH 5.6.*

Retroaldol Activity of Zinc Assemblies

Class I aldolases utilize an enamine based mechanism to catalyze the reversible reaction through formation of a Schiff base intermediate between an active site lysine and the carbonyl carbon of the substrate while Class II aldolases mediate this process by using a zinc cofactor that facilitate enolate formation by coordination to the substrate's carbonyl oxygen [47, 48].

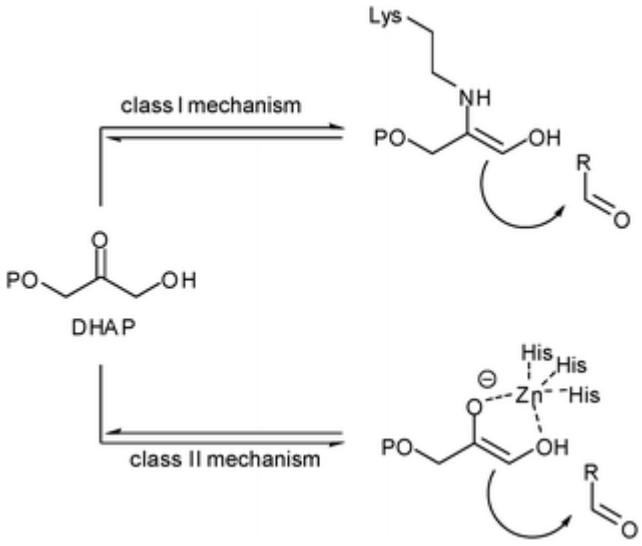

Figure 6-18: *Mechanism of class I and II aldolases. Adapted from [49].*

In Zn^{2+}-induced peptide nanotubes, zinc ions have tetrahedral coordination geometry, coordinating to two histidines, one amino group, and one water molecule, which is similar to zinc catalytic centers in most zinc enzymes. Therefore, the defined Zn^{2+} ions in Zn^{2+}-induced peptide assemblies could very likely serve as catalytic centers to mimic some zinc enzymes. As the binding ligands are at the N-terminal of the amyloid peptide and located on the surface of the peptide assemblies, it is possible to modify the binding ligands to generate the designed chemistry. Since zinc ions are packed on the

surfaces of peptide assemblies, the highly packed zinc catalytic centers may significantly enhance reaction efficiency. My hypothesis is that Zn^{2+}-Aβ peptide assemblies can mimic class II aldolase and catalyze a retro-aldol reaction.

It should be noted that Aβ(13-21)H14A contain a lysine residue and it forms fibers, the lysine residue should not be a problem since I have shown in the previous chapters that fibers are not catalytic. The difference between the Aβ(13-21)K16A and Aβ(13-21)H14A is that the former has two histidine residues while the later has one histidine and a lysine so the hydrophobicity of the two peptides is close.

The Zn^{2+}-Aβ catalyzed retro-aldol reaction was carried out under the same condition as the lysine catalyzed reaction with the exception of the buffer. Since Aβ(13-21)K16A assemblies are only stable in 25 mM MES pH 5.6, this buffer condition was used for all Aβ(13-21)K16A assemblies and 25 mM HEPES buffer pH 7.5 was used for all Aβ(13-21)H14A assemblies. Ac-KLVFFAL-NH_2 nanotubes that have been shown to catalyze the retro-aldol reactions was used as a control under the two buffer conditions to test the effects of the buffer change on the reaction.

Incubating the Aβ peptide assemblies with and without Zn^{2+} in the presence of 80 μM Methodol, both Ac-Aβ(13-21)H14A and NH_2-Aβ(13-21)K16A display little to no catalytic activity (Figure 6-19). Interestingly, Zn^{2+}-Ac-Aβ(13-21)H14A fibers was found to be catalytic at almost the same magnitude as the Ac-KLVFFAL-NH_2 nanotubes but surprisingly both Zn^{2+}-NH_2-Aβ(13-21)K16A ribbons and nanotubes were not catalytic (Figure 6-19). When Ac-KLVFFAL-NH_2 nanotubes was used to catalyze the retro-aldol reaction under the different buffer condition, it was observed that the activity of Ac-

KLVFFAL-NH_2 in MES buffer pH 5.6 was considerably lower (~65% decrease) than in HEPES buffer pH 7.5 (Figure 6-19). The unfavourable buffer condition could be responsible for the inactivity of Zn^{2+}-NH_2-Aβ(13-21)K16A assemblies, it could also be that the organization of the Zn^{2+} in the Zn^{2+}-NH_2-Aβ(13-21)K16A assemblies result in a structure that does not support catalysis. Further studies were done to check the catalytic capability of Co^{2+}, Cu^{2+} and Ni^{2+} coordinated Ac-Aβ(13-21)H14A fibers. Replacing Zn^{2+} in Zn^{2+}-Ac-Aβ(13-21)H14A with Co^{2+}, Cu^{2+} and Ni^{2+} abolished the retro-aldol activity (Figure 6-19) suggesting that only the Zn^{2+} is responsible for the activity of the Zn^{2+}-Ac-Aβ(13-21)H14A.

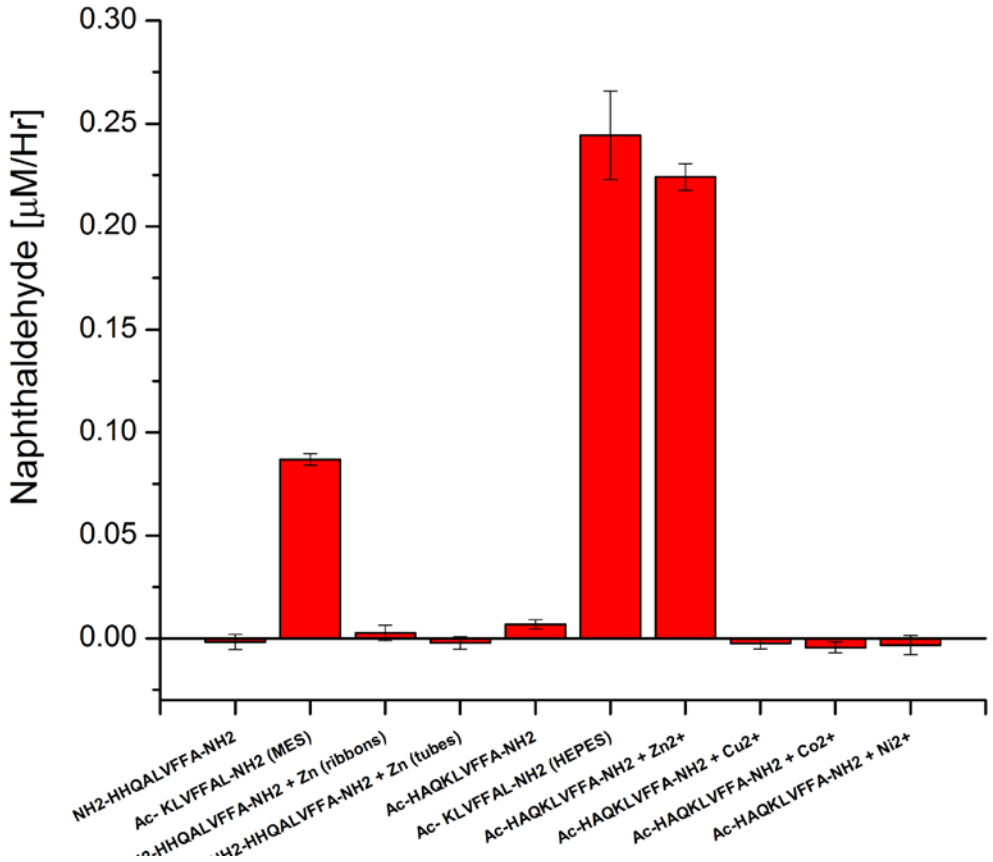

Figure 6-19: *Initial rate of production of 6-methoxy-2-naphthaldehyde by the indicated peptide assembly where the peptide concentration is 500 μM and the starting (±)-methodol concentration is 80 μM.*

Enantioselectivity studies show that the Zn^{2+}-Ac-Aβ(13-21)H14A fibers have a preference for S-methodol (Figure 6-20) just like the Ac-KLVFFAL-NH_2 nanotubes although the enantiomeric excess (ee) after 8 hours is 3±0.8%.

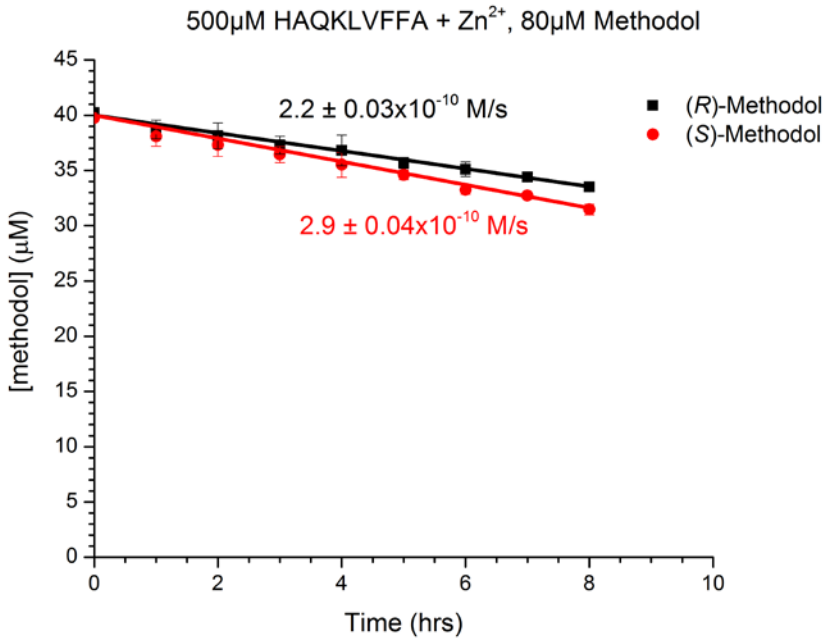

Figure 6-20: *Progressive monitoring of (±)-Methodol (80 μM) consumption in the presence of 500 μM Zn^{2+}-Ac-Aβ(13-21)H14A-NH_2 fibers over 8 hours shows little preference for S- Methodol.*

Conclusion

Copper binding to Aβ peptides is capable of inducing conformational changes that affect the aggregation and/or fibrillization processes [50]. There is ongoing debate concerning the direction of conformational changes induced by Cu^{2+}. While it has been suggested that copper binding to Aβ40 may induce β-sheet formation [51-53], others

studies suggests that copper binding prevents β-sheet formation [54-56]. Both my CD and TEM analysis suggest that copper binding increases the β-sheet content and results in fibrillization in the two model peptides Cu^{2+}-Ac-Aβ(13-21)H14A and Cu^{2+}-NH_2-Aβ(13-21)K16A studied. In fact, contrary to a previous study from our lab that Cu^{2+} inhibit the self-assembly of Cu^{2+}-NH_2-Aβ(13-21)K16A [20], I found that Cu^{2+}-NH_2-Aβ(13-21)K16A assembles at a longer incubation time. TEM images obtained demonstrate striking differences in the morphology of the structures formed by metal-free Aβ(13-21)K16A (fibers) in comparison to those generated in the presence of copper (ribbons).

There is a lot of interest in the electrochemical properties of Aβ and the electrochemical behaviour of Aβ(1–16), Aβ(1–28) and Aβ(1–42) complexes with Cu^{2+} have been described [31, 34] and the redox potentials determined for Cu^{2+}-Ac-Aβ(13-21)H14A is close to that reported whereas the redox potentials determined for Cu^{2+}-NH_2-Aβ(13-21)K16A is higher. The higher redox potential of Cu^{2+}-Ac-Aβ(13-21)K16A can be translated to the Cu^{+} state being more thermodynamically stable. The redox potential of Cu^{2+}-Aβ(13-21)H14A is high enough to react with antioxidants like ascorbic acid and cellular redox buffers like glutathione to produce the reduced Cu(I)-Aβ complex which can reduce oxygen to form H_2O_2 during the catalytic cycle but the redox potential of Cu^{2+}-Aβ(13-21)K16A falls outside the general redox potentials for H_2O_2 reduction. Amplex Red assay was used to determine the amount of H_2O_2 generation by both assemblies. The Cu^{2+}-Aβ(13-21)K16A generated more H_2O_2 than Cu^{2+}-Aβ(13-21)H14A. Although it is difficult to determine the precise reason for this difference, it may be that the different morphologies and the use of different buffering conditions for measuring redox potential and H_2O_2 generation could have resulted in lowering reduction potentials

of the Cu^{2+}-Aβ(13-21)K16A to a level to make H_2O_2 generation feasible. When correlated to amyloid toxicity, it has been shown that Cu^{2+}-Aβ(13-21)H14A is more toxic than Cu^{2+}-Aβ(13-21)K16A although in my result, Cu^{2+}-Aβ(13-21)K16A generated more H_2O_2 than Cu^{2+}-Aβ(13-21)H14A. Because the toxicity assay was done under different conditions and with different Cu^{2+}-Aβ(13-21)K16A morphology, it is possible that Cu^{2+}-Aβ(13-21)K16A soluble complexes might exhibit a different level of toxicity from Cu^{2+}-Aβ(13-21)K16A nanoribbons. Alternatively, it might be that H_2O_2 generation alone is not sufficient for toxicity. A detailed knowledge of the structure of the Cu^{2+}-Aβ(13-21)K16A structure is important to get a better understanding of this critical process of H_2O_2 generation. The fact that the redox potential measured for the peptides fall within the range of redox potentials customary for blue copper proteins (180-780 mV) [57] suggests that these Cu-Aβ assemblies can function like metalloenzymes and might be able to mimic natural type I cupro-enzymes.

Like copper, zinc have also been demonstrated to modulate amyloid-β aggregation [21, 58, 59]. Both Ac-Aβ(13-21)H14A and NH_2-Aβ(13-21)K16A assemble in the presence of Zn^{2+} with either an inter- or intra- sheet His-Zn^{2+}-His coordination mode. Temperature-dependent studies showed that increase in the incubation temperature of Zn^{2+}-Aβ(13-21)K16A altered the assembly morphology from ribbons (formed at 4ºC) to nanotubes (formed at 37ºC) suggesting that increasing the temperature tend to increase the extent of lamination. Ni^{2+} and Co^{2+} were found to also modulate amyloid-β aggregation either by accelerating the rate of assembly or slowing it down. While Ni^{2+} and Co^{2+} coordinate with Ac-Aβ(13-21)H14A to form fibers, incubation with NH_2-Aβ(13-21)K16A form ribbons and fibers respectively.

The Zn^{2+}-Ac-Aβ(13-21)H14A fibers catalyze the retro-aldol cleavage of methodol into 6-methoxy-2-naphthaldehyde with ~3% enantioselectivity for S-methodol while Zn^{2+}-NH_2-Aβ(13-21)K16A ribbons and nanotubes showed no catalytic activity. The metal-free Ac-Aβ(13-21)H14A was inactive so also the Co^{2+}, Cu^{2+} and Ni^{2+} analogues.

Enzyme active sites commonly contain metal ions to promote catalysis. Copper ions provide proteins with redox catalytic potential and I have shown that Cu^{2+}-Aβ is capable of redox activity. Also Aβ-Zn^{2+} assemblies contain Zn^{2+} ions aligned on their surfaces providing a high density of catalytic sites and chiral environment capable of retro-aldol catalysis similar to class II aldolase. Hence, rogue enzymatic activities by Aβ-M^{2+} may be considered as a possible source of amyloid toxicity.

Methods

Microwave Assisted Solid-Phase Peptide Synthesis

Peptides were synthesized using standard FMOC peptide synthesis protocols with a Liberty CEM Microwave Automated Peptide Synthesizer using a FMOC-Rink Amide MBHA Resin. Resin was filtered and washed with dichloromethane and allowed to air dry. Peptides were cleaved from the resin using trifluoroacetic acid/thioanisole/1,2-ethanedithiol/anisole (90: 5 : 3 : 2, v/v/v/v) at room temperature for 3 hrs. The peptide was then precipitated from the cleavage solution and washed repeatedly using excess ice-cold diethyl ether. Dried peptides were dissolved in 50% acetonitrile + 0.1% trifluoroacetic acid and reverse phase HPLC using a C18-reverse phase column was used for the peptide purification. The solvents used for purification were acetonitrile and

water, both of which contained 0.1% TFA. MALDI-TOF was used to confirm the molecular weight of each peptide used. The purified peptides were lyophilized for 5 days.

Peptide Assembly

The peptide was weighed and dissolved in metal-free H_2O and sonicated for 10 minutes followed by centrifugation at 13500 rpm for 10 minutes to remove any preformed aggregates. The supernatant was used as stock solution. The peptide stock solution was diluted to desired concentration and assembly condition with the following stock solution: 50 mM MES buffer, pH 5.6 (for K16A), 50 mM HEPES buffer, pH 7.2 (for H14A), 100 mM $ZnCl_2$ or $Zn(NO_3)_2$, 100 mM $CuCl_2$ or $Cu(NO_3)_2$, 100 mM $NiCl_2$ and 100 mM $CoCl_2$. Usually, the final peptide concentration is 2 mM with 2 mM metal concentration. Peptides were allowed to assemble for approximately 8 days at room temperature unless otherwise stated and the assembly monitored by CD β-sheet signature. UV-vis Spectroscopy was also used to confirm the M^{2+} binding to the peptide.

Transmission Electron Microscopy

10 µL of 2.5 mM peptide assemblies diluted 1:9 was added to TEM grids (200 mesh copper grids with a thin carbon film support – Electron Microscopy Sciences, Hatfield, PA). Peptide assemblies were allowed to adsorb on the grid for 1 minute before excess peptide solution was wicked away with filter paper. 10 µL of freshly prepared 2-wt % uranyl acetate solutions were added to TEM grids and incubated for 1-2 minutes for fibers and 4-5 minutes for nanotubes, before wicking away excess stain. The grids are then placed in a vacuum desiccator overnight or until imaging, to remove any residual solvents. All staining solutions were prepared fresh and filtered prior to staining to

minimize artifacts. TEM micrographs were recorded with a Hitachi 7500 TEM at magnifications ranging from 2000X to 200,000X with a Tungsten filament at an accelerating voltage of 75 kV. Widths measured from TEM were converted into diameters by setting 2 x width = the tube circumference and solving for the diameter. The standard deviations of the width measurements were converted into error bars.

Electrochemical Measurements

Cyclic voltammetry experiments were performed using a potentiostat (CH Instruments, model CHI600C) with a standard three-electrode arrangement. Experiments were carried out at room temperature. The reference electrode was a silver wire and the counter electrode was a platinum wire while the working electrode was a Pt electrode. 25 mM HEPES buffer pH 7.2, 25 mM MES buffer pH 5.6 and 100 mM NaCl were the supporting electrolyte. Cyclic voltammetry was carried out in the potential range of -0.2 to 0.8 V vs. Ag/AgCl at a scan rate of 0.1 Vs^{-1} with a sensitivity of 10^{-6}. Before each measurement, the solutions were degassed by bubbling N_2 through them for about 1 minute, and the working electrode was polished before use. Voltammograms of the buffer only and of copper in buffer were also acquired as control.

Hydrogen Peroxide Assay

This was carried out as previously described [16, 60]. Aliquots of peptide-metal assemblies were incubated with solutions of 2′,7′-dichlorofluorescein diacetate (DCF-DA) in dimethylsulfoxide, horse radish peroxidase was added and the fluorescence of 2′,7′-dichlorofluorescein (DCF), the product was recorded (λ_{ex} = 485 nm and λ_{em} = 530 nm) using a spectrofluorometer.

Amplex Red Assay

Hydrogen peroxide determination using an Amplex Red Hydrogen Peroxide Kit was performed according to the manufacturer's instructions (Molecular Probes, Eugene, OR, USA) with minor modifications. To increase the sensitivity of the assay, the content of Amplex Red was diminished to a final concentration of 1 μm, without changing the peroxidase content ($0.2\ U \cdot mL^{-1}$). Fluorescence measurements of resorufin were performed at 563 nm excitation and 587 nm emission [61]. All results were corrected for solvent contribution.

UV-Vis Absorption Spectroscopy

UV-Vis absorption spectra were obtained with a JASCO V-530 UV/VIS spectrometer, using a 1cm path length quartz cuvette. Background scattering/absorption was subtracted from the solution with corresponding Cu free-of-peptide.

Retro-Aldol Measurements:

A fluorescence-based assay is used as retro-aldol cleavage of 4-hydroxy-4-(6-methoxy-2-naphthyl)-2-butanone to yield the highly fluorescent 6-methoxy-2-naphthaldehyde [62]. The peptide assemblies solution was brought to final concentrations of 300 mM NaCl and 5 % DMSO to enhance the solubility of methodol using either 25 mM HEPES at pH 7.5 (H14A peptide assemblies) or 25 mM MES at pH 5.6 (K16A peptide assemblies). Fluorescence measurements for retro-aldol kinetics were collected on a Synergy HT Multi-detection microplate reader. Triplicate samples consisted of 200 μL reaction volumes with excitation at 360 nm and fluorescence emission observed at

460 nm at a sensitivity level of 50. Time point measurements were collected every 45 s, and plates were shaken for 20 revolutions per sec at an intensity level of 3.

Product enantiomeric excess was determined by chiral HPLC analysis using a Chiralpak AD-RH (Daicel) column. When eluted isocratically with 40% CH_3CN/Water at a flow rate of 0.5 mL/min, the retention times of (R)- and (S)-methodol were 18.6 and 21.3 minutes, respectively.

References

1. Zhu, X., et al., *Causes of oxidative stress in Alzheimer disease.* Cellular and Molecular Life Sciences, 2007. **64**(17): p. 2202-2210.

2. Allan Butterfield, D., *Amyloid beta-peptide (1-42)-induced Oxidative Stress and Neurotoxicity: Implications for Neurodegeneration in Alzheimers Disease Brain. A Review.* Free Radical Research, 2002. **36**: p. 1307-1313.

3. Bush, A.I., *The metallobiology of Alzheimer's disease.* Trends in Neurosciences, 2003. **26**(4): p. 207-214.

4. Bush, A.I., C.L. Masters, and R.E. Tanzi, *Copper, β-amyloid, and Alzheimer's disease: Tapping a sensitive connection.* Proceedings of the National Academy of Sciences of the United States of America, 2003. **100**(20): p. 11193-11194.

5. Adlard, P.A. and A.I. Bush, *Metals and Alzheimer's disease.* Journal of Alzheimer's Disease, 2006. **10**(2): p. 145-163.

6. Molina-Holgado, F., et al., *Metals ions and neurodegeneration.* Biometals, 2007. **20**(3-4): p. 639-654.

7. Allsop, D., et al., *Metal-dependent generation of reactive oxygen species from amyloid proteins implicated in neurodegenerative disease.* Biochemical Society Transactions, 2008. **36**: p. 1293-1298.

8. Glenner, G.G. and C.W. Wong, *Alzheimer's disease: Initial report of the purification and characterization of a novel cerebrovascular amyloid protein.* Biochemical and Biophysical Research Communications, 1984. **120**(3): p. 885-890.

9. Masters, C.L., et al., *Amyloid plaque core protein in Alzheimer disease and Down syndrome.* Proceedings of the National Academy of Sciences of the United States of America, 1985. **82**(12): p. 4245-4249.

10. Hardy, J. and G. Higgins, *Alzheimer's disease: the amyloid cascade hypothesis.* Science, 1992. **256**(5054): p. 184-185.

11. Dong, J., et al., *Metal Binding and Oxidation of Amyloid-β within Isolated Senile Plaque Cores: Raman Microscopic Evidence†.* Biochemistry, 2003. **42**(10): p. 2768-2773.

12. Beauchemin, D. and R. Kisilevsky, *A Method Based on ICP-MS for the Analysis of Alzheimer's Amyloid Plaques.* Analytical Chemistry, 1998. **70**(5): p. 1026-1029.

13. Miller, L.M., et al., *Synchrotron-based infrared and X-ray imaging shows focalized accumulation of Cu and Zn co-localized with [beta]-amyloid deposits in Alzheimer's disease.* Journal of Structural Biology, 2006. **155**(1): p. 30-37.

14. Huang, X.D., et al., *Cu(II) potentiation of Alzheimer A beta neurotoxicity - Correlation with cell-free hydrogen peroxide production and metal reduction.* Journal of Biological Chemistry, 1999. **274**(52): p. 37111-37116.

15. Lynch, T., R.A. Cherny, and A.I. Bush, *Oxidative processes in Alzheimer's disease: the role of A[beta]-metal interactions.* Experimental Gerontology, 2000. **35**(4): p. 445-451.

16. Opazo, C., et al., *Metalloenzyme-like Activity of Alzheimer's Disease β-Amyloid.* Journal of Biological Chemistry, 2002. **277**(43): p. 40302-40308.

17. Assaf, S.Y. and S.H. Chung, *Release of endogenous Zn2+ from brain tissue during activity.* Nature, 1984. **308**(5961): p. 734-6.

18. Bush, A., et al., *Rapid induction of Alzheimer A beta amyloid formation by zinc.* Science, 1994. **265**(5177): p. 1464-1467.

19. Childers, W., et al., *Peptides Organized as Bilayer Membranes.* Angewandte Chemie International Edition, 2010. **49**(24): p. 4104-4107.

20. Dong, J., et al., *Engineering metal ion coordination to regulate amyloid fibril assembly and toxicity.* Proceedings of the National Academy of Sciences, 2007. **104**(33): p. 13313-13318.

21. Dong, J., et al., *Modulating Amyloid Self-Assembly and Fibril Morphology with Zn(II).* Journal of the American Chemical Society, 2006. **128**(11): p. 3540-3542.

22. Morgan, D.M., et al., *Metal Switch for Amyloid Formation: Insight into the Structure of the Nucleus.* Journal of the American Chemical Society, 2002. **124**(43): p. 12644-12645.

23. Childers, W.S., et al., *Templating Molecular Arrays in Amyloid's Cross-β Grooves.* Journal of the American Chemical Society, 2009. **131**(29): p. 10165-10172.

24. Miura, T., et al., *Metal Binding Modes of Alzheimer's Amyloid β-Peptide in Insoluble Aggregates and Soluble Complexes†*. Biochemistry, 2000. **39**(23): p. 7024-7031.

25. Liu, S.-T., G. Howlett, and C.J. Barrow, *Histidine-13 Is a Crucial Residue in the Zinc Ion-Induced Aggregation of the Aβ Peptide of Alzheimer's Disease†.* Biochemistry, 1999. **38**(29): p. 9373-9378.

26. Lu, K., et al., *Exploiting Amyloid Fibril Lamination for Nanotube Self-Assembly.* Journal of the American Chemical Society, 2003. **125**(21): p. 6391-6393.

27. Benzinger, T.L.S., et al., *Propagating structure of Alzheimer's β-amyloid(10–35) is parallel β-sheet with residues in exact register.* Proceedings of the National Academy of Sciences of the United States of America, 1998. **95**(23): p. 13407-13412.

28. Dong, J., et al., *Engineering Metal Ion Coordination to Regulate Amyloid Fibril Assembly and Toxicity.* Proceedings of the National Academy of Sciences of the United States of America, 2007. **104**(33): p. 13313-13318.

29. Culotta VC, G.J., *Disorders of copper transport*, in *The Metabolic & Molecular Bases of Inherited Disease*, C.R. Scriver, Editor. 2001, McGraw-Hill.

30. Guilloreau, L., et al., *Redox chemistry of copper-amyloid-beta: The generation of hydroxyl radical in the presence of ascorbate is linked to redox-potentials and aggregation state.* Chembiochem, 2007. **8**(11): p. 1317-1325.

31. Jiang, D.L., et al., *Redox reactions of copper complexes formed with different beta-amyloid peptides and their neuropathalogical relevance.* Biochemistry, 2007. **46**(32): p. 9270-9282.

32. Smith, D.G., R. Cappai, and K.J. Barnham, *The redox chemistry of the Alzheimer's disease amyloid beta peptide.* Biochimica Et Biophysica Acta-Biomembranes, 2007. **1768**(8): p. 1976-1990.

33. Bard, A.J., R. Parsons, and J. Jordan, *Standard Potentials in Aqueous Solution*. 1985: Taylor & Francis.

34. Brzyska , M., et al., *Electrochemical and Conformational Consequences of Copper (CuI and CuII) Binding to β-Amyloid(1–40).* ChemBioChem, 2009. **10**(6): p. 1045-1055.

35. Conway, B.E., *Electrochemical Data*. 1952: Elsevier Pub. Co.

36. Nelson, D.L. and M.M. Cox, *Lehninger Principles of Biochemistry*. 2010: W. H.

Freeman.

37. Jia, W., et al., *Towards a high potential biocathode based on direct bioelectrochemistry between horseradish peroxidase and hierarchically structured carbon nanotubes.* Physical Chemistry Chemical Physics, 2010. **12**(34): p. 10088-10092.

38. Reuillard, B., et al., *Non-covalent functionalization of carbon nanotubes with boronic acids for the wiring of glycosylated redox enzymes in oxygen-reducing biocathodes.* Journal of Materials Chemistry B, 2014. **2**(16): p. 2228-2232.

39. Himes, R.A., et al., *Structural Studies of Copper(I) Complexes of Amyloid-β Peptide Fragments: Formation of Two-Coordinate Bis(histidine) Complexes.* Angewandte Chemie (International ed. in English), 2008. **47**(47): p. 9084-9087.

40. •M. M. Antonijevic*, S.C.A., M. B. Petrovic, M. B. Radovanovic and A. T. Stamenkovic, *The Influence of pH on Electrochemical Behavior of Copper in Presence of Chloride Ions.* Int. J. Electrochem. Sci., 2009. **4**(4): p. 516-524

41. Boyd, S.A., L.E. Sommers, and D.W. Nelson, *Infrared Spectra of Sewage Sludge Fractions: Evidence for an Amide Metal Binding Site.* Soil Science Society of America Journal, 1979. **43**(5): p. 893-899.

42. Delincé, G., *The Ecology of the Fish Pond Ecosystem: with special reference to Africa*. 2011: Springer Netherlands.

43. Curtain, C.C., et al., *Alzheimer's disease amyloid-beta binds copper and zinc to generate an allosterically ordered membrane-penetrating structure containing superoxide dismutase-like subunits.* J Biol Chem, 2001. **276**(23): p. 20466-73.

44. Schneider, J.P., et al., *Responsive hydrogels from the intramolecular folding and self-assembly of a designed peptide.* J Am Chem Soc, 2002. **124**(50): p. 15030-7.

45. Pochan, D.J., et al., *Thermally reversible hydrogels via intramolecular folding and consequent self-assembly of a de novo designed peptide.* J Am Chem Soc, 2003. **125**(39): p. 11802-3.

46. Ozbas, B., et al., *Salt-Triggered Peptide Folding and Consequent Self-Assembly into Hydrogels with Tunable Modulus.* Macromolecules, 2004. **37**(19): p. 7331-7337.

47. Fessner, W.D., et al., *The Mechanism of Class II, Metal-Dependent Aldolases.* Angewandte Chemie International Edition in English, 1996. **35**(19): p. 2219-2221.

48. Gijsen, H.J.M., et al., *Recent Advances in the Chemoenzymatic Synthesis of Carbohydrates and Carbohydrate Mimetics.* Chemical Reviews, 1996. **96**(1): p. 443-474.

49. Mlynarski, J. and S. Bas, *Catalytic asymmetric aldol reactions in aqueous media - a 5 year update.* Chemical Society Reviews, 2014. **43**(2): p. 577-587.

50. Yoshiike, Y., et al., *New insights on how metals disrupt amyloid beta-aggregation and their effects on amyloid-beta cytotoxicity.* J Biol Chem, 2001. **276**(34): p. 32293-9.

51. Tickler, A.K., et al., *Methylation of the imidazole side chains of the Alzheimer disease amyloid-beta peptide results in abolition of superoxide dismutase-like structures and inhibition of neurotoxicity.* J Biol Chem, 2005. **280**(14): p. 13355-63.

52. Danielsson, J., et al., *High-resolution NMR studies of the zinc-binding site of the Alzheimer's amyloid β-peptide.* FEBS Journal, 2007. **274**(1): p. 46-59.

53. Dai, X.-L., Y.-X. Sun, and Z.-F. Jiang, *Cu(II) Potentiation of Alzheimer Aβ1-40 Cytotoxicity and Transition on its Secondary Structure.* Acta Biochimica et Biophysica Sinica, 2006. **38**(11): p. 765-772.

54. Raman, B., et al., *Metal ion-dependent effects of clioquinol on the fibril growth of an amyloid {beta} peptide.* J Biol Chem, 2005. **280**(16): p. 16157-62.

55. Mold, M., et al., *Copper prevents amyloid-β(1–42) from forming amyloid fibrils under near-physiological conditions in vitro.* Scientific Reports, 2013. **3**: p. 1256.

56. Zou, J., K. Kajita, and N. Sugimoto, *Cu(2+) Inhibits the Aggregation of Amyloid beta-Peptide(1-42) in vitro.* Angew Chem Int Ed Engl, 2001. **40**(12): p. 2274-2277.

57. van Houwelingen, T., et al., *Isolation and characterization of a blue copper protein from Thiobacillus versutus.* European Journal of Biochemistry, 1985. **153**(1): p. 75-80.

58. Faller, P., C. Hureau, and O. Berthoumieu, *Role of metal ions in the self-assembly of the Alzheimer's amyloid-beta peptide.* Inorg Chem, 2013. **52**(21): p. 12193-206.

59. Viles, J.H., *Metal ions and amyloid fiber formation in neurodegenerative diseases. Copper, zinc and iron in Alzheimer's, Parkinson's and prion diseases.* Coordination Chemistry Reviews, 2012. **256**(19–20): p. 2271-2284.

60. Brzyska, M., A. Bacia, and D. Elbaum, *Oxidative and hydrolytic properties of β-amyloid.* European Journal of Biochemistry, 2001. **268**(12): p. 3443-3454.

61. Zhou, M., et al., *A stable nonfluorescent derivative of resorufin for the fluorometric determination of trace hydrogen peroxide: applications in detecting the activity of phagocyte NADPH oxidase and other oxidases.* Anal Biochem, 1997. **253**(2): p. 162-8.

62. List, B., C.F. Barbas, and R.A. Lerner, *Aldol sensors for the rapid generation of tunable fluorescence by antibody catalysis.* Proceedings of the National Academy of Sciences of the United States of America, 1998. **95**(26): p. 15351-15355.

63. Wagner, J., R.A. Lerner, and C.F. Barbas, III, *Efficient Aldolase Catalytic Antibodies That Use the Enamine Mechanism of Natural Enzymes.* Science, 1995. **270**(5243): p. 1797-1800.

Chapter 7: Conclusions- Amyloid as a Versatile Self-Propagating Catalyst

Amyloid assemblies share many common structural features of well folded enzymes including the capacity to bind and interact with small molecules and metal binding sites [1-4]. In contrast to enzymes which contain highly specific and effective single active sites, the amyloid assemblies contain multiple binding sites all organized side-by-side in a lattice arrangement templating small molecules at high density for chemical reaction.

In chapter 2, the possibility of the binding sites templating polymerization reactions was evaluated through imine condensation of 6-amino-2-naphthaldeyde. This substrate reacts in aqueous solutions of peptide nanotubes Ac-KLVFFAL-NH_2, Ac-HLVFFAL-NH_2 and Ac-RLVFFAL-NH_2 to form at least dimers. To test for polymerization, the amide dimer was prepared and shown to bind 100 folds weaker to the peptide nanotubes compared to the monomer. This unexpected result may be important for avoiding product inhibition in condensation reaction and also may limit polymerization, motivating the search for a reaction allowing the catalysis to be more completely explored.

Positioning of the nucleophilic lysine side chain within a hydrophobic groove of the nanotube surface is a feature similar to class I aldolases. The retro-aldol cleavage of methodol to fluorescent 6-methoxy-2-naphthaldehyde in chapters 3 and 4 proved valuable to dissect the catalytic mechanism. The β-rich peptide assemblies provided a catalytically competent scaffold where subtle changes in peptide sequence and/or assembly had significant impact on catalyst efficiency and enantioselectivity. Elimination of the binding pockets in fibers abolishes catalytic activity. Adding a charge to the binding grooves also eliminated activity, highlighting the role of substrate binding in these assemblies.

Shortening the primary amine tether of lysine significantly increased the rates of methodol conversion. A kinetic model was developed that suggests the chemical step of C-C cleavage is rate limiting and determines the enantioselectivity.

Based on these results, chapter 5 explored the condensation of 2-acetonaphthone and 6-methoxy-2-naphthaldehyde. The nanotubes catalyzed aldol product formation in less than 1 hour of incubation with high enantioselectivity, and the aldol formed binds effectively to the nanotubes. We suspect that the rigidity of the amide dimer reduces binding affinity and the flexibility of the aldol allows for a better match to the groove surface and a possible route to polymerization.

Enzyme active sites commonly contain metal ions that promote catalysis. Amyloid assemblies have been shown to create a two-dimensional organized array of metals at well-defined intervals along the entire solvent-accessible interface [1-3]. Chapter 6 explores copper binding with two model peptides Cu^{2+}-Ac-Aβ(13-21)H14A and Cu^{2+}-NH_2-Aβ(13-21)K16A that assembled as fibers and ribbon respectively. The copper ions provided these assemblies with redox sites. In chapters 6, Zn^{2+}-Aβ fibers are shown capable of retro-aldol catalysis similar to class II aldolase, further extending the catalytic range of these self-propagating Aβ assemblies.

The diversity of the catalytic capabilities of the assemblies is remarkable, representing easily accessible catalyst for the generation of a metabolic diversity that could well be critical to the emergence of chemical evolution.

Origins of the Biosphere

Life would not exist without enzymes. Within cells, enzymes initiate a myriad of chemical reactions that work in concert to create a virtual factory that drives cellular processes critical for life. These enzymes are so critically important because many metabolic reactions are sluggish and do not occur in water. The complexity of these polypeptide machines are now being computationally designed [5-8] through directed evolution of enzyme functions [9, 10], and detailed characterization of mechanisms [11]. Early events in the emergence of life would have benefited from such general and accessible catalysts to create the rich molecular inventory for metabolism. The probability of even a simple 100 amino acid catalytic enzyme emerging by successive random trials is $(1/20)^{100}$ or 1 chance in 1.27×10^{130} and seems unimaginable. One question that has been bothering scientists is where did enzymes come from? For polypeptides to fold into such complex and exquisite 3D morphology that results into enzymes, some sort of trial and error must have taken place at the beginning of our biosphere. Other polymers such as RNA have also been proposed as early ribozyme catalysts [12-14], however the molecular complexity of the ribonucleic acid molecular skeleton also presents hurdles for early emergence. Given the high improbabilities of enzyme emergence, are there catalysts with structural and functional complexity greater than simple mineral surfaces [15], but more probable than RNA or enzymes able to access complex folds?

Not only do simple peptides access amyloid folds, but these phases self-replicate [16-18], transmit conformational information with high fidelity [19-22], achieve polymorphic diversity [17, 23, 24], are environmentally responsive [25, 26] and have been suggested to be ancient folds [27]. This rich tapestry of dynamically interchangeable

catalytic surfaces presented by these supramolecular assemblies suggests an emergent, self-organizing strategy to build the complex reaction networks necessary for early protein network evolution.

In the Context of Disease

The cross-β architecture of amyloid is shared by the infective prions and dozens of misfolding protein diseases [28], yet the functional forms that propagate from these assemblies to compromise cellular processes remain unknown. Template-directed propagation enables prion amplification, and now minimal cross-β grooves, the common feature of all amyloids, are shown to rival designed retro-aldol catalysts [29-35]. The finding that assemblies of the simple nucleation core of the Aβ peptide display such diverse catalytic potential has profound implications for the nearly 50 protein misfolding diseases. The accumulation of such catalysts in cells and tissues could well provide the common etiological link between the disease states. When extended to binding unique arrays of transition metals [2, 36, 37], chromogenic substrates [38], and scaffolds for nucleobase-pairing [39], the range of chemical functions that could emerge from these assemblies seems limitless. But maybe more importantly, the proximity of the chiral catalytic sites along the amyloid is compatible with DNA registry. The ability of nucleic acids to template disease-relevant nucleoprotein structures [40, 41] could easily disrupt cellular information processing in disease [42-44].

In the Context of Materials

The diverse populations for the cross-β phases highlight them as a remarkable network, whether their properties can be extended or implemented in other scaffolds has

yet to be tested, but appear possible. Future studies will certainly continue to exploit and extend the capabilities of these paracrystalline phases.

Future Outlook

Amyloid self-assembling supramolecular systems holds great promise for the development of an innovative generation of highly active and recyclable catalysts. The flexible structures of peptides make it possible to put other special functional residues of complex protein into simple peptides which can then assemble to arrange abundant functional groups on the surface to achieve certain unexpected properties. The well-ordered nanostructures can also present an attractive scaffold for developing new enzymes. For example, mixing other enzymes with the peptide assemblies to achieve multi-enzyme systems. In addition, the supramolecular peptide nanotubes studied provides promiscuous enantioselective catalysts of carbon-carbon bond and carbonyl condensation reactions since same nanotubes that catalyze imine condensation also show aldol/retro-aldol activities. Hence, these nanotubes are potential valuable source of promiscuous catalytic activities which can be amplified and refined to generate diversified supramolecular catalysts with broadened substrate and reaction scope which opens the way for the possible development of a new class of synthetic peptide-based catalysts that might be adaptable for industrial application.

References

1. Dong, J., et al., *Engineering Metal Ion Coordination to Regulate Amyloid Fibril Assembly and Toxicity.* Proceedings of the National Academy of Sciences of the United States of America, 2007. **104**(33): p. 13313-13318.

2. Dong, J., et al., *Modulating Amyloid Self-Assembly and Fibril Morphology with Zn(II).* Journal of the American Chemical Society, 2006. **128**(11): p. 3540-3542.

3. Morgan, D.M., et al., *Metal Switch for Amyloid Formation: Insight into the Structure of the Nucleus.* Journal of the American Chemical Society, 2002. **124**(43): p. 12644-12645.

4. Childers, W.S., et al., *Templating Molecular Arrays in Amyloid's Cross-β Grooves.* Journal of the American Chemical Society, 2009. **131**(29): p. 10165-10172.

5. Jiang, L., et al., *De novo computational design of retro-aldol enzymes.* Science, 2008. **319**(5868): p. 1387-91.

6. Siegel, J.B., et al., *Computational design of an enzyme catalyst for a stereoselective bimolecular Diels-Alder reaction.* Science, 2010. **329**(5989): p. 309-13.

7. Thyme, S.B., et al., *Exploitation of binding energy for catalysis and design.* Nature, 2009. **461**(7268): p. 1300-4.

8. Rothlisberger, D., et al., *Kemp elimination catalysts by computational enzyme design.* Nature, 2008. **453**(7192): p. 190-5.

9. Liu, L., et al., *Directed evolution of an orthogonal nucleoside analog kinase via fluorescence-activated cell sorting.* Nucleic Acids Res, 2009. **37**(13): p. 4472-81.

10. Romero, P.A. and F.H. Arnold, *Exploring protein fitness landscapes by directed evolution.* Nat Rev Mol Cell Biol, 2009. **10**(12): p. 866-76.

11. Lassila, J.K., D. Baker, and D. Herschlag, *Origins of catalysis by computationally designed retroaldolase enzymes.* Proc Natl Acad Sci U S A, 2010. **107**(11): p. 4937-42.

12. Fedor, M.J. and J.R. Williamson, *The catalytic diversity of RNAs.* Nat Rev Mol Cell Biol, 2005. **6**(5): p. 399-412.

13. Cech, T.R., *The chemistry of self-splicing RNA and RNA enzymes.* Science, 1987. **236**(4808): p. 1532-9.

14. Gilbert, W., *Origin of life: The RNA world.* Nature, 1986. **319**(6055): p. 618-618.

15. Cody, G.D., *TRANSITION METAL SULFIDES AND THE ORIGINS OF METABOLISM.* Annual Review of Earth and Planetary Sciences, 2004. **32**(1): p. 569-599.

16. Takahashi, Y. and H. Mihara, *Construction of a chemically and conformationally self-replicating system of amyloid-like fibrils.* Bioorganic & Medicinal Chemistry, 2004. **12**(4): p. 693-699.

17. Eichner, T. and S.E. Radford, *A diversity of assembly mechanisms of a generic amyloid fold.* Mol Cell, 2011. **43**(1): p. 8-18.

18. Chiti, F. and C.M. Dobson, *Protein misfolding, functional amyloid, and human disease.* Annu Rev Biochem, 2006. **75**: p. 333-66.

19. Wickner, R.B., et al., *Amyloid diseases of yeast: prions are proteins acting as genes.* Essays Biochem, 2014. **56**: p. 193-205.

20. Wiltzius, J.J., et al., *Molecular mechanisms for protein-encoded inheritance.* Nat Struct Mol Biol, 2009. **16**(9): p. 973-8.

21. Maury, C.P.J., *Self-replicating protein conformations and information transfer: The adaptive β-sheet model.* Bioscience Hypotheses, 2008. **1**(2): p. 82-89.

22. Maury, C.P.J., *Self-Propagating β-Sheet Polypeptide Structures as Prebiotic Informational Molecular Entities: The Amyloid World.* Origins of Life and Evolution of Biospheres, 2009. **39**(2): p. 141-150.

23. Greenwald, J. and R. Riek, *Biology of Amyloid: Structure, Function, and Regulation.* Structure, 2010. **18**(10): p. 1244-1260.

24. Toyama, B.H. and J.S. Weissman, *Amyloid structure: conformational diversity and consequences.* Annu Rev Biochem, 2011. **80**: p. 557-85.

25. Westergard, L. and H.L. True, *Extracellular environment modulates the formation and propagation of particular amyloid structures.* Mol Microbiol, 2014. **92**(4): p. 698-715.

26. Lu, K., et al., *Macroscale assembly of peptide nanotubes.* Chemical Communications, 2007(26): p. 2729-2731.

27. Maury, C.P.J., *Origin of life. Primordial genetics: Information transfer in a pre-RNA world based on self-replicating beta-sheet amyloid conformers.* Journal of Theoretical Biology, 2015. **382**: p. 292-297.

28. Jahn, T.R., et al., *The common architecture of cross-beta amyloid.* J Mol Biol, 2010. **395**(4): p. 717-27.

29. Johnsson, K., et al., *Synthesis, structure and activity of artificial, rationally designed catalytic polypeptides.* Nature, 1993. **365**(6446): p. 530-532.

30. Reymond, J.-L. and Y. Chen, *Catalytic, enantioselective aldol reaction using antibodies against a quaternary ammonium ion with a primary amine cofactor.* Tetrahedron Letters, 1995. **36**(15): p. 2575-2578.

31. Wagner, J., R.A. Lerner, and C.F. Barbas, III, *Efficient Aldolase Catalytic Antibodies That Use the Enamine Mechanism of Natural Enzymes.* Science, 1995. **270**(5243): p. 1797-1800.

32. Hoffmann, T., et al., *Aldolase Antibodies of Remarkable Scope.* Journal of the American Chemical Society, 1998. **120**(12): p. 2768-2779.

33. Tanaka, F., *Development of protein, peptide, and small molecule catalysts using catalysis-based selection strategies.* The Chemical Record, 2005. **5**(5): p. 276-285.

34. Müller, M.M., et al., *A Rationally Designed Aldolase Foldamer.* Angewandte Chemie International Edition, 2009. **48**(5): p. 922-925.

35. Ruscio, J.Z., et al., *The Influence of Protein Dynamics on the Success of Computational Enzyme Design.* Journal of the American Chemical Society, 2009. **131**(39): p. 14111-14115.

36. Dong, J., et al., *Engineering metal ion coordination to regulate amyloid fibril assembly and toxicity.* Proc Natl Acad Sci, 2007. **104**(33): p. 13313-13318.

37. Rufo, C.M., et al., *Short peptides self-assemble to produce catalytic amyloids.* Nat Chem, 2014. **6**(4): p. 303-309.

38. Liang, Y., et al., *Light harvesting antenna on an amyloid scaffold.* Chemical Communications, 2008(48): p. 6522-6524.

39. Liu, P., et al., *Nucleobase-directed amyloid nanotube assembly.* Journal of the American Chemical Society, 2008. **130**(50): p. 16867-16869.

40. Ni, R. and Y. Chau, *Structural Mimics of Viruses Through Peptide/DNA Co-Assembly.* Journal of the American Chemical Society, 2014.

41. Braun, S., et al., *Amyloid-associated nucleic acid hybridisation.* PLoS ONE, 2011. **6**(5): p. e19125.

42. Supattapone, S., *What makes a prion infectious?* Science, 2010. **327**(5969): p. 1091-2.

43. Geoghegan, J.C., et al., *Selective Incorporation of Polyanionic Molecules into Hamster Prions.* Journal of Biological Chemistry, 2007. **282**(50): p. 36341-36353.

44. Grossman, A., B. Zeiler, and V. Sapirstein, *Prion protein interactions with nucleic acid: possible models for prion disease and prion function.* Neurochem Res, 2003. **28**(6): p. 955-963.